Radiative Models of Sagittarius A* and M87 from Relativistic MHD Simulations

Jason Dexter

A dissertation submitted in partial fulfillment of
the requirements for the degree of

Doctor of Philosophy

University of Washington

2011

Program Authorized to Offer Degree: Department of Physics

University of Washington
Graduate School

This is to certify that I have examined this copy of a doctoral dissertation by

Jason Dexter

and have found that it is complete and satisfactory in all respects,
and that any and all revisions required by the final
examining committee have been made.

Chair of the Supervisory Committee:

Eric Agol

Reading Committee:

Eric Agol

James Bardeen

Miguel Morales

Leslie Rosenberg

Date:

University of Washington

Abstract

Radiative Models of Sagittarius A* and M87 from Relativistic MHD Simulations

Jason Dexter

Chair of the Supervisory Committee:
Professor Eric Agol
Department of Astronomy

The discovery that the magnetorotational instability (MRI) is likely the mechanism of angular momentum transport and accretion has led to rapid progress in the theory of black hole accretion. General relativistic MHD (GRMHD) simulations currently provide the most realistic physical description of black hole accretion flows, but neglect radiation and are currently only applicable to low luminosity systems, where the radiation can be added in post-processing. To connect simulations with observations, we have developed codes for the semi-analytic computation of Kerr photon orbits (`geokerr`) and for the calculation of time-dependent, general relativistic radiative transfer via ray tracing (`grtrans`). The Galactic center black hole candidate, Sgr A*, provides an ideal first problem for study using GRMHD and these radiative transfer methods. Recent very long baseline interferometry (VLBI) observations detected the structure of its accretion flow on event horizon scales, allowing a direct comparison between accretion disk theory and observation. We compare millimeter wavelength images and light curves from a set of three-dimensional GRMHD simulations to VLBI and spectral observations of Sgr A* using general relativistic radiative transfer. The GRMHD models provide an excellent fit to current observations. Magnetic turbulence driven by the MRI naturally explains the observed millimeter variability. Fitting models to observations allows estimates of the inclination and position angles of the black hole, as well as of the median electron temperature in the millimeter emission region and the

accretion rate onto the black hole. The black hole shadow, a signature of the event horizon, is unobscured in all models and may be detectable with VLBI experiments in the next 5-10 years. We also consider "tilted" accretion disk models, where the angular momentum axis of the accretion flow is misaligned from the black hole spin axis. The additional degree of freedom in these models allows a wide range of viable possibilities for Sgr A*. Additional observations both of visibility amplitudes and closure phases will constrain the models further. We also study generic observational consequences of tilt in black hole accretion disks, and find that the radiation edge of these systems is independent of black hole spin; in stark contrast to the untilted disks where it decreases with increasing spin, roughly tracking the marginally stable orbit. Line profiles based on gravitational redshifts and Doppler shifts of these simulations vary strongly with observer azimuth. Coupled with precession, this may lead to strongly time-varying emission lines from tilted, geometrically thick disks. Finally, radiative models of M87 are constructed in a similar fashion to Sgr A*. The M87 spectrum can be fit by either a jet or a jet/disk model. The geometry in M87 can be reasonably constrained by observations of the extended jet emission, and the resulting millimeter images are fairly robust despite considerable model uncertainties. The Gaussian FWHM inferred from mm-VLBI on current telescopes should be 36-41 μas. Jet images are more compact than disk images, and in either case the shadow in M87 should be accessible to future VLBI observations.

TABLE OF CONTENTS

LIST OF FIGURES

Figure Number Page

LIST OF TABLES

ACKNOWLEDGMENTS

This work was supervised by Eric Agol, and I am grateful for his vision, patience and advice. Chris Fragile provided valuable mentorship, hospitality, travel support and simulation data. Thanks also to Jonathan McKinney for sharing simulation data. I had many stimulating conversations with Omer Blaes during my stay at the Kavli Institute for Theoretical Physics at UC Santa Barbara in 2008, and he also helped to make my first international conference memorable. Jim Bardeen provided useful feedback which improved this thesis, and I have benefitted from helpful conversations with Miguel Morales.

Graduate school was made far more enjoyable by Real Friends in the Physics department. In particular, Matthew Kerr has been a role model and a great friend throughout. I plan to print out our Gchat logs in their entirety and tape them to my wall. Thanks also to Stan Vlcek for processing fellowship applications with minimal lead time, and to the NASA Earth & Space Science Fellowship program for financial support during the last three years of my graduate career.

This work would not have been possible without the love and support of my family and my wife Kalista. Her tolerance of my increasingly laid-back attitude toward dirty dishes in the weeks prior to the completion of this thesis is especially appreciated. Finally, thanks to Seattle for its affordable happy hours, comfortable coffee shops and adorable electric trolley buses.

Chapter 1

INTRODUCTION

Black holes are the simplest macroscopic objects. In general relativity, they are exactly described by only three parameters: mass, spin and charge. Oppenheimer & Snyder [150] first showed that for sufficiently massive stars, the final outcome of stellar evolution is continual collapse until the gravitational force becomes so strong that light can no longer escape. The resulting black hole, initially called a "frozen star," remained a theoretical curiosity until the discovery of active galactic nuclei (AGN) and bright X-ray sources associated with stellar mass binary systems (black hole binaries; BHBs).

1.1 Astrophysical Black Holes

These astronomical sources were first postulated to be associated with black holes due to their extraordinary luminosities (AGN, [121, 12, 161]) or large inferred masses (BHBs, e.g., Cygnus X-1, [24, 198]). These two arguments are addressed in turn.

Although black holes themselves produce negligible electromagnetic radiation, the process of ambient matter falling into black holes (accretion) can be remarkably efficient at converting rest mass into photons. Net angular momentum either due to accretion from a binary companion (BHBs) or from a nearly plunging orbit originating at a large radius (AGN) causes infalling material to circularize into an accretion disk around the black hole. Stresses cause angular momentum to be transported outwards, allowing the inner material to accrete. The resulting infall can be very slow compared to the orbital time, and as long as the disk is massive enough (accretion rate, $\dot{M}$, is large enough), it cools efficiently and remains geometrically thin and optically thick (opaque) [176]. Under the assumption that all dissipated energy is radiated locally, the energy release is just the binding energy of the inner radius of the disk.

For a black hole, this inner radius is historically assumed to be the innermost stable circular orbit (ISCO), inside of which all bound particle trajectories pass through the event horizon. Then the radiative efficiency, $\eta \equiv L/\dot{M}c^2$, depends only on black hole spin, increasing from $\eta \simeq 0.06 - 0.4$ for $a = 0.0 - 0.998$, where 0.998 is the theoretical maximum in standard thin accretion disk theory [192], defined as the point where the specific angular momentum of material falling onto the black hole is equal to its spin angular momentum. The energy release from thin disk black hole accretion is about $10 - 50$ times larger than that from nuclear fusion, so that accretion onto supermassive black holes ($10^{6-9} M_\odot$) in the center of galaxies can explain the enormous luminosities of AGN. Dynamical measures of stellar velocities from our own and other nearby galaxies imply central point masses in this range, further evidence that not only are AGN likely associated with black hole accretion, but that massive black holes are likely present in the center of most, if not all, galaxies. Most of these black holes are not "active" (in the AGN phase) most of the time.

Dynamical measurements from some stellar binaries imply companion masses around $10 M_\odot$, called stellar mass black holes since no known stellar objects can prevent gravitational collapse at those masses. Many of these BHBs are also bright X-ray sources with large radiative efficiencies. Thin disk accretion onto black holes is actually less efficient than onto neutron stars, since energy can be lost to the event horizon in the black hole case. Powerful evidence for the existence of event horizons comes from the observed divide in efficiency between low (neutron star) and high (black hole) mass X-ray binaries, matching the theoretical expectation [137].

Stellar mass black holes form through the gravitational collapse of massive stars, but the formation of massive black holes is poorly understood. The two possible scenarios are growth of a stellar mass or massive seed ($\sim 1000 M_\odot$, [116, 19]) from accreting gas and subsequently merging with other black holes over the history of the Universe. The presence of supermassive black holes at relatively high cosmological redshift [71] is challenging to explain with growth from stellar mass seeds [180, 196], while there are problems with all formation scenarios for massive seed black holes.

In either scenario, there should also be a large number of black holes with masses in between the stellar and massive black hole ranges (intermediate mass black holes, $10^{3-6} M_\odot$). Presently, there is some tentative evidence for the existence of these objects in ultraluminous

X-ray sources [50].

All evidence for the existence of black holes is indirect. No other known object can explain observations of AGN and BHBs, but there is still no direct evidence for the existence of a black hole event horizon.

1.2 Millimeter Very Long Baseline Interferometry

The best studied massive black hole candidate is the compact radio source in the center of the Milky Way, discovered by Balick & Brown in 1974 (Sagittarius A*, abbreviated Sgr A*; [11]). The orbits of several young stars within tens of AU of the center of the Galaxy imply a point mass of $\simeq 4 \times 10^6 M_\odot$. Astrometric measurements of the change in centroid position of Sgr A* with time imply a mass of at least $4 \times 10^5 M_\odot$ [163] in the very long baseline interferometry (VLBI) size of $\lesssim$ 1AU [115, 187, 61]. This is about 2 orders of magnitude above the size of the event horizon for that mass, the most stringent limit on any black hole candidate. There is also compelling evidence for the lack of a hard surface (presence of an event horizon) in Sgr A* from its tiny size and small millimeter/infrared luminosity [34].

The VLBI observations provide a unique opportunity for the study of precision black hole astrophysics in the Galactic center, and for finding the first direct evidence for the existence of a black hole event horizon. Despite its relatively small mass, Sgr A* is one of the two largest black holes in angular size. (M87, a factor of $\simeq$ 2000 more massive and more distant, is the other main target for mm-VLBI.) The expected event horizons of these systems still only span about 10μas on the sky, and resolving such a scale is an enormous observational challenge. The observations must be done at millimeter (mm) wavelengths on earth-sized baselines ($\sim 10^3$km). The coherence time of the atmosphere at 1.3mm, the shortest wavelength used so far, is only about 10s on average [59]. There are few available mm telescopes with the necessary sensitivity and equipment (correlators and precise clocks) for use in the VLBI array. So far, Sgr A* has been detected at two separate epochs using telescopes between Arizona (Submillimeter Telescope Observatory, SMTO) and Hawaii (James Clerk Maxwell Telescope, JCMT) and once between Hawaii and California (Combined Array for Research in Millimeter-wave Astronomy, CARMA) [61, 74]. Interferometry experiments sample the Fourier transform (complex "visibility") of the spatial brightness distribution ("image") of the source at spatial frequencies corresponding to the lengths and orientations of the baselines (position vectors between telescopes, denoted u and v for spatial frequencies k_x and k_y with x and y the spatial position vectors corresponding to East-West and North-South, respectively) projected onto the plane of the sky. Reconstructing the image requires sufficient sampling of the spatial frequencies of the Fourier transform ("uv-plane"), both from many telescopes ($n(n-1)/2$ baseline pairs for n telescopes) and from long-term monitoring of a source since the projections of each baseline onto the sky change as the earth rotates (this technique for filling in the uv-plane is called "earth aperture synthesis").

Earth aperture synthesis may not be possible in Sgr A*, since it is variable at the $\simeq 40-50\%$ level on hour timescales, comparable to the timescale for baselines to change from the rotation of the Earth. The scarcity of available mm-VLBI telescopes and the short timescale variability of Sgr A* require that analysis be done in Fourier space and that interpretation of the data is necessarily model-dependent. Making use of the unparalleled extremely high-resolution data then requires accurate models of the brightness distribution of the source, which can be Fourier transformed and compared to the observations.

The observational data have been analyzed with two geometric models for the surface brightness: a symmetric Gaussian or a "ring" (annulus of constant brightness). The source FWHM when fit with a Gaussian brightness distribution is 37μas, *smaller* than the $\simeq 50\mu$as size of the circular photon orbit associated with the black hole shadow. However, the claim by Doeleman et al. that, "...a size of 37^{+16}_{-10} microarcseconds is less than the expected apparent size of the event horizon of the presumed black hole, suggesting that the bulk of Sgr A* emission may not be centred on the black hole..." is false although the conclusion turns out to be likely correct (see Chapter 5). The size they report is from assuming a Gaussian surface brightness distribution, while their own ring model shows that a model "larger" than the apparent size of the event horizon is viable. These difficulties demonstrate the necessity of properly fitting models to data rather than drawing conclusions from model-dependent parameters such as "size."

The ideal theoretical model of Sgr A* for comparison with the mm-VLBI observations should be general relativistic, since the millimeter emission is concentrated close to the black hole in all models. It should be time-dependent, since Sgr A* is significantly variable at mm wavelengths. In this thesis, we will argue that sophisticated numerical models of black hole accretion flows are uniquely suited to this problem.

The other source of interest for extremely high resolution mm-VLBI is M87, whose angular size is roughly the same as that of Sgr A*. M87 is similar to Sgr A*, except that it powers a Mpc-scale, ultrarelativistic jet. Depending on the emission model, the collimation region of this jet may be accessible to VLBI observations.

Before describing the spectral properties of Sgr A* and M87, the theory of black hole accretion flows is briefly summarized, with particular emphasis on models of low-luminosity accretion flows appropriate for these sources.

1.3 Black Hole Accretion Theory

Accretion is of profound importance in astrophysics, with applications ranging from star formation to supernovae. Black hole accretion flows are unique in that there is no "hard surface," so that internal energy stored in the accreting material can be lost through the event horizon of the black hole. This leads to a wide range of possible behaviors in black hole accretion flows, some of which are summarized below.

All of the following simplified models make common assumptions: the accreting material is assumed to act as a collisional, one-component fluid. Even when the flow is tenuous, a weak (sub-equipartition) magnetic field couples the particles, effectively creating collisions. The mean free path is then reduced to the Larmor radius, which for protons is smaller than the radius, r.[1] Although it was recognized early on that magnetic fields could be important to the physics of accretion [176], they are left out of the standard theory altogether.

1.3.1 Spherical Accretion

The simplest possible case is the accretion of material with no angular momentum. Then there is no preferred direction, all quantities depend only on the radius, r, and v^r is the only non-vanishing component of the fluid velocity. This was the first type of accretion flow

---

[1] The mean free path is only short perpendicular to the field lines and unchanged along them. Thus collisions are effectively created only when the field is incoherent or tangled on scales smaller than the mean free path.

studied [25], and is known as spherical or "Bondi" accretion.[2]

The equations of spherical accretion, from conservation of mass and momentum, are:

$$r^2\rho v = C_1, \tag{1.1}$$

$$\frac{v^2}{2} + \int_{p_0}^{p} \frac{dp}{\rho} - \frac{GM}{r} = C_2, \tag{1.2}$$

where $v = v^r$ in spherical coordinates, p_0 is the ambient pressure and $C_{1,2}$ are constants. These equations can be easily generalized to relativity [133]. The infall timescale is short, with the velocity nearing the speed of light in the general relativistic case. The particle density increases to the event horizon, and the temperature of the infalling gas is nearly virial, reaching $\simeq 10^{12}$K at the event horizon. Radiative properties of this solution are discussed in Section 2.4.3. Spherical accretion flows emit little light since the infall timescale time is so short. The particle densities are low enough that synchrotron radiation dominates the emission, and the bulk of the radiation is released at millimeter and far infrared wavelengths.

The assumption of zero angular momentum in spherical accretion is likely poor. In binary systems, where matter is stripped from the stellar companion, the accreting material will have net angular momentum. Even in sources accreting from the interstellar medium, material falls in from the black hole sphere of influence, $r_{\text{inf}} = GM/\sigma^2$, where σ is the local velocity dispersion. This is a ratio c_s^2/σ^2 larger than even the Bondi radius, where c_s is the speed of sound, so that pure plunging orbits are highly unlikely.[3] In both cases, the infalling material will circularize and lose its excess angular momentum before accreting. This leads to the formation of an accretion disk around the black hole.

---

[2] In the case where the black hole moves through an ambient medium at rest, it is known as "Bondi-Hoyle" accretion [26].

[3] As discussed in Chapter 4, the accretion rate onto the Galactic center black hole determined by several independent methods is $\sim 10^{-9} - 10^{-7} M_\odot \text{yr}^{-1}$, a factor of 10^{3-4} smaller than the estimate from Bondi accretion.

1.3.2 Thin Disk Accretion

This is the situation for luminous sources such as AGN and BHBs in the "thermal" state [164]. The theory describing these systems, still the standard theory of accretion today, was developed in the early 1970's and is known as thin disk accretion or the "alpha" model [176, 148]. The thin disk solution is elegant: from conservation laws and the assumptions mentioned above (local radiation of dissipated energy and truncation at the ISCO), this one-zone (vertically-averaged), steady-state solution predicts the luminosity of black hole accretion flows without any reference to the physical cause of angular momentum transport and accretion. It successfully explains the large luminosities of AGN, and the fact that AGN spectra peak in the ultraviolet while BHB thermal state spectra peak in X-rays.

The accretion flow is now assumed to be geometrically thin, such that quantities only depend on the cylindrical radius, R, and the equations are vertically integrated for tractability. The vertical structure remains unconstrained. The non-relativistic fluid equations then can be written as equations for conservation of mass, angular momentum, and energy [22]:

$$\begin{aligned} \dot{M} &= 4\pi R H \rho v, && (1.3) \\ \dot{M}\frac{d\ell}{dR} &= \frac{d}{dR}\left(4\pi R^2 H \tau_{R\phi}\right), && (1.4) \\ -4\pi R^2 H \tau_{R\phi}\frac{d\Omega}{dR} &= 2\pi R(2F^-), && (1.5) \end{aligned}$$

where Ω (v) is the orbital (radial) velocity and H is the disk height. ρ is the density, $\dot{M}$ is the (constant) accretion rate, $\tau_{R\phi}$ is the torque between disk annuli and F^- is the emergent flux leaving the disk vertically. In the thin disk context, the equation for conservation of radial momentum gives $\Omega^2 = GM/R^3$ so that the angular momentum profile is Keplerian.

Assuming the dissipation from torques in the disk all leaves immediately (the disk cools efficiently), the flux as a function of radius can be written as,

$$F^- = \frac{3GM\dot{M}}{8\pi R^3}\left[1 - \left(\frac{R_{in}}{R}\right)^{1/2}\right], \qquad (1.6)$$

where R_{in} is the inner boundary of the disk usually associated with the ISCO and we have made the standard (but controversial) assumption that the torque vanishes at the ISCO.

Integrating over the top and bottom of the disk, the total luminosity is then,

$$L = \int_{R_{in}}^{\infty} dR 2\pi R (2F^{-}) = \frac{GM\dot{M}}{2R_{in}}, \tag{1.7}$$

which is simply the binding energy of the inner disk radius. The radiative efficiency is then,

$$\eta = \frac{GM}{2R_{ISCO}c^2} \tag{1.8}$$

depending only on the spin a of the black hole. Relativistic effects alter the binding energy of the inner disk radius, leading to small corrections in the above formula and $\eta \simeq 0.05 - 0.4$ for $a = 0.0 - 0.998$. The peak effective temperatures from $L(r) = \sigma_b T_{\text{eff}}^4$ are then $\sim 10^4$K for AGN and $\sim 10^7$K for BHBs, whose blackbody peaks are located in the UV and X-ray, respectively.

Thin disk spectra, neglecting atmospheric radiative transfer effects, are multi-temperature blackbodies, with an effective temperature at each radius set by $L(r)$. The flux is proportional to M^{-1} for a fixed relative accretion rate ($\dot{M} \propto M$, $r \propto M$), so that $T_{\text{eff}} \propto M^{-1/4}$. This model works particularly well in fitting certain BHB spectra, but provides a marginal fit at best in the AGN case. Regardless of its limited ability to explain spectral and other measurements of AGN, thin disk theory is still commonly used to interpret observations.

A prescription for angular momentum transport is necessary to go further. Molecular viscosity is far too weak to produce appreciable accretion. The famous “alpha” prescription,

$$\tau_{R\phi} = \alpha P, \tag{1.9}$$

where the stress is proportional to the vertically integrated pressure, allows a solution known as the “alpha” model. Although the physical cause of angular momentum transport and accretion is completely ignored in this prescription, the resulting solution is predictive: most of the results for the structure of the disk are highly insensitive to the value of α.

The lack of a physical mechanism for accretion is one of many theoretical shortcomings of the alpha model. The vertical structure of the disk is left completely unconstrained. The model predicts that radiation pressure supports the disk in AGN and at small radius in BHBs, but is thermally and viscously unstable when this is the case [177, 114]. Other parameterizations have been used instead of Equation 1.9, with no physical motivation other than to avoid these instabilities.

1.3.3 Advection-Dominated Accretion

Most black holes, including those in nearby galaxies, are much less bright than AGN. Some, but not nearly all, of this discrepancy can be attributed to the gas supply at the center of the host galaxy. Still, most of these sources, including Sgr A* and M87, as well as the so-called low/hard state of BHBs, cannot be fit by the thin disk model even at low accretion rates. In other words, the accretion process in these sources is physically distinct. In the mid-1990s, the advection-dominated accretion flow solution was found to apply to these sources (ADAF, [139, 140]). At low accretion rates, coulomb collisions between ions and electrons become inefficient. Internal energy remains trapped in the ions and the accretion flow cannot cool efficiently by radiating away its energy and instead remains hot, carrying the bulk of the internal energy through the event horizon and into the black hole. The accretion flow is then hot and geometrically thick, and its weak luminosity means it is transparent (optically thin). These solutions typically have much lower electron than ion temperatures, since the electrons still cool via synchrotron radiation.

As in thin disk theory, the equations are vertically averaged.[4] The assumption from thin disk theory that all gravitational binding energy is immediately released locally as radiation is relaxed, and instead the flow is allowed to heat up. The fraction of the binding energy converted to radiation, f, is a free parameter in the model. For particular accretion rates, steady-state solutions at a given radius only exist for certain values of f. In the limits of $f \rightarrow 0$ and $f \rightarrow 1$, the solution can be shown to reproduce Bondi and thin disk accretion [139]. Thus, advection-dominated theory encompasses the other simplified solutions and predicts what type of flow should exist in different physical scenarios. With increasing f, the flow becomes increasingly geometrically thick and optically thin. The angular momentum profile becomes increasingly sub-Keplerian, and the infall time becomes shorter due to the lower centrifugal barrier.

---

[4] This assumption is much worse here, since the accretion flow is actually geometrically thick for a wide range of parameters.

Advection-dominated accretion flow solutions are also consistent with the presence of large-scale outflows associated with many black holes. The significant internal energy stored in the infalling gas can allow some of it to escape to infinity, given some mechanism for reversing its radial velocity [139]. Proposed mechanisms include convection [159, 138], strong (relative to equipartition) magnetic fields [130] and conduction [183, 184].

These are a few of the many theoretical variants on the ADAF theme, motivated by the presence of a convective instability in the ADAF solution, its inconsistency with observations of Sgr A* [3, 158] and by the need for a physical mechanism to explain the outflows associated with accretion disks. The contemporary term encompassing many of these solutions is the radiatively-inefficient accretion flow (RIAF), in contrast to the extremely high radiative efficiencies of thin accretion disks without reference to the specific cause of the inefficiency. These solutions have much smaller accretion rates and particle densities than the original ADAF solutions, but the concept remains unchanged [202].

The RIAF solution is appropriate for Sgr A*, M87, low-luminosity AGN, quiescent BHBs and possibly also the low/hard state of BHBs. These are the sources considered in the remainder of this thesis, both due to their interest for mm-VLBI (Sgr A* and M87) and because no realistic, 3D numerical models of luminous systems are computationally feasible yet. The emergent spectrum from RIAF models is in many ways similar to that from spherical accretion: synchrotron emission is the dominant source of radiation, and most of the energy is radiated at sub-millimeter wavelengths. The sub-millimeter "bump" in Sgr A* arises from synchrotron emission from thermal electrons in accretion disk models [202].

All observed black hole candidates radiate over huge frequency ranges, while the emission from thermal electrons in all cases is relatively narrow. The low-energy radio and high-energy X-ray emission seen in Sgr A*, M87 and BHBs in the low/hard state is attributed to non-thermal emission either from the accretion flow itself, a hot optically thin "corona" (analogous to the region that produces solar flares), or a relativistic jet. While a huge amount of dust prevents optical observations of the Galactic center, the optical emission from M87 arises from a spectacular, ultrarelativistic, galaxy-scale jet. In all cases, the emission mechanism is either synchrotron radiation from non-thermal electrons, or inverse

Compton scattering of disk photons by hot electrons.

Sources modeled with thin accretion disks also show broadband spectra. Many AGN show substantial radio emission ("radio loud"), and many ("radio galaxies") also have spectacular, bipolar jets that can produce huge radio "lobes" where the jet material interacts with the intergalactic medium. AGN also typically emit in the X-ray, which is also assumed to come from a corona.

1.4 Relativistic Effects

The semi-analytic solutions for accretion disk structure can be readily extended to general relativity appropriate for the description of material in the vicinity of spinning black holes. The thin disk results remain unchanged, but with multiplicative factors corresponding approximately to corrections to the radial and vertical gravitational "forces" [152]. The most important assumption for thin disks in general relativity is that the disk should truncate cleanly at the innermost stable circular orbit. In the Kerr metric, this location is [107],

$$\begin{aligned} r_{ISCO} &= M\left\{3+Z_2\pm[(3-Z_1)(3+Z_1+2Z_2)]^{1/2}\right\}, && (1.10)\\ Z_1 &= 1+\left(1-\frac{a^2}{M^2}\right)^{1/3}\left[\left(1+\frac{a}{M}\right)^{1/3}+\left(1-\frac{a}{M}\right)^{1/3}\right], && (1.11)\\ Z_2 &= \left(3\frac{a^2}{M^2}+Z_1^2\right)^{1/2}, && (1.12) \end{aligned}$$

which varies from M (9M) for maximal spin and prograde (retrograde) motion to 6M for zero spin.[5] The assumption that thin disks truncate at r_{ISCO} is still made in methods to estimate black hole spin from BHBs in the thermal state [174], despite ongoing controversy about its validity [109, 146].

Low-luminosity systems do not truncate cleanly at the ISCO. The RIAF solutions can also be extended to general relativity [203], although not as neatly as thin disk solutions.

---

[5] For much of this thesis, we use units with $G = c = 1$.

1.4.1 Observational Consequences

There are important observational consequences from the strong gravity in the vicinity of black hole accretion disks. First, the orbital velocities in both thin disk and ADAF/RIAF solutions are large near the black hole where the bulk of the radiation is produced. For systems viewed at any inclination (not face on), this leads to substantial Doppler boosting of light, causing the disk to appear asymmetric with a bright (dim) approaching (receding) side. For nearly edge-on viewing, this effect can dominate the appearance of the accretion disk.

Secondly, some photons emitted from the back of the disk are bent around the black hole to the observer. This causes the back of the disk to appear warped above the black hole.

Finally, photons have an equivalent to the ISCO for massive particles, known as the circular photon orbit. This is the boundary between light that is bound and unbound to the black hole. Inside of the circular photon orbit, only particles from the front side of the accretion flow can emit photons that reach the observer. Unless the flow is completely opaque, so that the photosphere everywhere is in front of the black hole, this leads to a "shadow" at the circular photon orbit, where the regions of the image outside of the projection of the circular photon orbit at infinity are brighter than those inside it. The combination of maximum path lengths at the circular photon orbit coupled with emission often peaking close to the black hole can lead to bright rings in images at this location, leading to maximal contrast with the shadow inside of it. The black hole shadow, a consequence of the presence of the circular photon orbit, is a prediction of black hole spacetimes and general relativity. Observing this feature would then provide the first direct evidence for the existence of a black hole event horizon.

1.5 Tilted Disks

In all accreting sources, the direction of net angular momentum of infalling material is unlikely to be aligned with the black hole spin axis. This misalignment leads to relativistic torques on the disk material. In the thin disk context, the torque tends to align the inner part of the disk with the black hole spin axis, a phenomenon known as the Bardeen-Petterson effect [14]. The result is likely to be a warped disk, with a transition at a radius with considerable theoretical uncertainty.

In low-luminosity systems where the accretion flow is geometrically thick, torques due to misalignment will instead cause bending waves to propagate through the disk and cause precession in the disk body [153, 117]. Using the alpha prescription, the transition between this "wave-like" regime and the Bardeen-Petterson, or "dissipative" regime is $\alpha \sim h/r$. Since $\alpha \lesssim 1$ (and significantly smaller on average in many simulations), the inner regions of geometrically thick accretion flows are not expected to align with the black hole spin axis. The resulting warped, twisted, precessing disk will be known as a "tilted" (or "misaligned") disk for the rest of this thesis. Although theoretical work using the alpha prescription has been done for the Bardeen-Petterson case, tilted disks remain poorly understood.

1.6 The MRI and GRMHD

Neither thin disk accretion theory nor advection-dominated accretion flow theory include the physics of angular momentum transport in the disk that allows material to fall into the black hole. The stress, $\tau_{R\phi}$, coupling orbital and plunging motions is assumed to be proportional to the pressure in these theories, $\tau_{R\phi} = \alpha P$, where P is the total pressure (gas+radiation) and α is an unknown parameter hiding the physics of stress in accretion flows. Molecular viscosity is much too weak to cause the accretion rates required by AGN, and the physical cause of accretion was unknown for decades.

The answer now appears to be that turbulent magnetic stresses transport angular momentum out through the disk, allowing accretion to proceed. Rotating magnetized fluids are unstable when $d\Omega/dR < 0$ [194, 44], and the realization that this is likely the mechanism for angular momentum transport in accretion disks was made by Balbus & Hawley in 1991 [10]. The instability is now known as the magnetorotational instability (MRI). Calculations including the MRI must be done numerically, as the non-linear instability drives turbulence in the accretion flow which can only be sustained in three spatial dimensions due to the anti-dynamo theorem. The discovery of the MRI and advances in numerical calculations have led to dramatic progress in the theoretical understanding of black hole accretion flows

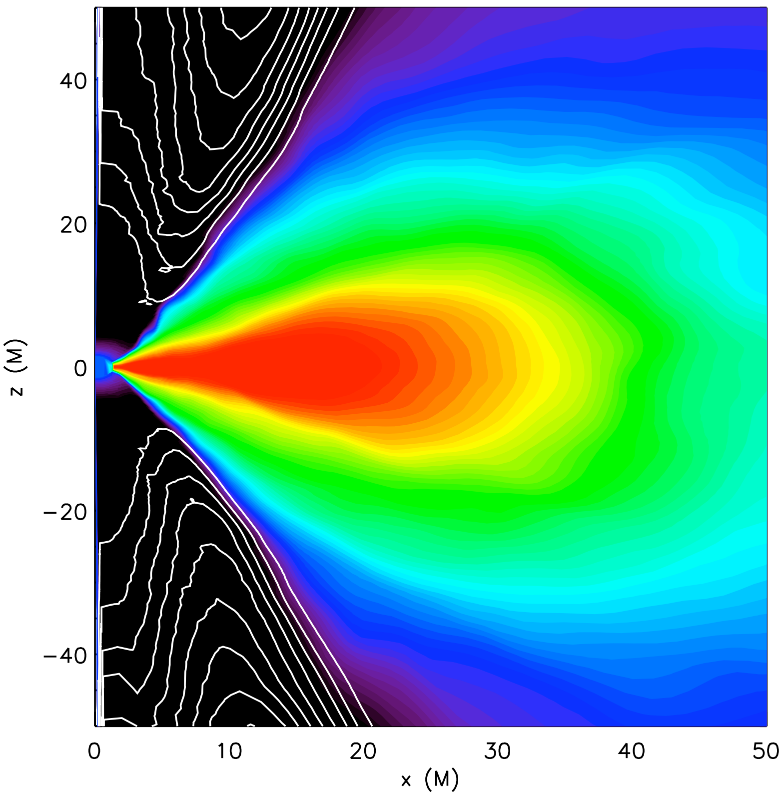

Figure 1.1 Azimuthally-averaged structure of a single timestep from a GRMHD simulation of a black hole accretion flow [129] shown in the logarithm of the fluid mass density (colors increasing from black to blue to green to red with a dynamic range of $\simeq 10^5$) and in the asymptotic Lorentz factor (white contours denoting intervals of 0.1 increasing outward from 1.1). The disk body, centered on the equatorial plane, contains the bulk of the mass which accretes onto the black hole inside of the pressure maximum of the initial torus ($r = 12$M in this case). The magnetic field is sub-equipartition in the disk body, but is stronger in the tenuous corona surrounding the disk and dominant in the polar jet.

in the past $15-20$ years.

Numerical calculations have been extensively studied both for entire accretion disks ("global" simulations) and for small patches of the disk ("local" or "shearing box" simulations). The local simulations can use much higher resolution and incorporate more physics than the much more computationally expensive global ones, but many of their properties depend on the assumed aspect ratio, spatial extent, or magnetic field configuration of the box. Both types of simulations must be done in three spatial dimensions to sustain MRI-driven turbulence.

The current state of the art are global, fully general relativistic, 3D magnetohydrodynamic (GRMHD) simulations. Starting from a torus of fluid in hydrostatic equilibrium seeded with a weak magnetic field in the Kerr metric, the MRI drives the fluid turbulent. The resulting magnetic stresses cause angular momentum transport outwards and allow accretion onto the central black hole, which occurs self-consistently in the simulations. The magnetic field strength saturates at roughly $1-50\%$ of equipartition in the disk body. These simulations evolve the whole inner accretion disk (out to $r = 10-25\mathrm{M}$ depending on the simulation) can be run for $\sim 10^4\mathrm{M}$, about $10-20$ orbits at the pressure maximum of the initial torus or several hundred at the event horizon.

An example of such a solution is shown in Figure 1.1. It contains a disk body centered on the equatorial plane, where the mass density is high and the velocity profile is nearly Keplerian, surrounded by a tenuous region of hot gas ("corona"). In the polar regions, some form of a jet develops depending on the initial magnetic field configuration of the simulation [52, 17, 129]. This region is shown in the Figure for the dipolar simulation in McKinney & Blandford (2009) [129] as contours of Lorentz factor observed at infinity. The disk scale height depends on the method used for energy evolution and whether any cooling is included. The simulation shown is thick ($H/R \simeq 0.3$), since it conserves energy and so is heated from numerical magnetic reconnection at the grid scale. Simulations which neglect this heating are somewhat thinner ($H/R \simeq 0.1-0.2$), while those that include artificial cooling can be quite thin ($H/R \simeq 0.02-0.05$, [145, 154]).

The existence of 3D GRMHD simulations has also allowed the study of tilted disks in the context of the MRI [80, 79, 81]. These simulations are consistent with the results of “warped” disks based on the alpha prescription, but have only been done in the geometrically thick “wave-like” regime where the Bardeen-Petterson configuration does not form. The limited spatial extent of the simulations leads to a nearly solid body precession. The orbital eccentricity from general relativistic gravitational torques leads to the formation of non-axisymmetric shocks. These shocks increase the effectiveness of outward angular momentum transport and cause the disk to truncate outside of the ISCO in a fashion roughly independent of spin [77] (see also Chapter 3).

Combined, MRI-based simulations represent a dramatic advance in the theoretical understanding of black hole accretion flows. Until recently, the bulk of research effort has been directed to understanding the physical properties of the simulations and in comparing them to thin disk and ADAF accretion theory. Ultimately, however, simulations must be confronted with observations, both in order to test their ability to explain and predict accretion phenomena as well as to infer the properties of astrophysical black hole accretion disks (spin, mass, accretion rate).

This is a difficult task. Current global simulations either neglect radiative cooling altogether and evolve hot, geometrically thick accretion flows [51, 85, 80, 129] or include artificial optically thin cooling functions [175, 144]. Local (shearing box) simulations can include simplified radiation dynamics in the form of flux-limited diffusion [193, 97, 98] but cannot be used to interpret observations.

1.7 Summary Of This Work

The goal of this thesis is to study the observational properties of global, 3D GRMHD simulations and to use them to construct detailed and physically realistic radiative models of individual sources. The simulations that neglect radiative cooling are appropriate for our sources of interest, where the emission is concentrated close to the black hole so that the simulation is spatially large enough and where the cooling is (thermo)dynamically unimportant. Then the radiation can be added in after the fact (in “post-processing”) without compromising the physical validity of the solution. This post-processing requires a radiation transfer calculation to compute the appearance of the accretion disk as viewed by a distant observer. The ray tracing and general relativistic radiation transport calculation and the numerical codes developed for this task are described in Chapter 2 and Appendix A. Previous codes to calculate null geodesics in the Kerr metric for ray tracing applications have numerically integrated the geodesic equations [119, 72, 102, 171, 147, 62]. Rauch & Blandford (1994) [160] treated the problem semi-analytically, with numerical integrations for the t and ϕ coordinates. This method was also used by Agol (1997) [2]. Our code extends these techniques to a semi-analytic treatment of all coordinates, and is published as Dexter & Agol (2009) [53].

The millimeter emission in Sgr A* is an excellent source for comparing simulations with observations. It has a tiny luminosity so that the radiation should be dynamically negligible. The emission mechanism is known, and the source size is small enough to be contained in simulations. Radiative models of Sgr A* have been constructed from non-relativistic 3D simulations [149, 90, 99, 43] or from axisymmetric GRMHD simulations [147, 136, 96, 186].

Our models based on GRMHD simulations are the first to include time-dependence, and to make physical predictions for the morphology of 3D black hole accretion flows. These time-dependent images are fit to mm-VLBI observations in Chapter 4. The radiative models calculated from GRMHD simulations provide excellent fits to the data, and combined with spectral index measurements allow us to constrain the parameters of the Galactic center black hole and its accretion flow. The "best fit" models, with the highest probability of describing current observations, are studied further in Chapter 5. We study their variability, compare their structure to expectations from RIAF theory and make predictions for future observations with mm-VLBI and other instruments. The portions of these chapters concerned with standard aligned (untilted) simulations are based on work published in Dexter et al. (2009, 2010) [54, 55].

The situation in low-luminosity AGN (including M87) and the low/hard state of BHBs is somewhat more uncertain. The geometry and emission mechanisms are unknown for the peak of the spectrum. In low-luminosity AGN with clear jets, like M87, the jet is the source of the high-frequency emission (optical/X-ray). Radio emission in the low/hard state arises in a jet, but the X-ray emission is either produced in a thin disk, possibly truncated and transitioning to an ADAF inside some radius, and/or in a Compton scattering corona (which may or may not be due to the ADAF).

Jet spectra are typically well described by power laws in the observed frequency, $F_\nu \propto \nu^{-\alpha}$, where α is the spectral index. This spectrum can be produced by synchrotron emission from a power law electron distribution, $N(E) \propto E^{-p}$, where $\alpha = (p-1)/2$ (see [168] and Appendix C for more details). We calculate jet emission from M87 in Chapter 6. These are the first radiative disc/jet models based on simulations of a jet forming from an accretion flow.

Our models of the low/hard state in Chapter 3 are necessarily simplified since we neglect Compton scattering throughout this thesis, and since the emission mechanisms and geometry are so uncertain. The goal in that case is to compare and contrast the observed properties of tilted and untilted geometrically thick accretion flows rather than to construct detailed models of the low/hard state, and the simplistic emission models used are sufficient for that purpose. This work is published as Dexter & Fragile (2011) [56], and builds on previous work to measure the inner edge of simulated disks [108, 18, 77] as well as to study the generic observational properties of GRMHD simulations [173].

Chapter 2

RAY TRACING AND RELATIVISTIC RADIATION TRANSPORT

2.1 Transport Methods

The radiative transfer problem of interest in this work is to calculate the appearance of a black hole accretion flow for a particular set of “camera” coordinates corresponding to a distant observer. In Newtonian physics, photon trajectories are trivial in the absence of scattering. In general relativity, this is no longer the case and three methods are commonly used to calculate observables at infinity.

The first method used is to solve the “emitter-observer” problem, that is to solve for the constants of motion describing a photon that reaches an observer from a particular location near the black hole [48, 195, 16]. This approach was initially popular due to the small spatial extent of the sources considered (orbiting stars or thin disks), so that only a small set of photon properties need to be calculated and the efficiency of shooting rays outward from the black hole or inward from infinity is small.

When scattering is important, multiple trajectories are traversed by each photon and shooting “packets” of photons outward from a grid of points in the source to infinity is the natural method [62, 172]. The scattering is handled using Monte Carlo methods, the same way as frequently done in Newtonian calculations [118], except that the photon energy changes due to gravitational redshift as well as Compton scattering.

For simplicity, the effects of electron scattering are ignored throughout this thesis and we restrict our analysis to sources and wavelengths of interest where it is insignificant.[1] The sources considered are also extended, in which case tracing photon trajectories backwards from infinity to the black hole is the method of choice [119]. The result of this ray tracing method is a theoretical image of the source, which in the case of Sagittarius A* is itself an

---

[1] The study of generic observational properties of tilted disks in Chapter 3 uses simplified emissivities instead of models for the Compton scattering corona in the low/hard state of BHBs.

observable. This is a significant advantage over ray tracing from the disk outwards, where calculating an image requires enough photons to populate cameras at infinity over the entire solid angle with adequate resolution.

2.2 Backwards Ray Tracing

Backwards ray tracing separates into two distinct steps [171]. First, the desired set of photon trajectories corresponding to a grid of "camera" coordinates must be computed. Second, for each of these trajectories the relativistic radiative transfer equation is solved for the desired dynamical and emission model. The first step is done by placing the camera at a large, finite distance from the black hole, chosen such that light bending is negligible from that location to infinity.[2] These camera coordinates have impact parameters α and β perpendicular and parallel to the black hole spin axis respectively, which can in turn be related to the constants of motion describing photons in the Kerr metric [48]:

$$\begin{aligned} l &= -\alpha(1-\mu_0^2)^{1/2}, && (2.1) \\ q^2 &= \beta^2 + \mu_0^2(\alpha^2 - \tilde{a}^2), && (2.2) \end{aligned}$$

so that each point on the observer's camera corresponds to a unique geodesic. The conserved quantities l and q^2 are the dimensionless z-component of the orbital angular momentum and Carter constant [42], $l \equiv L_z/E$ and $q^2 = Q/E$, and E is the photon energy [160]. These constants of motion, as well as the initial direction of photon propagation, completely specify the desired rays. The trajectories are calculated semi-analytically, exploiting the existence of the Carter constant which allows the separation of the Hamilton-Jacobi equation for null geodesics in the Kerr metric (see Appendix A for details of the geodesic calculation and implementation).

2.3 Radiative Transfer Equation

The unpolarized, non-relativistic radiative transfer equation in the absence of scattering is,

---

[2] Typically we take $1/u_0 = 100\max(\alpha^2 + \beta^2)$.

$$\frac{dI_\nu}{ds} = j_\nu - \alpha_\nu I_\nu, \tag{2.3}$$

where j_ν and α_ν are the emission and absorption coefficients, and I_ν is the observed intensity. This equation can be generalized to covariant form as [84],

$$\frac{d\mathcal{I}}{d\lambda} = \mathcal{J} - \mathcal{A}\mathcal{I}, \tag{2.4}$$

where the invariant intensity, emission and absorption coefficients are $\mathcal{I} \equiv I_\nu/\nu^3$, $\mathcal{J} \equiv j_\nu/\nu^2$, $\mathcal{A} \equiv \nu\alpha_\nu$. This clearly reduces to the standard non-relativistic form when the observed and emitted frequencies are equal.[3] The formal solution in the absence of polarization and scattering is,

$$I_{\nu_0}(\lambda) = g^3 I_\nu(\lambda_s) e^{-\tau_\nu(\lambda_s)} + \int_{\lambda_s}^{\lambda} e^{-(\tau_\nu(\lambda')-\tau_\nu(\lambda_s))} g^2 j_\nu \, d\lambda', \tag{2.5}$$

where ν_0 and ν are the observed and emitted frequencies, $g \equiv \nu_0/\nu$ is the gravitational redshift, $\tau_\nu \equiv \int \alpha_\nu / g d\lambda$ is the optical depth and λ is the affine parameter. Taking the initial point $\lambda_s = 0$ outside of the source so that $I_\nu(\lambda_s) = \tau_\nu(\lambda_s) = 0$ and solving for I_{ν_0}, Eq. 2.5 simplifies to:

$$I_{\nu_0} = \int_0^{\lambda} e^{-\tau_\nu(\lambda')} g^2 j_\nu \, d\lambda', \tag{2.6}$$

where λ is now the maximum relevant value of the affine parameter, either where the geodesic leaves the source or where the optical depth becomes large enough that negligible emission reaches the observer from further along the ray. The form in Eq. 2.6 is mixed frame: the *fluid-frame* emission and absorption coefficients are integrated to calculate the *observed* intensity. Neglecting polarization, the combined effects of gravitational redshift and Doppler shifts are entirely accounted for by g. When polarization is included, the transfer equations can be written as a set of four linear differential equations for the Stokes parameters. It is more convenient to numerically integrate these equations than to use the equivalent formal solution to (2.5), which is formidable in the polarized case [110].

---

[3] For the polarized case, see B.

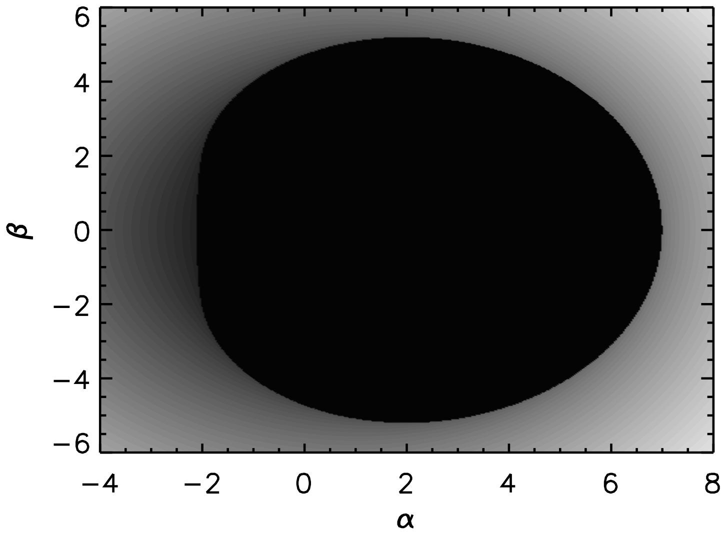

Figure 2.1 Image of a near extreme ($a = 0.998$) Kerr black hole viewed from the equatorial plane. Images intensities are taken to be the affine parameter evaluated upon termination at the black hole or after returning to the starting radius. Intensities are scaled linearly from the minimum value outside the shadow to the maximum.

2.4 Examples and Code Validation

We next describe a couple of relatively simple applications of our geodesic code `geokerr` to ray tracing problems as further validation and as examples of its utility. The first is the simplest illustration of the black hole shadow, which tests the determination of the roots of $U(u)$ and qualitatively parts of the time integral. Next are examples from the standard model of thin disk accretion. The disk image and simple spectrum from line emission test the routine that solves for u_f. The projection of a uniform grid at infinity onto the equatorial plane of the black hole also tests the calculation of ϕ, and hot spot emission provides a time-dependent test. Finally, spectra and images of synchrotron radiation from spherical accretion quantitatively test our radiative transfer routines.

In addition to these tests, the photon trajectories have been verified using the numerical integration code described in Dolence et al. (Figure 1 of Dolence et al. (2009) [62]).

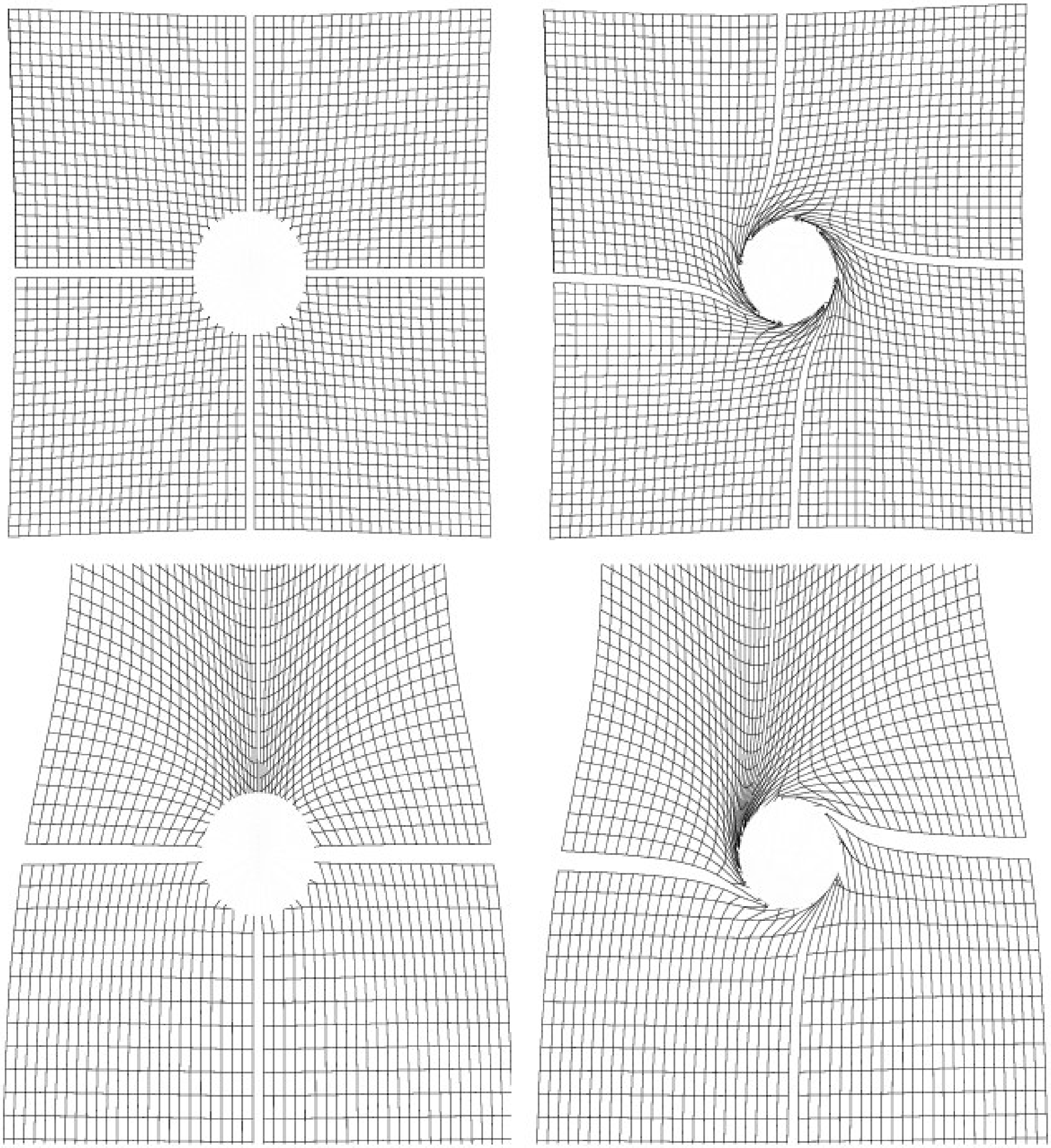

Figure 2.2 Projection of a uniform Cartesian grid in the image plane to the equatorial plane of the black hole for $\mu_0 = 1$ (top) and $\mu_0 = 0.5$ (bottom). Black hole spin is $a = 0$ (left) and $a = 0.95$ (right), and the area inside the horizon is removed from each image. Compare to Fig. 2 of Schnittman & Bertschinger (2004) [171].

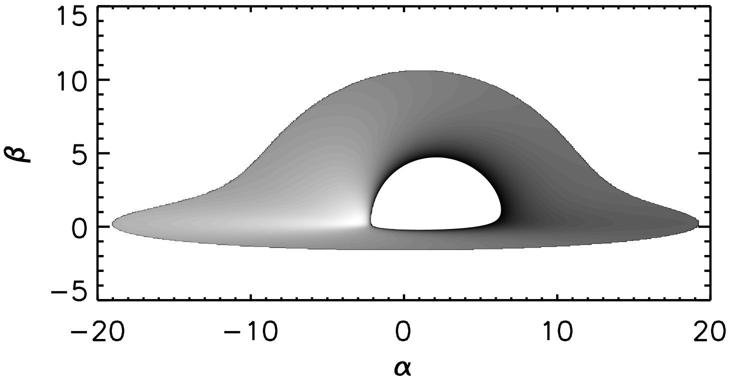

Figure 2.3 Image of an optically thick standard relativistic accretion disk around a near extremal black hole (a=0.998). The disk has outer radius $r_{out} = 18$, and the observer's inclination is 85°.

2.4.1 Image in Affine Parameter

As a first application of ray tracing, we can determine the appearance of the simplest possible black hole shadow. The image "intensities" are taken to be the affine parameter evaluated at the termination of the geodesic–either when it terminates at the black hole or reaches a turning point and re-emerges to the starting radius. Affine parameter is a proxy for the emission in this case, since it is qualitatively similar to the path length along a geodesic. The dimensionless affine parameter, λ', is given by (A.49). The equatorial plane result for a Kerr black hole with $a = 0.998$, to be compared to Bardeen (1973) Figure 6 [13], is shown in Figure 2.1. The image shown here is 400×400.

2.4.2 Thin Disk Accretion

The next set of applications imagine the emitting source as an infinitesimally thin disk in the equatorial plane of the black hole (e.g., 152, 176).

Grid Projection

The first check of the code for this case is in visualizing the projection of a uniform grid at infinity onto the equatorial plane of the black hole. This is done by solving for the final

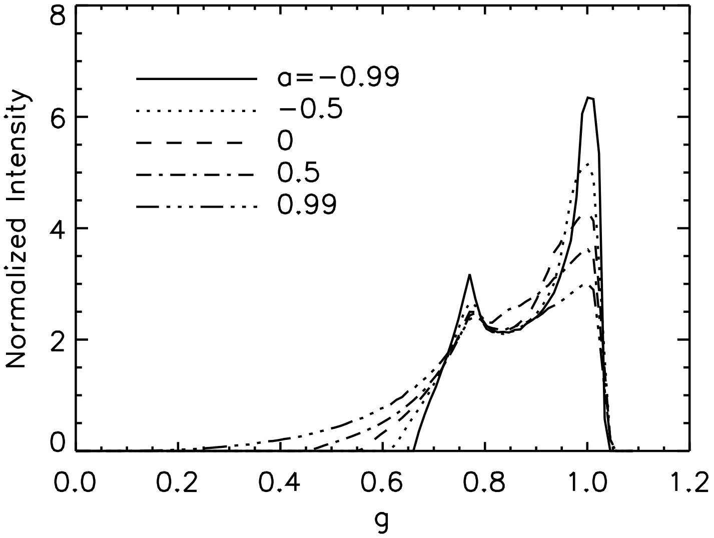

Figure 2.4 Normalized spectra of line emission from a thin accretion disk at an inclination of 30° for various black hole spins. The emissivity is taken to be proportional to u_f^2 between the marginally stable orbit and $R_{out} = 15$. Compare to Schnittman & Bertschinger (2004) Figure 3 [171].

radius, u_f, and azimuth where the geodesic intersects $\mu_f = 0$. Then, the new grid points are calculated using pseudo-Cartesian coordinates [171]:

$$x = \sqrt{r^2 + a^2}\cos\phi, \;\; y = \sqrt{r^2 + a^2}\sin\phi. \tag{2.7}$$

The result of this projection for two different initial observer inclinations and black hole spins is shown in Figure 2.2, and agrees with Figure 2 of Schnittman & Bertschinger (2004) [171]. The gravitational lensing effect can be seen in the Figures with $\mu_0 = 0.5$ as the bunching of grid points behind the black hole, while frame dragging is evident in those with $a = 0.95$

Thermal Disk Images

As a next step, we can use the standard thin disk results for the radial temperature profile (e.g., [107]) to produce images of the disk at various inclinations assuming it is optically thick everywhere, so that the intensity is that of a blackbody. Finding the radii of emission from a grid in impact parameters and calculating the intensity at each of these points produces an image of the disk as seen by a distant observer. The result for an inclination of 85° and black hole spin $a = 0.998$ is shown in Figure 2.3. The image shows the effects of relativistic beaming of the emission from gas moving towards the observer versus the redshift of that moving away, as well as the bending of the light from gas behind the black hole.

Line Emission

Next, following Schnittman & Bertschinger (2004) [171] and Bromley et. al. (1997) [35] we consider monochromatic emission from the disk, and give it an inner (outer) radius, $R_{in} = R_{ms}$ ($R_{out} = 15$), where R_{ms} is the location of the marginally stable circular orbit (e.g., 152). The emissivity is weighted by u_f^2, physically motivated by the fact that we expect the temperature of gas in the disk to increase with decreasing radius. The observed intensity is computed by exploiting the invariance of I_ν/ν^3 [134],[4]

$$I_{\nu_0} = g^3 I_\nu. \tag{2.8}$$

The combined effects of redshift and Doppler beaming encompassed in g are calculated using Equations 17 and 19 of Viergutz (1993) [195], taking advantage of a particular useful orthonormal frame in the Kerr metric known as the locally non-rotating frame (LNRF, [15]).

To see the effect of black hole spin on the emission in this case, we calculate I_{ν_0} as a function of g for several values of a by calculating the intensity of rays at a location with redshift in a certain range of g, and integrating them over the photographic plate. The result is plotted in Figure 2.4, and is in excellent agreement with Figure 3 of Schnittman & Bertschinger (2004) [171]. At higher black hole spin, the marginally stable orbit is much closer to the black hole where the redshift is much stronger, leading to a higher relative magnitude and broadening of the low frequency peak ("red wing").

---

[4] This is the limit of (2.6) where $j_\nu = I_\nu \delta(\ell - \ell_0)$, and $d\ell = g^{-1} d\lambda$ is the proper length.

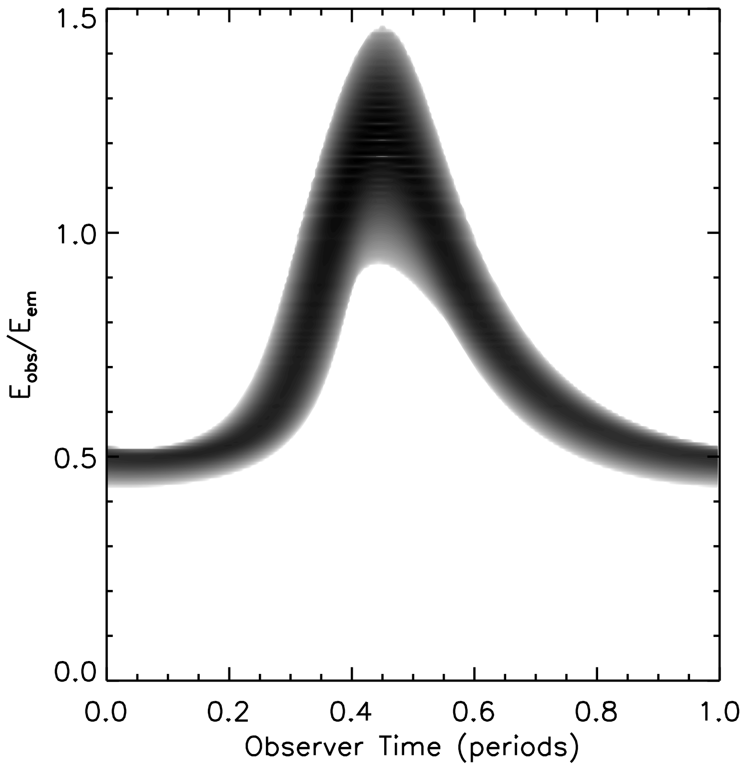

Figure 2.5 Spectrogram of a circular hot spot of radius $R_{spot} = 0.5$ at the marginally stable orbit of a Schwarzschild black hole. The observer is inclined at $\theta_0 = 60°$. Compare to Figure 4 of Schnittman & Bertschinger (2004) [171].

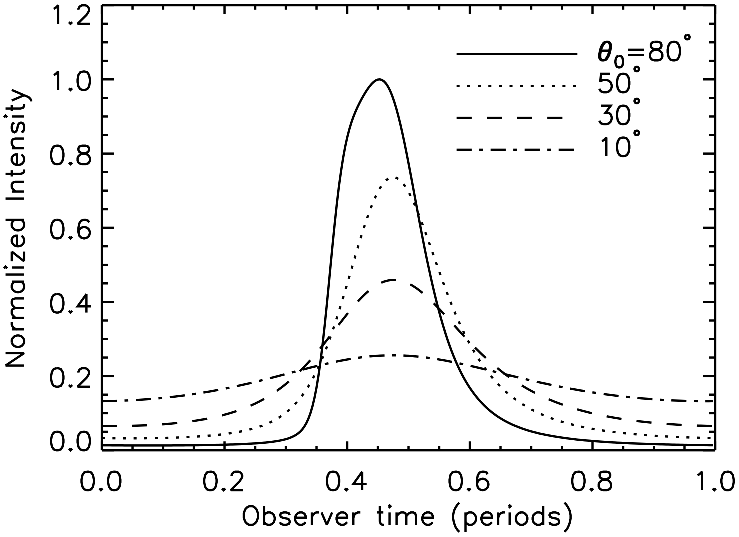

Figure 2.6 Light curves of the hot spot described in Figure 2.5 for various inclination angles. Intensities are normalized individually to the integrated intensity over each orbit and scaled to the maximum intensity from all inclinations. Compare to Figure 6 of Schnittman & Bertschinger (2004) [171].

Rotating Hot Spot

Finally, to test the time-dependence of the code, consider a circular hot spot of finite radius $R_{spot} = 0.5$ orbiting in the equatorial plane of a Schwarzschild black hole at its marginally stable radius ($R_{ms} = 6$). The emissivity of the spot is taken to be Gaussian in the locally flat space near the hot spot (for details, see 170),

$$j(\mathbf{x}) \propto \exp\left[-\frac{|\mathbf{x} - \mathbf{x}_{spot}(t)|^2}{2R_{spot}^2}\right], \tag{2.9}$$

where j is the monochromatic emissivity. For some observer coordinate time, t, the time delay and azimuthal position from the observer to points on the disk are used to determine where on the photographic plate the separation between geodesic and hotspot are less than $4R_{spot}$. For these points, the Gaussian emissivity and observed frequency (redshift) are tabulated. Repeating this procedure over a period of the motion gives a time-dependent spectrum, which is shown in Figure 2.5 for an observer inclination of 60° ($\mu_0 = 0.5$). This

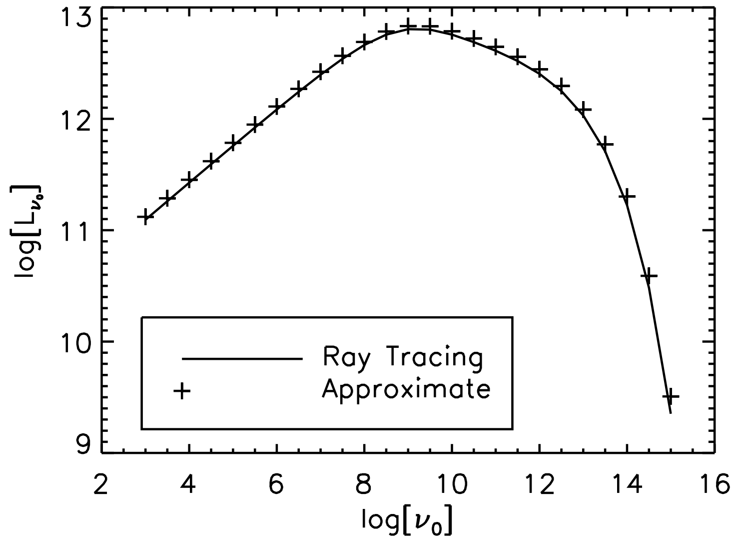

Figure 2.7 The spectrum of synchrotron radiation from optically thin spherical accretion onto a stellar mass black hole. The solid line is the ray tracing result, and the plotted points are the analytic results. The two curves agree to within 5% at low frequencies, where the radiation originates at larger radii and the bending of light should be unimportant.

figure is in good agreement with Figure 4 of Schnittman & Bertschinger (2004) [171].

Integrating over frequency (redshift), or equivalently over the impact parameters, gives the light curve. Figure 2.6 shows the light curves of the hotspot for several inclination angles. As the observer approaches edge-on viewing, the light curve becomes sharply peaked by a combination of the Doppler beaming of the spot as it moves toward the observer and the large gravitational lensing of the spot as it goes behind the black hole. The plot here is in excellent agreement with Schnittman & Bertschinger (2004) [171].

2.4.3 Synchrotron Radiation from Spherical Accretion

The geodesics code in conjunction with `grtrans`, our implementation of the ray tracing radiative transfer along rays described above (see below), is now applied to the particularly simple case of a stellar mass black hole at rest with respect to the interstellar medium with a temperature at infinity of 10^4 K and a density at infinity of $1\mathrm{cm}^{-3}$. Ionized hydrogen accretes onto the black hole, and the magnetic field threading the gas effectively creates collisions, so

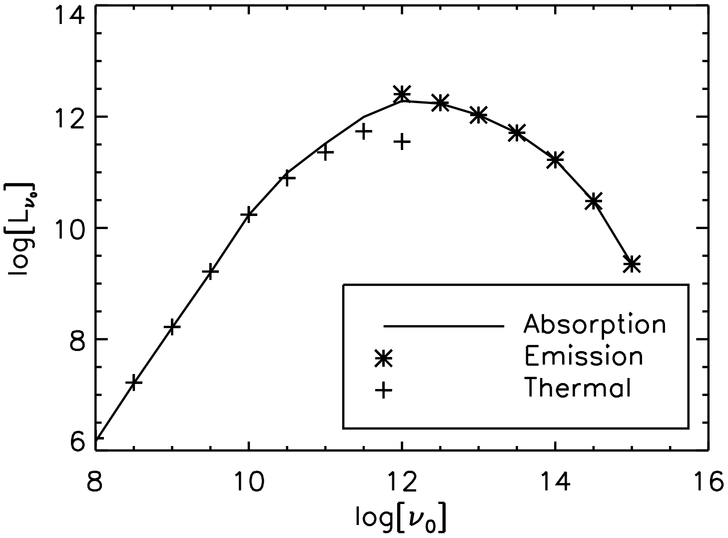

Figure 2.8 Spectrum of synchrotron radiation from spherical accretion onto a stellar mass black hole. The solid line is the ray tracing result including absorption. The spectrum is heavily attenuated at $\nu_0 \lesssim 10^{11}\,\mathrm{Hz}$, and in this region follows the optically thick approximation of thermal emission from the $\tau = 1$ surface. The spectrum agrees well with the emission only model for $\nu_0 \gtrsim 10^{12}\,\mathrm{Hz}$

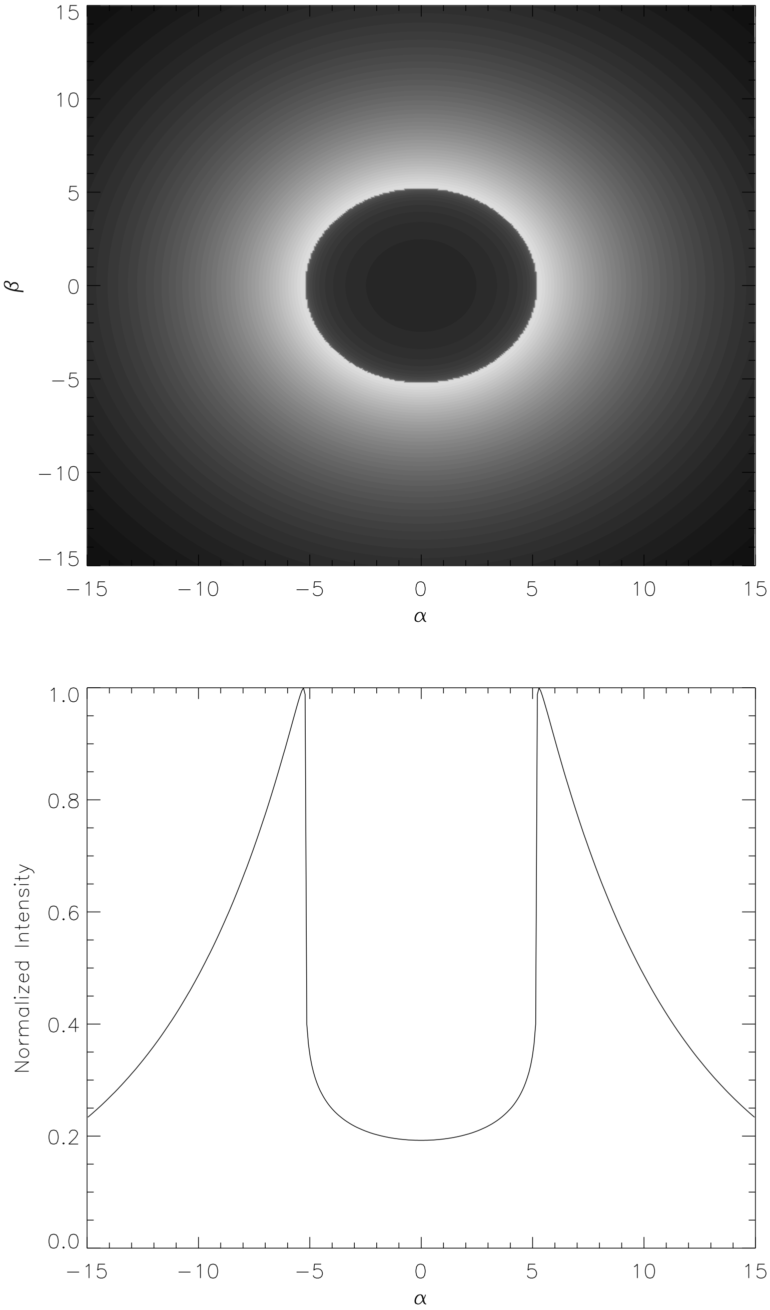

Figure 2.9 Image of a spherically accreting Schwarzschild black hole at $\nu = 10^{12}\,\mathrm{Hz}$ as a contour plot and a 1-d profile.

that the accreting gas can be considered a perfect fluid. In the model, magnetic turbulence establishes an equipartition of magnetic and gravitational energy [206]. Then

$$\frac{B^2}{8\pi} = \frac{GM\rho}{r}, \tag{2.10}$$

and cgs units are most convenient in this calculation. We assume an adiabatic equation of state with a piecewise adiabatic index [181],

$$\begin{aligned} \gamma &= \frac{5}{3}, \qquad \frac{3}{2}\frac{m_p}{m_e}T \leq 1 \\ &= \frac{13}{9}, \qquad \frac{3}{2}\frac{m_p}{m_e}T > 1, \end{aligned} \tag{2.11}$$

where m_p, m_e are the proton and electron mass and T is the temperature in units of proton rest energy. Then the fluid equations are non-linear, and can be solved numerically [133] to find the temperature and fluid velocity as functions of coordinate radius.

The dominant form of radiation produced is synchrotron radiation from the inner part of the accreting sphere, where the electrons are ultrarelativistic [179]. In this case, the emissivity can be well approximated analytically. Shapiro (1973) [178] performed the relativistic radiative transfer by approximating the photons as traveling on null geodesics in Minkowski spacetime, and calculating gravitational redshifts as well as the photon Doppler shifts along these paths.

Shapiro's formula for the radiated spectrum is

$$\begin{aligned} L_{\nu_0} &= 8\pi^2 \int_{2m}^{r_*} dr\, r^2 \times \\ &\quad \int_{-1}^{\cos\Theta_c} d(\cos\Theta')\, j_\nu\, \frac{1-v^2}{(1-v\cos\Theta')^2} \\ \nu_0 &= \nu\, \frac{\sqrt{(1-v^2)(1-2m/r)}}{1-v\cos\Theta'}, \end{aligned} \tag{2.12}$$

where $v(r)$ is the proper velocity seen by a stationary observer and

$$|\cos\Theta_c| = \left[\frac{27}{4}\left(\frac{2m}{r}\right)^2\left(\frac{2m}{r}-1\right)+1\right]^{1/2} \tag{2.13}$$

is the critical angle at which the light is recaptured by the black hole.

The synchrotron emissivity for thermal, ultrarelativistic electrons averaged over polarization and solid angle assuming isotropic emission in the rest frame is given by [151],

$$\begin{aligned} j_\nu(T) &= \nu \frac{ne^2}{2\sqrt{3}c} \left(\frac{m_e c^2}{kT} \right)^2 I\left(\frac{x_M}{\sin\theta} \right), & (2.14) \\ I(x) &\equiv \frac{1}{4\pi} \int d\Omega \, \frac{1}{x} \int_0^\infty dz \, z^2 \exp(-z) F\left(\frac{x}{z^2} \right), & (2.15) \end{aligned}$$

with $x_M = \frac{\nu}{\nu_c}$,

$$\nu_c = \left(\frac{3eB}{4\pi m_e c} \right) \left(\frac{kT}{m_e c^2} \right)^2, \tag{2.16}$$

and where

$$F(x) \equiv x \int_x^\infty K_{5/3}(y) dy \tag{2.17}$$

is the synchrotron function. Mahadevan et al. (1996) [122] have approximated $I(x)$ above analytically by matching the asymptotic forms for large and small x. They find

$$I\left(\frac{x_M}{\sin\theta} \right) \simeq \frac{4.0505}{x_M^{1/6}} \left(1 + \frac{0.40}{x_M^{1/4}} + \frac{0.5316}{x_M^{1/2}} \right) \exp(-1.8899 x_M^{1/3}). \tag{2.18}$$

Note that this function is denoted $I'(x)$ by Mahadevan et al. (1996) [122], and has a maximum error of $\approx 2.7\%$. The spectrum is calculated by integrating (2.12) numerically.

To compare with these results, the ray tracing code is used to create an image of the synchrotron radiation from the infalling gas in the same way as done previously with affine parameter. To create an image, one specifies a grid of points in α, β and calculates q^2 and l. This fully specifies the geodesic, and we can calculate the spacetime coordinates at which it intersects the accreting gas. The intensity along each geodesic represents a point in the image, which is why it is so important to be able to calculate geodesics rapidly.

For this problem, the flow is spherically symmetric and

$$g = \left(\gamma e^{-\eta} [1 - e^{\mu_1 + \eta} v^r \rho^{-2} r_{sgn} \sqrt{R}] \right)^{-1}, \tag{2.19}$$

with

$$e^{2\eta} \equiv \Delta\rho^2\Sigma^{-1}, \quad e^{2\mu_1} = \rho^2\Delta^{-1}, \quad \gamma = (1 - v^{r2})^{-1/2}, \tag{2.20}$$

and v^r is the radial component of the four-velocity. Written in terms of $u \equiv 1/r$ in the Schwarzschild metric, this simplifies to

$$g = \frac{\sqrt{1-2u}}{\gamma[1 + s_u(-1)^{N_u} v^u \sqrt{U}]}. \tag{2.21}$$

When the u-component of the four-velocity, v^u, vanishes, this reproduces the standard gravitational redshift [91].

We first ignore absorption and compare radiated spectra with the analytic calculation. The result is in Figure 2.7. Shapiro (1973) [179] points out that the synchrotron radiation is dominated by a thin spherical shell of gas with $\nu \simeq \nu_c$. Then the first part of the spectrum, where $L_{\nu_0} \sim \nu^{1/3}$, originates from the outer part of the sphere. The bending of light should be negligible in that region and the ray tracing should agree with the analytic result, which it does to within $\simeq 5\%$. At higher frequencies, the radiation is originating in the innermost radii, and the bending of light becomes significant. The difference is $\simeq 15\%$ at high frequencies.

Next, absorption is included. Figure 2.8 compares the spectra calculated with and without absorption. The radiation is heavily attenuated at frequencies $\lesssim 10^{11}$ Hz. At these frequencies, the luminosity is dominated by the innermost optically thin radius, which we take to be the radius where $\tau = 1$. Blackbody emission at the temperature of gas at this radius, converted to a luminosity by integrating over impact parameter, is labeled 'Thermal' in Figure 2.8 and is a decent approximation to the full spectrum when the fluid is optically thick.

From $\nu_0 \simeq 10^8$ Hz to $\nu_0 \simeq 10^{10}$ Hz, the gas is optically thick everywhere. Then only thermal emission from the outermost radius is seen, and the spectrum follows a Rayleigh-Jeans curve with $L_{\nu_0} \sim \nu_0^2$. From $\nu_0 \simeq 10^{10}$ Hz to $\nu_0 \simeq 10^{12}$, the innermost optically thin radius is changing, and the luminosity begins to turn over. Starting at $\nu_0 \simeq 10^{12}$ Hz, the gas is optically thin to the synchrotron radiation, and the spectrum reduces to that of emission

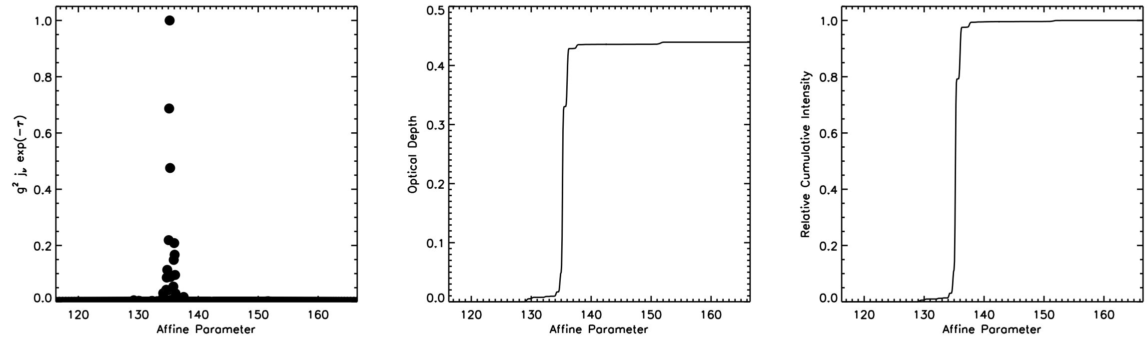

Figure 2.10 Sample plots of the intensity integrand (left panel), optical depth (middle panel) and cumulative intensity (right panel) along a ray for the case where the accretion flow is optically thin, defined as maximum optical depth $\lesssim 3$.

only (labeled 'Emission' in Figure 2.8). This result agrees reasonably well with the assertion made by Shapiro (1973) [179] that absorption is negligible when $\nu \gtrsim 10^{11}$ Hz.

Also of interest is the black hole shadow produced by various accretion models [70]. Figure 2.9 shows the shadow of the spherically accreting Schwarzschild black hole as a 2-d contour plot and a 1-d profile. The shadow is produced at $\alpha^2 + \beta^2 = 27$, and is caused by the difference in path length between geodesics which intersect the horizon and return to infinity, as well as the blueshift of radiation from infalling gas behind the black hole relative to the red shift of that nearest the observer. The asymmetry in Figure 2.1 is not seen here due to the spherical symmetry of the Schwarzschild metric.

Thus far, we have employed simple dynamical models to verify our ray tracing and geodesic implementations.. The goal of this thesis is to connect state of the art simulations of black hole accretion flows with observations. The techniques described above allow the calculation of observables from some emission model, i.e. with knowledge of the emission/absorption coefficients and redshifts (which depend on the fluid position and four-velocity). For the numerical models of interest, these quantities are specified on a grid in the Kerr metric with some coordinate system. We now describe the process of using simulation data in conjunction with the ray tracing radiative transfer method, rather than the simple dynamical models used in the examples above.

2.5 GRTrans: Relativistic Radiative Transfer via Ray Tracing

We have written the code `grtrans` to calculate the time-dependent image of a source at infinity in general relativity. In this thesis, the source will always be a black hole accretion flow and the spacetime will always be the Kerr metric. In general, extensions to other spacetimes or sources are straightforward. The necessary components describing the model are:

- A dynamical model specifying the fluid four-velocity and state variables at all points in space.
- A radiative model for converting the fluid state variables into variables used for computing emission and transfer coefficients (electron number density, temperature and magnetic field strength in the case of synchrotron emission for a thermal particle distribution).
- An emissivity for computing emission and transfer coefficients from radiative variables.

In this brief summary of the code, we discuss the implementation of the ray tracing procedure; the method for interpolating zone-based simulation quantities to points on rays; the loading, storage and updating of simulation data required for the interpolation; and the integration technique of the resulting emission model.

2.5.1 Implementation of Ray Tracing

The specification of the camera (viewing angle, grid size and shape) and calculation of geodesics is done using `geokerr` [53]. However, `grtrans` has capabilities for loading geodesic coordinates from a file as well as for computing them on the fly with `geokerr`, so that files for a given viewing angle, grid size and black hole spin may be re-used with many timesteps of simulation data or with different simulations or other models of the same black hole spin. This also makes the extension to other spacetimes (with different geodesics) straightforward.

Ray tracing using numerical data in three spatial dimensions is memory intensive. A typical calculation uses a camera of 150x150 pixels, with $\simeq$ 200-400 points per pixel (geodesic),

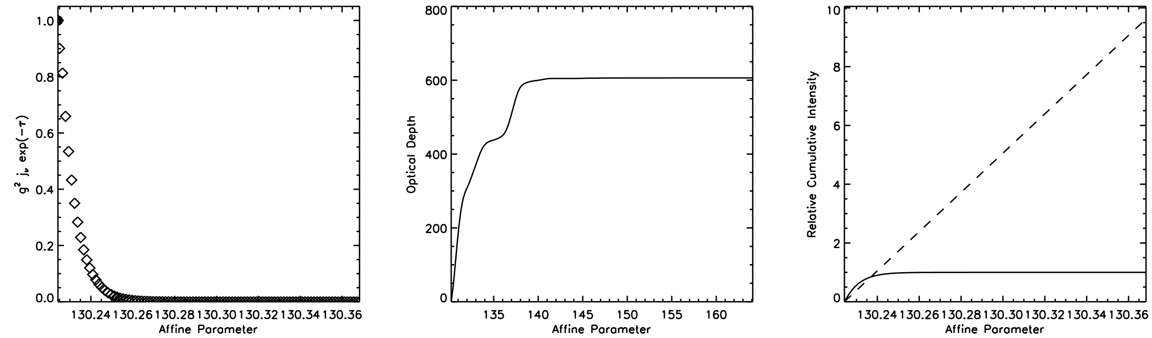

Figure 2.11 As in Figure 2.10, but for the optically thick case where the first point sampled has an optical depth $\gtrsim 10$ The solid points are from the initial sampling, while the open diamonds are from refining the region near the photosphere ($\tau \sim 1$).

while a typical GRMHD simulation uses $\sim 128^3$ zones per timestep. Storing the entirety of the geodesic and fluid information simultaneous is computationally prohibitive, so that one must be read on the fly while the other is kept in memory. We choose to load each geodesic and compute its intensity for the given model before moving on to the next. The alternative choice has been made as well,[5] and there is no obvious clear advantage to either method.

For a given geodesic, the fluid variables are found as discussed below and then intensities are calculated over a grid of observed frequency, mass unit (or accretion rate; see below), emissivity or other parameter. The code is extremely flexible, and scales well with the addition of parameters since the geodesic calculation and fluid variable finding are typically more computationally expensive than the emissivity calculation for the problems of interest here.[6]

2.5.2 Data Loading and Updating

The radiative transfer calculation accounts for all relativistic effects, including the time delay between photons emitted at different locations in the accretion flow. The image is

---

[5] Josh Dolence, private communication.

[6] In particular, for synchrotron emission from thermal particles as modeled here. The non-thermal power law synchrotron emissivity is slower, as would be any model adding a non-thermal tail to the thermal case.

taken at a particular *observer* time, which corresponds to a relatively wide range ($\lesssim$ 100M) of *simulation* time. Many timesteps of fluid data are then required to construct a single image. This is done by loading simulation data from the entire desired range of timesteps into memory (up to $\simeq$ 2GB in the most memory intensive cases) at the beginning of the calculation.

Due to the large number of timesteps often held in memory, it is typically most efficient to compute images from many observer times sequentially. Then instead of loading another large set of simulation data, only the number of steps corresponding to the observed time step need to be replaced. The data arrays for each fluid variable begin with data from every zone from the future-most timestep of simulation data and go backwards in time further into the array. To move to the next timestep, the data are shifted backwards into the array by the desired observed time step (always taken to be an integer multiple of the simulation time step). The earliest timesteps, now at the front of the data arrays, are then replaced with new data completing the observed time step.

2.5.3 Zone Finding and Interpolation

The fluid variables at each point on a geodesic, in "code" units ($G = c = M = 1$; see below), are calculated by interpolating the large data arrays described above. Before the interpolation can be done, the correct zone indices corresponding to the geodesic coordinates must be found. This step needs to be rapid for the scheme to work, and manually searching the array of zone centers for the correct coordinate locations is too slow. The simulations used here are performed on a regular (evenly spaced) grid in some coordinates which are not the Boyer-Lindquist coordinates used for the geodesic calculation. To find the zones corresponding to geodesic points, the geodesic coordinates are transformed to simulation coordinates to find the two nearest neighbors in simulation coordinates in each dimension. These nearest neighbors are then used to find the indices corresponding to the eight nearest neighbors in the data arrays. This step is trivial when there is no static mesh refinement, as in HARM type simulations [85, 129], but fairly complicated when there is, as is often used in Cosmos++ [80]. An equivalent procedure is then used in the time dimension, which is always straightforward.

The fluid quantities from these 16 nearest neighbors are then linearly interpolated in each dimension to find the fluid variables along the geodesic. (The interpolation is usually done in Boyer-Lindquist or Kerr-Schild coordinates, but the results are nearly identical with simulation coordinates). As discussed later (see Section 5.3.2 and Figure 5.15), interpolating in the time direction for simulations with relatively widely spaced timesteps ($\delta t \gtrsim 4\mathrm{M}$) can suppress the magnetic field strength and the resulting synchrotron emissivity. We usually use the nearest neighbor in the time direction and interpolate in the three spatial dimensions. Alternatively, if some other model is to be used for computing emission and transfer coefficients, they can be loaded directly into data arrays. Then the fluid variable finding and conversion to cgs units (see below) are dummy routines, and the emissivity simply does the interpolation in frequency.

The routines for loading and updating data, zone finding and interpolation are simulation specific. This maintains flexibility for adapting the code to new simulations, grids and/or coordinates.

2.5.4 Conversion to cgs Units

As discussed earlier, current numerical simulations of black hole accretion flows typically ignore radiation [85, 51] or in some cases use an artificial, optically thin cooling function [175, 144]. Then the problem is scale free, and $G = c = M = 1$ units are used ("code" units). To compute radiative transfer coefficients, these scales must be fixed [173]. Setting the black hole mass fixes the length and time scales. The mass of the accretion flow is negligible compared to that of the black hole and is scaled separately. Fixing the code mass unit is equivalent to choosing the accretion rate onto the black hole. The conversions are given as follows, where the desired accretion rate, $\dot{M}_{cgs}$, can either be specified directly or chosen as a fraction of the Eddington accretion rate, $L_{edd}/c^2 = \frac{4\pi G M m_p}{\sigma_T c}$, where σ_T is the Thompson cross section and m_p is the proton mass:

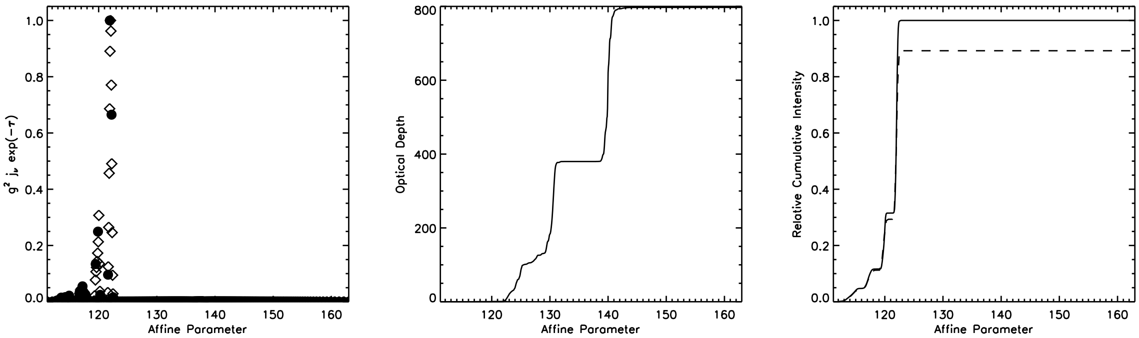

Figure 2.12 As in Figures 2.10 and 2.11, but for the marginally optically thick case where the first point sampled has an optical depth $\lesssim 10$ but the total optical depth $\gtrsim 3$. The solid points are from the initial sampling, while the open diamonds are from refining the region where the cumulative intensity changes rapidly.

$$\frac{\rho_{cgs}}{\rho_{cu}} = \frac{\dot{M}_{cgs}}{\dot{M}_{cu}}\frac{t_{cgs}}{l^3_{cgs}}, \tag{2.22}$$

$$\frac{p_{cgs}}{p_{cu}} = \frac{\rho_{cgs}}{\rho_{cu}}c^2, \tag{2.23}$$

$$\frac{b_{cgs}}{b_{cu}} = \sqrt{\frac{\rho_{cgs}}{\rho_{cu}}}c. \tag{2.24}$$

The subscript cgs (cu) indicates quantities in cgs (code) units.

2.5.5 Integration procedure

Given the emission and absorption coefficients, we can integrate the radiative transfer equation ((2.6)). This needs to be done with some care, however, since the integration is only trivial when the optical depth, τ, is small. We treat three regimes separately:[7]

- Optically thin: When the maximum value of τ along the geodesic is less than some critical value, usually $\simeq 3$, the radiative transfer equation is done as a quadrature using the trapezoid rule for the numerically tabulated geodesic points. A sample intensity integrand, optical depth and cumulative intensity along a ray are shown in Figure 2.10.

---

[7] All of the examples in this section are for synchrotron radiation, which is by far the most sharply peaked emissivity used in this thesis.

- Optically thick: When the value of τ jumps above $\simeq 10$ in the first few points on the geodesic, we analytically estimate the location of the $\tau = 1$ surface and generate many points between the beginning of the geodesic and that location. Then the procedure for finding emission and absorption coefficients is repeated for these new points, and the new maximum optical depth is found. If it is still too large or has become too small, the terminal affine parameter value is changed and the procedure is repeated until it's about right, and finally the trapezoid rule is used to compute the intensity. Note that whenever this case is used, the intensity is completely dependent on the location of the outer cutoff radius. In this sense, it is more intended to prevent code failure and to produce correct images than to obtain physical results which should be independent of the chosen outer cutoff radius. In practice, it is only used for low frequency synchrotron spectra where we do not expect agreement between models and data. A sample intensity integrand, optical depth and cumulative intensity along a ray, with and without this refinement, are shown in Figure 2.11.

- Mildly optically thick: When the maximum value of τ is larger than the critical value but that value is not reached in the first few points of the geodesic, we make sure not to miss the interesting portion of the ray by locating the points where the largest contributions to the intensity are generated (usually close to the photosphere). New points are generated in this region, and the radiative transfer equation is then integrated for the entire ray including the new higher resolution points near the region of interest. A sample intensity integrand, optical depth and cumulative intensity along a ray, with and without this refinement, are shown in Figure 2.12.

The code has been tested in all of these limits and typically converges with around $100 - 200$ points per geodesic. Usually $200 - 400$ are used instead to ensure convergence to within a few percent (see Figure 2.13). Although in the optically thick cases we refine the geodesic points and re-calculate fluid variables and emission and absorption coefficients, in practice to our working accuracy it would be sufficient to simply interpolate the logarithm of the coefficients themselves. An example is shown in Figure 2.14. Since the sources of

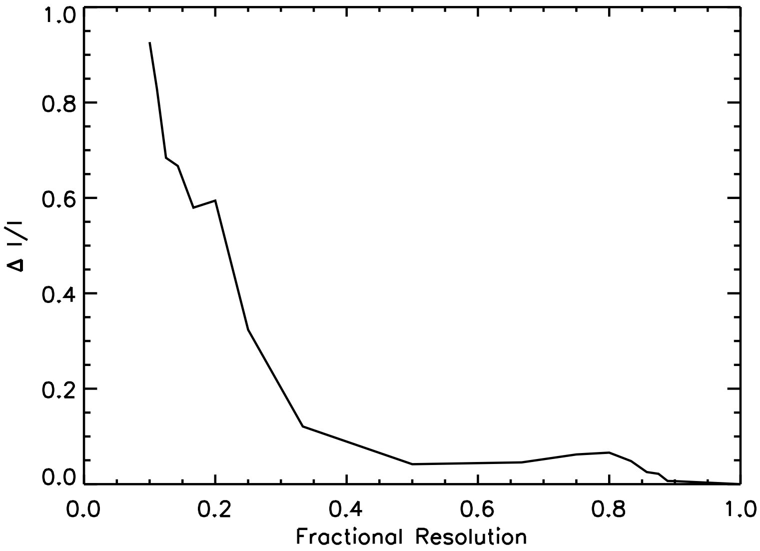

Figure 2.13 Fractional difference in intensity versus sampling used relative to our fiducial sampling of $\simeq$ 400 points per ray. The differences found by averaging many random resamplings of the fiducial data. Convergence to within a few percent is obtained when the rate reaches $\simeq 0.5$ ($\simeq$ 200 points per ray).

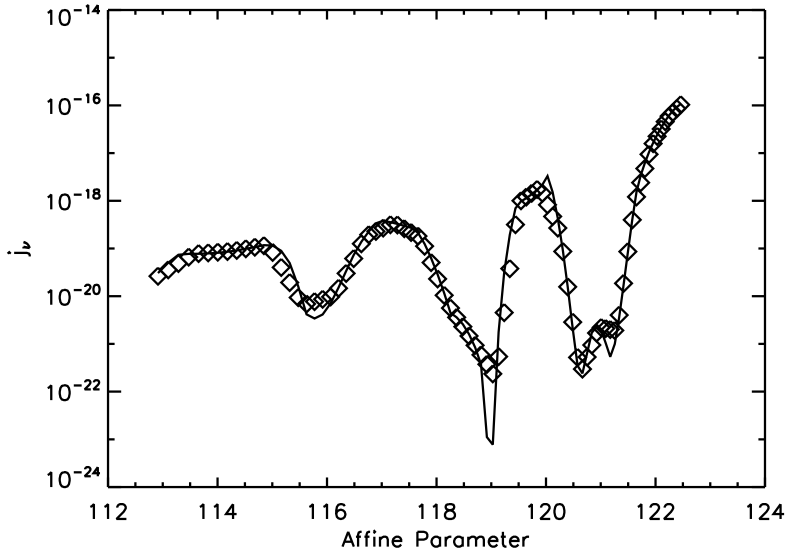

Figure 2.14 Emissivity j_ν along a ray found by interpolating geodesic coordinates, finding new fluid variables and re-calculating the emissivity (solid line) compared to directly interpolating the logarithm of the emission coefficients from the original ray (open diamonds). While we use the former method, in practice the latter would likely be sufficiently accurate.

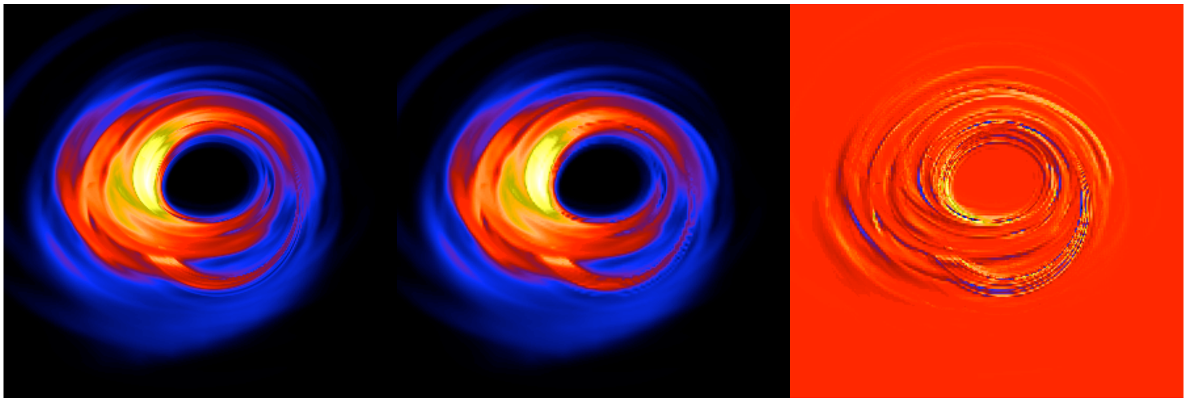

Figure 2.15 Sample image of Sgr A* with 300x300 resolution (left panel), 150x150 resolution (middle panel, re-sampled to 300x300) and the difference between the two (right panel). The largest residuals are $\simeq$ 10% of the maximum image intensities. Although minor features are poorly resolved in the 150x150 image, the integrated image intensities agree to within $\simeq$ 0.01%. The images are taken from the MBD simulation (see Section 4.3), and the parameters are $\nu_0 = 230$GHz, $i = 50°$ and $T_i/T_e = 3$.

interest are usually optically thin at the desired observed frequencies, the iterative procedures are not a large part of the computational expense of the code. Usually these are the interpolation of simulation data to geodesic points, which can involve transcendental coordinate transformations and root finding; and the emissivity calculations, which unlike the interpolation must be repeated at every desired output frequency and mass accretion rate.

A converged image consists of high enough pixel resolution and a large enough "camera," as measured in impact parameters at infinity. The camera size can be estimated as the projected size of the emission region. In practice, this is made slightly larger than necessary so that the same stored pixel coordinates can be re-used for many images. Visual inspection of images is often sufficient to ensure convergence, as underresolved regions of an image usually consist of sharp spikes in intensity between neighboring pixels. We find that an evenly-spaced, 150x150 pixel rectangular grid is sufficient for the purposes of this thesis and that is used except in the labor-intensive calculations for the "radiation edge" in Section 3.3.1, where simple emissivities are used and convergence in total flux can be achieved with a much coarser grid. Figure 2.15 shows a typical case in a model of Sgr A*. The left panel is 300x300, the same image at our fiducial resolution of 150x150 is in the middle panel and the right panel shows the residuals. The total flux in this case converges to $\lesssim 0.01\%$. We always find that 150x150 pixels is sufficient for $\lesssim 1\%$ convergence in the total flux. Actual cameras do not sample the intensity along a single ray, but rather average over a finite pixel area. We can approximate this by taking each ray to be a vertex of the camera and average sets of four rays to form pixels. This procedure differs negligibly from the simple one ray per pixel scheme used throughout this thesis.

The ray tracing method for relativistic radiative transfer calculations described in this chapter as implemented in the code `grtrans` is used for the remainder of this thesis to compute images, spectra and light curves from general relativistic MHD (GRMHD) simulations of black hole accretion flows. Simplified models of stellar mass black holes in the hard state or low-luminosity active galactic nuclei (AGN) are discussed in Chapter 3. Chapters 4 and 5 describe detailed radiative models of Sagittarius A*, and the model is extended to include jet emission to construct a model of M87 in Chapter 6.

Chapter 3

OBSERVATIONAL PROPERTIES OF TILTED BLACK HOLE ACCRETION DISKS

This chapter is devoted to the study of generic observational properties of tilted accretion disks, where the angular momentum axis of the accreting material is misaligned from the black hole spin axis. We discuss their relevance to observations of black hole x-ray binaries and signatures of the presence of tilt that can be studied in future observations. This work is also relevant to discussions of models of Sagittarius A* from tilted simulations in Chapters 4 and 5.

3.1 Introduction

In standard thin disk accretion theory [176, 148], the angular momentum axis of the accretion flow is assumed to be aligned with the black hole spin axis. Bardeen & Petterson [14] found that even if the initial angular momentum axis of the accretion flow is misaligned from the black hole spin axis, the inner part of the disk will still align on the viscous timescale. However, this so-called "viscous" regime only operates when $H/R \lesssim \alpha$, where H/R is the scale height of the accretion disk, and α is the parameterized viscosity [153]. This is applicable in active galactic nuclei (AGN) and the high/soft or thermal state of black hole X-ray binaries. On the other hand, advection-dominated accretion flows (ADAFs) are expected in the low/hard state of black hole X-ray binaries [140, 65] and in low-luminosity AGN. ADAFs are unable to cool through efficient radiation, and are geometrically thick. It is likely that the accretion flow in many of these sources is misaligned, or "tilted."

Contemporary general relativistic MHD simulations [GRMHD, 51, 85] currently provide the most physically realistic description of the inner portion of accretion flows around spinning black holes. Radiation can be calculated from these simulations in post-processing by assuming that it is dynamically and thermodynamically negligible. This method has been used to look for high frequency quasi-periodic oscillations (HFQPOs) in simulated data [173] and to create radiative models of Sagittarius A* ([147, 136] and Chapters 4 and 5) and M87 (Chapter 6).

All prior work assumed alignment between the angular momentum axis of the accretion flow and the black hole spin axis. Fragile et al. [80, 81, 77] were the first to do GRMHD simulations of disks with a tilt between these two axes. These new simulations yielded a number of unexpected features. First, the main body of the disk remained tilted with respect to the symmetry plane of the black hole; thus there was no indication of a Bardeen-Petterson effect in the disk at large. The torque of the black hole instead principally caused a global precession of the main disk body [78, 80]. The time-steady structure of the disk was also warped, with latitude-dependent radial epicyclic motion driven by pressure gradients attributable to the warp [79]. The tilted disks also truncated at a larger radius than expected for an untilted disk. In fact, based on dynamical measures, the inner edge of these tilted disks was found to be independent of black hole spin [77], in sharp contrast to the expectation that accretion flows truncate at the marginally stable orbit of the black hole. Finally, Henisey et al. (2009) [95] found evidence for trapped inertial waves in a simulation with a black spin $a = 0.9$, producing excess power at a frequency $118(M/10M_{\odot})^{-1}$ Hz.

In this work we use the relativistic ray tracing technique described in Chapter 2 to produce images and light curves of some of these numerically simulated tilted and untilted black-hole accretion disks. Our goal in this chapter is to discuss observable differences between the two types of accretion flows, and to identify observational signatures of tilted black hole accretion disks.

3.2 Methods

3.2.1 Simulation Data

The simulations used here are from Fragile et al. [80, 81, 77]. The parameters are given in Table 3.1. All of the simulations used the Cosmos++ GRMHD code [6], with an effective resolution of 128^3 for the spherical-polar grid (except near the poles where the grid was purposefully underresolved) and $128 \times 64 \times 64 \times 6$ for the cubed-sphere grid. The simulations were initialized with an analytically solvable, time-steady, axisymmetric gas torus [51],

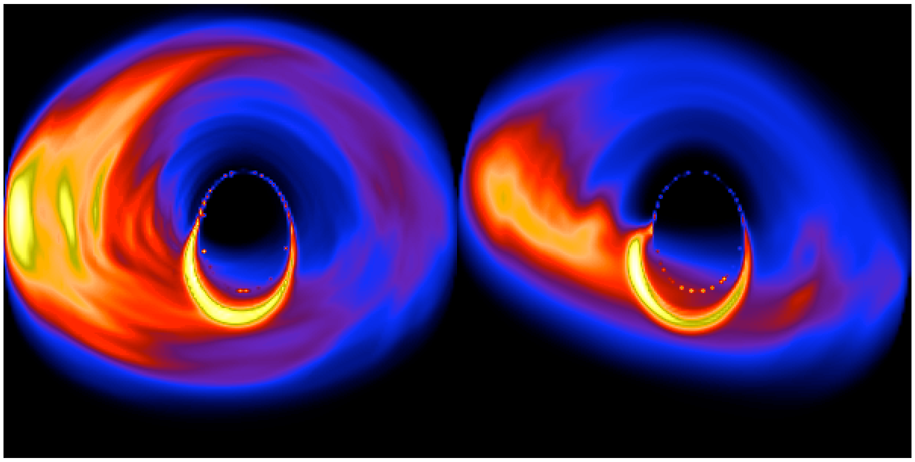

Figure 3.1 Sample images of the thermal emission model for the 90h (left) and 915h (right) simulations at 60° inclination. The observed photon energy is $E_0 = 10$keV for a $10M_\odot$ black hole, and each panel is $54M$ across. The color scale is linear, increasing from blue to red to yellow to white.

threaded with a weak, purely poloidal magnetic field that follows the isodensity contours and has a minimum $P_{gas}/P_{mag} = 10$ initially. The magnetorotational instability (MRI) arose naturally from the initial conditions, and the disk quickly became fully turbulent. The simulations were all evolved for ∼8000M, or ∼40 orbits at $r = 10$M in units with $G = c = 1$. Only data from the final 2/3 of the simulation are used in this analysis, once the disks are fully turbulent as measured by a peak in the accretion rate and in the mass inside of $r = 10$M. This is chosen to utilize as much of the simulation data as possible, and none of our results depend on which time interval in the simulation is used.

These simulations all evolved an internal energy equation, and injected entropy at shocks. Such a formulation does not conserve energy, and produces a more slender, cooler torus than conservative formulations which capture the heat from numerical reconnection of magnetic fields [82]. The scale height spanned the range $H/R \sim 0.05 - 0.1$ in these simulations, with larger scale heights for higher spin simulations.

Table 3.1. Simulation Parameters

Simulation	a/M	Tilt Angle	Grid
0H[a]	0	...	Spherical-polar
315H[b]	0.3	15°	Spherical-polar
50H[a]	0.5	0°	Cubed-sphere
515H[a]	0.5	15°	Spherical-polar
715H[b]	0.7	15°	Spherical-polar
90H[c]	0.9	0°	Spherical-polar
915H[c]	0.9	15°	Spherical-polar

[a] Fragile et al. (2009) [81]

[b] Fragile (2009) [77]

[c] Fragile et al. (2007) [80]

3.2.2 Ray Tracing

Relativistic radiative transfer is computed from simulation data via ray tracing. Starting from an observer's camera, rays are traced backwards in time assuming they are null geodesics (geometric optics approximation), using the public code `geokerr` described in Appendix A. In the region where rays intersect the accretion flow, the radiative transfer equation is solved along the geodesic [28] in the form given in Fuerst & Wu (2004) [84], which then represents a pixel of the image. This procedure is repeated for many rays to produce an image, and at many time steps of the simulation to produce time-dependent images (movies). Light curves are computed by integrating over the individual images. Sample images of two simulations are given in Figure 3.1. Doppler beaming causes asymmetry in the intensity from approaching (left) and receding (right) fluid. Photons emitted from the far side of the accretion flow are deflected toward the observer, causing them to appear above the black hole. The thick, central ring is due to gravitational lensing from material passing under the black hole, while the underresolved circular ring is caused by photons that orbit the black hole one or more times before escaping. These ring features are in excellent agreement with the predictions made by Viergutz (1993) [195].

To calculate fluid properties at each point on a ray, the spacetime coordinates of the geodesic are transformed from Boyer-Lindquist to the Kerr-Schild coordinates used in the simulation. Since the accretion flow is dynamic, light travel time delays along the geodesic are taken into account. Data from the sixteen nearest zone centers (eight on the simulation grid over two time steps) are interpolated to each point on the geodesic. Between levels of resolution near the poles on the spherical-polar grid, data from the higher resolution layer are averaged to create synthetic lower resolution points, which are then interpolated. Very little emission originates in the underresolved regions of the simulation.

The simulations provide mass density, pressure, velocity and magnetic field in code units. These are converted into cgs units following the procedure described in Schnittman et al. (2006) [173] and Chapter 2. The length- and time-scales are set by the black hole mass, taken to be $10M_{\odot}$ throughout.

We consider two emission models. The thin line emissivity from Schnittman et al. is a toy model that traces the mass density in the accretion flow. Their thermal emission model uses free-free emission and absorption coefficients, and is used as a model for the high/soft state. Although we do not expect tilted disks to accurately represent the high/soft state, this model may be appropriate for sources radiating at an appreciable fraction of Eddington, where the infall time is shorter than the radiative diffusion time and the accretion flow becomes geometrically "slim." When taking the temperature from the ideal gas law rather than the radiation-dominated equation of state used in Schnittman et al., this model may be qualitatively appropriate for modeling the low/hard state in X-ray binaries or low-luminosity AGN.

In §3.3.1, we consider emission from inside of $r = 15$M, while in §3.3.2 and 3.3.3 fluid inside of $r = 25$M is used for the ray tracing. For all results here, we take the temperature from the ideal gas law rather than assuming a radiation-dominated equation of state. All of our results are qualitatively identical when using the radiation-dominated equation of state to calculate the temperature.

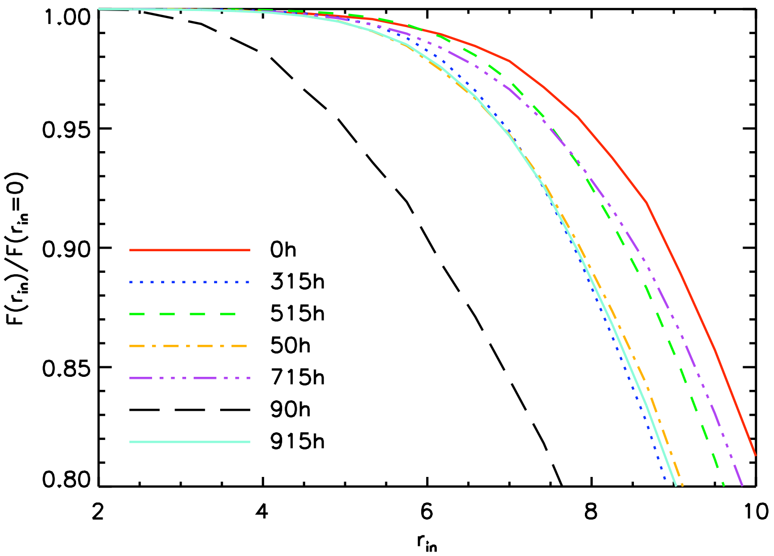

Figure 3.2 Comparison of relative intensities for all simulations using the thin line emissivity. The flux from grids of images over observer time, inclination and azimuth for each simulation have been averaged to create these curves.

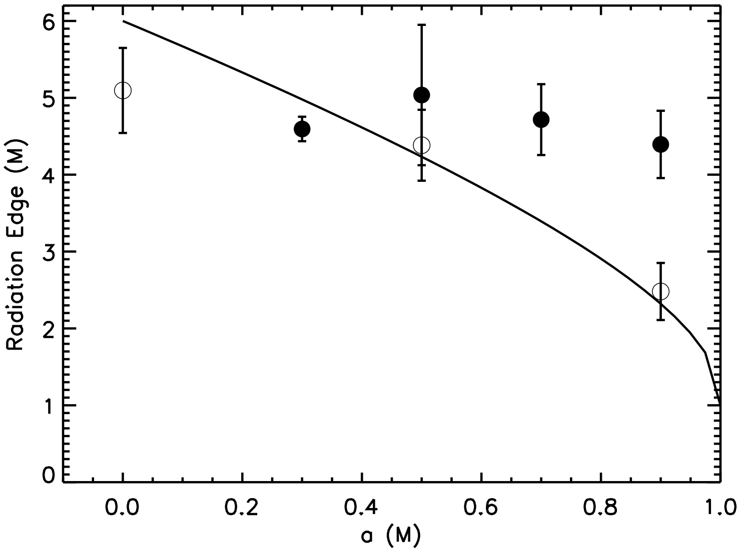

Figure 3.3 Radiation edge as a function of spin for untilted (open) and tilted (solid) simulations for the thin line emissivity. The error bars show the one standard deviation time variability in the radiation edge, averaged over other parameters. The solid line is the marginally stable orbit.

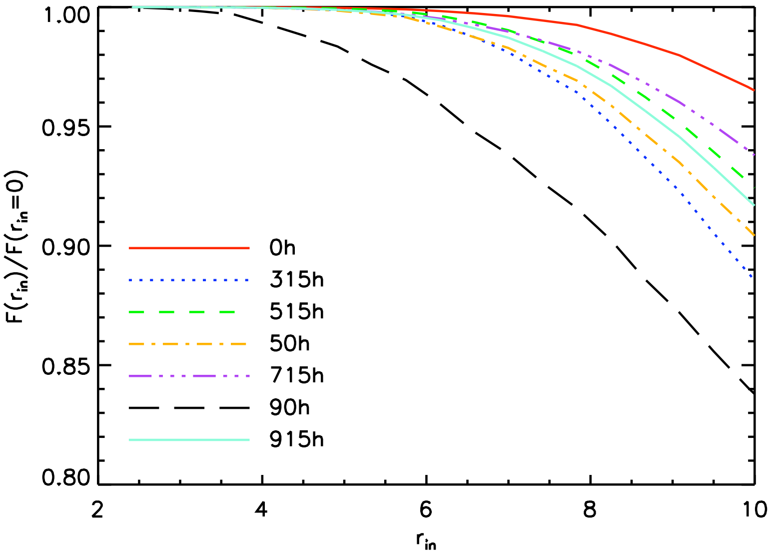

Figure 3.4 Comparison of relative intensities for all simulations using the thermal emissivity at $E_0 = 1$ keV. The flux from grids of images over observer time, inclination and azimuth for each simulation have been averaged to create these curves.

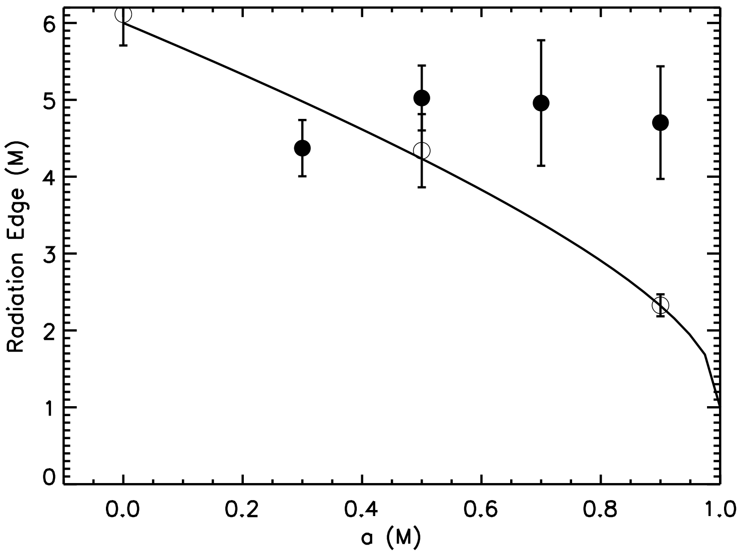

Figure 3.5 Radiation edge as a function of spin for untilted (open) and tilted (solid) simulations for the thermal emissivity at $E_0 = 1$keV. The error bars show the one standard deviation time variability in the radiation edge, averaged over other parameters. The solid line is the marginally stable orbit.

3.3 Results

3.3.1 Radiation Edge

Inferring the inner edge of accretion flows is important for attempts to measure spin from broad iron lines [e.g. 200] or continuum fitting [e.g. 174, 49]. Such measurements assume that the disk has a sharp cutoff at the innermost stable circular orbit, which depends on spin [15]. Fragile (2009) [77] used four different dynamical measures [108] to compare the inner edges of simulated tilted and untilted accretion disks. Here we use the ray traced models to locate the "radiation edge," the radius inside of which the contribution to the total flux is negligible.

For each emission model, images are calculated for all simulations over a grid of observer inclination, observer time, and observer azimuth (for the tilted simulations). We then compute images cutting out fluid inside of successive values of the radius $r_{\rm in}$. The radiation edge is functionally defined as the radius where the ratio of intensities, $F(r_{\rm in})/F(0)$, drops below an arbitrary fraction f, chosen so that the untilted radiation edge agrees as well as possible with $r_{\rm ms}$, the marginally stable orbit.

Figure 3.2 shows a plot of $F(r_{\rm in})/F(0)$ as a function of $r_{\rm in}$ averaged over observer time, azimuth and inclination for the thin line emissivity. From these curves we extract values of the radiation edge, $r_{\rm edge}$. Results are shown in Figure 3.3, where the error bars are computed from the standard deviation of $r_{\rm edge}$ as a function of time, averaged over the other parameters. This result agrees well with the dynamical measures from Fragile (2009) [77]. While the radiation edge moves in towards the black hole with increasing spin for untilted simulations, there is no such trend in the tilted simulations. Instead, the radiation edge appears to be independent of spin.

Figures 3.4 and 3.5 show the same plots for the thermal emission model with observed photon energy $E_0 = 1$ keV. The conclusions are identical with this emission model. The untilted simulations have radiation edges which agree quite well with $r_{\rm ms}$, while the tilted simulations show no correlation between spin and $r_{\rm edge}$. Again, these results are consistent with Fragile (2009) [77], although we find no trend of *increasing* radiation edge with spin, as was found for a couple of the dynamical measures used by Fragile. Plots from other observed

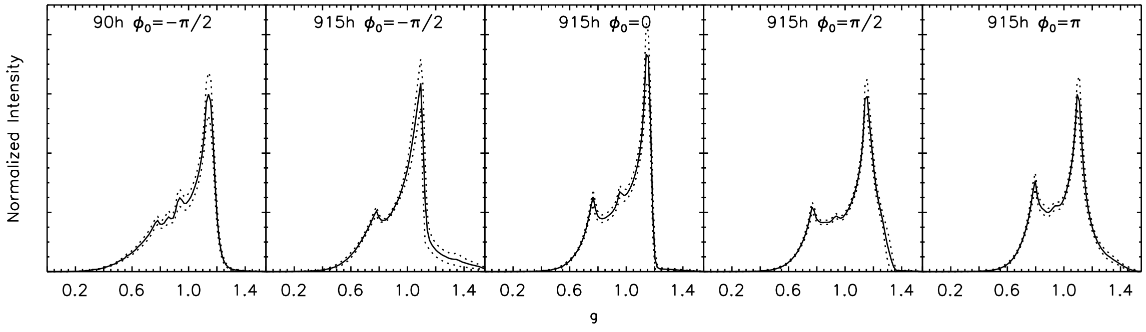

Figure 3.6 Emission line profiles for simulations with a=0.9. The emissivity is $j \propto \rho r^{-3}$ and the observer inclination is 60° in all cases. The dotted lines show the 1σ range, taken from the time variability.

photon energies are not shown; although the relative flux falls off much more quickly with increasing $r_{\rm in}$ at higher photon energies, the results for the radiation edge remain completely unchanged.

3.3.2 Emission Line Profiles

Spectra from AGN and X-ray binaries typically include strong emission and absorption features. As the observed line shapes are sensitive to both the velocity of the emitting/absorbing fluid, and also to the local gravitational redshift, they can provide information about the dynamics of the accretion flow [66, 111].

Untilted accretion flows have nearly Keplerian velocity distributions outside the marginally stable orbit, where the velocities smoothly transition to plunging. Simulated tilted accretion disks, on the other hand, show three major differences. The Keplerian velocity structure is now tilted.

Secondly, the warped structure of the tilted disks leads to epicyclic motions with velocity magnitudes comparable to the local geodesic orbital velocity [79]. Finally, the larger radiation edge values of the tilted disks identified in §3.3.1 means that the transition to plunging orbits occurs at larger radius than in untilted disks.

These effects indicate that we should expect a number of differences in line profiles from tilted accretion flows [83]. The maximum blueshift should be larger for tilted accretion

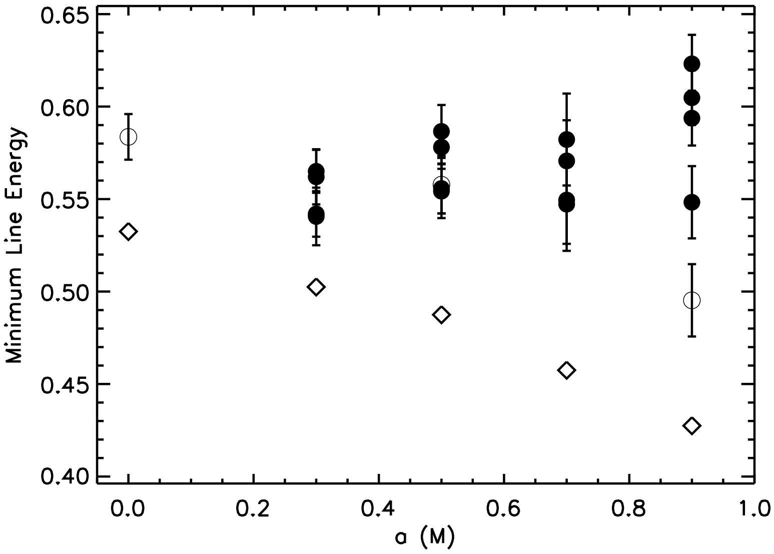

Figure 3.7 Minimum line energy vs. spin for all simulations. The tilted (untilted) simulations are denoted by solid (open) circles, and four observer azimuths are plotted for the tilted simulations. The open diamonds are from a thin disk in the equatorial plane with an emissivity $j \propto r^{-3}$ similar to that used in Schnittman & Bertschinger (2004) [171] and in Section 2.4.2. The minimum line energy is defined as the lowest energy contained in the set of intensities comprising 99% of the total line intensity. The 1σ errors are taken from the time variability.

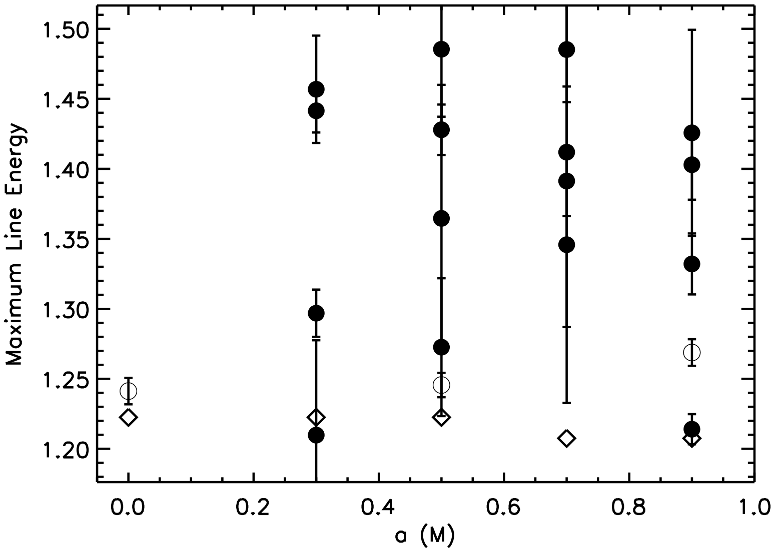

Figure 3.8 As in Figure 3.7, but for the maximum line energy.

disks, except for edge-on viewing. For $i < 90° - \beta$, where i is the observer's inclination angle and β is the initial tilt angle, both relative to the black hole spin axis, the tilted accretion flow should mimic an untilted one with a larger inclination. In contrast, the red wing should be less pronounced in the tilted disks due to their larger truncation radii. On the redshifted side, tilted disks behave similar to lower spin, untilted disks.

Producing a detailed reflection spectrum would require a significant number of assumptions to model the metallicity, ionization levels, and incident X-ray flux throughout the accretion flow. For simplicity, we instead use toy model emissivities of the form $j \propto \rho r^{-s}$, where ρ is the fluid mass density, j is the photon-energy integrated emissivity and $s = 2{,}3$. The two values correspond to assuming the emitted line flux is proportional to the incident flux from an irradiating source on the spin axis and to local dissipation of heat, respectively [e.g., 83]. This simple form allows us to focus on general features to be expected from emission lines from tilted black hole accretion disks.

Figure 3.6 shows sample line profiles for an inclination of $i = 60°$ for four observer azimuths, ϕ_0, from the 915h simulation. Only a single observer azimuth from the 90h simulation is shown, since the time-averaged emission line is independent of observer azimuth for untilted simulations. In all cases, the lines consist of a strong peak near the rest energy of the line ($g \equiv E_0/E_{em} = 1$), a smaller peak at lower energy and a "red wing," whose extent and strength depends on the amount of emission arising very close to the black hole (small g). The location of the "blue" peak (large g) depends on the maximum velocity along the line of sight in the accretion flow. For an untilted disk, this corresponds directly to the observer's inclination angle, since all fluid velocities are essentially in the equatorial plane.

For the tilted model shown in Figure 3.6, the location and strength of the blue peak changes significantly with observer azimuth. When the angular momentum axis of the accretion flow is in the plane of the sky ($-\pi/2 \lesssim \phi_0 \lesssim -\pi/4$, depending on the simulation time), its fluid velocities are maximally aligned with the observer's line of sight, leading to the largest blueshifts. This is the same condition as an untilted disk being viewed edge-on. For other orientations, the blue tail can extend to significantly higher photon energies in the tilted simulations because the largest effective inclination is approximately $i_{\text{eff}} = i + \beta$. When the accretion flow is not edge-on, there will exist orientations where $i_{\text{eff}} > i$, and

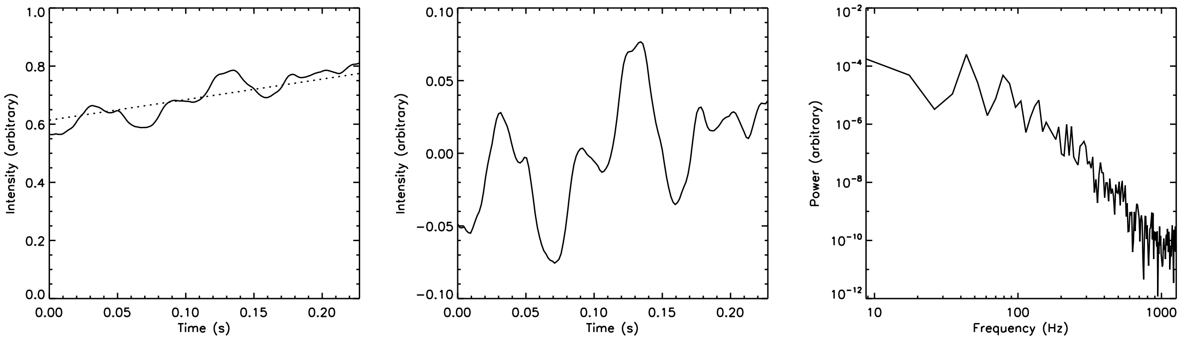

Figure 3.9 Sample light curve and linear fit (left), light curve with linear fit subtracted (middle) and power spectrum (right). The units are scaled to a 10 solar mass black hole.

the blue peak for a tilted simulation will occur at higher energy than possible for untilted accretion flows. The red wing, on the other hand, remains largely unchanged with observer azimuth, since it is caused by gravitational redshifts rather than Doppler boosts. Since the radiation edge for the 915h simulation was found to occur at significantly larger radius than that of 90h, it is expected that the red wing should extend further in the 90h simulation. The effect is subtle, but identifiable in Figure 3.6.

To quantify these trends, for all simulations we compute the extent of the line profile, as well as the strengths and locations of their red and blue peaks. Most clear are the results for the line extents, shown for $i = 60^\circ$ in Figures 3.7 and 3.8. As expected, the red wing extends to lower photon energies at higher spins for untilted simulations, while there is no similar trend for the tilted models. Also as expected, the blue wing extends to systematically higher photon energies in the tilted simulations because of the difference between $i_{\rm eff}$ and i noted above and the epicyclic motion in the tilted simulations.

Perhaps the most striking feature of the line profiles is the variation with observer azimuth seen in all tilted simulations. These changes in line shape between different observer azimuths are typically larger than the full range of changes seen between different spins for untilted simulations. This suggests that the most powerful means of recognizing a tilted accretion disk may be to measure changes in an emission line profile over time as the disk precesses.

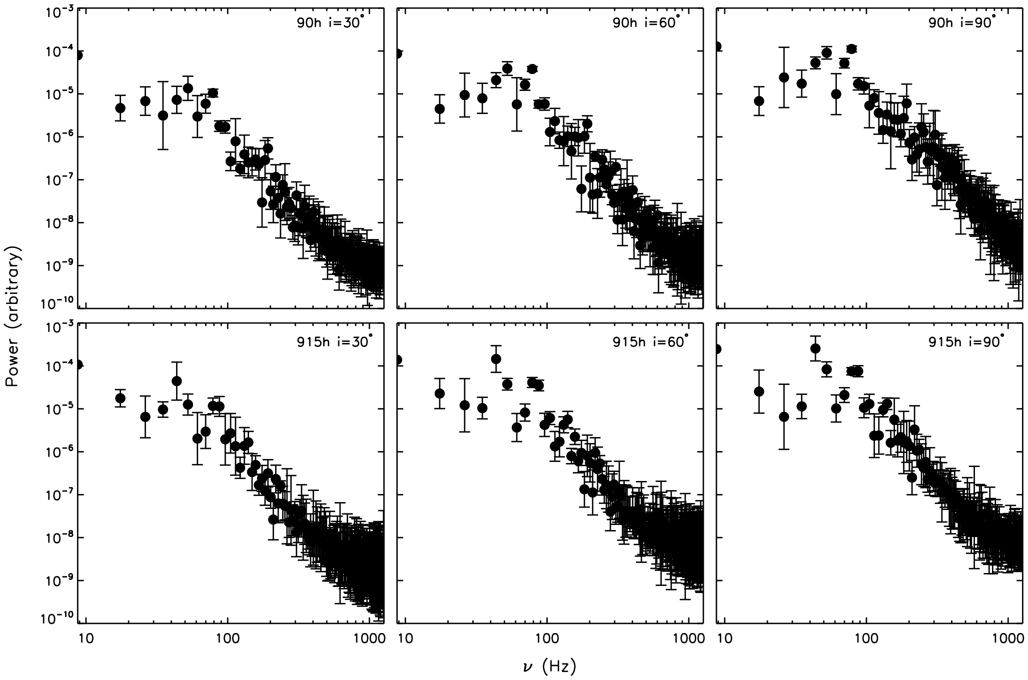

Figure 3.10 Median power spectra for $i = 30°$, $60°$, $90°$ from the 90h and 915h simulations. The errors are estimated from the standard deviations of the set of power spectra at observed photon energies of 1, 3, 10 keV at four observer azimuths. All power spectra are well described by the broken power law model, with break frequencies around 100Hz.

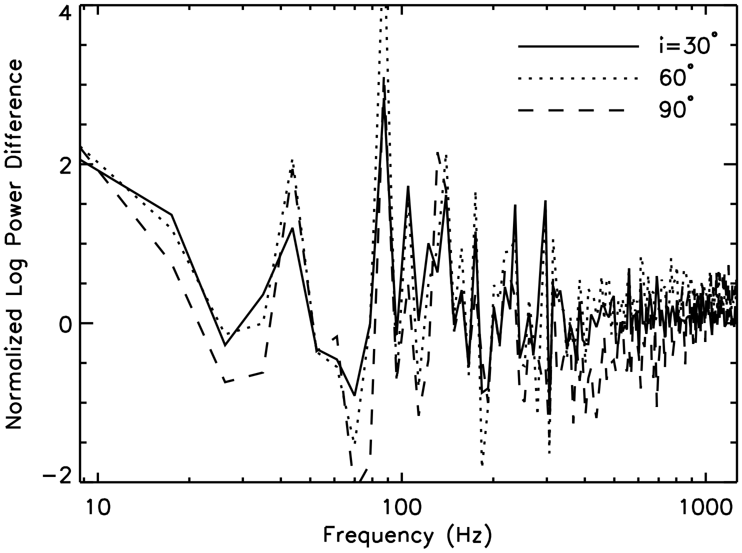

Figure 3.11 Difference in the logarithms of median 90h and 915h power spectra, normalized to their combined standard deviations for $i = 30°$, $60°$, $90°$. The median 90h power spectra are shifted to account for their lower mean power.

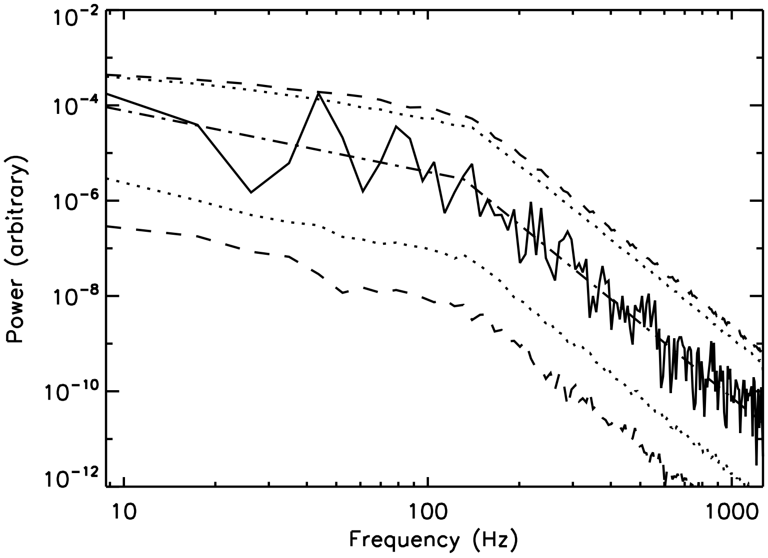

Figure 3.12 Sample power spectrum (solid), best fit broken power law model (dot-dashed) and upper and lower 99% (dotted) and 99.9% (dashed) significance contours.

3.3.3 Variability

X-ray timing of black hole binaries has allowed the characterization of power spectra and the detection of transient QPOs [for a review, see 164]. High-frequency QPOs are seen in the steep power law state (SPL), while low-frequency QPOs have been observed in both the hard state and the SPL. The geometry of the accretion flow in both these states is uncertain, and there is no reason to assume complete alignment between the accretion flow angular momentum and black hole spin axes in these states. Given the time-dependent nature of the ray tracing, we can analyze the variability of the simulated accretion flows for the simplistic emission models used here to analyze the shape of their power spectra and to look for possible QPOs.

The best time sampling of the simulations is in 90h and 915h, which are used here at 8 observer azimuths, 3 inclinations and 3 observed photon energies using the thermal emission model. Each light curve captures roughly 6 (20) orbits at $r = 25$M (10M), corresponding to a total observer time, $\Delta t_{\rm obs} = 0.23 M_{10}$ s, where M_{10} is the black hole mass in units of $10 M_\odot$. This duration is about 1/8 of the total precession period for the torus in the 915h simulation.

Figure 3.9 shows sample light curves and power spectra from the thermal emission model at 10keV for an observer inclination of $i = 60°$. The secular trend is removed by subtracting the linear best fit from the light curve before computing the power spectrum.

All power spectra are well fit by broken power law models of the form:

$$\begin{aligned} P(\nu) &= A\nu^{-\gamma_1} && \nu \le \nu_b \\ &= A{\nu_b}^{\gamma_2-\gamma_1}\nu^{-\gamma_2} && \nu > \nu_b, \end{aligned} \tag{3.1}$$

where γ_1, γ_2 are power law indices and the break frequency, ν_b, lies near 100Hz M_{10}^{-1} in both simulations. The tilted disk power spectra tend to flatten out at the highest sampled frequencies, ~1000Hz M_{10}^{-1}. Figure 3.10 shows median power spectra for the three different inclination angles from each simulation. The error bars are estimated from the standard deviation in $\log$ Power over observer azimuths and photon energies. At higher inclinations, the peaks in the power around 100Hz grow, especially for the tilted simulations. This would be expected from a source of excess power in the inner radii, where the larger Doppler shifts at higher inclination would enhance the signal.

To quantitatively compare the power spectra between the two simulations, the ratio between median power spectra in untilted and tilted simulations is plotted for each inclination in Figure 3.11. The values are normalized to the combined uncertainties at each frequency. The overall plots are shifted according to the mean ratio between power spectra.

At almost all frequencies, these ratios are within $\pm 2\sigma$, and are unlikely to be observed as significant features. However, there are a few noteworthy features near $100 M_{10}^{-1}$Hz. These are particularly interesting given the finding by Henisey et al. (2009) [95] that the tilted simulation 915h contains excess power due to trapped inertial waves at $118 M_{10}^{-1}$Hz.

To assess the significance of possible features in the PSDs, the power spectrum is fit with a broken power law model. The parameters from the best fit are used to simulate many random light curves with the same parameters, and which contain no significant features. The significance is determined by comparing the values for the power at each frequency for each model power spectrum with the distribution of random ones. An example is shown in Figure 3.12, where a single power spectrum from the 915h simulation is shown, as well as the best fit broken power law model and upper and lower 99.9% confidence intervals from simulating random light curves.

No obvious QPO features show up in this analysis. In several of the 915h light curves, the feature near $50 M_{10}^{-1}$Hz shows up as 99.9% significant. It appears at high significance in more of the light curves at high inclinations. In the 90h simulations, almost all significant features are found at very high frequencies $\sim 1000 M_{10}^{-1}$Hz. These are spurious, caused by slight errors in the fit to the post-break slope incurred by ignoring all frequencies larger than $800 M_{10}^{-1}$Hz. Including the highest frequencies in the fit can favor models with break frequencies $\sim 500\ M_{10}^{-1}$Hz, steep initial slopes and shallow post-break slopes. This occurs due to the denser sampling of the PSD at high frequencies. Simply ignoring the highest frequencies gives better results than a variety of more complicated weighting schemes. The features near $100 M_{10}^{-1}$Hz from Figure 3.12 never show up at more than 99% significance. In general, while the feature near $50 M_{10}^{-1}$Hz in the tilted simulations is more convincing than anything from the untilted simulations, it does not appear at high enough significance at

Table 3.2. Broken Power Law Fit Parameters

	90h			915h		
	30°	60°	90°	30°	60°	90°
γ_1	1.6 ± 0.6	0.7 ± 0.3	0.4 ± 0.7	1.2 ± 0.3	0.9 ± 0.3	0.7 ± 0.9
γ_2	3.3 ± 0.6	3.8 ± 0.3	4.0 ± 0.7	3.4 ± 0.8	3.2 ± 1.0	3.7 ± 0.8
ν_b	80 ± 20	90 ± 5	100 ± 20	90 ± 10	90 ± 20	100 ± 30

enough observer frequencies and azimuths to be identified as a QPO.

Finally, fitting the sets of power spectra provides a general idea for the range of best fit values of the broken power law parameters. The median parameters found from the tilted and untilted simulation are listed in Table 3.2, where the quoted uncertainties are the standard deviations from light curves with different observer azimuths and frequencies. Break frequencies have the units M_{10}^{-1}Hz. The break in slope becomes more pronounced at higher inclination as the initial slope becomes shallower while the post-break slope becomes steeper. The post-break slope is slightly shallower in the tilted simulations, while the initial slope is more strongly dependent on inclination in the untilted case.

3.4 Physical Cause of Disk Truncation

The observable signatures of tilted disks discussed so far are, for the most part, due to two main differences between tilted and untilted disks: tilted disks precess, and they are truncated outside $r_{\rm ms}$. Fragile et al. (2007) [80] discussed why the simulated accretion flows precess. It is our interest to better understand the physical cause for the large truncation radius.

The first thing to note is that rapidly rotating black holes allow stable circular orbits at smaller radius than slowly rotating black holes. Therefore, the angular momentum extraction mechanism at play in the tilted disks must be more effective at higher spin to cause material to plunge from the same location. This is confirmed in Figure 3.13, where we plot the difference in density-weighted, shell-averaged specific angular momentum for tilted and

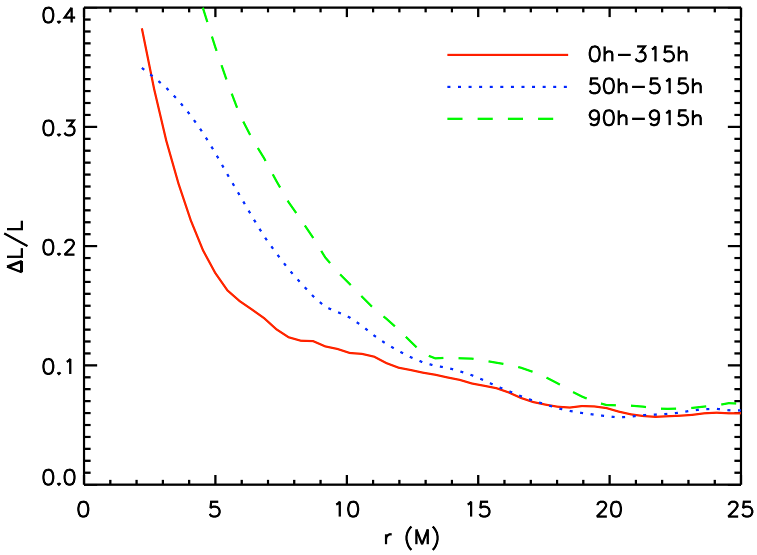

Figure 3.13 Fractional difference in shell-averaged angular momentum between tilted and untilted simulations with similar spins. The untilted simulations are nearly geodesic, while the tilted simulations are increasingly sub-geodesic with decreasing radius.

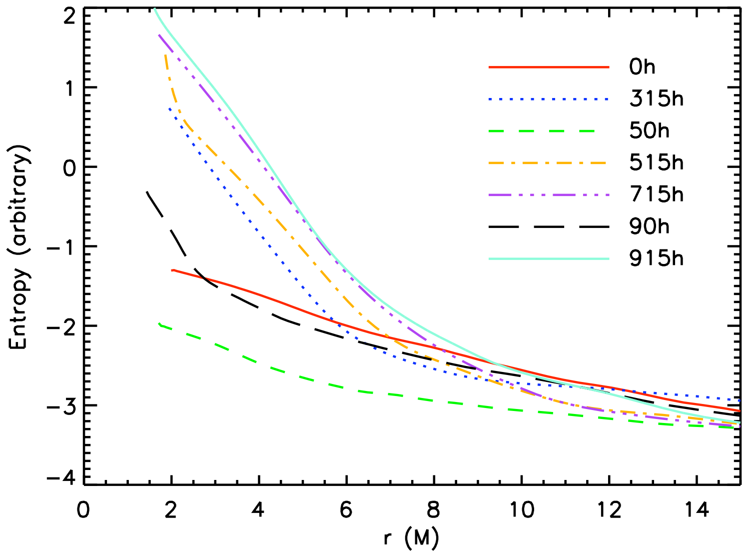

Figure 3.14 Shell-averaged entropy distributions for all simulations. Excess entropy inside $r \sim 10\text{M}$ is generated by non-axisymmetric standing shocks in the tilted simulations.

untilted simulations of comparable spin. The angular momentum is defined as $\ell = -u_\phi/u_t$, where u^μ is the fluid four-velocity and the shell-average of a quantity x is given by,

$$\langle x \rangle = \frac{1}{A} \int\int d\Omega \sqrt{-g}\, x, \tag{3.2}$$

where Ω is the coordinate solid angle, g is the metric determinant and $A = \int\int d\Omega\sqrt{-g}$. The density-weighted shell-average of x is defined as $\langle \rho x \rangle / \langle \rho \rangle$. The angular momentum profiles for the untilted simulations are nearly geodesic outside of $r \sim 5$M. Inside of $r \sim 10$M, the tilted simulations become increasingly sub-geodesic, with the higher spin cases deviating more than the lower spin ones. The same trend holds when comparing the tilted simulations to the analytic result for the angular momentum profile of material on geodesic orbits in an equatorial disk inclined 15° to the black hole spin axis.

Fragile & Blaes (2008) [79] suggested that the non-axisymmetric standing shocks that occur in the inner radii above and below the midplane of the disk may enhance the outward transport of angular momentum, causing fluid to plunge from outside the marginally stable orbit. To connect the enhanced angular momentum loss of the tilted disks with the standing shocks, we next look at a plot of the density-weighted, shell-averaged entropy profiles in Figure 3.14. Since these simulations conserve entropy except across shocks, the excess inside of $r \sim 7$M in the tilted simulations signifies the presence of extra shocks. The steepness of the entropy gradient gives some measure of the strength of these shocks. Again, we see that the effect is greatest in the simulations with the fastest spinning black holes.

Further evidence linking the sub-geodesic angular momentum profiles of the tilted simulations with the standing shocks can be found from looking at the time-dependence of the shell-averaged angular momentum. While the untilted simulation remains nearly geodesic, the tilted simulations are continuously transporting angular momentum outward from $r \sim 10$M for the first ~ 5000M before reaching a steady state, as would be expected from a dynamical mechanism. Finally, vertically integrated contour plots such as Figure 3.15 show that the angular momentum in the tilted simulations is non-axisymmetrically distributed. The regions of depleted angular momentum correspond to the standing shocks, which appear as regions of excess entropy in the bottom panels of Figure 3.15.

Following Fragile & Blaes, we postulate that the standing shocks are caused by deviations from circular orbits near the black hole. Figure 3.16 shows the shell-averaged eccentricities of the orbits in each simulation, estimated at one scale-height in the disk using

$$e = -\frac{r}{6M}\frac{\partial(\beta \sin\gamma)}{\partial r} \ , \tag{3.3}$$

where β is the tilt and γ is the precession of each orbital shell.[1] All quantities are calculated from fitting the shell-averaged disk tilt and twist (Eqs. 32 and 41 of 80) with power laws, and using the resulting expressions in Equation (3.3). The increase in eccentricity toward smaller radii leads to a crowding of orbits near their apocenters [101], which leads to the formation of the standing shocks. The eccentricity is larger for higher black hole spin, except inside the plunging region where the fits become poor and the eccentricity is ill-defined. Equation (3.3) may indicate how these results depend on the initial tilt of the simulations. If we assume that the strongest dependence of e on tilt is through β and that $\partial\beta/\partial r$ and $\partial\gamma/\partial r$ remain unchanged for different tilts, then equation (3.3) suggests that the eccentricity of the orbits should vary roughly linearly with the initial tilt, at least for small angles. This prediction is tentatively confirmed by a simulation we have done that started with an initial tilt of 10°.

3.5 Discussion

Tilted accretion flows will inevitably be present in a significant fraction of black hole sources with $L/L_{edd} \lesssim 0.05$ and possibly $L/L_{edd} \gtrsim 0.3$ (thick or slim disks). Using relativistic ray tracing and a set of simple emissivities, we have compared the radiation edge, emission line profiles and power spectra of simulated black hole accretion flows with a tilt of 15° to their untilted counterparts. We find the radiation edge is independent of black hole spin, while the untilted simulations agreed with the expected qualitative trend of decreasing inner radius with increasing spin. These results for the radiation edge confirm the work of Fragile (2009) [77], who used dynamical measures to locate the inner edge. The marginally stable orbit itself does move outwards for orientations outside the equatorial plane at non-zero

---

[1] This definition of e differs from that used by Ivanov & Illarionov (1997) [101] by a phase factor of $\pi/2$ in γ. Fragile & Blaes used the formula from Ivanov & Illarionov without modification.

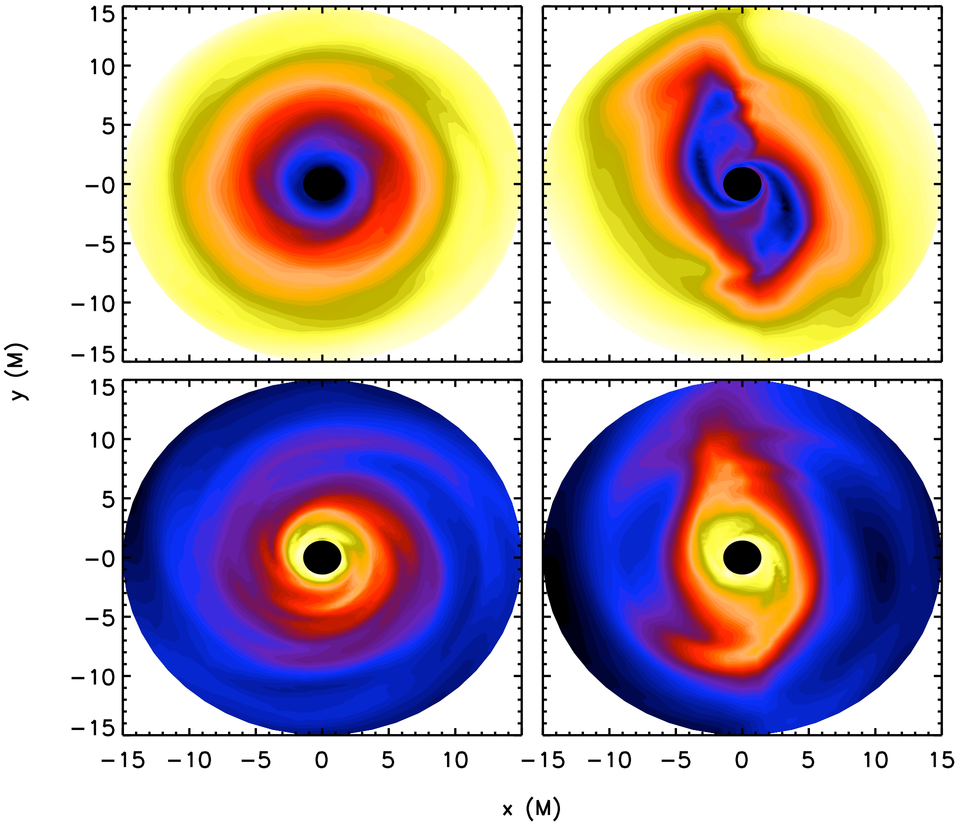

Figure 3.15 Vertically integrated contour plots of specific angular momentum (top) and entropy (bottom) for snapshots of the 90h (left) and 915h (right) simulations. The color scale is linear, increasing from blue to red to yellow to white. The non-axisymmetric shocks in 915h correspond to regions with deficit (excess) angular momentum (entropy).

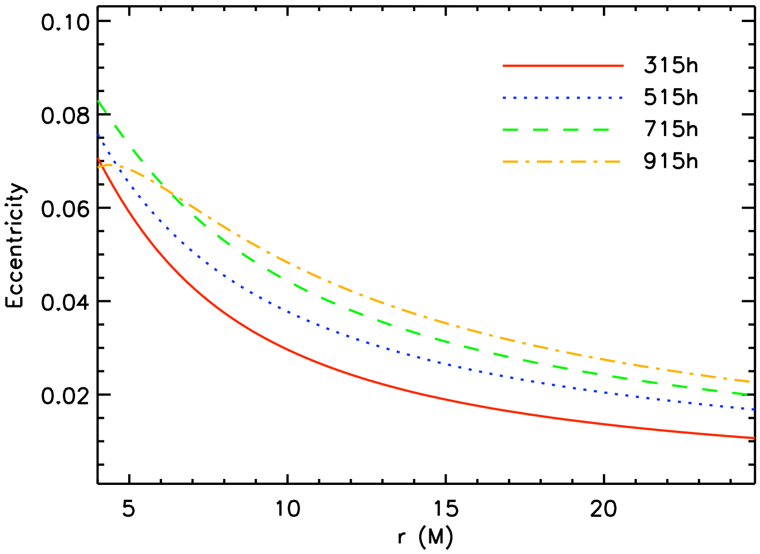

Figure 3.16 Shell-averaged orbital eccentricities for all tilted simulations, estimated at one scale-height in the disk. The increasing eccentricity of orbits toward smaller radii leads to a crowding of orbits at their apocenters, which, in turn, can generate standing shocks.

spin. For example at a 90° tilt, r_{ms} is equal to its $a = 0$ value at all spins. However, the effect is negligible for the 15° tilt angle considered here (see Fragile et al. (2007) [80] Figure 5) and the difference in radiation edge between tilted and untilted simulations is entirely due to the accretion physics.

Due to the independence of inner edge on spin, the red wing of tilted accretion flow emission line profiles is also fairly independent of spin. This introduces a possible complication for attempts to measure black hole spin from sources which may be geometrically thick. In general, measurements of small spin (large inner radius) may be unreliable unless the disk is known to be untilted. A reliable estimate of a large black hole spin (small inner radius), in contrast, could rule out the presence of a tilted disk. The tilt angle may also be constrained or measured using X-ray polarization measurements, as precession may cause its degree and position angle to exhibit time-dependence.

The blue wing can be much broader for tilted accretion flows, and the tilted-disk line profiles depend strongly on the observer azimuth as well as inclination. Since a tilted disk is expected to precess [80], highly variable emission line profiles could signify the presence of a tilted accretion flow, as has been pointed out in the context of warped thin disks [92]. Since many LLAGN and X-ray binaries in the low/hard state should be tilted, time-variable emission lines should be quite common, and this effect is unlikely to significantly depend on accurate reflection spectrum modeling. Although the simulations can only be run for a short time compared to the precession time scale, precession is a possible source of low frequency quasi-periodic oscillations when the accretion flow is optically thin due to the modulation of Doppler shifts as the velocities in the accretion flow align and misalign with the observer's line of sight [see 100, for more discussion of QPOs from precessing tilted disks]. The typical amplitude of the oscillation for emission models used here is $\simeq 20\%$, about the same as the intrinsic variability. This means that the feature will have to be found by looking at the power spectrum, since there may be less intrinsic variability on long timescales.

Finally, we have studied power spectra for our simple models. We find broken power law spectra with break frequencies around $100M_{10}^{-1}$Hz and power law indices in the range 0-2 (3-4) pre- (post-) break for both tilted and untilted simulations. Previous studies [7, 143] found single power laws with index ∼2. Armitage & Reynolds (2003) [7] found that power spectra from individual annuli are well described by broken power laws where the break frequency is close to the local orbital frequency – the averaging of many annuli with an emissivity that falls with radius smooths the power spectrum into a single power law. We see the same behavior in our simulations; the break frequencies from power spectra of individual radial shells agree with the local orbital frequency for both simulations 90h and 915h. A break frequency $100M_{10}^{-1}$Hz then implies a radius of $r \approx 16$M. Our broken power law spectra are therefore likely due to the fact that our emissivity peaks relatively near the outer radius used for the ray tracing, $r = 25$M. A larger radial domain would likely shift the break to smaller frequencies.

Observed break frequencies in the low/hard state are typically $\nu_b \sim 0.1 - 1$Hz, which may be caused by the transition from a thin disk to a thicker, ADAF flow [65]. That would imply a transition radius $r_t \simeq 200 - 1000 M_{10}^{2/3} M$. Our results for pre- and post-break slopes from both tilted and untilted simulations agree with those found in Cygnus X-1 [166] for an inclination $i = 30°$. In GRO J1655-40 [165] our pre-break slopes agree for all inclinations.

However, the PSD for that source is well described by a single power law.

There is no clear evidence in our work for high frequency QPOs due to the trapped inertial waves identified by Henisey et al. (2009) [95], although there are more features in power spectra from the 915h simulation at higher significance than in 90h. Even when computing PSDs for sets of spherical shells from the simulations, there are no clear features in the tilted power spectra that are not also present in the untilted case. It is possible that this result could depend on the chosen emissivity. Alternatively, the excess power in trapped inertial waves could be insufficient to rise above the red noise continuum.

The independence of the inner radius of the tilted simulations on black hole spin is attributable to the extra angular momentum transport provided by the asymmetric standing shocks. These shocks are only present in the tilted simulations. Their strength scales with black hole spin, which is a necessary condition for countering the greater centrifugal support at higher spins. The standing shocks, in turn, appear to be attributable to epicyclic motion within the disk driven by pressure gradients associated with the warped structure. Again, this effect scales with the spin of the black hole, which contributes to the stronger shocks.

For small tilt angles, the orbital eccentricity scales as $e \sim \beta$. This suggests that significant deviations between the spin-dependence of the radiation edge and the marginally stable orbit should be present even at modest tilt angles $\beta \gtrsim 5^\circ$. At larger tilts, it is unclear if the increasing eccentricity will lead to an inner edge that increases with spin. This is both due to the uncertainty in the radial tilt and twist profiles $\beta(r)$ and $\gamma(r)$ at larger tilts, and to the lack of a quantitative connection between inner disk edge and eccentricity. The dynamical measures from Fragile (2009) [77] place the location of the inner edge in a simulation with $a = 0.9M$ and $\beta = 10^\circ$ closer to the location of 915h than 90h. This data point supports the idea that a noticeable departure between r_{edge} and r_{ms} should exist between tilted and untilted disks even for $\beta \gtrsim 5^\circ$. It also suggests that at larger tilt angles, r_{edge} is likely to increase with spin unless the effect saturates at $\beta \approx 15^\circ$. Simulations with larger tilt angles will be able to address this question with certainty. Future simulations should also be done with a total energy conserving algorithm to verify that the precession and non-axisymmetric shocks are independent of numerical code used. Simulations with a range of tilt angles and scale heights will be necessary to build up a numerical understanding of the physics of tilted disks in the limits of low-spin at non-zero tilt and in low disk thickness where the torus should align with the black hole. In the latter case, the value of the transition radius is uncertain and may also be measured by future simulations.

Chapter 4

RADIATIVE MODELS OF SAGITTARIUS A*: MODEL FITTING AND PARAMETER CONSTRAINTS

4.1 Introduction

Due to its large angular size, the Galactic supermassive black hole candidate Sagittarius A* (Sgr A*) is a promising laboratory for precision black hole astrophysics using very long baseline interferometry (VLBI) at millimeter wavelengths. Previous measurements [187, 60, 106] at 7 and 3.5mm found a small instrinsic source size for Sgr A* (100–200 μas FWHM), but at those wavelengths interstellar scattering is the dominant contribution to the observed size and blurs the image into an elliptical Gaussian. Recent measurements at 1.3mm are the first at short enough wavelengths to avoid contamination due to interstellar scattering and at long enough baselines to achieve event horizon scale resolution [61, 74]. Future measurements may detect the black hole shadow, providing the first direct evidence of an event horizon [13, 70].

Sgr A* is moderately variable in the radio and millimeter [207, 63, 125, 113, 204] with order of magnitude flares in the IR and X-ray [8, 86, 87]. Its spectral energy distribution (SED) rises from the radio to a millimeter peak ("submillimeter bump"). Baganoff et al. (2003) [9] detected a much lower quiescent luminosity in the X-ray, while a quiescent infrared state has not been definitively detected. The submillimeter bump is thought to arise from relativistic, thermal electrons in the innermost portion of a hot, thick, advection-dominated accretion flow (ADAF; [141]). Polarization measurements have shown that the peak electron number density and mass accretion rate must be much smaller than in the original ADAF model [3, 158], and contemporary variants are known collectively as radiatively inefficient accretion flow (RIAF, [202]) models. The radio spectrum can be explained either by a small amount of the internal energy being injected into nonthermal electrons in the accretion flow [202] or by a short, mildly relativistic, optically thick jet [68]. The quiescent X-ray emission is a combination of Compton scattering from submillimeter or IR seed photons, and bremsstrahlung from cooler electrons further from the black hole, near the Bondi radius.

Broderick & Loeb (2006) [32] modeled the infrared flaring as being due to orbiting inhomogeneities ("hot spots") in the inner radii of the accretion flow. Recently, correlated multiwavelength flares have instead favored an adiabatically expanding blob model [204], which can explain the observed time lags between the infrared, X-ray and millimeter flares. The jet emission model can explain the time lags between flaring events in the radio and millimeter [69]. The RIAF, jet, hotspot and expanding blob models for Sgr A* emission provide a variety of competing pictures of the accretion flow. These models are either completely non-relativistic or modified later to be consistent with relativity. They neglect the magnetic fields responsible for outward angular momentum transport and accretion via the magnetorotational instability (MRI, 194, 44, 10). None can self-consistently account for quiescent and flaring behavior.

Magnetohydrodynamic (MHD) simulations can provide a more physical description of the accretion flow. They have been used to model the synchrotron emission from Sgr A*, either in three spatial dimensions with a pseudo-Newtonian potential [149, 90, 99, 43] or in two dimensions in full general relativity [147, 136, 96]. Non-relativistic simulations are especially inappropriate for modeling the millimeter emission, which originates in the innermost portion of the accretion flow where relativistic effects are strongest. Axisymmetric simulations cannot sustain the MRI, and cannot accurately model variability.

The submillimeter bump is of particular interest. This is the frequency range where VLBI can both resolve the black hole event horizon, and where the measurements are no longer dominated by interstellar scattering. Unlike the radio, IR, and X-ray emission the dominant emission mechanism and electron distribution function is known in the millimeter. Broderick et al. (2009) [29] fit a non-relativistic, semi-analytic RIAF model to spectral and mm-VLBI data.

In this Chapter, we fit time-dependent images of millimeter synchrotron emission from three-dimension GRMHD simulations to millimeter (mm) observations of Sgr A*. Simulations in the sample both conserve energy [129] and evolve the internal energy, injecting entropy at shocks [80, 81]. Images are fit to the spectral index measurements from Marrone

(2006) [124] as well as the mm-VLBI data [61, 74], and two-temperature models of the accretion flow are considered.

The fitting procedure in this chapter both demonstrates that radiative models based on contemporary simulations of black hole accretion flows provide excellent descriptions of current millimeter observations, and allows estimates of the parameters of the black hole and its accretion flow. In the next chapter, the "best fit" models with the highest probability of describing the data are studied in more detail to learn about the physical properties of the millimeter emission region and the synchrotron variability mechanism, and to make predictions for future observations.

4.2 Methods

Relativistic synchrotron radiation is computed from the simulations by tracing rays backwards from an observer's camera at infinity through the accretion flow as implemented in `grtrans` (Section 2.5). Each ray constitutes a pixel of the image, which are spaced uniformly on a rectangular grid. The points along each ray are assumed to be null geodesics of the Kerr spacetime, and their trajectories are computed using the public code `geokerr` (Appendix A). The code computes all coordinates of the geodesics, and the ray tracing procedure is fully time-dependent. Tracing rays backwards is ideal for Sgr A*, where the images themselves are observables.

We find that an image resolution of 150x150 pixels (rays), with maximum spacing of .2M in impact parameter at infinity is sufficient for total flux convergence to $\simeq 1\%$ relative to 300x300 or 600x600. The largest single pixel errors are $\simeq 5-10\%$, concentrated near the circular photon orbit. We find ~ 400 points on each geodesic to be adequate for all models. These points are spaced evenly in $1/r$, except near radial turning points, where `geokerr` uses the polar angle as the independent variable for better resolution.

The unpolarized synchrotron emission coefficient is computed from Leung et al. (2011; accepted) by linearly interpolating simulation fluid variables to the points along each ray. For reasons discussed below, we often use data from the nearest time step rather than interpolating in the time direction. The absorption coefficient is obtained from Kirchoff's Law. The gas pressure, magnetic field and particle density are taken from the simulations and scaled to physical units with a single free parameter representing the total torus mass. This parameter fixes the mass accretion rate. Only emission from fluid within $r = 25$M is used for computing images, and only the last $\sim 60\%$ of the simulation data is used, after transients from the onset of turbulence have died down (see Table 4.1). The millimeter emission in the models considered is always concentrated well within both our radial boundary and the initial pressure maximum for all simulations.

The simulations evolve the total gas pressure of electrons and ions, while only the electron temperature is used in calculating the emergent radiation. We follow previous work [90, 136] and generate images using two-temperature models with constant ratios of T_i/T_e, which is then another free parameter.

The models are fit to both the VLBI observations at 1.3mm [61, 74] and the spectral index measurements between .4mm and 1.3mm [124]. This gives the probability of observing the measured values from a particular model. Following Broderick et al. (2009) [29], this distribution is converted to the probability distribution as a function of our parameters given the observations using Bayes' theorem. The result is two separate probability distributions: $p_v(\dot{M}_v, t_v, \xi, T_i/T_e, a)$ and $p_s(\dot{M}_s, t_s, T_i/T_e, a)$, where t is the observer time, $\dot{M}$ is the time-averaged accretion rate, ξ is the orientation of the black hole spin axis projected on the sky, T_i/T_e is the ion electron temperature ratio, and a is the spin value of the simulation used. The subscripts v and s refer to the VLBI and spectral fits respectively, and the simulations differ in more respects than just the value of the black hole spin. To produce parameter estimates, we average over observer time and marginalize over accretion rate and multiply the resulting distributions. To estimate the value of a single parameter, we then marginalize the combined probability distributions over the other parameters. To estimate the accretion rate, we average over observer time, combine the resulting distributions, and then marginalize over all other parameters.

For each simulation, images are produced over a grid of the above parameters at .4mm and 1.3mm. VLBI fits are done as follows. Visibility amplitudes are calculated by taking the absolute value of the Fourier transform of the 1.3mm image averaged over 10 minute intervals to match the observations. The visibility is then rotated to the desired sky orientation, and multiplied by an elliptical Gaussian to account for interstellar scattering as done in Fish et al. (2009) [73] using the fits from Bower et al. (2006) [27]. The rotated, scatter-broadened visibility amplitude is then interpolated to the baseline locations of the VLBI measurements, and fit to their measured values.

The total fluxes at .4mm and 1.3mm are time-averaged over 2.5hr intervals to mimic the observations. Since the individual measurement errors from Marrone (2006) [124] are smaller than the flux differences between the measurements, the data provide information about source variability as well as a time-averaged value. To account for this, we fit to each measurement separately. Our light curves have also been analyzed using averaged 1.3mm fluxes and spectral indices between 0.4mm and 1.3mm. Using the former method provides tighter constraints for individual models, but the parameter estimates and best fit models discussed in the following chapter are identical between the two methods. Note that the 1.3mm flux during these observations was $\sim 20\%$ higher on average than that from VLBI measurements [74]. Image intensities are converted to fluxes using a black hole mass of $4 \times 10^6 M_\odot$ and a distance of 8kpc.

4.3 Simulation Data

Relativistic, three dimensional simulations are necessary to produce a physical, realistic description of the time-dependent accretion flow structure. Axisymmetric simulations cannot sustain turbulence and exaggerate variability. Previous studies using 2D simulations have time-averaged the fluid structure, but even then the statistical steady state is not correct due to the decay of the MRI on the local orbital time. The ideal approach would be to use a single code to run a grid of 3D simulations over black hole spin, initial magnetic field configuration and initial torus location and geometry. However, given the formidable computational expense of such a project, we instead leverage a subset of existing 3D GRMHD simulations from two different groups. The simulations and their parameters are listed in Table 4.1. All tilted simulations have names ending in "15h'," while the others assume alignment between the angular momentum axis of the initial torus and the black hole spin axis.

The two sets of standard, aligned simulations from different groups use different initial conditions and energy evolution equations. Simulations from Fragile et al. [80, 81] evolve

Table 4.1. Key to the Simulations

Name	Spin (M)	Energy Scheme	Δt (Used in Modeling)	Initial Conditions	Reference
0h	0.00	Internal	7900M (4600M)	De Villiers et al. (2003) [51]	Fragile et al. (2009) [81]
50h	0.50	Internal	7900M (4600M)	De Villiers et al. (2003) [51]	Fragile et al. (2009) [81]
90h	0.90	Internal	7900M (4600M)	De Villiers et al. (2003) [51]	Fragile et al. (2007) [80]
MBD	0.92	Total	3500M (2000M)	Gammie et al. (2003) [85]	McKinney & Blandford (2009) [129]
MBQ	0.94	Total	5500M (3000M)	Gammie et al. (2003) [85] with quadrupolar field	McKinney & Blandford (2009) [129]
315h	0.30	Internal	7900M (4600M)	De Villiers et al. (2003) [51]	Fragile (2009) [77]
515h	0.50	Internal	7900M (4600M)	De Villiers et al. (2003) [51]	Fragile et al. (2009) [81]
715h	0.70	Internal	7900M (4600M)	De Villiers et al. (2003) [51]	Fragile (2009) [77]
915h	0.90	Internal	7900M (4600M)	De Villiers et al. (2003) [51]	Fragile et al. (2007) [80]

internal energy and use the initial torus configuration from De Villiers et al. (2003) [51], whereas those from McKinney & Blandford [129] conserve total energy and use an initial torus placed much closer to the black hole [85]. The two simulations from McKinney & Blandford [129] differ slightly in black hole spin, as well as in initial magnetic field configuration. The simulation labeled MBD uses a standard, small-scale dipolar loop. The MBQ simulation has a large-scale quadrupolar field, which leads to a stronger MRI, slightly higher magnetic pressures and a larger accretion rate.

Total energy conserving simulations are probably more appropriate for modeling Sgr A*, since its inferred radiative efficiency is relatively low ($\epsilon \sim .001 - .01$). We have computed a radiative efficiency from numerical energy losses of $\epsilon \sim 0.1$ for the 90h simulation, and a bolometric "luminosity" exceeding that of Sgr A* by a factor of a few. However, few energy conserving three dimensional GRMHD simulations have been run to date [175, 144, 143, 129, 145]. Only McKinney & Blandford [129] simulated a thick, advection-dominated accretion flow. The simulations used here do not include radiative cooling, which is likely a good approximation for an ADAF. Non-conservative simulations, where a significant amount of energy is lost to artificial numerical cooling, are still advection-dominated.

For comparison, we have also run a set of axisymmetric simulations using the publicly available HARM code [85, 142] at black hole spins $a/M = 0.00$, 0.50, 0.75, 0.90, 0.92, and 0.94 ($G = c = 1$ is used throughout this paper). They are not used for fitting to observations due to the problems with axisymmetric simulations described above. Instead, they give a sense of the spin dependence of total energy conserving simulations, which helps to break the degeneracies between black hole spin and initial conditions in our 3D simulations. They also provide an opportunity for direct comparison with results from previous work using similar simulations.

4.4 Fitting Models to Observations

The model of the millimeter emission from Sgr A* as realized in the simulations is of a compact, hot, magnetized accretion flow in the vicinity of a black hole. The spectrum peaks at millimeter wavelengths, where the majority of the radiation is produced. The emission comes from thermal electrons near the midplane of the disk in the inner radii, with

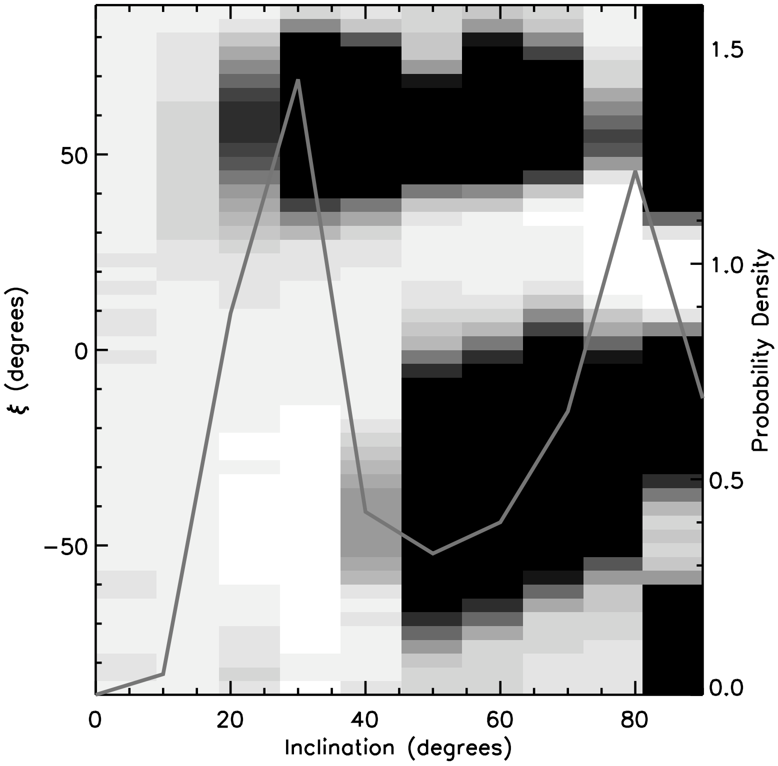

Figure 4.1 Grid of best fit reduced effective χ^2 values vs. inclination and sky orientation ξ. The scale is from $\chi^2 = 1$ (white) to 2.5 and greater (black). We find excellent fits at low inclinations, which are roughly independent of sky orientation. At high inclinations, our results show a similar shape to that found by Broderick et al. [29]. Overplotted is the probability density vs. inclination, marginalized over observer time, accretion rate and sky orientation.

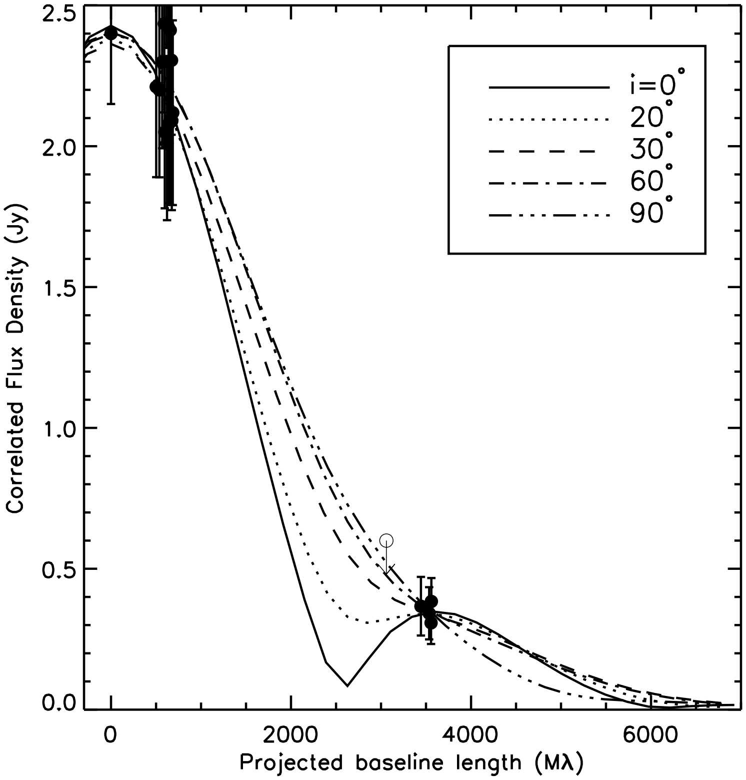

Figure 4.2 Best fit visibility profiles for low and high inclinations from the 90h simulation, plotted along the line in the UV plane corresponding to the average location of the long baseline measurements from the first mm-VLBI measurements [61]. The visibilities naturally divide into two types. At low inclinations, the nearly circular shadow leads to a minimum in the visibility profile, similar to the ring model in Doeleman et al. At inclinations $\gtrsim 30°$, the profiles monotonically decrease with baseline length. A detection in place of the current upper limit (open circle with arrow) should favor one set of profiles.

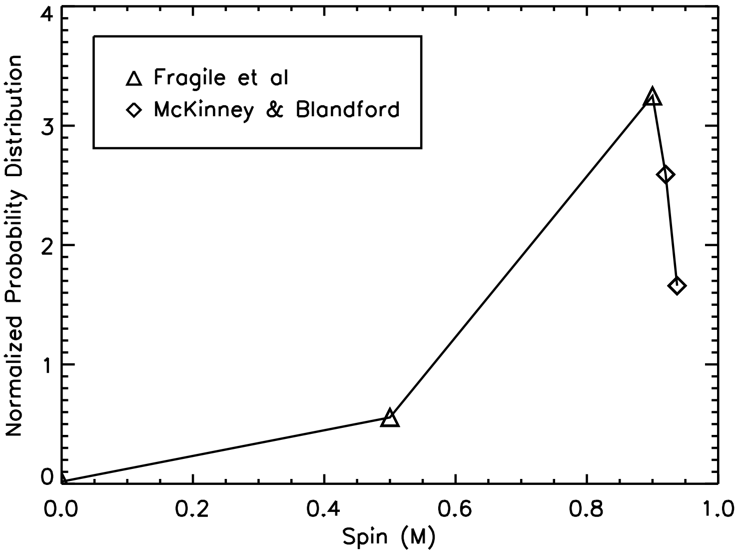

Figure 4.3 Normalized probability density as a function of black hole spin, marginalized over inclination angle and T_i/T_e. Triangles denote the first three entries in Table 4.1, from Fragile et al. [80, 81]. Diamonds represent the last two entries in Table 4.1 from McKinney & Blandford [129].

typical values of $n \sim 5 \times 10^7 \mathrm{cm}^{-3}$, $B \sim 50$G, and $T_e \sim 5 \times 10^{10}$K. These typical values have been found by a number of modelers [202, 90, 136].

As a first example, we consider a model from the 90h simulation with $T_i = T_e$. Visibilities were interpolated to the detections in Doeleman et al. (2008) [61], and an effective χ^2 was computed as defined in Broderick et al. (2009) [29]. Grids of minimum effective, reduced χ^2 are shown in Fig. 4.1 over inclination angle and sky orientation for the 90h simulation. The orientation is well constrained at high inclinations, since the general image shape is nearly static and asymmetric, and the long baseline VLBI measurements pick out a specific orientation for the visibility ellipse. The two distinct bands of good fits are due to the (approximate) up-down symmetry of the image. The model from 90h provides good fits (reduced $\chi^2 \lesssim 1.2$) at all inclinations. This is especially evident from the curve of $p(i)$ vs. i overplotted in Fig. 4.1. Inclinations $i \lesssim 20°$ are less probable due to the $\sin i$ prior and large variation of probability density with observer time. Although the best fit χ^2 is roughly the same for low inclinations at all ξ, at any given observer time good fits are restricted to less

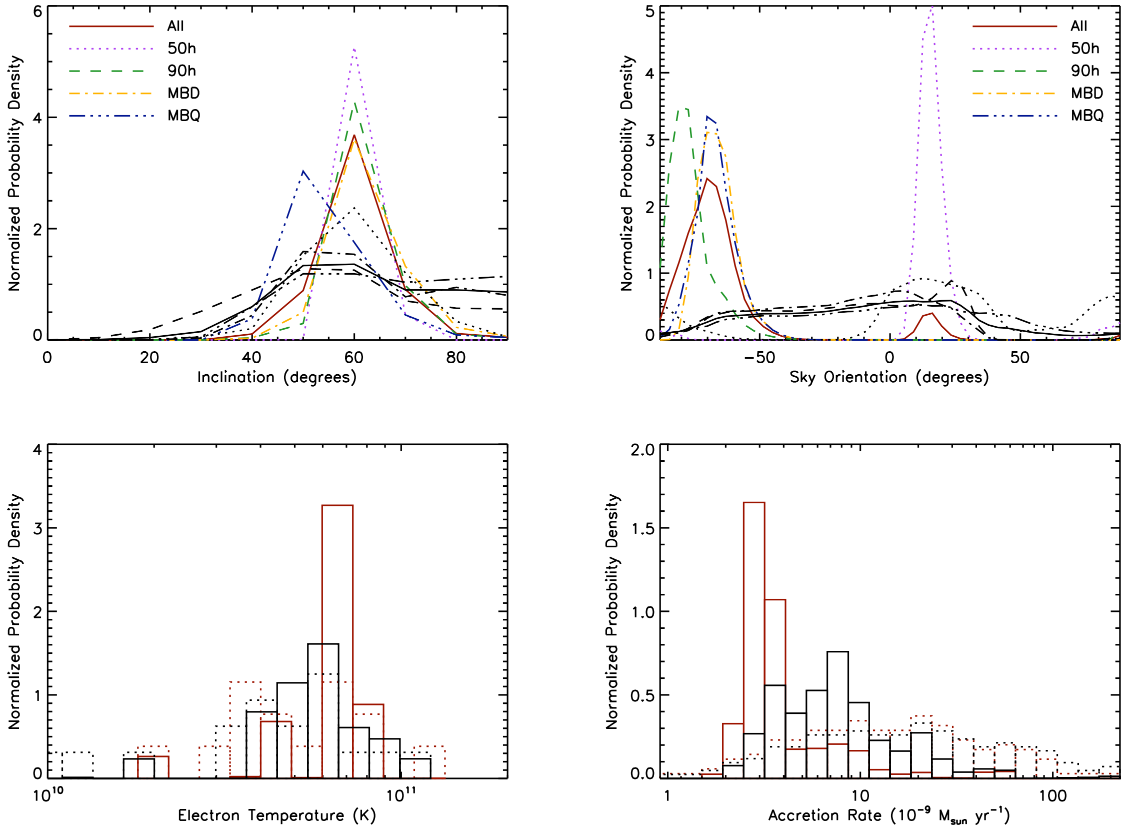

Figure 4.4 Normalized probability densities for all untilted simulations using all VLBI data (colored curves) and just the Doeleman et al. (2008) data (grayscale curves) as functions of observer inclination and sky orientation (top left and right), electron temperature (bottom left) and average mass accretion rate (bottom right). The geometric distributions are marginalized over T_i/T_e and $\dot{M}$, and plotted for each simulation separately and marginalized over simulation (black hole spin). The 0h simulation isn't included due to its negligible contribution to the overall curve. The electron temperature probability distribution is created by binning the median electron temperature in the region of largest emissivity and summing the probability densities of the models in each bin. The mass accretion rate probability distribution is created by marginalizing over orientation and inclination angles and simulation, and multiplying the separate distributions from the VLBI and spectral fits. In both cases, the dotted histogram is the result of assigning equal probability to each model sampled.

than half the range of sky orientations.

Visibility profiles from the best fits at many inclinations are shown in Fig. 4.2. The profiles represent the 2D visibility plotted along the line representing the average angle in the UV plane of the long baseline measurements from Doeleman et al. [61]. Also plotted are the data from that work. At low inclinations, the profile reaches a minimum as described above, whereas at $i \geq 30°$, the profile decreases monotonically with baseline length. Our best fit face-on visibility profile is almost identical to that of the ring model from Doeleman et al. The local minimum in the visibility profile of ring type models is a signature of the black hole shadow, and its detection would constitute direct evidence for a black hole event horizon.

Our low inclination images are strongly peaked at the circular photon orbit, as can be seen in Fig. 3.1. In addition to the ring model, a delta function intensity profile at the circular photon orbit roughly matches the observations, as does the spherical accretion model from Chapter 2 scaled to the mass of Sgr A*. In fact, any model sharply peaked at the circular photon orbit should approximately match the visibility data. This is because the ratio of the zeroth to first maximum in the visibility for such a model is roughly the same as that of the zeroth order Bessel function, and agrees with the ratio of the visibility amplitude at $\sim 3500\mathrm{M}\lambda$ to the total flux. These low inclination models are theoretically appealing, but are strongly disfavored by spectral index measurements, since they are too optically thin at 1.3mm, and by the additional mm-VLBI data from Fish et al. (2011) [74]. Thus, the black hole shadow is unlikely to be detected with current mm-VLBI telescopes (see Chapter 5 for shadow predictions with future telescopes).

Two-temperature models from all of the GRMHD simulations also provide excellent fits to the observed millimeter emission from Sgr A* (reduced $\chi^2 \leq 1.5$ frequently for all simulations). This is still true when we incorporate spectral index information as described above. The inclusion of that observational constraint and the rest of the aligned simulations (see below for the tilted simulations) allow us to strongly disfavor the low inclination models discussed above and to estimate some parameters of the accretion flow. Single parameter probability distributions are found by marginalizing the combined spectral and VLBI probability distributions over the others. To estimate confidence intervals, we use the technique described in Broderick et al. (2009) [29]. The probability distribution is integrated from its maximum value, p_{max}, down to a cutoff value p_{min} so that the cumulative probability enclosed between p_{min} and p_{max} is equal to the desired confidence interval. Then the estimated value, lower and upper bounds of the parameter x are $x(p_{max})$, $\min[x(p \geq p_{min})]$, and $\max[x(p \geq p_{min})]$ respectively.

4.4.1 Parameter Constraints

We estimate the electron temperature in the millimeter emission region, the accretion rate onto the black hole, the inclination angle of the accretion flow relative to the observer and the projection of the black hole spin axis on the sky. Unfortunately, our use of existing simulations precludes us from determining a constraint on the black hole spin. A plot of $p(a)$ is shown in Fig. 4.3. The large peak at high spin is deceptive, and is due to the differences between the simulations rather than black hole spin. While it appears we might be able to rule out low spin simulations, the 0h simulation is probably a special case. Low electron temperatures in that simulation cause it to have a large photosphere ($r \sim 10$M) even when $T_i = T_e$, and therefore it fits the observations poorly. The axisymmetric HARM simulations, which are more similar to a 3D conservative simulation like MBD/MBQ, have larger electron temperatures at all spins and are optically thin for $T_i = T_e$. So although the 0h model is ruled out, low spin conservative simulations should have larger electron temperatures and provide better fits. We do not consider the 0h simulation for the remainder of the paper due to its negligible influence on the overall probability distributions.

All best fit models have similar probability distributions in inclination angle. These are shown in the top left panel of Figure 4.4, along with the combined probability distribution after marginalizing over all other parameters. From this we estimate the inclination angle from the first epoch of VLBI data as $i = 50^{\circ}{}^{+35^{\circ}}_{-15^{\circ}}$ with 90% confidence. This interval may change with more complete sampling of the spin and initial conditions parameter space; however the similarity of the curves from different simulations suggests that such changes will be minor. The face-on, black hole shadow fits at $i \lesssim 20^{\circ}$ found above from the single temperature 90h model are now ruled out to 3σ confidence as discussed above. The VLBI measurements also depend on the sky orientation, ξ, the position of the black hole spin axis projected on the sky measured E of N. A plot of $p(\xi)$ is shown in the top right panel of Figure 4.4. The distribution is quite broad, and we estimate a value from the first epoch of VLBI data of $\xi = -23^\circ{}^{+97^\circ}_{-22^\circ}$ with 90% confidence. Both the estimated values and the probability distributions shown here are in excellent agreement with Broderick et al. (2009) (c.f. [29] Fig. 7).

For all simulations, the probability distribution over T_i/T_e has a peak value between 1 and 10. The best fit T_i/T_e rises with MHD temperature, so that roughly the same electron temperature fits best across all simulations. The probability distribution of emissivity averaged electron temperature is plotted in the bottom left Figure 4.4. The dotted histogram shows the result of assigning equal probability density to each model. With better sampling, the distribution would likely be much more smooth. The electron temperature from the first epoch of VLBI data is estimated to be $(5.4 \pm 3.0) \times 10^{10}$K with 90% confidence. As discussed below, our simulated light curves are consistent with an isothermal emission region. This electron temperature is consistent with electron temperatures found in previous work [202, 90, 182, 136].

Similarly, the accretion rate can be constrained from the joint fits despite the different ranges found for best fit parameters for each simulation (see Table 5.1). The probability distribution over accretion rate is shown in the bottom right panel of Figure 4.4, and we estimate its value from the first epoch of VLBI data to be $\dot{M} = 5^{+15}_{-2} \times 10^{-9} M_\odot \mathrm{yr}^{-1}$ with 90% confidence. The probability distributions from the two observational constraints have been combined to produce the plot, despite the fact that the total flux is $\sim 50\%$ higher during the spectral index measurements. This procedure favors models with substantial variability. However, probability distributions from the two constraints separately are similar to the one in Figure 4.4, with slightly broader ranges of allowed accretion rates and estimated values in agreement with that of the joint fit.

Including the most recent mm-VLBI data [74] significantly improves the parameter constraints, particularly on the inclination and orientation angles (red curves in Figure 4.4). The numerical values to 90% confidence, including all mm-VLBI data, are $i = 60 \pm 15^\circ$, $\xi = -70^\circ{}^{+86^\circ}_{-15^\circ}$, $T_e = 6 \pm 2 \times 10^{10}$K and $\dot{M} = 3^{+7}_{-1} \times 10^{-9} M_\odot \mathrm{yr}^{-1}$. These parameters are in excellent agreement with those from the first epoch of data alone, and remain in agreement with those from RIAF data [30]. They are also in agreement with parameters from spectral and polarization fits using time- and azimuthally-averaged GRMHD data [186].

In the context of these aligned GRMHD (and RIAF) models, the millimeter emission region in Sgr A* has a well constrained geometry and parameter values. Additional observations, at least at the existing baseline orientations, have thus far only confirmed this picture and lowered the errors in the various parameters. The major exception is the black hole spin, perhaps the most interesting parameter, which is poorly constrained by observations in RIAF models [30]. Tighter constraints may be obtained by including millimeter polarization data [186]. It is also unclear whether the mm-VLBI data constrain the black hole spin in the context of GRMHD models, since a set of appropriate simulations spanning various initial conditions and spin has not yet been run.

4.5 Tilted Disk Models

Perhaps the most important assumption made thus far is that of alignment between the angular momentum axis of the accretion flow and the black hole spin axis. As discussed in Chapter 3, this is unlikely to be the case in low luminosity systems and has significant implications for the physical structure and dynamics of the accretion flow. Sgr A* is an extreme example in this respect, and there is no reason to assume alignment. Using additional simulations from Fragile et al. [80, 77, 81] (simulations ending with “15h” in Table 4.1), we have repeated the above analysis for the case of a 15° misalignment (“tilt”) between these two axes. The grid of images is produced exactly as before, but with one additional free parameter: ϕ_0, the azimuthal viewing angle. Tilted simulations are non-axisymmetric, and we can no longer exploit the azimuthal symmetry of the accretion flow on timescales longer than the orbital time.

The consistent picture above for reasonably well constrained parameters in agreement between individual simulations does not hold up in the tilted case. Figure 4.5 shows the probability distributions over inclination and orientation angles, accretion rate and electron temperature for the tilted simulations. No clear picture emerges from the set of simulations, and we do not attempt to estimate parameter values. Even within individual simulations

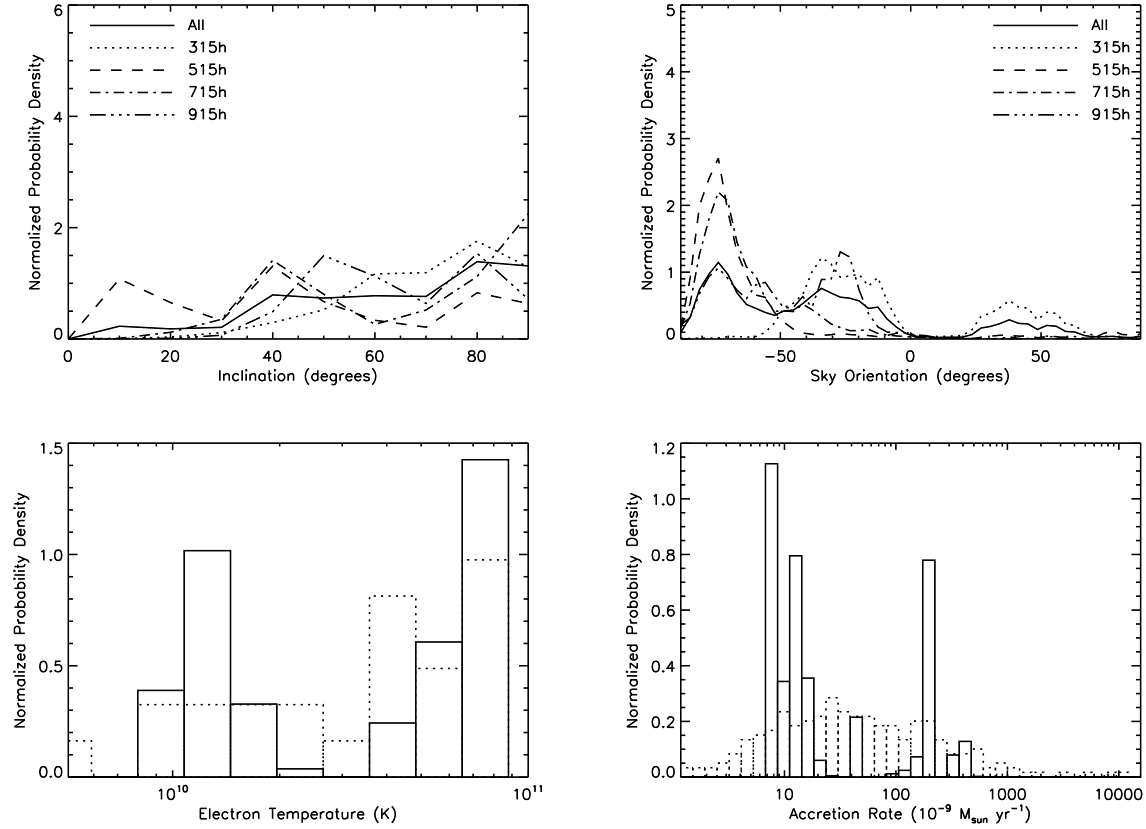

Figure 4.5 As in Figure 4.4, but for the models from tilted simulations. The full VLBI dataset is used in all panels.

there are viable models at different inclinations, orientations, T_i/T_e and $\dot{M}$. As found in Chapter 3, large changes in the images occur with the azimuthal viewing angle. That extra degree of freedom appears to make the difference between the fairly concrete picture of the aligned simulations (additional observations lead to tighter parameter constraints) and the murky picture of the tilted simulations. It may turn out that the extra degree of freedom means that proportionally more observations are required to form a clear picture. The 315h simulation in particular is unique, in that it provides excellent fits with small electron temperatures ($T_i/T_e = 5$ from a relatively cold simulation), which in turn requires large accretion rates and leads to the bimodal distributions seen in the bottom two panels of Figure 4.5.

4.6 Discussion

The submillimeter bump in Sgr A* provides a unique laboratory for connecting observations with theoretical models of black hole accretion flows. We have performed radiative transfer as a post-processor on the output from existing three dimensional GRMHD simulations and fit them to VLBI and spectral index observations of the Galactic center black hole. The simulations provide excellent fits to the existing millimeter observations, and allow us to estimate the roughly constant temperature of the millimeter emission region and the inclination and sky orientation angles of the black hole. These are found to be $i = 60 \pm 15^\circ$, $\xi = -70^\circ{}^{+86^\circ}_{-15^\circ}$, $T_e = 6 \pm 2 \times 10^{10}\mathrm{K}$ and $\dot{M} = 3^{+7}_{-1} \times 10^{-9} M_\odot \mathrm{yr}^{-1}$ confidence when all VLBI data are included. The estimates for inclination and orientation angles are in excellent agreement with those found by Broderick et al. for RIAF models [29, 30], despite significant differences between the dynamical models used. Our accretion rate constraint of $\dot{M} = 3^{+7}_{-1} \times 10^{-9} M_\odot \mathrm{yr}^{-1}$ is consistent with but independent of estimates from the observed linear polarization and Faraday rotation measures [3, 158, 126].

Face-on models, which provide excellent fits in the 90h simulation to the first epoch of mm-VLBI data, are ruled out to 3σ due to the spectral index constraint for 90h, and the paucity of good VLBI and spectral fits at low inclinations in the other simulations when including all of the mm-VLBI data. For this reason, it may not be possible to detect the shadow of the black hole from visibility measurements using current mm-VLBI telescopes.

There are many uncertainties in the analysis presented in this chapter. While GRMHD allows for a self-consistent solution of the primitive variables, it is unknown whether the MHD approximation is valid for the low densities at the Galactic center. In addition, there are a range of possible solutions, depending on the energy prescription and initial conditions used. Current simulations also neglect the interplay between ions and electrons, which should be handled self-consistently. Finally, it is likely that the global GRMHD simulations used in this analysis are significantly underresolved for some measures of convergence [93] and may underestimate the relative strength of the magnetic field. A stronger magnetic field could lead to smaller best fit images and lower inclination angles, electron temperatures and/or accretion rates. Qualitatively, the results of this analysis should still hold, particularly that each of the diverse sample of simulations gives comparable results for Sgr A*.

If Sgr A* is radiatively inefficient, simulations which conserve total energy (MBD, MBQ) are probably more appropriate. We estimate the time-averaged energy dissipation rate from numerical losses in the 90h simulation as $\sim 10^{37}$ ergs s^{-1} for an accretion rate of $1.6 \times 10^{-9} M_{\odot} yr^{-1}$. This is larger than the bolometric luminosity of Sgr A*, and gives an effective radiative efficiency of ~ 0.1. The accretion flow is advection dominated, in that an order of magnitude more energy is lost to the black hole than to numerical reconnection.

The sample of simulations used does not span the parameter space of black hole spin, initial torus geometry and initial magnetic field configuration even ignoring differences in the energy evolution. This incompleteness prevents an estimate of the black hole spin, and may affect our other parameter estimates. However, the universality of the images, light curves, probability distributions and emission region characteristics from all viable simulations considered here suggests that the changes will probably be minor (see Chapter 5). The disk thickness is especially important, since the emission region scale height mimics that of the disk. A thicker disk will also have larger MHD temperatures, and thus larger values of T_i/T_e will be necessary to fit the observations. If the disk thickness can be constrained by VLBI observations, a constraint on T_i/T_e follows. This parameter would constrain the strength of ion-electron coupling in collisionless plasmas.

We find that the high spin simulations provide significantly better fits, but have not used any low spin simulations that conserve energy. Other work fitting to spectral and polarization measurements disfavors low spin ($a \lesssim 0.5$) energy conserving simulations even without constraints from VLBI data [186]. Simulations with misaligned angular momentum and black hole spin axes [80, 79, 81] are also of interest, since they produce standing shocks which lead to considerably different image morphologies. These models with a tilt angle of 15° also provide excellent fits to current data, but the parameters are poorly constrained. Additional measurements will be necessary to break the degeneracies in geometry as well as black hole spin and tilt angle.

Broderick et al. also estimated the parameters of Sgr A* from VLBI and spectral constraints by fitting semi-analytic RIAF models. The structure of $p(i)$ and $p(\xi)$ in their Figure 7 (middle and right panels) are in excellent agreement with ours in Figure 4.4. Further, we find that future observations on baselines of similar length but orthogonal orientation to the existing Hawaii-Arizona baseline have the best chance of discriminating between our best fit models. This conclusion is in agreement with Fish et al. (2009) [73], who point out that ideal baselines for such measurements would be between Chile and one or more of California, Arizona or Mexico. A simultaneous measurement of the 345 or 690 GHz flux during future 230 GHz VLBI observations would provide a significant additional constraint.

A grid of time-averaged images and spectra over black hole spin, inclination and T_i/T_e from axisymmetric, total energy conserving GRMHD simulations were compared to millimeter observations by Mos̀cibrodzka et al. (2009) [136]. Their finding that $T_i/T_e = 1$ models are inconsistent with observations agrees with our results here for MBD and MBQ. As we have shown, for simulations with lower MHD temperatures, smaller values of T_i/T_e will be necessary to reach the required electron temperature in the millimeter emission region. This is why the non-conservative simulations considered here (0h, 50, 90h) are all best fit by small values of T_i/T_e. It also suggests that such models are only appropriate for modeling Sgr A* when they produce large enough MHD temperatures that the electron temperature lies within the range estimated here. At low spin, this seems to require either a hotter initial condition or a total energy conserving simulation.

For the 315h simulation, with $a = 0.3$ and a tilt of 15°, the models provide excellent fits to VLBI data even at $T_i/T_e = 5$, where the fluid is cold. This exception is due to a combination of an unusually low $\beta \equiv p_{gas}/p_{mag}$ and a radial density profile that peaks at very small radius. Thus, the accretion flow can generate the observed Sgr A* millimeter flux even at low temperatures with large accretion rates without becoming optically thick. In all the other simulations, low electron temperatures and high accretion rates lead to an extended photosphere, which is inconsistent with the VLBI observations. The properties of the emission regions of both the tilted and untilted Sgr A* models are discussed more in the next chapter.

In all but the "best-bet" model from Mos̀cibrodzka et al., $T_i/T_e = 10$ is required for consistency with multiwavelength spectral observations. Millimeter spectral index results from our own HARM simulations modeled in the same fashion are for the most part in good agreement with theirs, indicating that the results of these studies are probably robust to the ray tracing code and interpolation scheme employed. However, $T_i/T_e = 10$ models for the various HARM models, MBD and MBQ are all too large to fit the VLBI data due to their extended photospheres. In addition, we find good fits at $T_i/T_e = 3$ for MBD and MBQ at moderate to edge-on inclinations. We have not computed IR or X-ray emission, and therefore do not fit to the quiescent X-ray luminosity from Baganoff et al. (2003) [9], or to the upper limits to the IR emission. These limits are violated in Mos̀cibrodzka et al. for nearly edge-on inclinations and at high spin. Including them could disfavor high inclinations, but is unlikely to change our best fit models. This could especially be a problem in the tilted models, where the spectra extend to higher energies as shown in the following chapter.

Chapter 5

RADIATIVE MODELS OF SAGITTARIUS A*: PROPERTIES OF BEST FIT MODELS

In the previous chapter, radiative models of Sgr A* were constructed from 3D GRMHD simulations with simplifying assumptions made for the electron distribution function, left unconstrained by the simulations. The models were fit to mm-VLBI and spectral observations to constrain the geometry and physical properties of the accretion flow. Overall, the models are extremely successful at reproducing observations. This is the case both for aligned simulations, and those where the angular momentum axis of the initial accreting torus is misaligned (tilted) from the black hole spin axis. Here, the properties of the best fitting aligned and misaligned models are discussed in more detail.

5.1 Image Morphology

5.1.1 Best Fit Models

Table 5.1 lists the parameters for best fit untilted models from the viable simulations (excluding 0h), as determined by the joint spectral index and VLBI fits. Images and visibilities from these models at 1.3mm and .87mm are shown in Fig. 5.1, at the time of best fit to the 1.3mm VLBI observations. The emission from the portion of the accretion disk receding from the observer is negligible compared to that from the approaching side, but the front

Table 5.1 Best Fit Model Parameters

Name	Spin (M)	$\dot{M}(10^{-9}M_\odot\text{yr}^{-1})$	i	T_i/T_e
50h	0.50	$50-60$	60°	1
90h	0.90	$3-5$	60°	1
MBD	0.92	$3-10$	60°	3
MBQ	0.94	$9-12$	50°	5

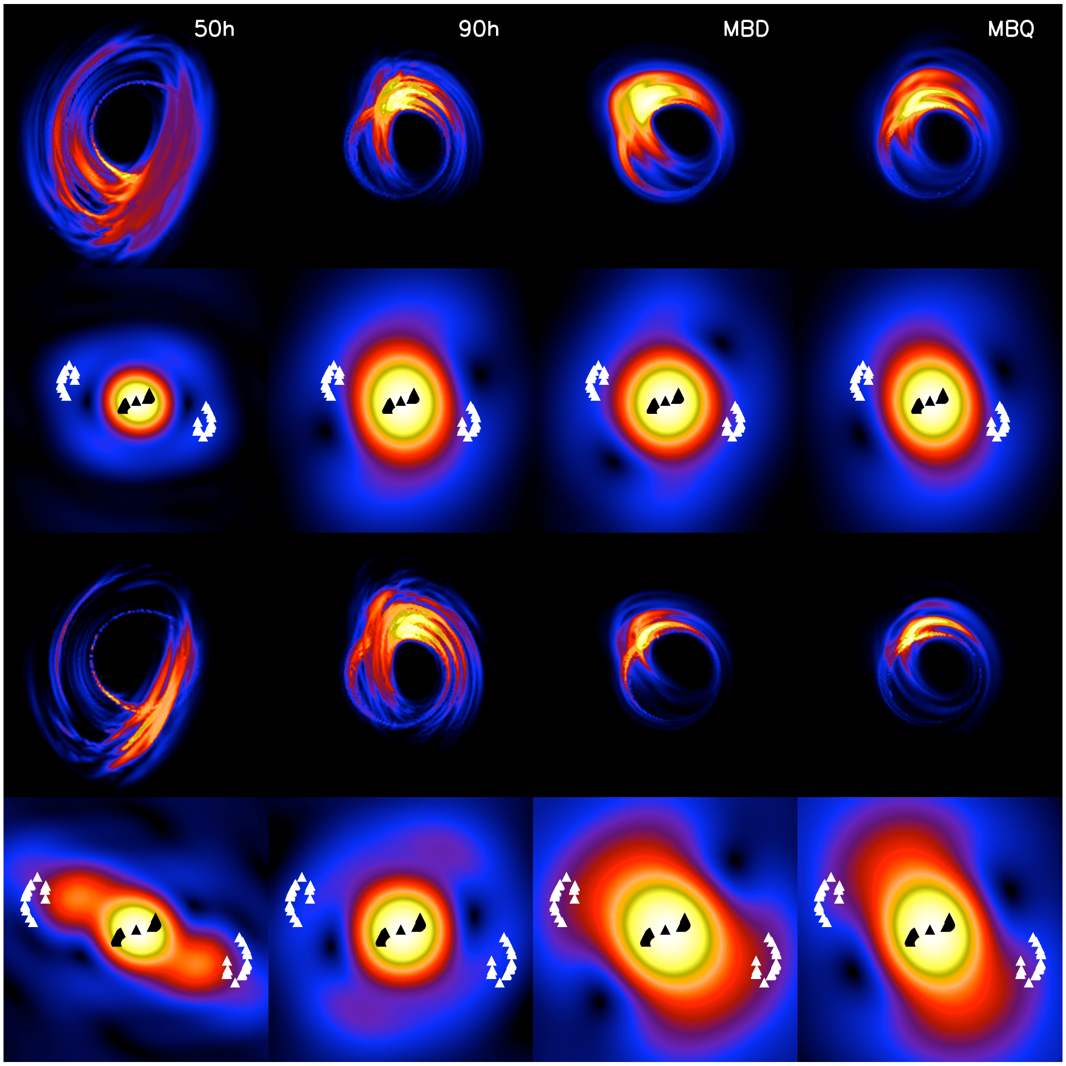

Figure 5.1 Images and visibility amplitudes at 1.3mm (first two rows) and .87mm (bottom two rows) for the best fit models. The first and third rows are images, while the second and fourth are the corresponding visibility amplitudes. All are rotated to their best fit positions. The uv-plane locations of the baselines used in the 1.3mm VLBI observations are over-plotted on the visibilities. The panel size is 150μas, and 12 $G\lambda$ for the visibilities. The columns are labeled by simulation, and each panel is scaled to its maximum value. At 1.3mm, the maximums are always $\simeq$ 2.4Jy. However, the total flux can vary between simulations at .87mm. Since the images and visibilities form a Fourier transform pair, in general a larger image corresponds to a smaller visibility and vice versa.

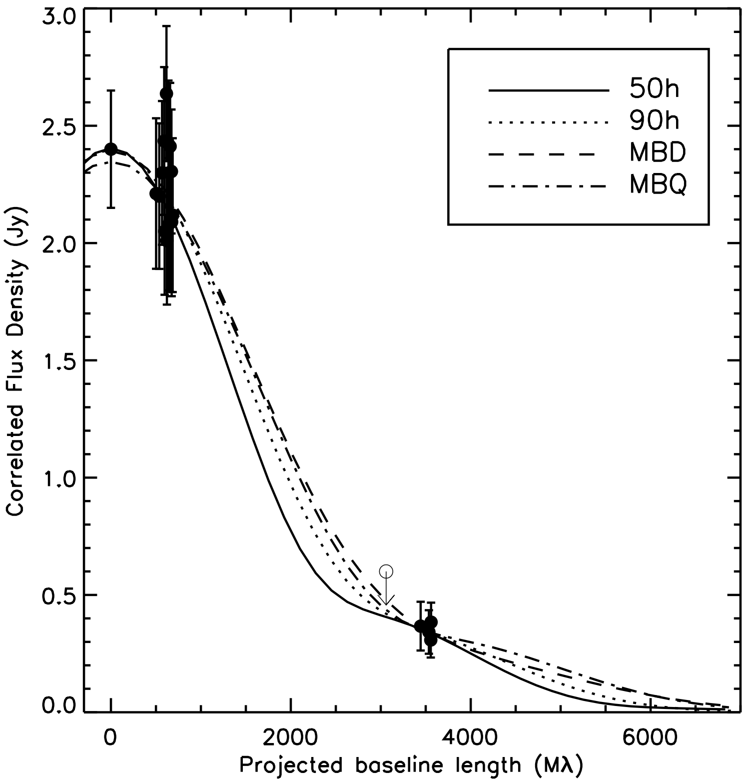

Figure 5.2 One dimensional visibility profiles along the line of the average long baseline location from Doeleman et al. (2008) [61]. All of these profiles decrease monotonically with baseline length.

Table 5.2 Best Fit Tilted Model Parameters

Name	Spin (M)	$\dot{M}(10^{-9}M_{\odot}\mathrm{yr}^{-1})$	i	T_i/T_e
315h	0.3	$100-200$	80°	3
515h	0.5	$9-15$	40°	1
715h	0.7	$10-15$	90°	1
915h	0.9	$9-12$	80°	1

and back (bottom and top of image, respectively) still contribute significantly. This combination causes all best fit images to be essentially crescents, one due to this combination of Doppler beaming of gas approaching the observer and gravitational lensing warping the back of the accretion disk to appear at the top of the image. A second crescent is also visible, and is due to the circular photon orbit. This feature is basically fixed in size regardless of the "size" of the accretion flow, depending only on the mass of and distance to the black hole, nearly independent of its spin. It should appear as either a ring (low inclination) or crescent (high inclination) as long as the accretion flow is optically thin.

The shadow of the black hole, caused by the transition between bound and unbound photons at the circular photon orbit, is prominent along the vertical axis as a local minimum in the visibility amplitude due to the contrast between it and the emission from the front and back of the accretion flow. One dimensional visibility profiles, plotted along the line of the average location of the long baseline measurements from Doeleman et al. (2008) [61], are shown in Fig. 5.2. In all models, the visibility profile decreases monotonically with baseline length along this axis.

The crescent geometry present in all our viable models of Sgr A* is a sort of intermediate between a Gaussian and a ring, the two model-independent geometries used to fit the images [61, 74]. The orientation probed by the baselines currently available with mm-VLBI is the Gaussian axis, while the ring axis is rotated away from us. As discussed below, depending on the model and the orientation, the ring axis may be accessible to observations in the near future. This would allow the first detection of a black hole shadow, direct evidence for the existence of an event horizon.

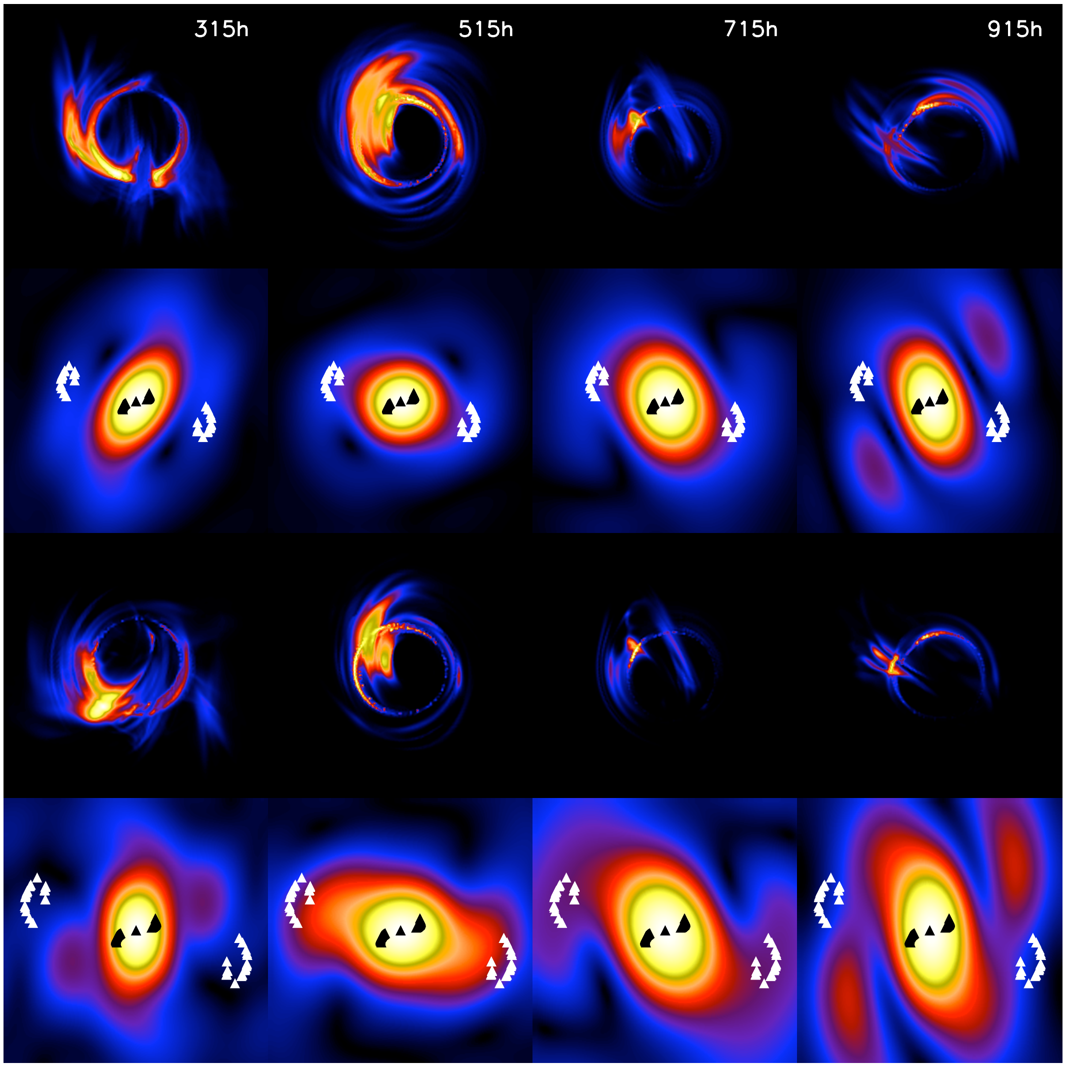

Figure 5.3 Images and visibility amplitudes at 1.3mm (first two rows) and .87mm (bottom two rows) for the best fit models from the tilted simulations as in Figure 5.1. The image morphologies are more complex and varied than in untilted simulations, but are still basically crescents due to Doppler beaming and gravitational lensing.

5.1.2 Tilted Disk Image Morphology

The "best fit" models for the simulations with misaligned angular momentum and black hole spin axes ("tilted" simulations) described previously are much less certain, since the parameters are so poorly constrained and a variety of viable models exist for each simulation. Despite this uncertainty, it is possible to get a feel for the similarities and differences between the aligned models and these tilted ones by simply choosing the inclination, orientation, observer azimuth and mass normalization (time-averaged accretion rate) with the lowest χ^2 value in analogous fashion to the well-defined best fit models for the aligned simulations.. The parameters of these models are listed in Table 5.2.

Figure 5.3 shows the same grid of images and visibilities as in Figure 5.1, but for the best fit tilted models. Typically the image morphologies for misaligned models are more complex than the simple crescent from Doppler beaming and gravitational lensing found before. However, those elements are still present in all images. Overall, the images are dominated by narrow rings or crescents near the circular photon orbit. The disk body is no longer clearly visible in the images, however.

The image morphology changes considerably depending on the observer's azimuth. That angle is completely unconstrained for Sgr A*, which explains much of the variety present in the tilted models and hence the lack of clear parameter constraints from current data. The situation is similar to the dependence of line profiles on observer azimuth for models of stellar mass black holes in Section 3.3.2 (see Figure 3.6), and is one of the most striking observable consequences of tilted black hole accretion disks.

5.2 Prospects for Future Observations

The presence of the black hole shadow in an image causes a local minimum in the corresponding visibility profile. The amplitude of the local minimum is set by the image contrast across the circular photon orbit. The shadow is detectable from the two dimensional visibilities at baselines of similar length and roughly orthogonal orientation to those used by Doeleman et al. [61] in all tilted or untilted best fit models. At .87mm, the resolution of the array improves, but the images are also smaller. Depending how optically thin the model is

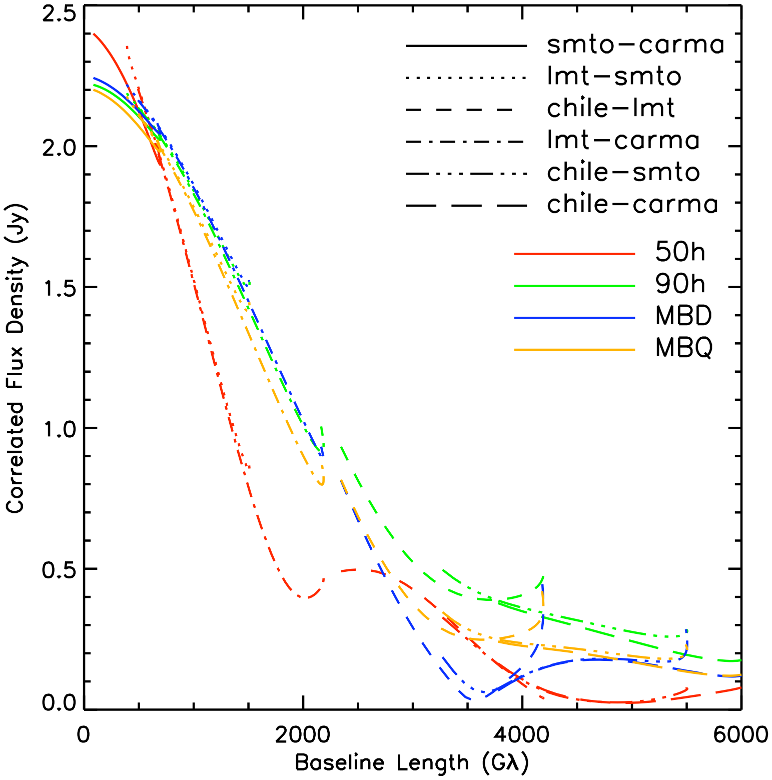

Figure 5.4 Visibility amplitude as a function of baseline length for best fit models at 1.3mm. The telescopes considered are in Arizona (SMTO), California (CARMA), Mexico (LMT) and Chile (APEX/ASTE/ALMA). The black hole shadow appears as a minimum in the 1D profile.

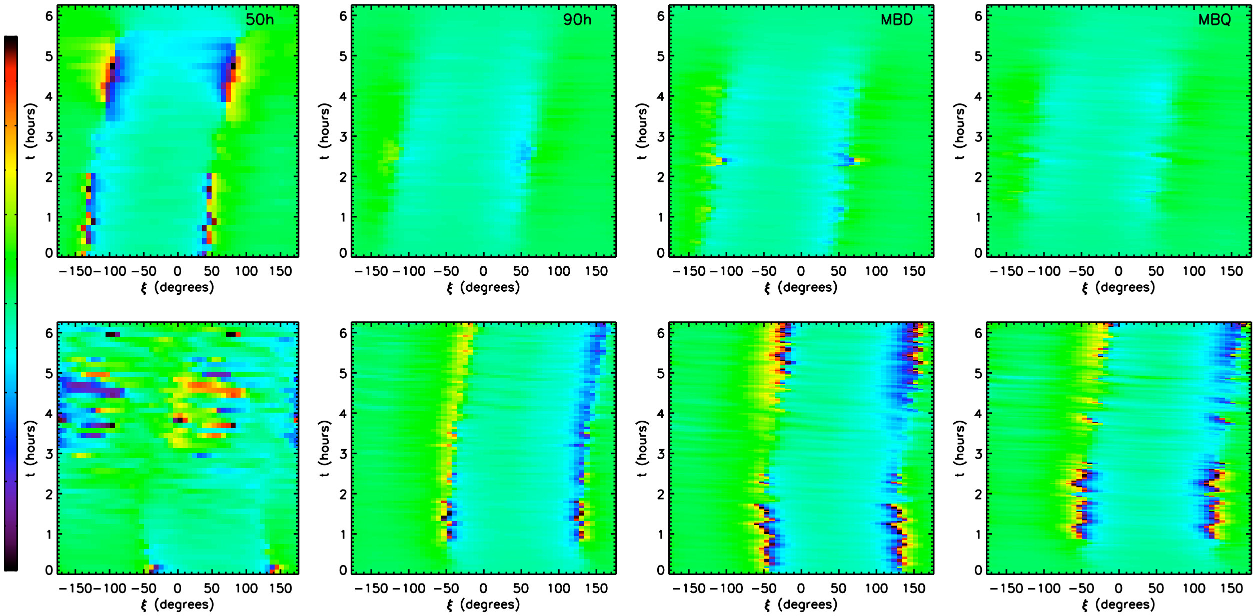

Figure 5.5 Closure phase as a function of observer time and sky orientation for best fit models on triangles of baselines between Arizona/California/Hawaii (top) and Arizona/Mexico/Chile (bottom).

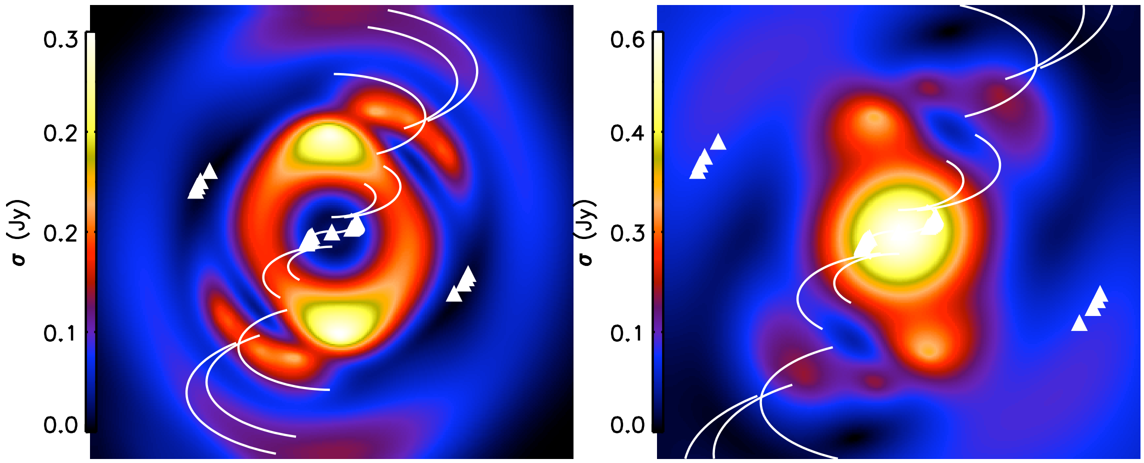

Figure 5.6 Standard deviations of the best fit visibility amplitudes at 1.3mm and .87mm. The uv-plane locations of the VLBI observations at 1.3mm are over-plotted as triangles. Future baselines between Chile/Mexico/California/Arizona are over-plotted as solid lines.

(how large and negative the spectral index is), the image can be extremely small as is the case for MBQ. For a spectral index similar to that observed by Marrone (2006) [124], the image will still be large at .87mm, and the shadow should be observable from the visibility.

To demonstrate this explicitly, visibility amplitude as a function of baseline length is plotted in Fig. 5.4 for the best fit models, considering baselines made up of combinations of telescopes used in ongoing observations in California (CARMA) and Arizona (SMTO), and those that should be added in the near future in Mexico (LMT) and Chile (APEX/ASTE/ALMA). The shadow is detectable for the best fit MBD and MBQ models on the Chile–Mexico and Chile-Arizona baselines. The differences in the predictions from the models in Fig. 5.4 are almost exclusively caused by their different best fit sky orientations.

Since Sgr A* varies significantly on timescales short compared to its mutual visibility between current and future VLBI telescopes, the profiles shown in Fig. 5.4 will necessarily include source variability. In addition, the short coherence time of the atmosphere and varying signal/noise between telescopes in the arrays may prevent proper calibration of the visibilities [58]. In these cases, the closure phase [167], the sum of the phases measured along a triangle of baselines, may be used as a non-imaging observable. It is independent of calibration errors, and probes the source structure in the uv-plane. Doeleman et al. (2009) [58] used a RIAF+hotspot model to compute predicted closure phases for future VLBI experiments. We make predictions for the best fit models discussed here, whose time-dependent structure comes directly out of the turbulence driven by the MRI.

Fig. 5.5 shows the closure phase maps vs. observer time and source sky orientation for the current Arizona/California/Hawaii triangle and a future one consisting of Arizona/Mexico/Chile. Due to the moderate inclination favored by the VLBI and spectral observations, the closure phase is relatively robust over time, except over a narrow range of sky orientations. At these positions, one of the baselines in the triangle is sampling the black hole shadow, which causes a sudden rotation of the phase when the real part of the visibility switches sign. The earth's rotation moves the baseline positions, slowly changing the sky orientations at which this effect is visible. For large phase rotations, the visibility amplitude is usually quite small ($\lesssim 0.1$Jy) and will be difficult to detect. However, it could be observed as a transition in phase over a short timescale, where Sgr A* is detected at one fairly stable closure phase, goes to an undetectable amplitude, and reappears at a different stable closure phase. The most recent VLBI data constrain the closure phase between existing telescopes to be ±40° [74], providing another independent constraint on the models. This value is consistent with our results from the best fit models for the viable ranges of sky orientation from Figure 4.4. The best fit models generically predict a closure phase of $\simeq -30^\circ - 0^\circ$ depending on the simulation and sky orientation.

If the sky orientation of Sgr A* is $\sim -50 - 0^\circ$, this shadow signature would be detectable using the Arizona/Mexico/Chile triangle. The best fit images for MBD, MBQ and 90h in Fig. 5.4 are in this range. Note that the exact value of the phase rotation and how often it occurs in time are model-dependent – in Fig. 5.5 it is usually $\sim \pi/2$ and occurs at $1 - 3$ observer times. Regardless of the value of the position angle, the black hole shadow can be detected from closure phase measurements on some triangle of baselines in this way. Closure phases from a larger set of baselines will constrain the structure of the accretion flow in a similar fashion to the current measurements of the visibility amplitude. For simplicity, the closure phases shown here are for almost co-linear baseline trios. Much more complex and time-dependent closure phase signatures are found on nearly triangular baseline arrangements, such as those including Hawaii, Chile and California/Arizona/Mexico.

We calculate the standard deviation of the small sample of best fit visibilities, as done for a large ensemble of RIAF images by Fish et al. (2009) [73]. The result from the best fit 3D GRMHD models, shown in Fig. 5.6, is in relatively good agreement with their Figure 2. The best baselines for constraining the accretion flow are of similar to slightly shorter length as the existing measurements ($\sim 2000 - 4000$km), but at roughly orthogonal orientation. The peak values of the variance are larger at .87mm. This is expected since we fit to existing measurements at 1.3mm, while at .87mm only the total flux is somewhat constrained by the spectral index between .4mm and 1.3mm from Marrone (2006) [124].

Interpolating the best fit visibilities to the locations of future VLBI baselines (Figure 5.7) provides a similar picture as in the aligned models: the shadow of the black hole should appear on baselines of future interest in a significant fraction of the models. The predicted closure phases for viable sky orientations in Figure 5.8 are consistent with the constraint of ±40° from the most recent VLBI observations, and these models predict the actual value

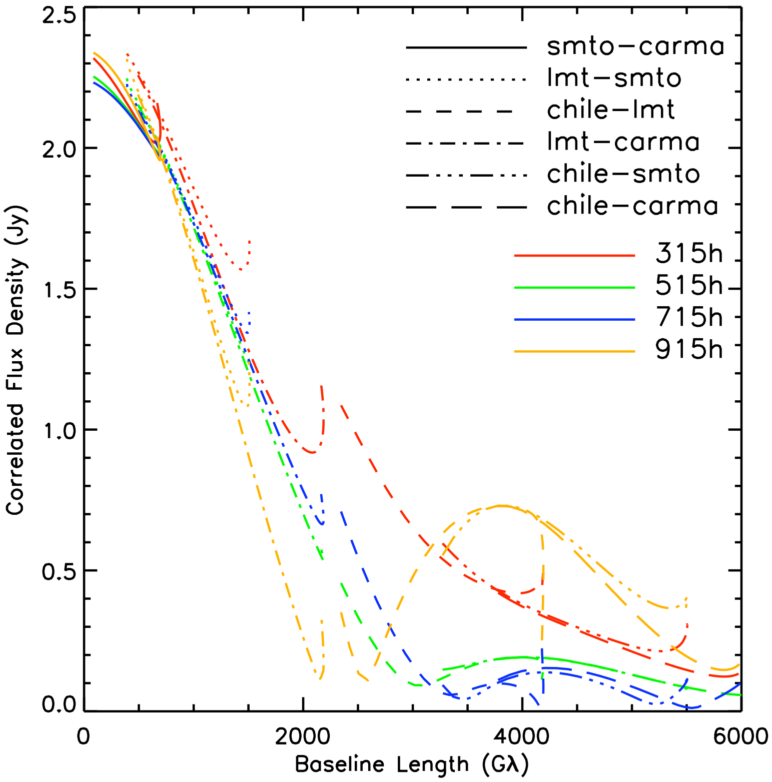

Figure 5.7 Visibility amplitude as a function of baseline length for best fit tilted models at 1.3mm. The telescopes considered are the same as in Figure 5.4. As in the untilted models, a significant fraction of viable tilted models predict the appearance of the black hole shadow (local minimum in the visibility profile) on baselines from Mexico/Chile and the US.

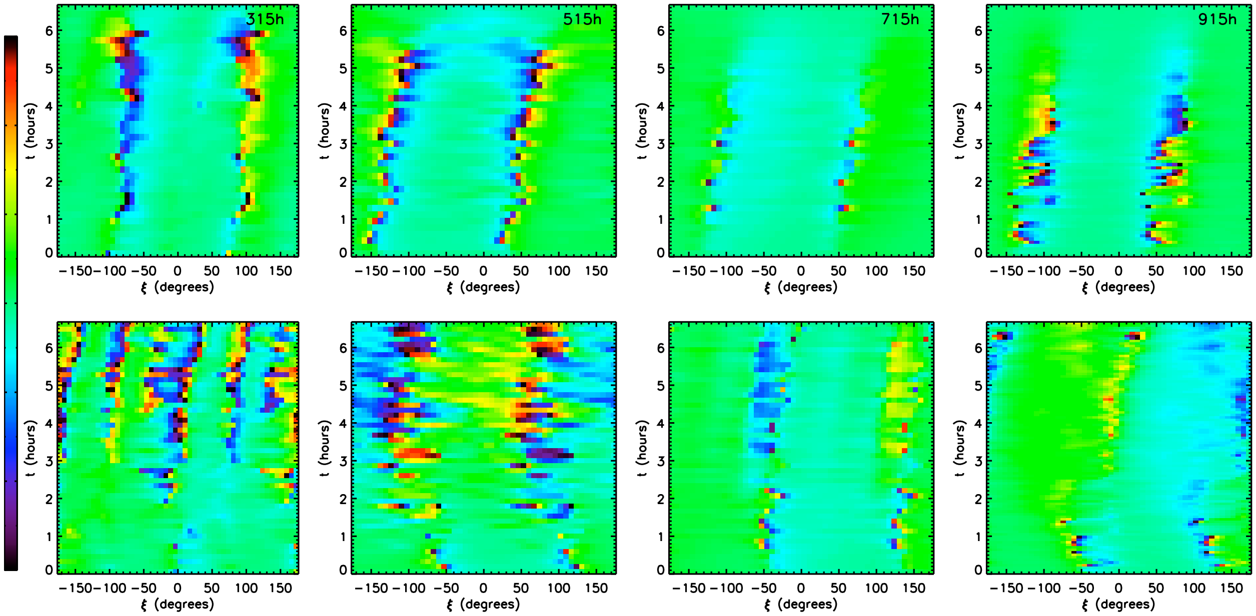

Figure 5.8 Closure phase as a function of observer time and sky orientation for best fit tilted models on triangles of baselines between Arizona/California/Hawaii (top) and Arizona/Mexico/Chile (bottom). The predicted closure phase signatures are similar to those from untilted models.

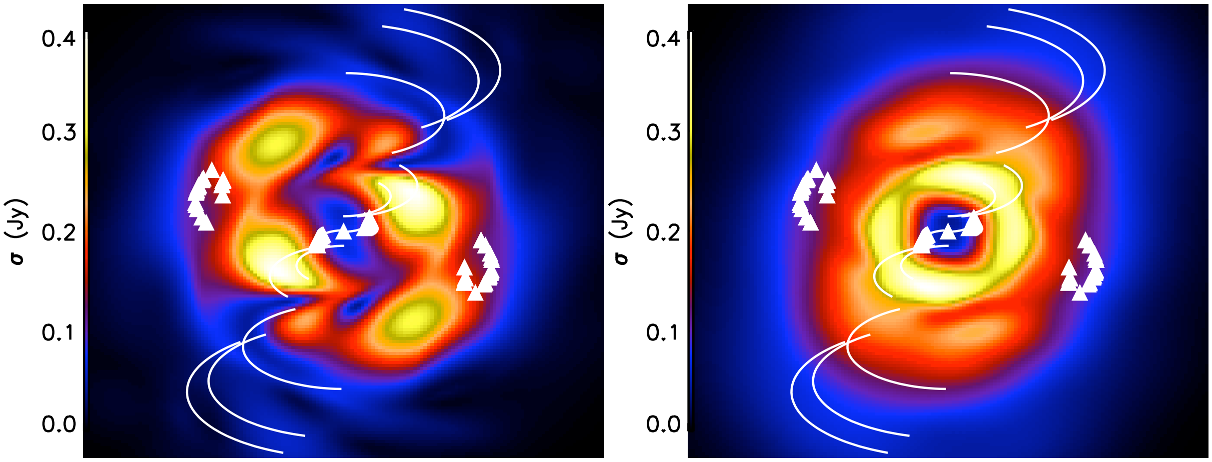

Figure 5.9 Standard deviations of the best fit visibility amplitudes considering all models (right) and just the best fit from each simulation (left). The uv-plane locations of the VLBI observations are over-plotted as triangles. Future baselines between Chile/Mexico/California/Arizona are over-plotted as solid lines.

should be $\simeq -30 - 0^{\circ}$, exactly the same as for the untilted models.

Due to the lack of a coherent picture of the viable tilted models, future measurements will easily be able to constrain their properties further. Perhaps with a complementary orientation, a clearer picture of these models will emerge. This is shown explicitly at 1.3mm in Figure 5.9 (compare to Figure 5.6 for untilted models). Viable tilted disk models span a large range of possibilities, so that future measurements on almost all baselines will provide useful further constraints.

5.3 Variability and Millimeter Flares

A major advantage of using GRMHD simulations in place of semi-analytic models is the ability to study variability from the same dynamical model used to produce spectra and visibilities. Previous work has used hotspots [31, 58] to study variability, but this introduces extra free parameters, complicating attempts to extract black hole parameters. Two sample light curves from the 90h simulation are shown in Figure 5.10 for inclinations $i = 10^{\circ}$, 70°. The variability on short timescales is slightly more noticeable for the $i = 70^{\circ}$ case, while the longer time scale flaring behavior is more pronounced in the $i = 10^{\circ}$ light curve due to the lower optical depth along the line of sight at lower inclination. The power spectra are well described by red noise spectra with power law index $\Gamma = 2.4$, 1.7 for $i = 10^{\circ}$, 70°. These are both steeper than the observed power law index of $\Gamma = 1$ in Mauerhan et al. (2005) [127] at 3mm wavelength. These general statements hold for light curves from all simulations considered in this thesis for all viable model parameters.

Twin flares occur simultaneously in both light curvesin Figure 5.10, rising over half an hour with 2–3.5 hour durations. The flux modulation is 50% (40%) at $i = 10^{\circ}$ (70°), measured from the peak of the flare to the average of the light curve immediately preceding it. All of these features are consistent with mm flare observations of Sgr A* [63, 125, 207, 113]. Since the flares are seen at low inclinations, they are not caused by Doppler shifts from hotspots. The peak intensity is attenuated at large inclination due to rising optical depth. The flares are caused by a rise in magnetic field strength near the midplane in the inner radii ($r \sim 2$–6M). They are not due to heat from magnetic dissipation since this is not possible in the simulation used here. Thus heating from magnetic reconnection is not

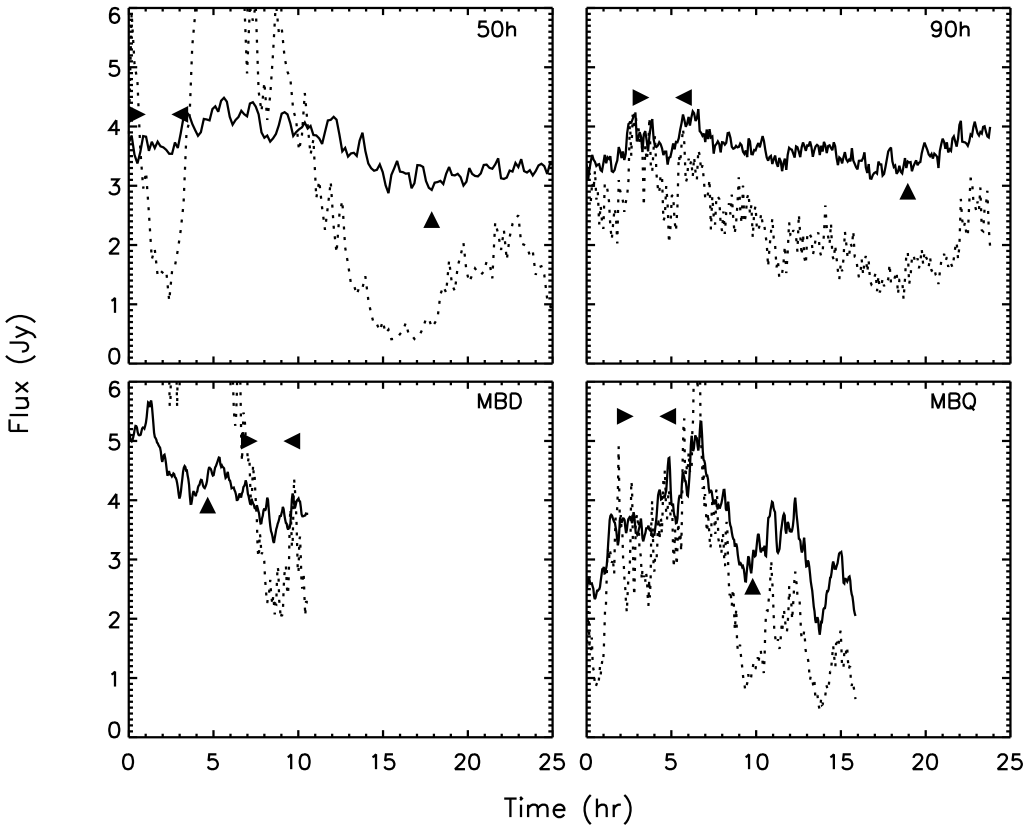

Figure 5.10 Light curves for best fit parameters (see Table 5.1) from each simulation at 1.3mm (solid) and .4mm (dotted). The vertical arrow denotes the time of best fit to the VLBI measurements, while the horizontal arrows denote the averaged interval corresponding to the best fit to the spectral index observations. The accretion rate used for the plots is not necessarily the best fit, since that value can differ between the two constraints. The McKinney & Blandford (2009) [129] simulations were run for shorter times since the torus was initially placed at smaller radius.

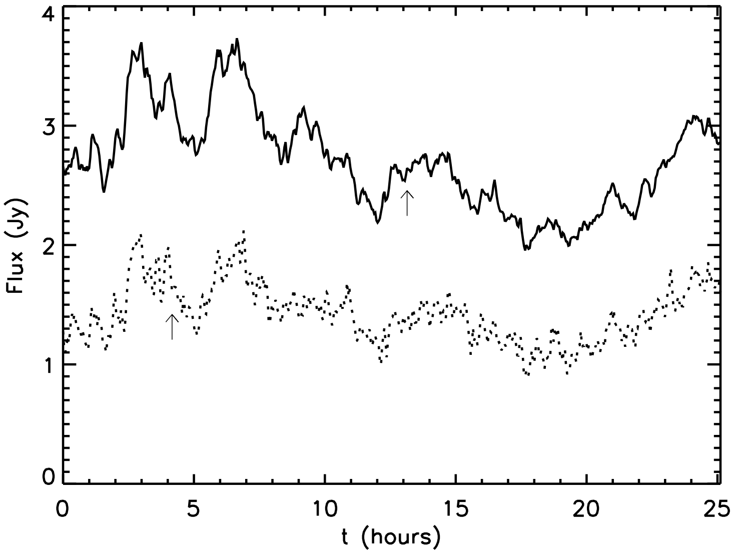

Figure 5.11 Light curves of the last 2/3 of the 90h simulation from Fragile et al. (2007) at inclinations of 10° (top) and 70° (bottom) for $T_i/T_e = 1$. The $i = 70°$ light curve has been shifted downwards by 1.5 Jy for clarity. Both light curves exhibit consecutive flares starting at $t \sim 2$ hours, which are consistent with those observed from Sgr A* at mm wavelengths. They are more prominent at $i = 10°$ due to higher optical depth between the observer and the flaring region at high inclinations. The arrows denote the 10 minute intervals corresponding to the best fit images shown in Fig. 3.1.

necessary to produce the mm flares of Sgr A*.

Light curves at 1.3mm (230 GHz) and .4mm (690 GHz) for best fit parameters from all viable simulations (excluding 0h) are shown in Fig. 5.10. All light curves show millimeter flares that are consistent with the observations, and with the behavior described above for the 90h simulation. The spectral index rises during the flares, often above zero, due to stronger variability at 690 GHz where the flow is completely optically thin. Only $1-2$ flares occur in each theoretical light curve, which is consistent with their observed frequency.

The flares are caused by increased magnetic field strength in the inner radii of the accretion flow where the synchrotron emissivity is highest. This is the case even in total energy conserving simulations, where the gas can be heated from reconnecting magnetic fields. Reconnection events, while present, do not seem related to the millimeter variability. Likewise, the variability is not produced by local inhomogeneities (hotspots), but rather

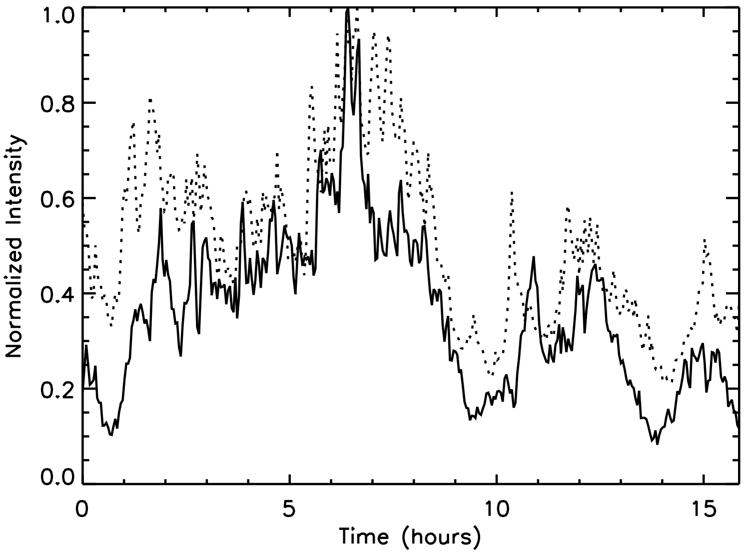

Figure 5.12 Light curve at .4mm (solid) and accretion rate at the inner boundary of the MBQ simulation (dotted) with best fit parameters (see Table 5.1). Both quantities are scaled to their maximum value.

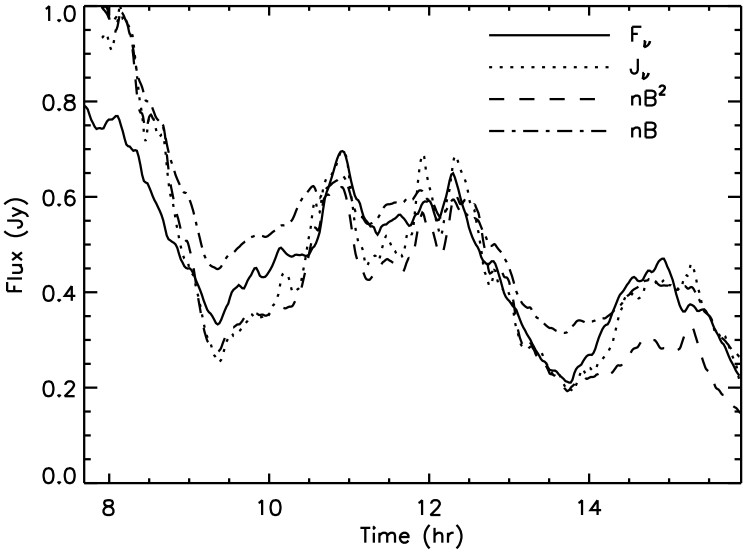

Figure 5.13 Last half of the 1.3mm light curve of MBQ with $T_i/T_e = 3$, $i = 10°$ (F_ν) compared to the volume integrated synchrotron emissivity (j_ν) and approximate volume integrated emissivities, nB and nB^2 where n is the electron density and B is the magnetic field strength. The emissivities are normalized to their maximum values, while the light curve is scaled so that it matches the synchrotron emissivity at ~ 11 hours.

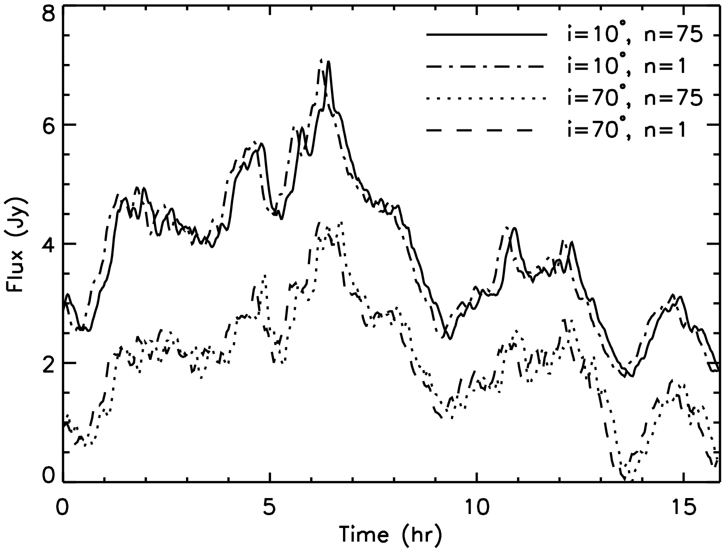

Figure 5.14 Light curves of MBQ at $i = 10$ and 70 degrees for $n = 1, 75$ where n is the number of simulation time steps used to compute the intensity at a single observer time. $n = 1$ neglects the effects of finite light travel time through the fluid.

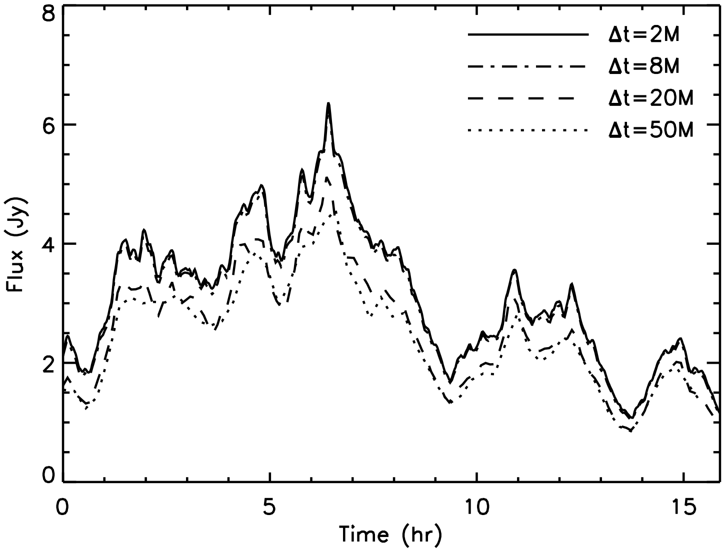

Figure 5.15 Light curves of MBQ at 10 degrees using simulation time steps separated by $\Delta t = 2$, 8, 20 and 50M, where 2M is the value used for other MBD and MBQ light curves, while $\Delta t = 4$M for the 50h and 90h simulations.

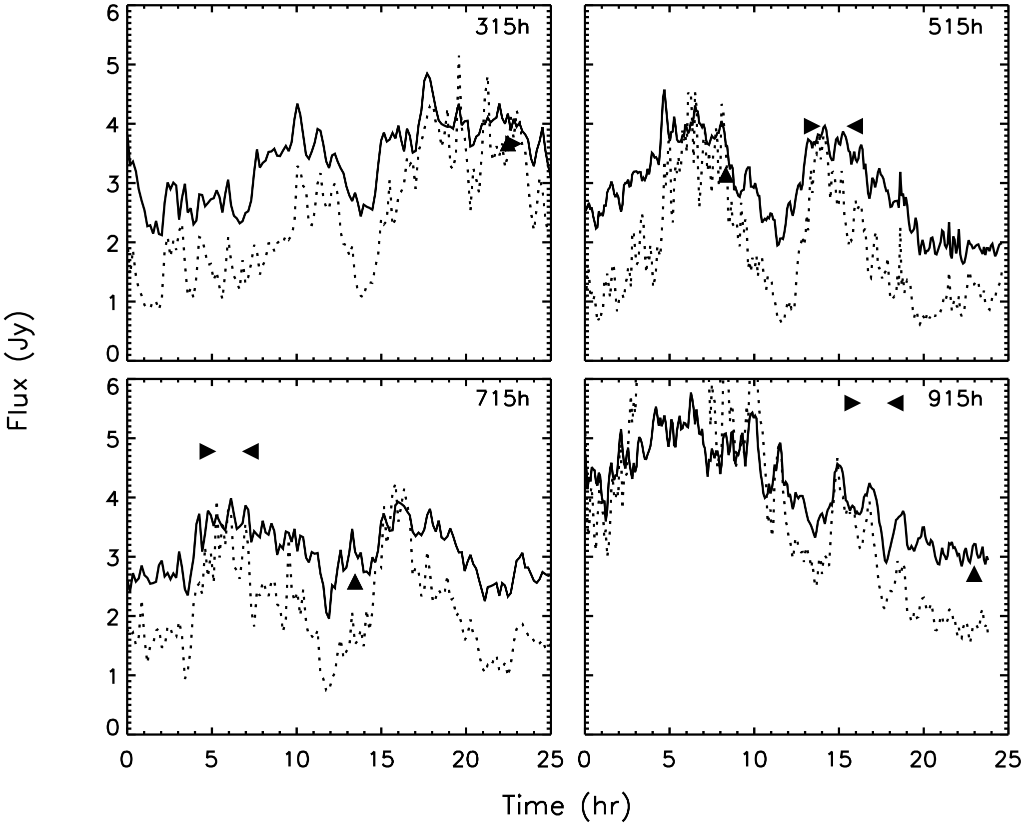

Figure 5.16 Light curves for best fit parameters from tilted simulations (see Table 5.2) at 1.3mm (solid) and .4mm (dotted) as in Figure 5.10. The variability is slightly stronger in tilted simulations, but the flaring behavior remains consistent with observations of Sgr A*.

by relatively global increases in the magnetic field strength in the inner radii. The light curves at .4mm are strongly correlated with variability in the accretion rate, as shown for simulation MBQ in Fig. 5.12. There are no robust lags found between the variability in the millimeter light curves and the accretion rate, and we cannot definitively determine the cause and effect.

Since only the millimeter emission is modeled here, it is unclear if the flares produced are consistent with the observed x-ray, IR and millimeter flares [63, 125, 57, 204]. At 1.3mm, the flares are weaker at higher inclination, where they are attenuated by higher optical depth between the observer and the emission region. Due to the presence of a significant photosphere, the correlations with accretion rate variability are much weaker at longer wavelengths as well.

5.3.1 Simple Variability Model

The 1.3mm light curve shapes are closely reproduced by assuming the optically thin synchrotron emission comes from an isothermal region with a magnetic field satisfying $\nu/\nu_c \sim 1-20$, where $\nu_c = 6.27\times10^{18} B(kT)^2$ (cgs) is the critical frequency for synchrotron emission. Then the emissivity is $j_\nu \sim nB^\alpha$, with $1 \leq \alpha \leq 2$. The light curve from simulation MBD is compared to the integrated synchrotron emissivity as well as these simplified isothermal models in Fig. 5.13. A low inclination light curve is used to lessen the impacts of Doppler beaming and optical depth. The flaring behavior is captured without any temperature fluctuations, and the variations are caused by those in the magnetic field strength and particle density. In models with significant photospheres, including most at high inclination, these simple formulas still work to describe the integrated synchrotron emissivity, but tend to be more variable than the light curves which include self-absorption.

5.3.2 Effect of Light Travel Time Delays

Including the time delays along geodesics means that many different time steps of simulation data are used to compute the intensity along each geodesic. Fig. 5.14 shows a comparison of light curves with and without accounting for time delays. The light curves are virtually identical at both low and high inclinations, except for a systematic shift in observer time, indicating the constant time lag between $r = 25M$, where we begin following geodesics, to the emission region.

This is surprising, especially given the results of Noble & Krolik (2009) [143]. They found significantly steeper power spectra at high frequencies when accounting for time delays. However, the simulation from that work used an artificial emissivity, lower time resolution ($\Delta t = 20M$) and only a $\pi/2$ wedge in ϕ. We've tried matching their $\pi/2$ wedge in ϕ and sampling with the same time resolution. In all cases, we find no systematic differences when accounting for light travel time through the accretion flow, and the errors due to neglecting time delays are at the 10% level (Fig. 5.14), comparable to the overall uncertainty in the interpolation scheme or emissivity used. The largest errors occur at high inclination, where the light travel time to different parts of the emission region is largest. When using both the limited domain in ϕ and $\Delta t = 20M$, the slope of the power spectrum is slightly steeper when using time delays. However the deviation is considerably smaller than that reported by Noble & Krolik, possibly due to the differing emissivities or disk scale heights. They also included cooling self-consistently in the simulation.

Their use of a $\pi/2$ wedge in ϕ is predicated on the assumption that the dominant azimuthal spatial structure is in modes with $m \simeq 4$ and higher [173]. We test this by expanding fluid variables in spherical harmonics for different simulations and time slices. In all cases, we find that the $m = 1, 2$ power is larger than at higher orders, as found previously by Henisey et al. (2009) [95] for a tilted simulation. This suggests that the use of restricted ϕ domains incorrectly approximates the spatial structure of a fully global simulation. In particular, we find that the power law index of the power spectrum is significantly steeper when using the full 2π, indicating that using a limited wedge in ϕ introduces spurious variability on shorter timescales. Studying variability using simulations probably requires using the full ϕ domain.

We also caution that interpolating magnetic field vectors between time steps with insufficient time resolution results in systematic suppression of the total flux. This occurs when magnetic timescales are significantly shorter than the time step between simulation data dumps, causing interpolation between uncorrelated magnetic field vectors. For the

MBD and MBQ simulations, $2 - 8$M time resolution is sufficient, as shown in Fig. 5.15. However, when interpolating magnetic fields between time steps in the 90h simulation, the flux is systematically $\sim 10\%$ lower with a time spacing of 4M. Our radiative transfer code uses time steps equal to an integer multiple of the simulation time step so that these errors cannot cause spurious features in the light curves. Regardless, we use data from the nearest time step rather than interpolating magnetic fields when the time steps are too large.

5.3.3 Variability in Tilted Disk Models

The variability properties discussed above apply just as well to tilted as to the untilted simulations discussed above. Figure 5.16 shows the best fit light curves in the same fashion as in Figure 5.11. The millimeter variability properties are almost identically between the two sets of simulations, although the amplitudes are slightly higher in tilted simulations. The correlation with accretion rate is just as strong as that shown in Figure 5.12, and the variability in the tilted simulations is still well described by the simple isothermal model based on variations in the magnetic field and electron density.

5.3.4 Time-dependent Spectra and Centroid Position

The radio spectra from all models are shown in Fig. 5.17. The shaded gray regions show the extent of the variability at each frequency. Below $\sim 10^{11}$Hz, a substantial portion of the emission is produced outside $r = 25$M, and so is not included here. In addition, we do not model emission from nonthermal electrons, and so do not expect to be able to fit the observations outside of the millimeter peak. The variability increases with frequency, due to the decreasing optical depth. The 50h simulation produces a large amount of variability, which may be inconsistent with the range observed from Sgr A*.

In addition to VLBI observations, there are constraints on the time-dependent structure of the accretion flow from astrometry. The centroid wander of Sgr A* at 7mm was constrained by Reid et al. (2008) [162] to be $\lesssim 100\mu$as on timescales of a few hours. Fig. 5.18 shows x and y centroid positions as functions of time for the best fit models at 345GHz. The position wander for all models considered here is $\lesssim 30\mu$as at millimeter frequencies on

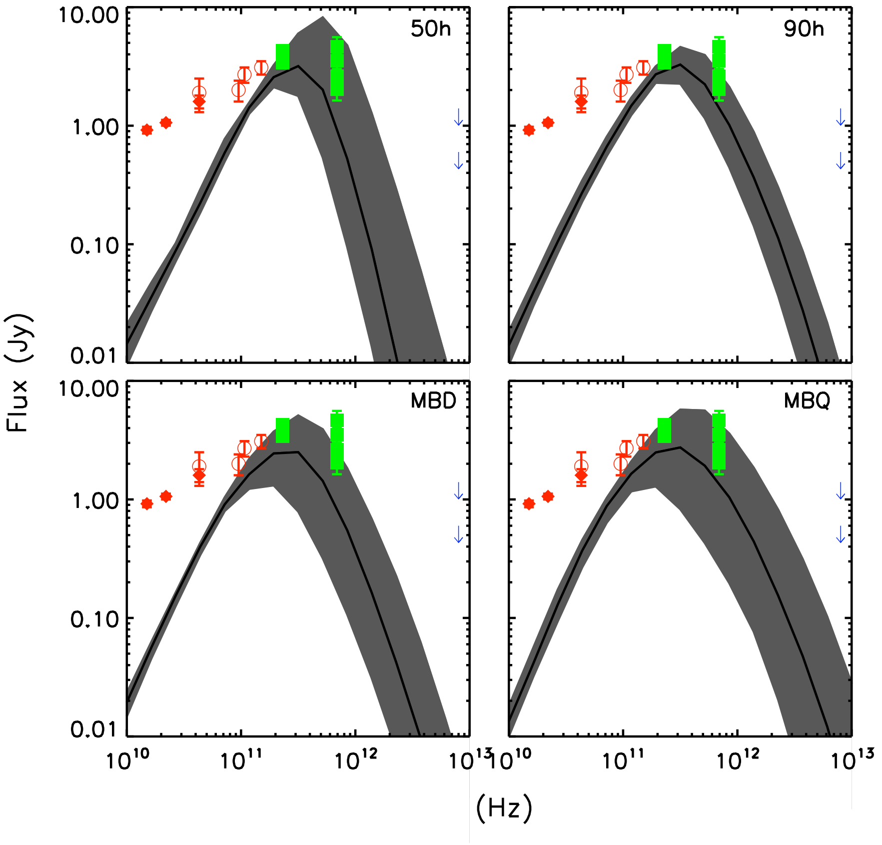

Figure 5.17 Millimeter spectra for the best fit models. The solid curves are the median values at each frequency, while the dark gray envelope shows the range reached during the simulations. Data points are from Falcke et al. [67] (open circles), An et al. [5] (filled diamonds) and Marrone [124] (filled squares). The models are fit to the Marrone [124] data, while at lower frequencies the emission is dominated by emission outside of the simulation domain, and nonthermal emission from electrons either in the accretion flow [202] or in a short jet [68].

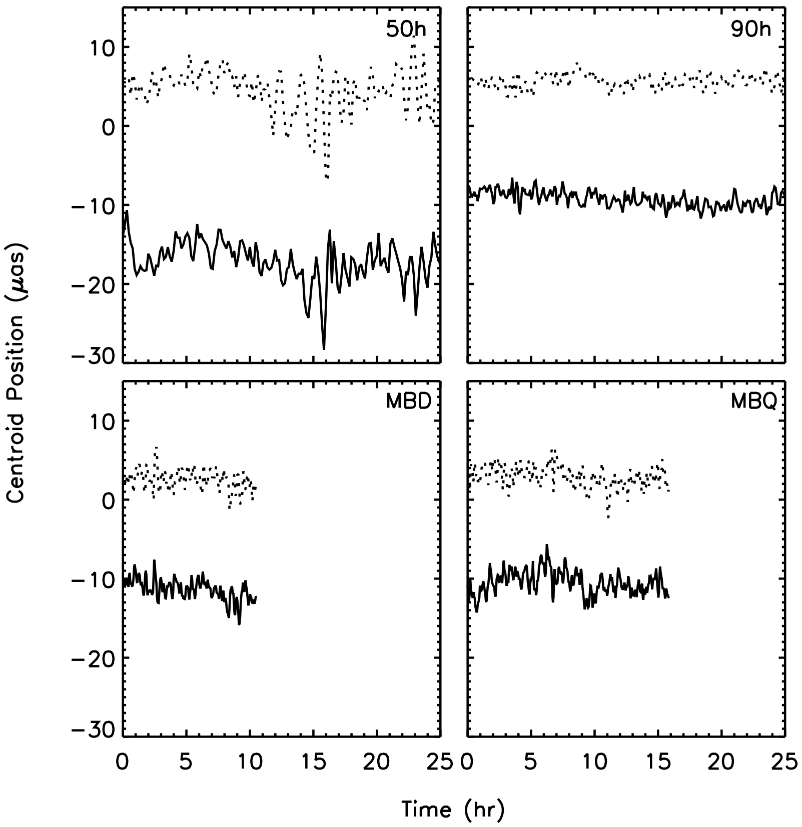

Figure 5.18 X (solid) and Y (dotted) centroid positions vs. observer time for the best fit models from tilted simulations at 345GHz. The position wander is similar for all frequencies in Fig. 5.17, although the average centroid position changes with frequency.

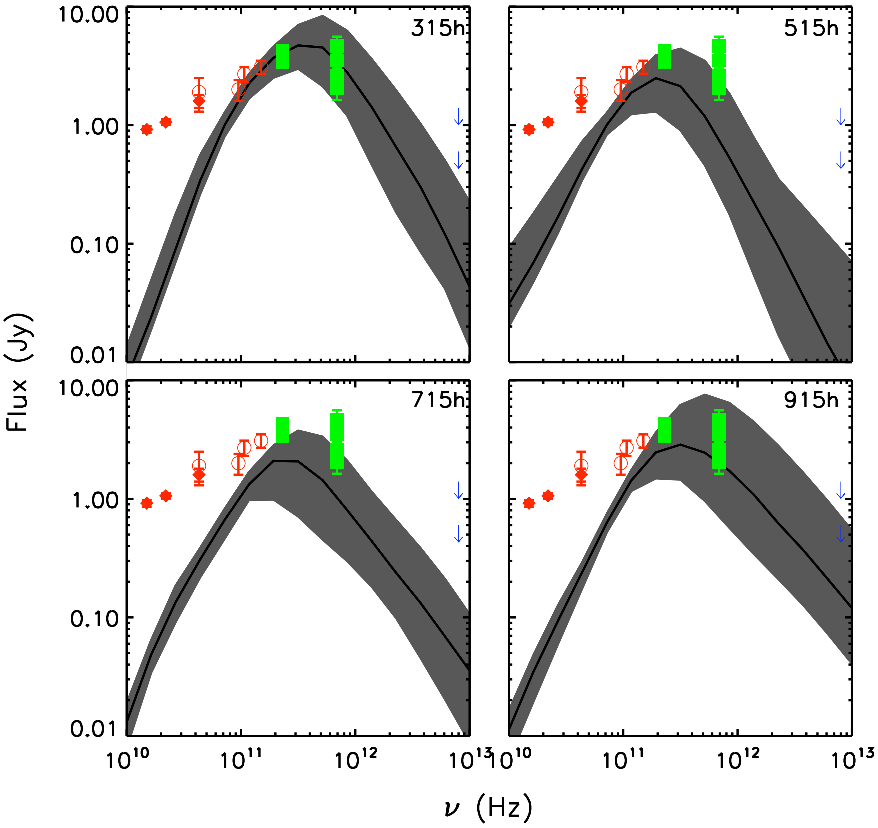

Figure 5.19 Millimeter spectra for the tilted best fit models as in Figure 5.17.

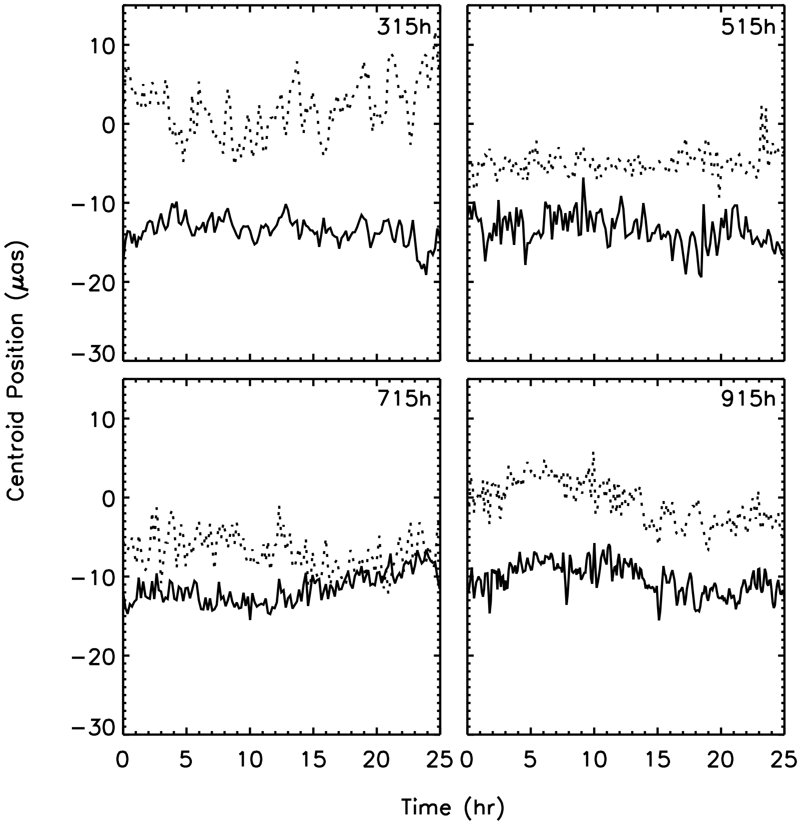

Figure 5.20 X (solid) and Y (dotted) centroid positions vs. observer time for the tilted best fit models at 345GHz as in Figure 5.18.

all timescales, well within the observed upper limit. A prediction of the simulations is that the millimeter position wander shouldn't exceed that level, even during flares. This is due to the robustness of the time-dependent image structure at all inclinations, and a result of the fact that the variability is produced globally in the inner radii, rather than by small, orbiting inhomogeneities (hotspots).

The instrument GRAVITY at the Very Large Telescope (VLT) will provide $\simeq 15\mu$as precision astrometry of Sgr A* in the infrared (IR). If the IR flaring is due to a relatively global process such as Compton scattering from millimeter seed photons, centroid measurements from thermal synchrotron emission in the IR may be similar to those during the flares. Since the position wander from our models rarely exceeds the detection limit of GRAVITY at any frequency, it should be easy to distinguish such IR flare mechanisms from nonthermal events involving hotspots or expanding blobs, which would lead to larger centroid movements [205].

The spectra from best fit tilted disk models (Figure 5.19) extend to higher frequencies than their untilted counterparts (Figure 5.17). This is partially due to the higher inclinations of the best fit models for 315h, 715h and 915h but is also due to higher temperatures in portions of the tilted models (not in the underresolved poles). The stronger variability in the tilted models is also evident. Finally, Figure 5.20 shows the (x,y) centroid locations as functions of time for the best fit tilted models. Although the position wander is larger here than for the untilted simulations (Figure 5.18), if the position wander is similar in the IR it will only be at the detection limit for the future VLT instrument GRAVITY.

5.4 Emission Region Properties

The millimeter emission region is in the innermost radii of the accretion flow, peaked in the midplane. The emission is dominated by synchrotron emission from thermal electrons [202]. The saturated magnetic field strengths are typically $\sim 0.01 - 0.1$ of equipartition (plasma $\beta \simeq 10 - 100$), and both the particle density and magnetic pressure are proportional to the accretion rate. These quantities, then, are scaled together to produce the observed total flux from Sgr A*. For these reasons, the quantities that differ most between simulations are the electron temperature and the radial density profile. The radial distribution of particle density and the electron temperature in large part determine the image structure and viability of the model.

As expected for accretion disks with aligned angular momentum and black hole spin axes, the effective inner radius of the disk in all simulations moves closer to the black hole with increasing spin. However, the density at the event horizon is usually only a factor ~ 5 lower than at the peak. There is no sharp inner boundary to the accretion flow.

Optical Depth Effects

For best fit parameter combinations, the 1.3mm photosphere is quite compact and the flow is mostly optically thin, especially at low inclination. In the 0h and 50h simulations, however, as well as for $T_i/T_e = 10$ in all models, the photosphere at 1.3mm extends well outside of the region of peak emissivity, at $r \sim 5$M. In general, the photosphere gets smaller at higher electron temperatures, since those models require lower accretion rates to match the observed flux from Sgr A*. Optical depth effects are also more important at high inclination. This is because Doppler beaming increases the absorption along rays between the observer and the approaching gas.

Single temperature conservative models (MBD, MBQ) have no noticeable photosphere. This leads to a small image size, and low accretion rates. Since the Marrone (2006) [124] observations find that the turnover in the synchrotron spectrum occurs between 1.3mm and .4mm, they are inconsistent with models that are completely optically thin at 1.3mm. The VLBI observations also disfavor such models due to their small image sizes. For $T_i/T_e = 10$, we have the opposite situation. VLBI rules out these models due to their large photospheres and hence image sizes, while they are generally also optically thick enough that the synchrotron turnover occurs shortward of .4mm. For all simulations, the best fit T_i/T_e occurs when there is a photosphere inside of $r \sim 5$M.

Comparison to RIAF Models

There are significant differences between the simulated and semi-analytical RIAF accretion disks. In the RIAF model, the disk is assumed to have a constant scale height $H/R =$

1, whereas for all simulations considered here $H/R \sim 0.1 - 0.3$ in the regions of peak millimeter synchrotron emissivity, as measured by fitting a Gaussian to the particle density at the median radius of peak synchrotron emissivity. The Gaussian fits describe the vertical particle density distribution, and their parameters are stable over time. The emissivity has the same vertical profile.

Thinner disks have higher particle density, stronger magnetic fields and smaller temperatures. These effects are largely mitigated in the Sgr A* models, since the electron temperature scaling is a free parameter, and the magnetic pressure and density scale with accretion rate. The parameter $\beta = P_g/P_m$ is independent of accretion rate and electron temperature. In regions of peak synchrotron emissivity, it has a median value around $\sim 3 - 10$ for the high spin simulations 90h, MBD and MBQ. The lower spin, non-conservative simulations 0h and 50h have median $\beta \sim 10 - 20$. In RIAF models, β is assumed to be a constant, usually around ~ 10. The trend of increasing β with decreasing spin is also seen in the axisymmetric HARM simulations. Although β varies spatially in the simulations, the emission region is small enough that these variations aren't larger than an order of magnitude, so that constant β is likely a good approximation.

We have also fit radial profiles of density, temperature and magnetic field strength to compare the simulations to the RIAF models. In general, simple power laws $r^{-\alpha}$ describe the radial distribution of temperature and magnetic field strength within the millimeter emission region. The power law indices for the temperature distribution are around $\alpha \sim 0.7$, which is quite close to the RIAF value of 0.84. The conservative MBD and MBQ simulations have magnetic field indices of $\alpha \sim 1.1 - 1.2$, while the 0h, 50h and 90h simulations range from $\alpha \sim 0.3 - 0.7$. The RIAF value is 1.05. In the 50h, 90h and 2D HARM simulations, the magnetic field power law index increases with spin.

Other than the disk thickness, the main discrepancy between RIAF models and GRMHD simulations is in the radial particle density profile. The simulations find flat or decreasing density profiles towards the horizon from a point at $\sim 2r_{ms}$, where r_{ms} is the marginally stable orbit. In RIAF models, the density increases up until the horizon as a fixed power law. This is especially inaccurate at low spin, where the 0h, 50h, and HARM simulations find peaks in the radial density profile at $r \sim 10 - 15$M, depending on the value of the spin.

Finally, running the axisymmetric HARM simulations also allows a direct comparison to the spectral index values found in Mošcibrodzka et al. (2009) [136] for different ray tracing codes and interpolation schemes. Values of the spectral index, time-averaged as discussed in that work, are in good agreement with their results in most cases. This is even true when we use the angle-averaged emissivity from Mahadevan et al. (1996) [122]. The emissivity from Leung et al. (2010; submitted) takes into account the angle θ between the ray and the magnetic field. The largest differences between the emissivities are at extreme inclinations, where a factor of $\sin\theta$ in ν_c causes the spectrum to peak at larger (smaller) frequencies at low (high) inclinations. Individual images and spectra can significantly differ between emissivities. However, all parameter estimates, probability distributions, light curves and best fit models presented here are robust to the choice of emissivity.

5.4.1 Tilted Disk Emission Region

Tilted simulations are geometrically thicker than untilted simulations run with the same code (Cosmos++), and the emission region moves to slightly *larger* radius with increasing spin. This was found for some dynamical measures of the inner radius by Fragile (2009) [77], while the calculations in Chapter 3 found that the radiation edge is roughly independent of spin. The tilted Sgr A* models all produce the bulk of their emission at $r \simeq 3-7$M, similar to the 90h untilted simulation. All tilted models have significantly stronger magnetic fields relative to equipartition than their untilted counterparts, with the median plasma beta in the synchrotron emission region $\simeq 2-10$, *increasing* with increasing spin, again the opposite as found in untilted simulations.

The compact emission region and large magnetic field strength at low spin in tilted simulations makes 315h a particularly likely model for Sgr A*. It can produce the observed millimeter flux without becoming optically thick even at much smaller electron temperatures than the other simulations, and in large part prevents parameter estimates from the tilted simulations as a group. The fact that in many ways low spin tilted simulations resemble high spin untilted ones suggests that the limit $a \to 0$ at finite tilt should be interesting for further study, as presumably the accretion flow must smoothly transition from effectively high spin to zero spin without a significant change in the actual spin parameter.

5.4.2 Precession

All of the GRMHD simulations only evolve the inner portion of an accretion disk. Since the initial condition is a torus in hydrostatic equilibrium, the outward angular momentum transport driven by the MRI causes some of the torus material to move outwards. Thus, the actual accretion disk only forms inside of some radius smaller than the location of the initial torus. In the simulations considered here, that location is $r \simeq 15-25$M, much smaller than the expected "size" of the accretion flow in Sgr A*. The simulated, tilted disks precess essentially as solid bodies once an initial radial tilt and warp profile is established [80, 79]. The timescale for this precession is sensitive to the outer boundary of the accretion flow, where infalling material couples to the rest of the disk.

Since the physics of this transition in a thick, tenuous, magnetized flow like that in Sgr A* is uncertain, this timescale is essentially unconstrained. If the flow only begins to precess at a reasonably small radius $r \sim 100-1000$M, then the timescale could be on the order of days-years, accessible to observations. Then the strong dependence of image morphology on observer azimuth would cause the characteristics of Sgr A* as measured by mm-VLBI to vary with observational epoch, much in the same way as described for line profiles in Section 3.3.2. The variation of inferred parameters from this fitting process with time would then be a signature of a tilted accretion flow. Current observations are insufficient to test for this effect.

5.5 Discussion

Radiative models from all simulations provide excellent fits to the current mm data (VLBI and spectral). The observational constraints provide a generic picture of the accretion flow onto Sgr A*. The observed flux is due to synchrotron emission from thermal electrons at $r \simeq 3-10$M near the midplane of the flow. In the case where the black hole spin axis and torus angular momentum axis are aligned, the electron temperature, accretion rate and viewing geometry are also well constrained. In the misaligned case (with 15° tilt), the additional free parameter leaves a much larger range in the viable models. The resulting black hole images as viewed at infinity are essentially a superposition of two crescents in all cases: one from the combined effects of gravitational lensing of the back of the disk to the top of the image and Doppler beaming causing approaching (receding) material to appear brighter (dimmer), and the other from the same Doppler beaming but of the emission from the immediate vicinity of the circular photon orbit.

The detectability of the black hole shadow, caused by the contrast between the transition between bound and unbound photon orbits at the strongly lensed circular photon orbit, depends on the degree of Doppler beaming and in turn on the inclination angle. For the aligned models, the inclination is moderate so that the black hole shadow should be detectable over a range of orientations that are inaccessible to current telescopes. The high spin simulations used here predict that the shadow should be detectable on baselines between Chile or Mexico and California or Arizona. The shadow appears both in measurements of the visibility amplitude obtained to date, or through observations of the closure phase. These same baselines are also the most promising for further constraining black hole parameters, and testing accretion flow models. The misaligned simulations also predict the shadow should be detectable for some range of orientations a significant fraction of the time, but again the picture from these models is much less clear.

In addition to detecting the shadow, it has been suggested [103] that the no-hair theorem in the Kerr metric could be tested through testing its size and position relative to the black hole. This is appealing because as shown here, the feature (crescent or ring) from the circular photon orbit has a size independent of the details of the accretion flow. However, our models indicate that this procedure will be extremely difficult. Detecting the shadow at all will require relatively complete baseline coverage both in terms of many telescopes and long observation periods. Highly sensitive measurements will also be required to detect a local minimum in the visibility amplitude and/or a sudden change in the closure phase. Since the images are superpositions of *two* crescents (see Figure 5.1), and since the size of the shadow in most models depends critically on the details of the accretion physics rather than just the properties of the Kerr metric, inferring the size and location of the circular photon orbit will require disentangling it from the accretion flow portion of the image. Even if the observations eventually provide a fairly sensitive image of the accretion flow, this will require detailed understanding of the physics of the accretion flow.

Radiative models based on 3D GRMHD simulations are inherently time-dependent, and the variability of the synchrotron emission in the accretion flow provides another test of its validity. Millimeter light curves from all best fit models from both aligned and tilted simulations show flaring events with $\sim 50\%$ amplitudes and few hour durations at a frequency of $1-2$ per day, consistent with the millimeter flaring behavior of Sgr A*. These flares are caused by rises in magnetic field strength near the midplane of the inner radii of the accretion flow, due to magnetic turbulence driven by the MRI. They do not appear to be linked to heating from magnetic reconnection, and are accurately reproduced by a simple model assuming an isothermal emission region with $\nu/\nu_c \sim 20$. The variability in the light curves for all simulations at .4mm is strongly correlated with that in the accretion rate onto the black hole. However, there is no clear evidence for a characteristic lag between the two.

Due to the uncertainties in their emission mechanisms and electron distribution functions, we do not model the radio, IR or X-ray portions of the spectrum, and so are unable to test for the presence of correlated multiwavelength flares. Maitra et al. (2009) [123] showed that the observed time lags between the radio and millimeter flares may be reproduced by a jet model, where perturbations in the accretion rate near the black hole expand as they flow outward. Since the millimeter variability is strongly correlated with the accretion rate, that mechanism could explain the correlations between radio and millimeter flares even if the millimeter emission is produced in an outflow rather than an accretion disk.

Additional constraints may come from the degree and orientation of linear polarization first detected by Aitken et al. (2000) [4]. Huang et al. (2009) [99] modeled the polarization from a pseudo-Newtonian model. It is important to use relativistic simulations for such studies, since the degree of polarization is strongest close to the black hole. This has also been done for 3D GRMHD data averaged in time and azimuth [186], but it's unclear how sensitive the polarization is to this averaging procedure. Future VLBI observations may make use of the closure phase between triangles of baselines to probe changing structures in the accretion flow [58]. Fish et al. (2009) [75] extended this work to include polarization. Both of these papers used a RIAF+hotspot model. We have computed the first closure phase signatures from more physically realistic GRMHD simulations, and find that the signature of the black hole shadow is present in the predicted closure phases. Detailed comparison of observed and predicted closure phases will be able to constrain the accretion flow in the same fashion as direct sampling of the visibility amplitude.

Chapter 6

RADIATIVE MODELS OF M87

6.1 M87

M87 is a giant elliptical galaxy in the Virgo cluster. At a distance of 16 Mpc, it is $\simeq$2000 times farther away from Earth than Sgr A*. The putative central supermassive black hole in M87 (from this point on M87 will refer to the source coincident with the central black hole rather than the galaxy itself) is $\simeq 6.3 \times 10^9 M_\odot$, $\simeq$1600 times larger than Sgr A*. The expected angular size, $\delta\theta \propto M/D$, is then about 4/5 that of Sgr A*.

For this reason, M87 is just as if not more promising a mm-VLBI target as Sgr A*. M87 is in the northern sky, offering much longer mutual visibility with current telescopes than Sgr A*. Its enormous black hole implies a proportionally longer dynamical time, so that the light crossing timescale at its event horizon is $\sim$1 day. This means that unlike in Sgr A*, earth aperture synthesis could be used to fill in the uv-plane, possibly (with additional telescopes) allowing the use of imaging techniques to create an image of the source directly instead of the model-dependent uv-space fitting techniques used in this thesis for Sgr A*.

From a physics standpoint, M87 is known for its galaxy-scale, ultrarelativistic jet. The exquisite resolution of mm-VLBI then offers the possibility of imaging the jet launching region, which would provide the opportunity to compare directly with physical models of jet collimation.

The spectral properties of M87 are well known: it is an inverted radio source with a power law tail extending from the spectral peak in the millimeter (similar to Sgr A*) all the way to the optical. Existing VLBI images at 7mm [105, 120, 197] show extended jet structure on milliarcsecond scales, emanating from an unresolved bright core.

Previous semi-analytic work has modeled the low-frequency radio emission as arising from (mostly non-thermal) synchrotron radiation in a “truncated” accretion disk with constant density and magnetic field strength out to some small radius, where both quantities fall off as power laws. The millimeter and high-frequency emission is modeled as non-thermal synchrotron radiation as well, but with different physical parameters attributed to unknown jet physics. These models can fit the spectrum [201, 33] and accomodate the presence of extended jet structure at 7mm. Synthetic jet images have also been produced as predictions for mm-VLBI from one of these semi-analytic models [33].

Jet formation has recently become accessible to global GRMHD simulations [129]. In the simulation MBD used for modeling Sgr A* (Chapter 4, Table 4.1), an ultrarelativistic jet is produced which propagates out to 1000M ($\lesssim$ 1mas in M87) before it interacts with the simulation boundary. The same ray tracing techniques discussed previously (Chapter 2) are used in this chapter to create a time-dependent spectral model of M87 for comparison with ongoing mm-VLBI observations.

6.2 Radiative Modeling

Unlike in Sgr A*, there is no consensus for the electron distribution or geometry responsible for the millimeter emission in M87. The presence of an extended jet at 7mm indicates that the jet is at least comparable in luminosity to the disk there. Given that our model consists of a GRMHD simulation where a jet is produced from accretion onto the black hole from a disk, we also include a disk component. We assume that synchrotron emission dominates at all wavelengths from radio to optical, and neglect inverse Compton scattering of the synchrotron seed photons to higher energies.

6.2.1 Jet Emission

We assume that the jet emission is entirely non-thermal, while the accretion disk component is entirely thermal. The thermal component is computed in the same fashion as the previous chapter for Sgr A*, including the assumption of a constant ion-electron temperature ratio. Previous models have also included non-thermal disk emission, which could be important for explaining the radio spectrum. The non-thermal particle distribution is taken to be a power law in electron energy (Lorentz factor) with a constant index p between low- and high-energy cutoffs, $\gamma_{min,max}$. The synchrotron emission and absorption coefficients for

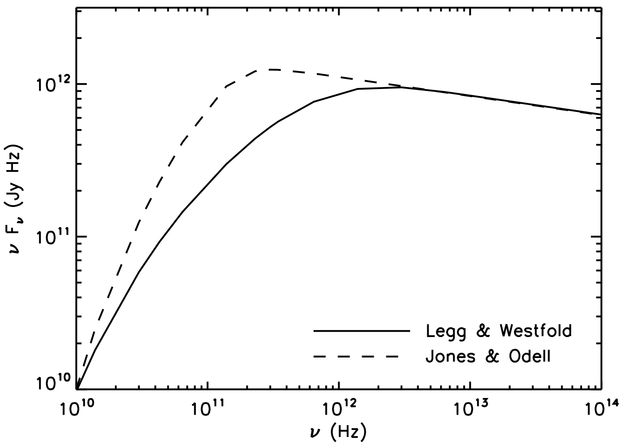

Figure 6.1 Spectra from jet model used in [33] with the exact emissivity calculated from [112] (solid) and the approximate form given by [104] (dashed). The approximate form overestimates the emission in the vicinity of the low frequency cutoff ($\simeq 10^{11}$Hz here). The parameters are $\gamma_{min} = 100$, $p = 3$.

this distribution are taken from Equations C.22 and C.42 and the required integrals are tabulated for the desired values of p.

It is necessary to use this form of the emissivity rather than approximate forms commonly found in the literature that assume an observed frequency far from those corresponding to the cutoff Lorentz factors. In M87, the low-frequency cutoff is located at $\nu_0 \simeq 10^{10-11}$Hz for the range of low-energy Lorentz factor cutoff used here, $\gamma_{min} = 10 - 100$. This is quite close to the frequencies of interest for mm-VLBI. Figure 6.1 shows the difference in the spectrum between the two forms. Taking the low-frequency cutoff into account broadens the spectrum and smoothes the turnover from optically thick to thin.

The magnetic field strength everywhere is taken directly from the simulation. For the jet emission, we need to calculate a non-thermal particle density. In the magnetically-dominated jet, the particle density and internal energy from energy conserving simulations are highly inaccurate due to the artificially enforced floor values used for numerical stability. Instead of using these compromised values, we scale the internal energy to the magnetic energy with a constant of proportionality, η:

$$u_{nth} = \eta \frac{b^2}{8\pi}, \tag{6.1}$$

where u_{nth} is the non-thermal internal energy density and b is the magnetic field strength in cgs units. Then the particle density, n_{nth}, is taken from,

$$n_{nth} = \eta \frac{b^2}{8\pi} \frac{p-2}{p-1} (m_e c^2 \gamma_{min})^{-1}, \tag{6.2}$$

which implicitly assumes that all of the internal energy is in electrons rather than protons, or equivalently that the thermal energy in all particles is negligible and that all the protons are thermal.

The rest energy of these non-thermal particles should still be less than the magnetic energy density, since this procedure is unjustified outside of magnetically-dominated regions. This leads to the condition,

$$\eta \lesssim \frac{m_e}{m_{e,p}} \frac{p-1}{p-2} 8\pi \gamma_{min}, \tag{6.3}$$

where $m_{e,p}$ correspond to leptons (baryons) producing the jet. The strictest condition on η is found by assuming a baryonic jet, in which case (for $p = 3 - 3.5$),

$$\eta \lesssim .25 \frac{\gamma_{min}}{10}. \tag{6.4}$$

This inequality is satisfied in all our models as the maximum η considered is 0.1.

6.2.2 Jet/Disk Boundary Condition

The GRMHD simulation consists of a smooth solution for a single component fluid, neglecting particle acceleration or distributions. Defining a disk/jet solution for M87 then requires choosing a condition for the boundary between the two components. There are several possibilities.

First, the general structure of GRMHD simulations consists of a dense, thick disk with scale height $H/R \sim 0.2-0.3$ centered on the equatorial plane, surrounded by a tenuous wind and then a polar jet. One straightforward method is then to define the jet/disk boundary at a particular polar angle. Typically this is chosen to be $\simeq 30^\circ$.

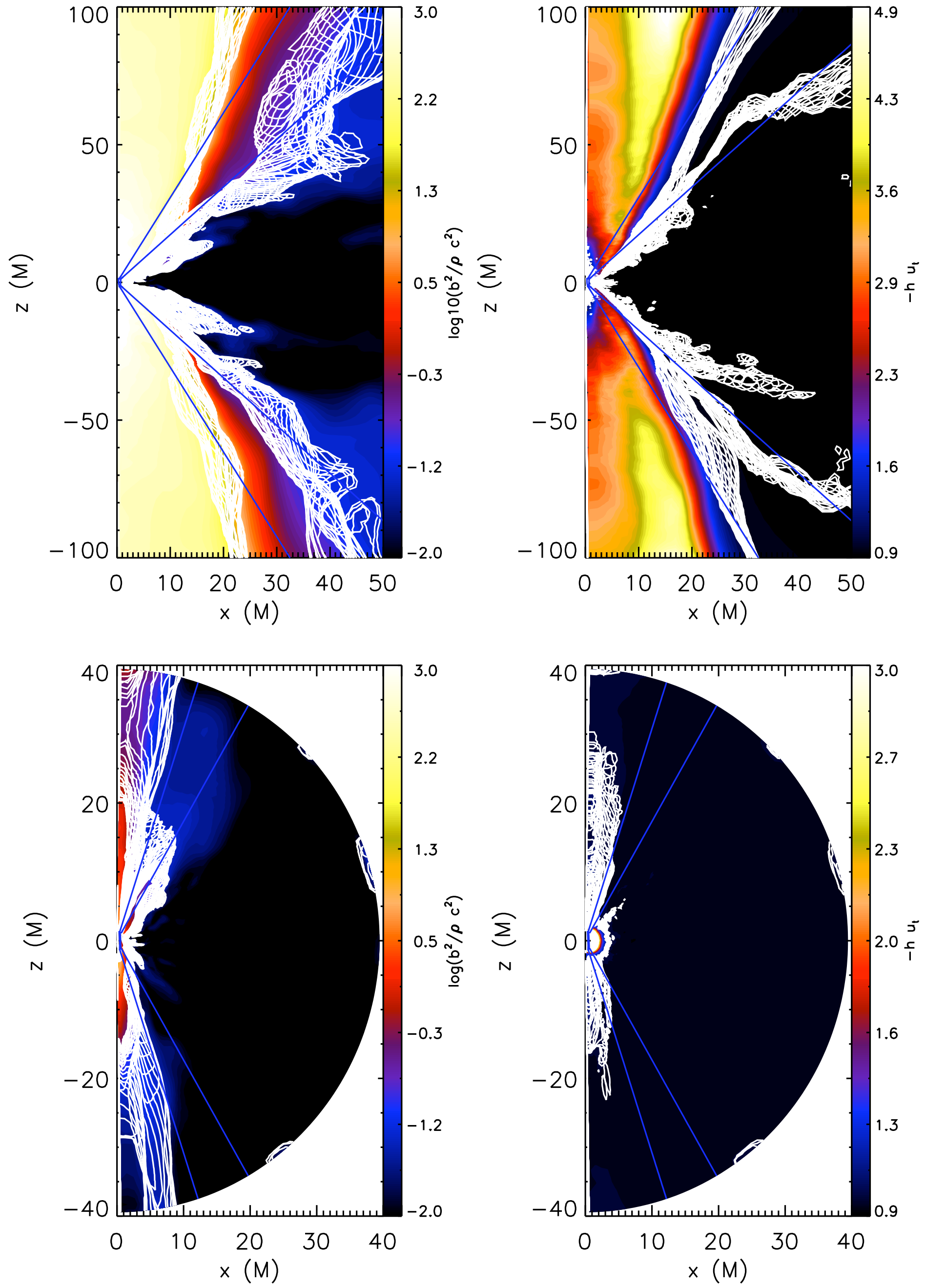

Figure 6.2 Ratio of magnetic to rest energy (left) and specific enthalpy measured at infinity (right) for a single time step of the MBD (top) and MBQ (bottom) simulations. The azimuthally averaged data are shown in color, while contours of $b^2/\rho c^2 = 0.1$, 8π and $-hu_t = 1.0, 1.1$ for the full range of azimuths are overplotted. Also overplotted in blue are lines of constant polar angle, $\theta = 18°$, $30°$. The jet is clearly identified by either measure in MBD, but only roughly corresponds to lines of constant θ. There is no persistent jet in the MBQ simulation.

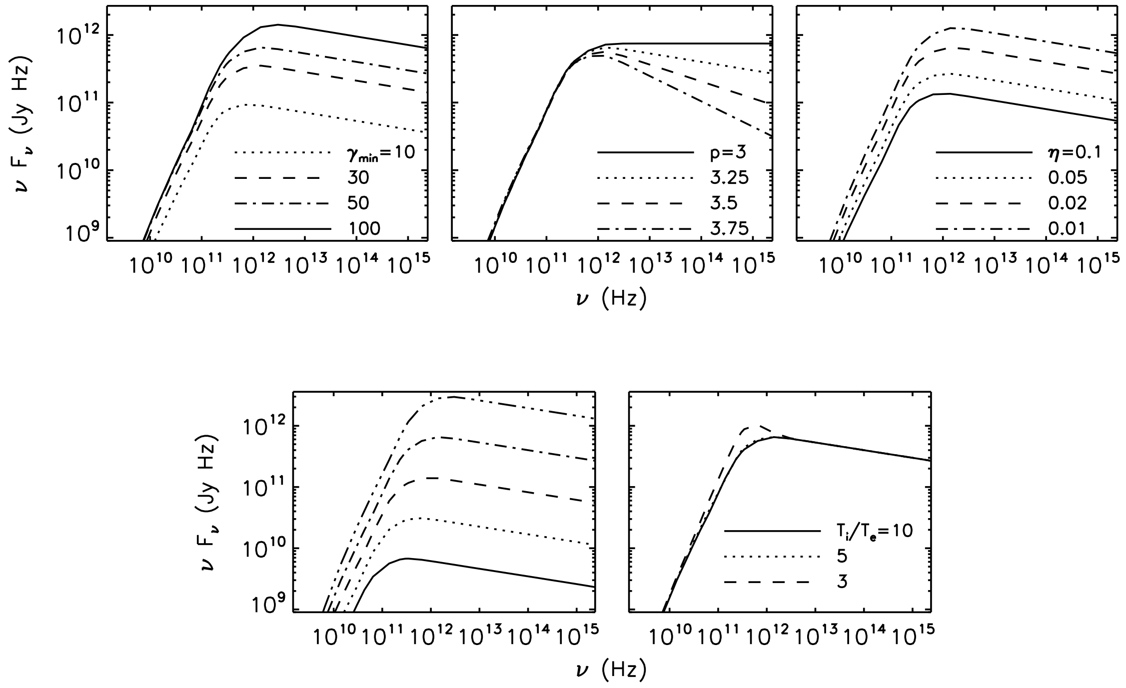

Figure 6.3 Sample disk/jet spectra varying each parameter separately: γ_{min} (top left), p (top middle), η (top right), $\dot{m}$ (bottom left) and T_i/T_e (bottom right).

Secondly, the outflows in GRMHD simulations arise in magnetically-dominated regions [52, 128]. Motivated by this, we can define the jet as anywhere that $b^2/\rho c^2 > f$, where $f \simeq 0.1 - 8\pi$ depending how much of the "disk wind" is to be included in the jet.

Finally, the jet/disk components can be separated as the boundary between inflow/outflow. In this case, all unbound fluid elements are taken to comprise the jet ($-hu_t > 1$, where h is the specific enthalpy and u_t is the time-component of the covariant fluid four-velocity [52]). Any combination of these criteria can also be used instead of just one. A comparison of the three criteria for an azimuthally-averaged single timestep of the simulation is shown in Figure 6.2, and as expected they all lead to roughly the same definition of the jet. We also show the same criteria applied to the MBQ simulation, where no persistent jet forms. Little of the polar region in this simulation would qualify as a jet by our criteria that fluid be magnetically-dominated or unbound.

6.2.3 Model Parameters

These are the required elements to define a radiative model of M87. Unlike in Sgr A*, the inclination of M87 is fairly well constrained from superluminal motion in the jet [94], implying $i \lesssim 30°$. We fix $i = 25°$ in this chapter. The black hole spin is also fixed at $a = 0.92$, since we only consider a single simulation.

A given radiative model of M87 then has the following parameters: T_i/T_e for the disk component, $\dot{M}$ and the jet/disk boundary selection criterion for both components and $\gamma_{min,max}$, p, η for the jet component. We take $\gamma_{max} = 10^5$ throughout, leaving five free parameters. This is many more free parameters than in the models of Sgr A* presented previously. Rather than fitting extensively to data, we pick two fiducial models that give a sense for the range of viable models of M87 and the limitations of modeling with current GRMHD simulations. Sample spectra showing the effects of independently varying the parameters are shown in Figure 6.3. The electron/ion temperature ratio T_i/T_e (bottom right panel) fixes the relative disk contribution. At $T_i/T_e = 10$, the disk emission is negligible at all wavelengths while at $T_i/T_e = 3$, the best fit ratio for this simulation for Sgr A*, the jet portion dominates except in the millimeter, where there's a sub-millimeter bump from thermal disk emission. The normalization and peak frequency are affected by both γ_{min} (for the jet portion, upper left panel) and $\dot{m}$ (bottom left panel). The fraction of magnetic energy converted into non-thermal jet particles, η, changes the normalization of the jet spectrum (top right panel). Finally, p fixes the spectral slope between the millimeter and high frequency IR/optical emission.

6.3 Fiducial Models

To identify viable models, we compute spectra from a single timestep of the MBD simulation data over a grid spanning reasonable values of the various parameters: $T_i/T_e = (3, 5, 10)$, $\dot{m} = (1, 2.2, 4.6, 10, 22, 46, 100) \times 10^{-7}$, $p = (3, 3.25, 3.5, 3.75)$, $\gamma_{min} = (10, 30, 50, 100)$ and $\eta = (0.01, 0.02, 0.05, 0.10)$. The relative accretion rate is defined as $\dot{m} \equiv \dot{M}c^2/L_{edd}$, where L_{edd} is the Eddington luminosity.

The resulting spectra are fit to multi-wavelength observations. We fit to average values

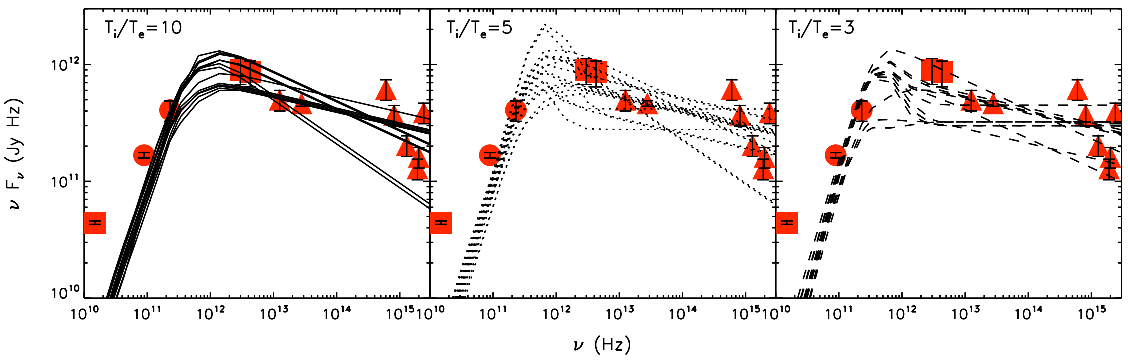

Figure 6.4 Viable spectra with $T_i/T_e = 10$ (left), 5, (middle), 3 (right). The red symbols are the observational data used as either upper limits (squares), data points (circles) or waveband-averaged data points (triangles).

in the optical [188] and near infrared [155, 156] and to the measured values at 3.3mm and 1.3mm [190]. The far infrared measurements are treated as upper limits due to their possible contamination by dust in the host galaxy [156]. The radio data are also treated as upper limits, since as in Sgr A* the limited spatial extent of the physically realistic region of the simulation prevents the modeling of the large-scale emission. The uncertainties are taken as 30% in all cases irrespective of measurement errors, since we are interested in finding qualitatively reasonable spectra rather than to quantitatively constrain parameters as done for Sgr A* in Chapter 5.

There are many reasonable models within our grid of spectra. Many examples are shown in Figure 6.4. The lines are all spectra for which $\chi^2 < 0.5$, split up by ion-electron temperature ratio. The χ^2 values are low because of our artificial inflation of the error bars, and the number of observational constraints is equal to the number of free parameters in our model. For both of these reasons we make no attempt to quantify a goodness of fit for the model spectra.

These jet/disk models are much different from those used previously to model M87 [201, 33]. The jet and disk emission both peak in the millimeter, unlike "truncated" disk models where the disk emission peaks in the radio. The peak frequency of the disk spectrum and its normalization are fixed by T_i/T_e and $\dot{m}$. The electron/ion temperature ratio is

Table 6.1. Fiducial Model Parameters

Model	T_i/T_e	$\dot{m}(10^{-6})$	γ_{min}	p	η
DJ1	3	1	50	3.25	0.05
J2	10	1	50	3.50	0.10

unlikely to exceed unity, while increasing the relative accretion rate both increases the normalization of the spectrum and moves its peak to higher frequencies. Within these constraints, it is not possible to produce the observed radio emission from the GRMHD accretion flow. It could, however, be produced by thermal or nonthermal disk electrons at large radius outside of the simulation volume. Then the truncated disk is most closely related to our model with $T_i/T_e = 10$, where the disk contributes negligibly.

The jet spectrum has the additional degrees of freedom η and γ_{min}, which allow the possibility of a spectral peak in the radio. However, this is seemingly in conflict with 7mm VLBI observations, which find extended jet emission on a milliarcsecond scale [105]. In our jet models and those from Broderick & Loeb (2009), the emission is extended when optically thick to synchrotron self-absorption. Then the existing VLBI observations suggest that the jet spectrum is still rising in the millimeter. Moving the spectral peak of the jet component also requires extreme values of the relevant parameters, with $\dot{M} \gtrsim 10^{-5}$, $\eta \sim 1$ and $\gamma_{min} \sim 1$. For both reasons, we do not pursue these models further.

6.3.1 Viable Parameter Ranges

From the spectra providing the best fit to the chosen data, we select one with $T_i/T_e = 3$ (DJ1) and one with $T_i/T_e = 10$ (J2). This parameter fixes the relative contribution of the disk, which peaks at millimeter wavelengths in a similar fashion to Sgr A*. The parameters of the two fiducial models are listed in Table 6.1, and their spectra are plotted in Figure 6.5, showing the total spectrum as well as split up by jet and disk components.

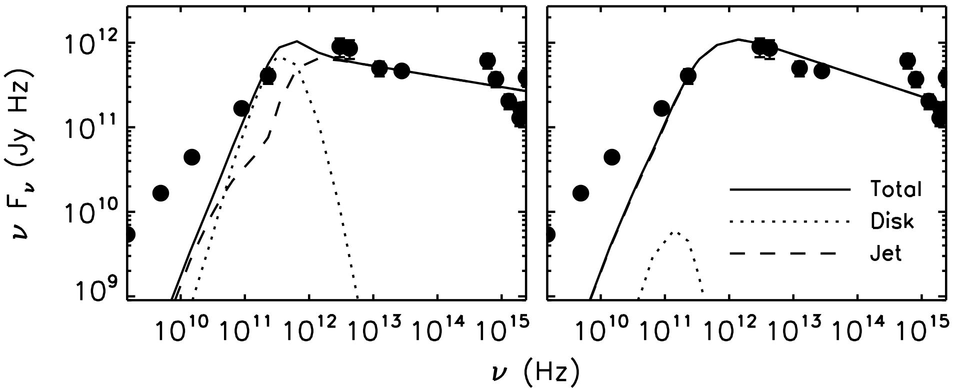

Figure 6.5 Total (solid), disk (dotted) and jet (dashed) spectra from the two fiducial models along with the observational data points. The error bars shown are from the measurements, whereas for the fitting 30% uncertainties were used. In the two models with larger electron temperatures (left panel), the disk emission becomes important at millimeter wavelengths and dominates the emission there. For small electron temperatures (right panel), the entire spectrum is from the jet component.

6.3.2 Jet Only or Jet/Disk

With $T_i/T_e = 10$, the disk emission is negligible at all wavelengths. The jet spectrum peaks in the millimeter, with a long power law tail extending to the IR/optical. Models with larger T_i/T_e are still jet-dominated at low and high frequencies, but the thermal emission leads to a submillimeter bump. This not only leads to significant disk emission at frequencies of interest for mm-VLBI, but the thermal absorption can also attenuate the jet emission from small radius. Thus, the spectrum alone cannot distinguish between jet or disk emission dominating in the millimeter.

6.4 Image Morphology

Images of the fiducial models as well as their separate jet and disk components are shown in Figure 6.6 at 1.3mm and 0.87mm, the two wavelengths of interest for mm-VLBI. As expected, images of M87 dominated by thermal particles in the accretion flow (DJ1) are nearly identical to those of Sgr A*. Doppler beaming is significant even at the low expected inclination of M87, but weaker than for preferred inclinations of Sgr A*. The image is a

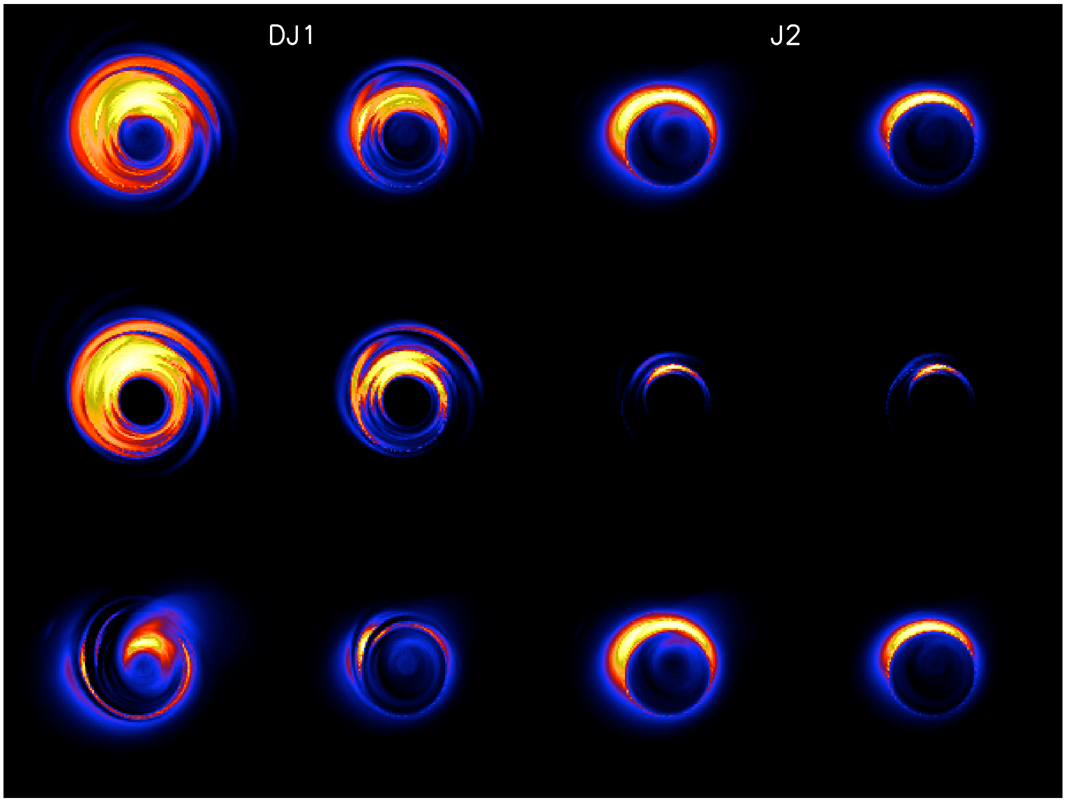

Figure 6.6 Images from total (top row), disk (middle row) and jet (bottom row) components for the two fiducial models (left two columns and right two columns) at 1.3mm (first and third columns) and 0.87mm (second and fourth columns). The colors are scaled linearly from blue to red to yellow to white, with a dynamic range of 60. The images are taken from the same time step used for the spectra in Figure 6.5, and have been rotated 75° to align with the position angle of the larger scale jet at 7mm.

crescent from the combined effects of beaming and gravitational lensing, but with a stronger drop in intensity inside the black hole shadow. The jet emission arises from near the pole offset slightly above the black hole. This allows a significant portion of its emission to appear in the shadow region.

When the disk emission is negligible, the image "size" is smaller due to the smaller size of the jet footprint relative to the thicker accretion disk. The image is still a crescent, although the Doppler beaming is much stronger due to the helical rather than Keplerian motion in the jet. At 1.3mm, the circular photon orbit is still ring-like enough to produce a shadow. At 0.87mm, both images are smaller. The jet component in DJ1 is less significant, and the J2 image is essentially just a single crescent from Doppler beaming of the jet material moving toward the observer.

Unlike in Sgr A*, the orientation angle of the M87 black hole spin axis projected on the plane of the sky can be reasonably assumed to align with the orientation of the 7mm jet structure. This assumes that the jet is launched along the spin axis, and that the jet remains coherent on parsec scales. The images in Figure 6.6 have all been rotated to this favored orientation.

6.4.1 Predictions for mm-VLBI

The first mm-VLBI observations of M87 were conducted recently [74], but the results are not yet available. We therefore make predictions for both current and future telescopes, assuming a geometry (inclination and orientation) based on larger scale jet observations. With sufficient telescopes (baselines), sensitivity and observing time it will be possible to construct observational images in the future. However, for now the small number of available telescopes restricts the observations to the uv-plane and we again Fourier transform the images to visibilities, whose amplitudes are shown along with the total intensity images for both mm-VLBI wavelengths in Figure 6.7. Possible locations of current measurements are shown as the green lines, and the visibility amplitudes are interpolated to those locations and plotted against baseline length in the left panel of Figure 6.8. As with the best fit models of Sgr A*, in both fiducial models the current telescopes are at an orientation where the

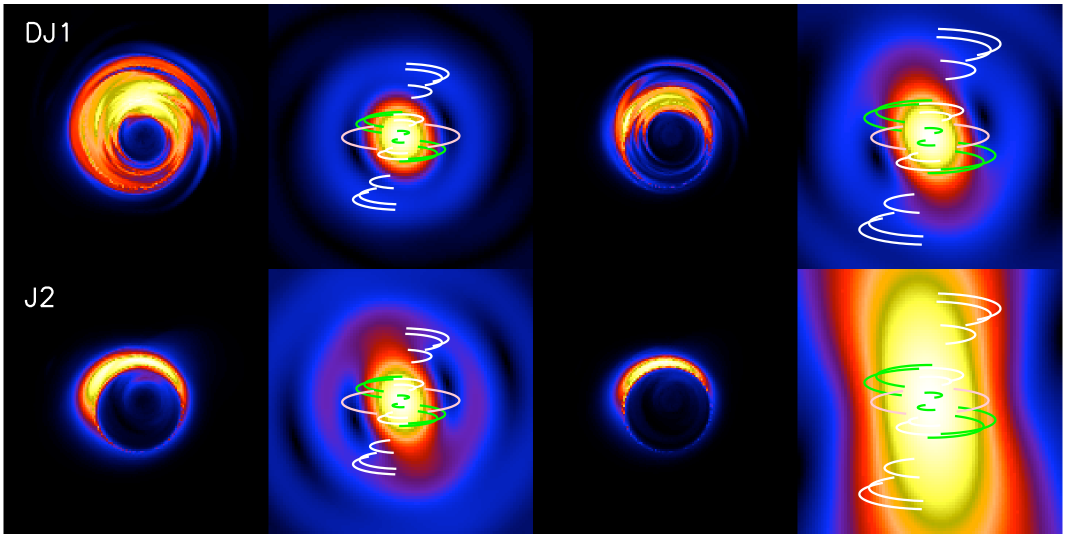

Figure 6.7 Images (first and third columns) and corresponding visibility amplitudes (second and fourth columns) from the two fiducial models (rows) at 1.3mm (first two columns) and 0.87mm (right two columns). The baseline orientations available to current (green) and near future (white and pink) telescopes are overplotted as lines. At this orientation, set by the crescent image morphology and the direction of the 7mm jet, the black hole shadow is accessible to future observations on a Hawaii-Mexico baseline.

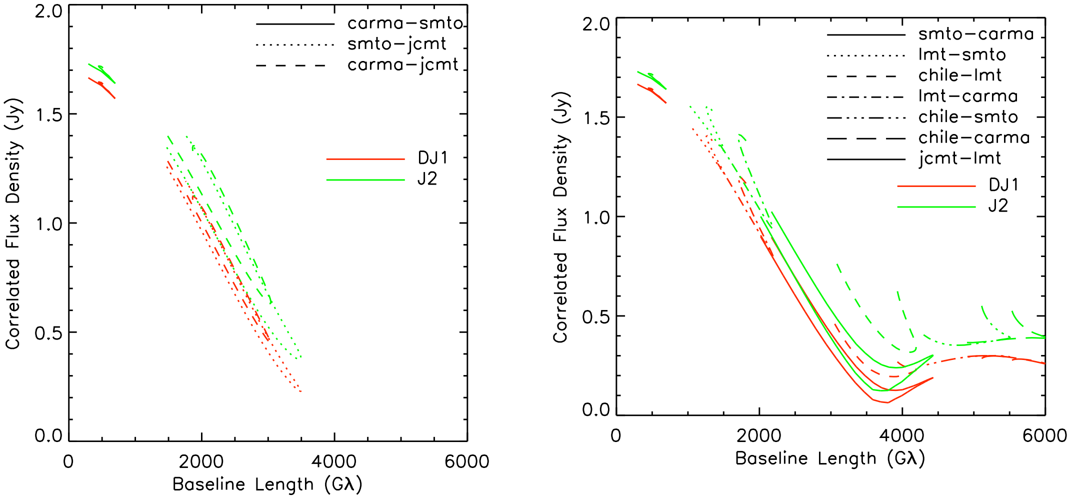

Figure 6.8 Model visibility amplitude vs. baseline length for orientations using current (left) and near future (right) telescopes. The visibility amplitude falls off monotonically with baseline length for current measurements, while the local minimum corresponding to the black hole shadow is accessible to a future baseline between Hawaii and Mexico.

visibility amplitude decreases monotonically with baseline length. We then predict similar results for M87 as those obtained from Sgr A* so far. Fit with a symmetric Gaussian model, the source size is 41 (36) μas for model DJ1 (J2).

The same procedure is applied for telescopes in Chile[1] and Mexico[2] in the right panel of Figure 6.8. In both cases, the black hole shadow is accessible to observations between Mexico and Hawaii[3]. In the jet-dominated model, the shadow also appears on baselines between Chile and Mexico.

6.5 Variability

The M87 models are also time variable. Light curves from the fiducial models are shown in Figure 6.9 at 1.3mm and 0.87mm. The variability is more pronounced in the jet model, while the disk model light curve looks similar to that for the same simulation in the Sgr A* modeling (lower right panel of Figure 5.10). The jet model is more highly variable, particularly at lower frequencies. For this reason, it is more consistent with the finding that M87 varies at about $1\mathrm{Jy}\,\mathrm{yr}^{-1}$ [189]. However, since the variability in the jet model is a result of one event, it is unclear whether this is due to a transient effect in the jet formation/propagation or a recurrent variable activity. The image centroid in the mm is highly stable in both models (Figure 6.10).

6.6 Discussion

In this chapter, we have created the first images, spectra and light curves from jet/disk models of M87 based on GRMHD simulations. The jet/disk boundary is taken as a contour in the ratio of magnetic to rest mass energy or in the particle specific enthalpy as measured at infinity, with similar results in either case. The disk portion is modeled as described in the previous chapters, while the internal energy in the jet region is scaled as a fixed fraction of the magnetic energy density. The models have as many free parameters as spectral

---

[1] Atacama Pathfinder Experiment, APEX; Atacama Submillimeter Telescope Experiment, ASTE; or Atacama Large Millimeter Array, ALMA

[2] Large Millimeter Telescope, LMT

[3] James Clerk Maxwell Telescope, JCMT or Submillimeter Array, SMA

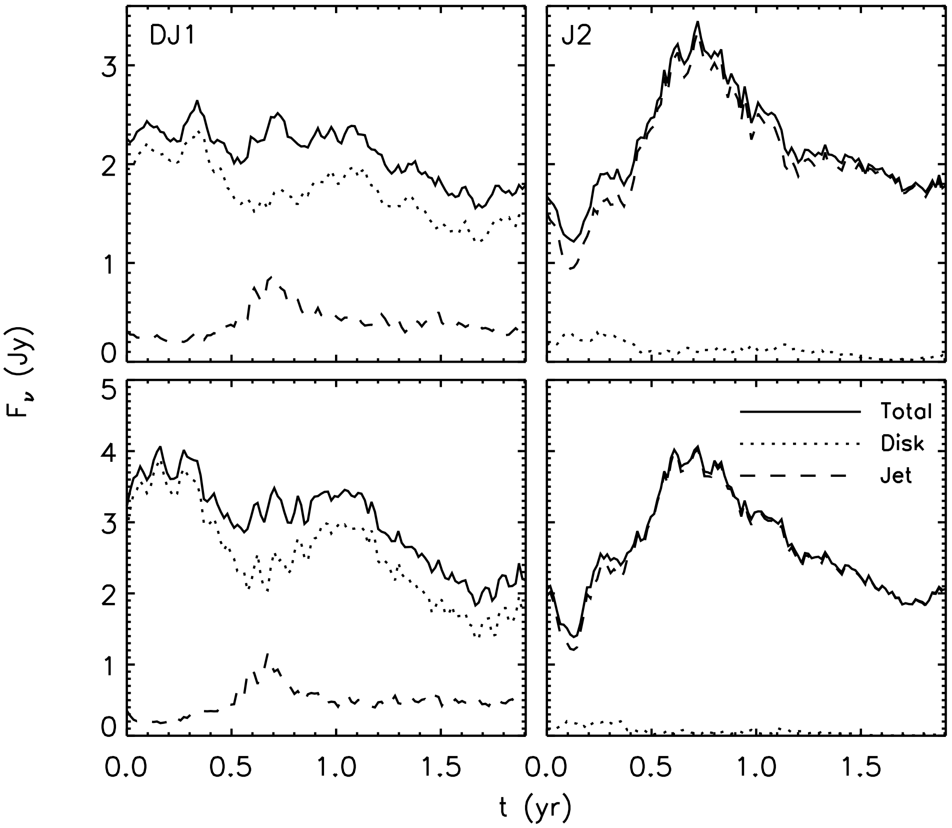

Figure 6.9 Light curves from the two fiducial models (left and right columns) at 1.3mm (top row) and 0.87mm (bottom row).

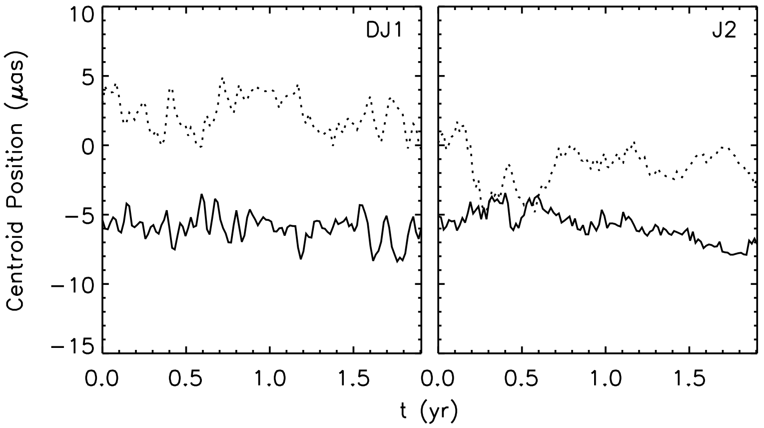

Figure 6.10 x (solid) and y (dotted) centroid position as functions of time. The centroid is remarkably stable in both models.

constraints, so that it is possible to find two separate classes of models. In one class of models, the disk emission is negligible at all frequencies and the jet produces the entire spectrum. In the other, the jet produces the low- and high-frequency emission, while the synchrotron radiation from thermal disk electrons peaks in the millimeter. In this case, mm-VLBI of M87 would be similar to that of Sgr A*.

In general, the favored jet parameter combinations are $\gamma_{min} = 30 - 100$ (although we have not tried higher values which may also work), $p = 3.25 - 3.5$ and $\eta = 0.02 - 0.10$. The favored average accretion rate is $\dot{m} = 1 - 2 \times 10^{-6}$, or $\dot{M} = 1 - 2 \times 10^{-5} M_{\odot}\mathrm{yr}^{-1}$. For the jet portion, the parameters $\dot{m}$, η and γ_{min} are some what degenerate. The spectral slope, p, is fixed by the near IR and optical observations, while the ion-electron temperature ratio T_i/T_e is unconstrained. The favored value for this simulation from Sgr A* models, $T_i/T_e = 3$, leads to a disk-dominated image in the millimeter.

The viewing geometry of M87 is more constrained than in Sgr A*. Assuming that the jet propagates along the black hole spin axis, the orientation angle is constrained to be roughly $75 \pm 30^{\circ}$ measured E of N. The inclination has been estimated to be $\simeq 25^{\circ}$ from the Lorentz factor of the jet [94, 21]. For these parameters, we can make predictions for ongoing mm-VLBI observations. On the current baselines, we predict that M87 should appear as a compact source similar to Sgr A*. The fiducial models have FWHM sizes of 36 and $41\mu as$ when fit with symmetric Gaussian models. The black hole shadow is accessible to future observations on baselines between Mexico and Hawaii and possibly Mexico and Chile. Although the predicted Gaussian sizes for current telescopes are nearly identical for both fiducial models, future observations with additional telescopes or epochs should be able to distinguish between the two. This is because the 2D structure of the images is significantly different and future baselines will probe orientations where the predictions are substantially different. The variability in the jet model is stronger, so that its total flux may also be expected to fluctuate more between observational epochs.

Both images are crescents, as in the case of Sgr A*, with the relative importance of Doppler beaming and gravitational lensing set by the inclination and velocity profile of the material. The sky orientation determines the portions of the image accessible to each VLBI baseline. When this geometry is fixed and the velocities are roughly Keplerian disk motion and helical jet motion, the resulting image is qualitatively independent of the details of the physics in the innermost part of the accretion flow. Thus, our qualitative predictions for event-horizon scale mm-VLBI with current and future telescopes are fairly robust as long as the assumed geometry is reasonably accurate, despite the fact that the fiducial models chosen here are only representative of a wide range of possibilities that could explain the spectral properties of M87.

Nevertheless, there are many uncertainties in this analysis. The assumption that the internal energy in non-thermal particles scales with magnetic field energy density may be reasonable, but it is made out of necessity. Both the internal energy (pressure) and mass density from the simulation are dominated by the artificial numerical floor required when $b^2/\rho c^2 \gg 1$, the region of interest for jet launching. The post-processing technique of adding radiation after the fact is used, despite the fact that M87, while underluminous, is $\sim 4-5$ orders of magnitude closer to Eddington than Sgr A*. Further, it has been found that cooling both via synchrotron radiation and Compton scattering of synchrotron photons is dynamically important in axisymmetric GRMHD simulations of M87 [135]. It will be possible to include those forms of cooling in future simulations, but a method for evolving non-thermal particle density self-consistently is much more difficult. Using the simple prescriptions adopted in this chapter may not have any real effect on the dynamics, since the floor values determine the mass density and internal energy in the jet. If anything, including cooling in this case may make energy conservation in the simulations worse. The simulation used here is the first to produce a large-scale, relativistic jet from an accretion disk. The accretion flow solution is likely underresolved [93], and underestimates the relative magnetic field strength of a simulation with much higher resolution. The convergence properties of this jet solution are not understood, and the resulting magnetic field structure should be compared to similar simulations without an accretion disk [191] and to future simulations with a range of initial magnetic field configurations and torus geometries.

Previous semi-analytic jet/disk models of M87 have invoked a truncated disk, with a low, constant particle density and magnetic field strength throughout the inner disk. This configuration can produce the observed radio emission. We find that the magnetic field strength in the simulation falls off too rapidly with radius to produce the observed flux at small peak field strength, and instead as with Sgr A* the disk emission peaks in the millimeter. Both the disk and jet models used here are unlikely to be valid outside the innermost radii. The disk emission peaks at such a small radius that this is unlikely to significantly affect the results. However, there are so few studies of jets launched from GRMHD simulations that it is unclear what the domain of validity is. For example, the cartoon jet model from Broderick & Loeb (2009) [33], based on MHD simulations of jet propagation in the absence of a disk, exhibits large-scale emission especially at low frequencies that does not show up in our models. For this reason, the models presented here are not valid in the radio and cannot match the extended jet emission seen at 7mm.

Chapter 7

CONCLUSIONS AND FUTURE DIRECTIONS

The goal of this thesis was to connect contemporary three-dimensional, time-dependent simulations of black hole accretion flows based on the magnetorotational instability (MRI) with observations. Low-luminosity objects are most suitable for this comparison, where the radiation is dynamically unimportant and can be added after the fact via radiative transfer calculations. To this end, we have written a public, semi-analytic code to compute photon trajectories in the vicinity of spinning black holes and incorporated it into a framework for time-dependent, general relativistic radiative transfer calculations from dynamical models specified either analytically or numerically in up to three spatial dimensions. We are in the process of generalizing the code to include polarization.

There is no reason to assume alignment between the angular momentum axis of the accretion flow and the black hole spin axis in the low luminosity sources of interest in this thesis. The radiation edge in these misaligned ("tilted") disks, the innermost location where emission is produced, is independent of black hole spin; in stark contrast to the results from standard, untilted simulations where the radiation edge roughly tracks the innermost stable circular orbit (ISCO) of the black hole. These ray tracing results confirm findings based on dynamical measures. We have shown that non-axisymmetric, standing shocks in the tilted disks transport angular momentum outwards, truncating tilted disks outside of the ISCO. Further simulations will be necessary to determine the tilt dependence of the radiation edge. Images and emission line profiles of tilted simulations strongly depend on the observer azimuth. This type of tilted, radiative inefficient flow may be present in the inner portion of low/hard state of black hole binaries. The precession of the tilted disk would then cause significant variability in the line profiles or possibly spectra on long timescales. There is no evidence for high-frequency quasi-periodic oscillations in power spectra of tilted simulations for the simplistic emission models used in this thesis.

The Galactic center black hole, Sagittarius A* (Sgr A*), at millimeter wavelengths provides a uniquely suitable source for modeling with simulations due to its extremely low luminosity and accessibility to very long baseline interferometry (VLBI) with event-horizon scale resolution. Detailed radiative models of the millimeter emission from Sgr A* were constructed from simulations by computing images and light curves over a grid of parameters and fitting them to existing mm-VLBI and spectral data. The models provide excellent fits to existing observations. A clear picture emerges from untilted simulations, where in all cases at relatively high spin ($a = 0.5 - 0.9$), the viable models have moderate inclinations ($i \simeq 60°$), low accretion rates ($\dot{M} \simeq 5 \times 10^{-9} M_{\odot}\mathrm{yr}^{-1}$) and high electron temperatures ($T_e \simeq 6 \times 10^{10}\mathrm{K}$). The emission arises from synchrotron radiation by thermal electrons in the innermost parts of the accretion flow ($r \simeq 5\mathrm{M}$). The range of viable models based on simulations with a tilt angle of 15° is much larger, and the parameters are basically unconstrained. This is both due to the additional free parameter of observer azimuth and the unique properties of low spin, tilted disks which combine attributes of tilted disks and higher spin, untilted ones. It will be interesting to see whether this unique situation remains in simulations that conserve total energy. If so, the limit $a \rightarrow 0$ at finite tilt would be an interesting situation to study in future work, since the accretion flow must transition from this unique solution to the Schwarzschild solution over a small range of black hole spin. Both the tilted and untilted models will be further constrained by future mm-VLBI measurements including telescopes in Mexico (Large Millimeter Telescope; LMT) and Chile (Atacama Large Millimeter Array; ALMA) and by robust measurements of the VLBI closure phase. Thus far, the geometric parameter constraints from radiative models based on GRMHD simulations are nearly identical with those from semi-analytic radiatively inefficient accretion flow solutions [29, 30].

The black hole images are all crescents with significant asymmetry from Doppler beaming and the black hole shadow visible due to the contrast between the front and back of the accretion flow. All GRMHD models predict a significant chance of observing the shadow, direct evidence for a black hole event horizon, on baselines between LMT or ALMA and existing mm-VLBI telescopes (Combined Array for Research in Millimeter-wave Astronomy, CARMA or Sub-Millimeter Telescope Observatory, SMTO). This detection will be difficult, since the shadow appears as a local minimum in the observed visibility amplitude and as a rapid change in the closure phase. It may be seen as two detections bracketing an upper limit in the visibility amplitude, with significantly different closure phases, all occurring over a short period of time ($\sim$ 1hr).

The radiative models constructed here are inherently time-dependent, and the variability of the viable models of Sgr A* all naturally reproduce the observed millimeter flaring behavior with $30-50\%$ amplitude and few hour durations. The variability in the simulations is caused by magnetic turbulence driven by the MRI rather than heating from magnetic reconnection or hotspots orbiting in the disk. These radiative models do not incorporate IR or X-ray emission, since the emission mechanism and geometry at those wavelengths is uncertain. It may be from non-thermal electrons in a disk, corona or jet or from Compton scattering of millimeter photons by hot electrons. A complete radiative model will have to produce the full multiwavelength spectrum of Sgr A*, including the large simultaneous IR/X-ray flares. Time-dependent polarization should also be included, as there are radio/millimeter polarization constraints and future mm-VLBI observations will measure the polarized visibility. The small-scale polarization may be quite high, since the magnetic field in the simulations is toroidal and fairly coherent, and the emission is dominated by fluid approaching the observer.

M87 is the other major target for mm-VLBI observations, and the beginnings of its ultrarelativistic jet may be accessible at extremely high resolution. Radiative models of M87 were constructed in similar fashion to Sgr A*, except that the M87 models necessarily include a non-thermal, jet component from a power law distribution of electrons. The jet/disk boundary can be defined either in terms of magnetically-dominated portions of the simulation or specific enthalpy (bound/unbound particles) with similar results. It is important to use an emissivity that includes the effect of the low Lorentz factor cutoff in computing millimeter emission, as it tends to move the peak of the SED to significantly higher frequencies. The spectrum can either be described by a jet model at all frequencies, or a jet at low- and high-frequencies with a disk dominating the millimeter emission. With reasonable assumptions for the geometry, we predict a Gaussian source size of 36 or 41μas on current mm-VLBI baselines. The black hole shadow is accessible to future baselines between Hawaii (James Clerk Maxwell Telescope, JCMT) and Mexico (LMT) and possibly between Mexico (LMT) and Chile (ALMA). The event-horizon scale images are again crescents in both cases, dominated by the effects of gravitational lensing and Doppler beaming. Predictions for ongoing mm-VLBI are then fairly robust on small scales, despite the large uncertainty in the disk/jet models themselves. The jet and disk/jet models can be distinguished in future mm-VLBI measurements due to the much smaller jet image, dominated by Doppler beaming particularly at 0.87mm. The jet is found to contain larger amplitude variability than the disk, while the disk variability is similar to that in the Sgr A* models. Future polarized VLBI observations may also be able to discriminate between disk and jet origins for the millimeter emission.

BIBLIOGRAPHY

[1] M. Abramowitz and I. A. Stegun. *Handbook of mathematical functions with formulas, graphs, and mathematical tables.* Dover Books on Advanced Mathematics, New York: Dover, 1965.

[2] E. Agol. *The Effects of Magnetic Fields, Absorption, and Relativity on the Polarization of Accretion Disks around Supermassive Black Holes.* PhD thesis, University of California, Santa Barbara, 1997.

[3] E. Agol. Sagittarius A* Polarization: No Advection-dominated Accretion Flow, Low Accretion Rate, and Nonthermal Synchrotron Emission. ApJ, 538:L121–L124, August 2000.

[4] D. K. Aitken, J. Greaves, A. Chrysostomou, T. Jenness, W. Holland, J. H. Hough, D. Pierce-Price, and J. Richer. Detection of Polarized Millimeter and Submillimeter Emission from Sagittarius A*. ApJ, 534:L173–L176, May 2000.

[5] T. An, W. M. Goss, J.-H. Zhao, X. Y. Hong, S. Roy, A. P. Rao, and Z.-Q. Shen. Simultaneous Multiwavelength Observations of Sagittarius A*. ApJ, 634:L49–L52, November 2005.

[6] P. Anninos, P. C. Fragile, and J. D. Salmonson. Cosmos++: Relativistic Magnetohydrodynamics on Unstructured Grids with Local Adaptive Refinement. ApJ, 635:723–740, December 2005.

[7] P. J. Armitage and C. S. Reynolds. The variability of accretion on to Schwarzschild black holes from turbulent magnetized discs. MNRAS, 341:1041–1050, May 2003.

[8] F. K. Baganoff, M. W. Bautz, W. N. Brandt, G. Chartas, E. D. Feigelson, G. P. Garmire, Y. Maeda, M. Morris, G. R. Ricker, L. K. Townsley, and F. Walter. Rapid X-ray flaring from the direction of the supermassive black hole at the Galactic Centre. Nature, 413:45–48, September 2001.

[9] F. K. Baganoff, Y. Maeda, M. Morris, M. W. Bautz, W. N. Brandt, W. Cui, J. P. Doty, E. D. Feigelson, G. P. Garmire, S. H. Pravdo, G. R. Ricker, and L. K. Townsley. Chandra X-Ray Spectroscopic Imaging of Sagittarius A* and the Central Parsec of the Galaxy. ApJ, 591:891–915, July 2003.

[10] S. A. Balbus and J. F. Hawley. A powerful local shear instability in weakly magnetized disks. I - Linear analysis. II - Nonlinear evolution. ApJ, 376:214–233, July 1991.

[11] B. Balick and R. L. Brown. Intense sub-arcsecond structure in the galactic center. ApJ, 194:265–270, December 1974.

[12] J. M. Bardeen. Kerr Metric Black Holes. Nature, 226:64–65, April 1970.

[13] J. M. Bardeen. Timelike and null geodesics in the Kerr metric. In B. S. DeWitt and C. DeWitt, editors, *Black holes (Les astres occlus)*, page 215. New York: Gordon and Breach, 1973.

[14] J. M. Bardeen and J. A. Petterson. The Lense-Thirring Effect and Accretion Disks around Kerr Black Holes. ApJ, 195:L65+, January 1975.

[15] J. M. Bardeen, W. H. Press, and S. A. Teukolsky. Rotating Black Holes: Locally Nonrotating Frames, Energy Extraction, and Scalar Synchrotron Radiation. ApJ, 178:347–370, December 1972.

[16] K. Beckwith and C. Done. Extreme gravitational lensing near rotating black holes. MNRAS, 359:1217–1228, June 2005.

[17] K. Beckwith, J. F. Hawley, and J. H. Krolik. The Influence of Magnetic Field Geometry on the Evolution of Black Hole Accretion Flows: Similar Disks, Drastically Different Jets. ApJ, 678:1180–1199, May 2008.

[18] K. Beckwith, J. F. Hawley, and J. H. Krolik. Where is the radiation edge in magnetized black hole accretion discs? MNRAS, 390:21–38, October 2008.

[19] M. C. Begelman. Evolution of supermassive stars as a pathway to black hole formation. MNRAS, 402:673–681, February 2010.

[20] A. M. Beloborodov. Gravitational Bending of Light Near Compact Objects. ApJ, 566:L85–L88, February 2002.

[21] J. A. Biretta, W. B. Sparks, and F. Macchetto. Hubble Space Telescope Observations of Superluminal Motion in the M87 Jet. ApJ, 520:621–626, August 1999.

[22] O. M. Blaes. Course 3: Physics Fundamentals of Luminous Accretion Disks around Black Holes. In V. Beskin, G. Henri, F. Menard, & et al., editor, *Accretion Discs, Jets and High Energy Phenomena in Astrophysics*, pages 137–185, 2004.

[23] G. R. Blumenthal and R. J. Gould. Bremsstrahlung, Synchrotron Radiation, and Compton Scattering of High-Energy Electrons Traversing Dilute Gases. *Reviews of Modern Physics*, 42:237–271, 1970.

[24] C. T. Bolton. Identification of Cygnus X-1 with HDE 226868. Nature, 235:271–273, February 1972.

[25] H. Bondi. On spherically symmetrical accretion. MNRAS, 112:195–+, 1952.

[26] H. Bondi and F. Hoyle. On the mechanism of accretion by stars. MNRAS, 104:273–+, 1944.

[27] G. C. Bower, W. M. Goss, H. Falcke, D. C. Backer, and Y. Lithwick. The Intrinsic Size of Sagittarius A* from 0.35 to 6 cm. ApJ, 648:L127–L130, September 2006.

[28] A. E. Broderick. Radiative transfer along rays in curved space-times. MNRAS, 366:L10–L12, February 2006.

[29] A. E. Broderick, V. L. Fish, S. S. Doeleman, and A. Loeb. Estimating the Parameters of Sagittarius A*'s Accretion Flow Via Millimeter VLBI. ApJ, 697:45–54, May 2009.

[30] A. E. Broderick, V. L. Fish, S. S. Doeleman, and A. Loeb. Evidence for Low Black Hole Spin and Physically Motivated Accretion Models from Millimeter-VLBI Observations of Sagittarius A*. ApJ, 735:110–+, July 2011.

[31] A. E. Broderick and A. Loeb. Imaging bright-spots in the accretion flow near the black hole horizon of Sgr A*. MNRAS, 363:353–362, October 2005.

[32] A. E. Broderick and A. Loeb. Frequency-dependent Shift in the Image Centroid of the Black Hole at the Galactic Center as a Test of General Relativity. ApJ, 636:L109–L112, January 2006.

[33] A. E. Broderick and A. Loeb. Imaging the Black Hole Silhouette of M87: Implications for Jet Formation and Black Hole Spin. ApJ, 697:1164–1179, June 2009.

[34] A. E. Broderick, A. Loeb, and R. Narayan. The Event Horizon of Sagittarius A*. ApJ, 701:1357–1366, August 2009.

[35] B. C. Bromley, K. Chen, and W. A. Miller. Line Emission from an Accretion Disk around a Rotating Black Hole: Toward a Measurement of Frame Dragging. ApJ, 475:57–+, January 1997.

[36] P. F. Byrd and M. D. Friedman. *Handbook of elliptic integrals for engineers and scientists*. Second edition, Springer, New York, 1971.

[37] B. C. Carlson. A table of elliptic integrals of the third kind. *Mathematics of Computation*, 51(183):267–280, jul 1988.

[38] B. C. Carlson. A table of elliptic integrals: cubic cases. *Math. Comp.*, 53(187):327–333, 1989.

[39] B. C. Carlson. A table of elliptic integrals: one quadratic factor. *Math. Comp.*, 56(193):267–280, 1991.

[40] B. C. Carlson. A table of elliptic integrals: Two quadratic factors. *Mathematics of Computation*, 59(199):165–180, jul 1992.

[41] B. C. Carlson. Jacobian elliptic functions as inverses of an integral. *J. Comput. Appl. Math.*, 174(2):355–359, 2005.

[42] B. Carter. Global Structure of the Kerr Family of Gravitational Fields. *Physical Review*, 174:1559–1571, October 1968.

[43] C.-k. Chan, S. Liu, C. L. Fryer, D. Psaltis, F. Özel, G. Rockefeller, and F. Melia. MHD Simulations of Accretion onto Sgr A*: Quiescent Fluctuations, Outbursts, and Quasiperiodicity. ApJ, 701:521–534, August 2009.

[44] S. Chandrasekhar. The Stability of Non-Dissipative Couette Flow in Hydromagnetics. *Proceedings of the National Academy of Science*, 46:253–257, February 1960.

[45] S. Chandrasekhar. *The mathematical theory of black holes.* Oxford/New York, Clarendon Press/Oxford University Press, 1983.

[46] P. A. Connors and R. F. Stark. Observable gravitational effects on polarised radiation coming from near a black hole. Nature, 269:128–+, September 1977.

[47] P. A. Connors, R. F. Stark, and T. Piran. Polarization features of X-ray radiation emitted near black holes. ApJ, 235:224–244, January 1980.

[48] J. M. Cunningham and C. T. Bardeen. The Optical Appearance of a Star Orbiting an Extreme Kerr Black Hole. ApJ, 183:237–264, July 1973.

[49] S. W. Davis, C. Done, and O. M. Blaes. Testing Accretion Disk Theory in Black Hole X-Ray Binaries. ApJ, 647:525–538, August 2006.

[50] S. W. Davis, R. Narayan, Y. Zhu, D. Barret, S. A. Farrell, O. Godet, M. Servillat, and N. A. Webb. The Cool Accretion Disk in ESO 243-49 HLX-1: Further Evidence of an Intermediate-mass Black Hole. ApJ, 734:111–+, June 2011.

[51] J.-P. De Villiers and J. F. Hawley. A Numerical Method for General Relativistic Magnetohydrodynamics. ApJ, 589:458–480, May 2003.

[52] J.-P. De Villiers, J. F. Hawley, J. H. Krolik, and S. Hirose. Magnetically Driven Accretion in the Kerr Metric. III. Unbound Outflows. ApJ, 620:878–888, February 2005.

[53] J. Dexter and E. Agol. A Fast New Public Code for Computing Photon Orbits in a Kerr Spacetime. ApJ, 696:1616–1629, May 2009.

[54] J. Dexter, E. Agol, and P. C. Fragile. Millimeter Flares and VLBI Visibilities from Relativistic Simulations of Magnetized Accretion Onto the Galactic Center Black Hole. ApJ, 703:L142–L146, October 2009.

[55] J. Dexter, E. Agol, P. C. Fragile, and J. C. McKinney. The Submillimeter Bump in Sgr A* from Relativistic MHD Simulations. ApJ, 717:1092–1104, July 2010.

[56] J. Dexter and P. C. Fragile. Observational Signatures of Tilted Black Hole Accretion Disks from Simulations. ApJ, 730:36–+, March 2011.

[57] K. Dodds-Eden, D. Porquet, G. Trap, E. Quataert, X. Haubois, S. Gillessen, N. Grosso, E. Pantin, H. Falcke, D. Rouan, R. Genzel, G. Hasinger, A. Goldwurm, F. Yusef-Zadeh, Y. Clenet, S. Trippe, P.-O. Lagage, H. Bartko, F. Eisenhauer, T. Ott, T. Paumard, G. Perrin, F. Yuan, T. K. Fritz, and L. Mascetti. Evidence for X-Ray Synchrotron Emission from Simultaneous Mid-Infrared to X-Ray Observations of a Strong Sgr A* Flare. ApJ, 698:676–692, June 2009.

[58] S. S. Doeleman, V. L. Fish, A. E. Broderick, A. Loeb, and A. E. E. Rogers. Detecting Flaring Structures in Sagittarius A* with High-Frequency VLBI. ApJ, 695:59–74, April 2009.

[59] S. S. Doeleman, R. B. Phillips, A. E. E. Rogers, J. M. Attridge, M. Titus, D. Smythe, R. Cappallo, T. Buretta, A. R. Whitney, T. P. Krichbaum, D. A. Graham, W. Alef, A. G. Polatidis, U. Bach, A. Witzel, J. A. Zensus, A. Greve, M. Grewing, R. Freund, P. Strittmatter, L. Ziurys, T. L. Wilson, H. Fagg, and G. Gay. 2mm Wavelength VLBI of SiO Masers and AGN. In E. Ros, R. W. Porcas, A. P. Lobanov, & J. A. Zensus, editor, *Proceedings of the 6th EVN Symposium*, pages 223–+, June 2002.

[60] S. S. Doeleman, Z.-Q. Shen, A. E. E. Rogers, G. C. Bower, M. C. H. Wright, J. H. Zhao, D. C. Backer, J. W. Crowley, R. W. Freund, P. T. P. Ho, K. Y. Lo, and D. P. Woody. Structure of Sagittarius A* at 86 GHZ using VLBI Closure Quantities. AJ, 121:2610–2617, May 2001.

[61] S. S. Doeleman, J. Weintroub, A. E. E. Rogers, R. Plambeck, R. Freund, R. P. J. Tilanus, P. Friberg, L. M. Ziurys, J. M. Moran, B. Corey, K. H. Young, D. L. Smythe, M. Titus, D. P. Marrone, R. J. Cappallo, D. C.-J. Bock, G. C. Bower, R. Chamberlin,

G. R. Davis, T. P. Krichbaum, J. Lamb, H. Maness, A. E. Niell, A. Roy, P. Strittmatter, D. Werthimer, A. R. Whitney, and D. Woody. Event-horizon-scale structure in the supermassive black hole candidate at the Galactic Centre. Nature, 455:78–80, September 2008.

[62] J. C. Dolence, C. F. Gammie, M. Mościbrodzka, and P. K. Leung. grmonty: A Monte Carlo Code for Relativistic Radiative Transport. ApJS, 184:387–397, October 2009.

[63] A. Eckart, R. Schödel, M. García-Marín, G. Witzel, A. Weiss, F. K. Baganoff, M. R. Morris, T. Bertram, M. Dovčiak, W. J. Duschl, V. Karas, S. König, T. P. Krichbaum, M. Krips, D. Kunneriath, R.-S. Lu, S. Markoff, J. Mauerhan, L. Meyer, J. Moultaka, K. Mužić, F. Najarro, J.-U. Pott, K. F. Schuster, L. O. Sjouwerman, C. Straubmeier, C. Thum, S. N. Vogel, H. Wiesemeyer, M. Zamaninasab, and J. A. Zensus. Simultaneous NIR/sub-mm observation of flare emission from Sagittarius A*. A&A, 492:337–344, December 2008.

[64] A. Erdélyi, W. Magnus, F. Oberhettinger, and F.G. Tricomi, editors. *Higher Transcendental Functions*, volume II. Robert E. Krieger Publishing Company, Malabar, U.S.A., 1981.

[65] A. A. Esin, J. E. McClintock, and R. Narayan. Advection-dominated Accretion and the Spectral States of Black Hole X-Ray Binaries: Application to Nova MUSCAE 1991. ApJ, 489:865–+, November 1997.

[66] A. C. Fabian, M. J. Rees, L. Stella, and N. E. White. X-ray fluorescence from the inner disc in Cygnus X-1. MNRAS, 238:729–736, May 1989.

[67] H. Falcke, W. M. Goss, H. Matsuo, P. Teuben, J.-H. Zhao, and R. Zylka. The Simultaneous Spectrum of Sagittarius A * from 20 Centimeters to 1 Millimeter and the Nature of the Millimeter Excess. ApJ, 499:731–+, May 1998.

[68] H. Falcke and S. Markoff. The jet model for Sgr A*: Radio and X-ray spectrum. A&A, 362:113–118, October 2000.

[69] H. Falcke, S. Markoff, and G. C. Bower. Jet-lag in Sagittarius A*: what size and timing measurements tell us about the central black hole in the Milky Way. A&A, 496:77–83, March 2009.

[70] H. Falcke, F. Melia, and E. Agol. Viewing the Shadow of the Black Hole at the Galactic Center. ApJ, 528:L13–L16, January 2000.

[71] X. Fan, V. K. Narayanan, R. H. Lupton, M. A. Strauss, G. R. Knapp, R. H. Becker, R. L. White, L. Pentericci, S. K. Leggett, Z. Haiman, J. E. Gunn, Ž. Ivezić, D. P. Schneider, S. F. Anderson, J. Brinkmann, N. A. Bahcall, A. J. Connolly, I. Csabai,

M. Doi, M. Fukugita, T. Geballe, E. K. Grebel, D. Harbeck, G. Hennessy, D. Q. Lamb, G. Miknaitis, J. A. Munn, R. Nichol, S. Okamura, J. R. Pier, F. Prada, G. T. Richards, A. Szalay, and D. G. York. A Survey of z¿5.8 Quasars in the Sloan Digital Sky Survey. I. Discovery of Three New Quasars and the Spatial Density of Luminous Quasars at z˜6. AJ, 122:2833–2849, December 2001.

[72] C. Fanton, M. Calvani, F. de Felice, and A. Cadez. Detecting Accretion Disks in Active Galactic Nuclei. PASJ, 49:159–169, April 1997.

[73] V. L. Fish, A. E. Broderick, S. S. Doeleman, and A. Loeb. Using Millimeter VLBI to Constrain RIAF Models of Sagittarius A*. ApJ, 692:L14–L18, February 2009.

[74] V. L. Fish, S. S. Doeleman, C. Beaudoin, R. Blundell, D. E. Bolin, G. C. Bower, R. Chamberlin, R. Freund, P. Friberg, M. A. Gurwell, M. Honma, M. Inoue, T. P. Krichbaum, J. Lamb, D. P. Marrone, J. M. Moran, T. Oyama, R. Plambeck, R. Primiani, A. E. E. Rogers, D. L. Smythe, J. SooHoo, P. Strittmatter, R. P. J. Tilanus, M. Titus, J. Weintroub, M. Wright, D. Woody, K. H. Young, and L. M. Ziurys. 1.3 mm Wavelength VLBI of Sagittarius A*: Detection of Time-variable Emission on Event Horizon Scales. ApJ, 727:L36+, February 2011.

[75] V. L. Fish, S. S. Doeleman, A. E. Broderick, A. Loeb, and A. E. E. Rogers. Detecting Changing Polarization Structures in Sagittarius A* with High Frequency VLBI. ApJ, 706:1353–1363, December 2009.

[76] J. A. Font, J. M. Ibáñez, and P. Papadopoulos. Non-axisymmetric relativistic Bondi-Hoyle accretion on to a Kerr black hole. MNRAS, 305:920–936, May 1999.

[77] P. C. Fragile. Effective Inner Radius of Tilted Black Hole Accretion Disks. ApJ, 706:L246–L250, December 2009.

[78] P. C. Fragile and P. Anninos. Hydrodynamic Simulations of Tilted Thick-Disk Accretion onto a Kerr Black Hole. ApJ, 623:347–361, April 2005.

[79] P. C. Fragile and O. M. Blaes. Epicyclic Motions and Standing Shocks in Numerically Simulated Tilted Black Hole Accretion Disks. ApJ, 687:757–766, November 2008.

[80] P. C. Fragile, O. M. Blaes, P. Anninos, and J. D. Salmonson. Global General Relativistic Magnetohydrodynamic Simulation of a Tilted Black Hole Accretion Disk. ApJ, 668:417–429, October 2007.

[81] P. C. Fragile, C. C. Lindner, P. Anninos, and J. D. Salmonson. Application of the Cubed-Sphere Grid to Tilted Black Hole Accretion Disks. ApJ, 691:482–494, January 2009.

[82] P. C. Fragile and D. L. Meier. General Relativistic Magnetohydrodynamic Simulations of the Hard State as a Magnetically Dominated Accretion Flow. ApJ, 693:771–783, March 2009.

[83] P. C. Fragile, W. A. Miller, and E. Vandernoot. Iron-Line Emission as a Probe of Bardeen-Petterson Accretion Disks. ApJ, 635:157–166, December 2005.

[84] S. V. Fuerst and K. Wu. Radiation transfer of emission lines in curved space-time. A&A, 424:733–746, September 2004.

[85] C. F. Gammie, J. C. McKinney, and G. Tóth. HARM: A Numerical Scheme for General Relativistic Magnetohydrodynamics. ApJ, 589:444–457, May 2003.

[86] R. Genzel, R. Schödel, T. Ott, A. Eckart, T. Alexander, F. Lacombe, D. Rouan, and B. Aschenbach. Near-infrared flares from accreting gas around the supermassive black hole at the Galactic Centre. Nature, 425:934–937, October 2003.

[87] A. M. Ghez, S. A. Wright, K. Matthews, D. Thompson, D. Le Mignant, A. Tanner, S. D. Hornstein, M. Morris, E. E. Becklin, and B. T. Soifer. Variable Infrared Emission from the Supermassive Black Hole at the Center of the Milky Way. ApJ, 601:L159–L162, February 2004.

[88] V. L. Ginzburg and S. I. Syrovatskii. Cosmic Magnetobremsstrahlung (synchrotron Radiation). ARA&A, 3:297–+, 1965.

[89] V. L. Ginzburg and S. I. Syrovatskii. Developments in the Theory of Synchrotron Radiation and its Reabsorption. ARA&A, 7:375–+, 1969.

[90] J. E. Goldston, E. Quataert, and I. V. Igumenshchev. Synchrotron Radiation from Radiatively Inefficient Accretion Flow Simulations: Applications to Sagittarius A*. ApJ, 621:785–792, March 2005.

[91] J. B. Hartle. *Gravity : an introduction to Einstein's general relativity.* San Francisco, CA, USA: Addison Wesley, 2003.

[92] S. A. Hartnoll and E. G. Blackman. Reprocessed emission from warped accretion discs with application to X-ray iron line profiles. MNRAS, 317:880–892, October 2000.

[93] J. F. Hawley, X. Guan, and J. H. Krolik. Assessing Quantitative Results in Accretion Simulations: From Local to Global. *ArXiv e-prints*, March 2011.

[94] S. Heinz and M. C. Begelman. Analysis of the Synchrotron Emission from the M87 Jet. ApJ, 490:653–+, December 1997.

[95] K. B. Henisey, O. M. Blaes, P. C. Fragile, and B. T. Ferreira. Excitation of Trapped Waves in Simulations of Tilted Black Hole Accretion Disks with Magnetorotational Turbulence. ApJ, 706:705–711, November 2009.

[96] G. Hilburn, E. Liang, S. Liu, and H. Li. Monte Carlo simulations of the broad-band spectra of Sagittarius A* through the use of general relativistic magnetohydrodynamics. MNRAS, 401:1620–1627, January 2010.

[97] S. Hirose, O. Blaes, and J. H. Krolik. Turbulent Stresses in Local Simulations of Radiation-dominated Accretion Disks, and the Possibility of the Lightman-Eardley Instability. ApJ, 704:781–788, October 2009.

[98] S. Hirose, J. H. Krolik, and O. Blaes. Radiation-Dominated Disks are Thermally Stable. ApJ, 691:16–31, January 2009.

[99] L. Huang, S. Liu, Z.-Q. Shen, Y.-F. Yuan, M. J. Cai, H. Li, and C. L. Fryer. Polarized Emission of Sagittarius A*. ApJ, 703:557–568, September 2009.

[100] A. Ingram, C. Done, and P. C. Fragile. Low-frequency quasi-periodic oscillations spectra and Lense-Thirring precession. MNRAS, 397:L101–L105, July 2009.

[101] P. B. Ivanov and A. F. Illarionov. The oscillatory shape of the stationary twisted disc around a Kerr black hole. MNRAS, 285:394–402, February 1997.

[102] M. Jaroszynski and A. Kurpiewski. Optics near Kerr black holes: spectra of advection dominated accretion flows. A&A, 326:419–426, October 1997.

[103] T. Johannsen and D. Psaltis. Testing the No-hair Theorem with Observations in the Electromagnetic Spectrum. II. Black Hole Images. ApJ, 718:446–454, July 2010.

[104] T. W. Jones and S. L. Odell. Transfer of polarized radiation in self-absorbed synchrotron sources. I. Results for a homogeneous source. ApJ, 214:522–539, June 1977.

[105] W. Junor, J. A. Biretta, and M. Livio. Formation of the radio jet in M87 at 100 Schwarzschild radii from the central black hole. Nature, 401:891–892, October 1999.

[106] T. P. Krichbaum, D. A. Graham, A. Witzel, A. Greve, J. E. Wink, M. Grewing, F. Colomer, P. de Vicente, J. Gomez-Gonzalez, A. Baudry, and J. A. Zensus. VLBI observations of the galactic center source SGR A* at 86 GHz and 215 GHz. A&A, 335:L106–L110, July 1998.

[107] J. H. Krolik. *Active Galactic Nuclei: From the Central Black Hole to the Galactic Environment.* Princeton: Princeton University Press, 1998.

[108] J. H. Krolik and J. F. Hawley. Where Is the Inner Edge of an Accretion Disk around a Black Hole? ApJ, 573:754–763, July 2002.

[109] A. K. Kulkarni, R. F. Penna, R. V. Shcherbakov, J. F. Steiner, R. Narayan, A. Sä Dowski, Y. Zhu, J. E. McClintock, S. W. Davis, and J. C. McKinney. Measuring black hole spin by the continuum-fitting method: effect of deviations from the Novikov-Thorne disc model. MNRAS, pages 620–+, May 2011.

[110] E. Landi Degl'Innocenti and M. Landi Degl'Innocenti. On the solution of the radiative transfer equations for polarized radiation. Sol. Phys., 97:239–250, June 1985.

[111] A. Laor. Line profiles from a disk around a rotating black hole. ApJ, 376:90–94, July 1991.

[112] M. P. C. Legg and K. C. Westfold. Elliptic Polarization of Synchrotron Radiation. ApJ, 154:499–+, November 1968.

[113] J. Li, Z.-Q. Shen, A. Miyazaki, L. Huang, R. J. Sault, M. Miyoshi, M. Tsuboi, and T. Tsutsumi. The Variability of Sagittarius A* at 3 Millimeter. ApJ, 700:417–425, July 2009.

[114] A. P. Lightman and D. M. Eardley. Black Holes in Binary Systems: Instability of Disk Accretion. ApJ, 187:L1+, January 1974.

[115] K. Y. Lo, Z.-Q. Shen, J.-H. Zhao, and P. T. P. Ho. Intrinsic Size of Sagittarius A*: 72 Schwarzschild Radii. ApJ, 508:L61–L64, November 1998.

[116] A. Loeb and F. A. Rasio. Collapse of primordial gas clouds and the formation of quasar black holes. ApJ, 432:52–61, September 1994.

[117] S. H. Lubow, G. I. Ogilvie, and J. E. Pringle. The evolution of a warped disc around a Kerr black hole. MNRAS, 337:706–712, December 2002.

[118] L. B. Lucy. Computing radiative equilibria with Monte Carlo techniques. A&A, 344:282–288, April 1999.

[119] J.-P. Luminet. Image of a spherical black hole with thin accretion disk. A&A, 75:228–235, May 1979.

[120] C. Ly, R. C. Walker, and J. M. Wrobel. An Attempt to Probe the Radio Jet Collimation Regions in NGC 4278, NGC 4374 (M84), and NGC 6166. AJ, 127:119–124, January 2004.

[121] D. Lynden-Bell. Galactic Nuclei as Collapsed Old Quasars. Nature, 223:690–694, August 1969.

[122] R. Mahadevan, R. Narayan, and I. Yi. Harmony in Electrons: Cyclotron and Synchrotron Emission by Thermal Electrons in a Magnetic Field. ApJ, 465:327–+, July 1996.

[123] D. Maitra, S. Markoff, and H. Falcke. A time-dependent jet model for the emission from Sagittarius A*. A&A, 508:L13–L16, December 2009.

[124] D. P. Marrone. *Submillimeter properties of Sagittarius A*: The polarization and spectrum from 230 to 690 GHz and the submillimeter array polarimeter.* PhD thesis, AA(Harvard University), 2006.

[125] D. P. Marrone, F. K. Baganoff, M. R. Morris, J. M. Moran, A. M. Ghez, S. D. Hornstein, C. D. Dowell, D. J. Muñoz, M. W. Bautz, G. R. Ricker, W. N. Brandt, G. P. Garmire, J. R. Lu, K. Matthews, J.-H. Zhao, R. Rao, and G. C. Bower. An X-Ray, Infrared, and Submillimeter Flare of Sagittarius A*. ApJ, 682:373–383, July 2008.

[126] D. P. Marrone, J. M. Moran, J.-H. Zhao, and R. Rao. An Unambiguous Detection of Faraday Rotation in Sagittarius A*. ApJ, 654:L57–L60, January 2007.

[127] J. C. Mauerhan, M. Morris, F. Walter, and F. K. Baganoff. Intraday Variability of Sagittarius A* at 3 Millimeters. ApJ, 623:L25–L28, April 2005.

[128] J. C. McKinney. General relativistic magnetohydrodynamic simulations of the jet formation and large-scale propagation from black hole accretion systems. MNRAS, 368:1561–1582, June 2006.

[129] J. C. McKinney and R. D. Blandford. Stability of relativistic jets from rotating, accreting black holes via fully three-dimensional magnetohydrodynamic simulations. MNRAS, 394:L126–L130, March 2009.

[130] D. L. Meier. Magnetically Dominated Accretion Flows (MDAFS) and Jet Production in the Lowhard State. Ap&SS, 300:55–65, November 2005.

[131] D. B. Melrose. On the Degree of Circular Polarization of Synchrotron Radiation. Ap&SS, 12:172–192, July 1971.

[132] D. B. Melrose. *Plasma astrohysics. Nonthermal processes in diffuse magnetized plasmas - Vol.1: The emission, absorption and transfer of waves in plasmas; Vol.2: Astrophysical applications.* New York: Gordon and Breach, 1980, 1980.

[133] F. C. Michel. Accretion of Matter by Condensed Objects. Ap&SS, 15:153–+, 1972.

[134] C. W. Misner, K. S. Thorne, and J. A. Wheeler. *Gravitation.* San Francisco: W.H. Freeman and Co., 1973.

[135] M. Mościbrodzka, C. F. Gammie, J. C. Dolence, and H. Shiokawa. Pair Production in Low-luminosity Galactic Nuclei. ApJ, 735:9–+, July 2011.

[136] M. Mościbrodzka, C. F. Gammie, J. C. Dolence, H. Shiokawa, and P. K. Leung. Radiative Models of SGR A* from GRMHD Simulations. ApJ, 706:497–507, November 2009.

[137] R. Narayan, M. R. Garcia, and J. E. McClintock. Advection-dominated Accretion and Black Hole Event Horizons. ApJ, 478:L79+, April 1997.

[138] R. Narayan, I. V. Igumenshchev, and M. A. Abramowicz. Self-similar Accretion Flows with Convection. ApJ, 539:798–808, August 2000.

[139] R. Narayan and I. Yi. Advection-dominated accretion: A self-similar solution. ApJ, 428:L13–L16, June 1994.

[140] R. Narayan and I. Yi. Advection-dominated Accretion: Underfed Black Holes and Neutron Stars. ApJ, 452:710–+, October 1995.

[141] R. Narayan, I. Yi, and R. Mahadevan. Explaining the spectrum of Sagittarius A* with a model of an accreting black hole. Nature, 374:623–625, April 1995.

[142] S. C. Noble, C. F. Gammie, J. C. McKinney, and L. Del Zanna. Primitive Variable Solvers for Conservative General Relativistic Magnetohydrodynamics. ApJ, 641:626–637, April 2006.

[143] S. C. Noble and J. H. Krolik. GRMHD Prediction of Coronal Variability in Accreting Black Holes. ApJ, 703:964–975, September 2009.

[144] S. C. Noble, J. H. Krolik, and J. F. Hawley. Direct Calculation of the Radiative Efficiency of an Accretion Disk Around a Black Hole. ApJ, 692:411–421, February 2009.

[145] S. C. Noble, J. H. Krolik, and J. F. Hawley. Dependence of Inner Accretion Disk Stress on Parameters: The Schwarzschild Case. ApJ, 711:959–973, March 2010.

[146] S. C. Noble, J. H. Krolik, J. D. Schnittman, and J. F. Hawley. Radiative efficiency and thermal spectrum of accretion onto Schwarzschild black holes. *ArXiv e-prints*, May 2011.

[147] S. C. Noble, P. K. Leung, C. F. Gammie, and L. G. Book. Simulating the emission and outflows from accretion discs. *Class. and Quant. Gravity*, 24:259–+, June 2007.

[148] I. D. Novikov and K. S. Thorne. Astrophysics of black holes. In B. S. DeWitt and C. DeWitt, editors, *Black holes (Les astres occlus)*, pages 343–450. New York: Gordon and Breach, 1973.

[149] K. Ohsuga, Y. Kato, and S. Mineshige. Spectral Properties of Three-dimensional Magnetohydrodynamic Accretion Flows. ApJ, 627:782–789, July 2005.

[150] J. R. Oppenheimer and H. Snyder. On Continued Gravitational Contraction. *Physical Review*, 56:455–459, September 1939.

[151] A. G. Pacholczyk. *Radio astrophysics. Nonthermal processes in galactic and extragalactic sources.* San Francisco: Freeman, 1970.

[152] D. N. Page and K. S. Thorne. Disk-Accretion onto a Black Hole. Time-Averaged Structure of Accretion Disk. ApJ, 191:499–506, July 1974.

[153] J. C. B. Papaloizou and D. N. C. Lin. 0n the dynamics of warped accretion disks. ApJ, 438:841–851, January 1995.

[154] R. F. Penna, J. C. McKinney, R. Narayan, A. Tchekhovskoy, R. Shafee, and J. E. McClintock. Simulations of magnetized discs around black holes: effects of black hole spin, disc thickness and magnetic field geometry. MNRAS, 408:752–782, October 2010.

[155] E. S. Perlman, J. A. Biretta, W. B. Sparks, F. D. Macchetto, and J. P. Leahy. The Optical-Near-Infrared Spectrum of the M87 Jet fromHubble Space Telescope Observations. ApJ, 551:206–222, April 2001.

[156] E. S. Perlman, R. E. Mason, C. Packham, N. A. Levenson, M. Elitzur, J. J. Schaefer, M. Imanishi, W. B. Sparks, and J. Radomski. The Mid-Infrared Emission of M87. ApJ, 663:808–815, July 2007.

[157] W. H. Press, S. A. Teukolsky, W. T. Vetterling, and B. P. Flannery. *Numerical recipes in FORTRAN. The art of scientific computing.* Cambridge: University Press, 1992.

[158] E. Quataert and A. Gruzinov. Constraining the Accretion Rate onto Sagittarius A* Using Linear Polarization. ApJ, 545:842–846, December 2000.

[159] E. Quataert and A. Gruzinov. Convection-dominated Accretion Flows. ApJ, 539:809–814, August 2000.

[160] K. P. Rauch and R. D. Blandford. Optical caustics in a kerr spacetime and the origin of rapid X-ray variability in active galactic nuclei. ApJ, 421:46–68, January 1994.

[161] M. J. Rees. Black Hole Models for Active Galactic Nuclei. ARA&A, 22:471–506, 1984.

[162] M. J. Reid, A. E. Broderick, A. Loeb, M. Honma, and A. Brunthaler. Limits on the Position Wander of Sgr A*. ApJ, 682:1041–1046, August 2008.

[163] M. J. Reid and A. Brunthaler. The Proper Motion of Sagittarius A*. II. The Mass of Sagittarius A*. ApJ, 616:872–884, December 2004.

[164] R. A. Remillard and J. E. McClintock. X-Ray Properties of Black-Hole Binaries. ARA&A, 44:49–92, September 2006.

[165] R. A. Remillard, E. H. Morgan, J. E. McClintock, C. D. Bailyn, and J. A. Orosz. RXTE Observations of 0.1-300 HZ Quasi-periodic Oscillationsin the Microquasar GRO J1655-40. ApJ, 522:397–412, September 1999.

[166] M. Revnivtsev, M. Gilfanov, and E. Churazov. High frequencies in the power spectrum of Cyg X-1 in the hard and soft spectral states. A&A, 363:1013–1018, November 2000.

[167] A. E. E. Rogers, H. F. Hinteregger, A. R. Whitney, C. C. Counselman, I. I. Shapiro, J. J. Wittels, W. K. Klemperer, W. W. Warnock, T. A. Clark, and L. K. Hutton. The structure of radio sources 3C 273B and 3C 84 deduced from the 'closure' phases and visibility amplitudes observed with three-element interferometers. ApJ, 193:293–301, October 1974.

[168] G. B. Rybicki and A. P. Lightman. *Radiative processes in astrophysics.* New York, Wiley-Interscience, 1979.

[169] V. N. Sazonov. Generation and Transfer of Polarized Synchrotron Radiation. Soviet Ast., 13:396–+, December 1969.

[170] J. D. Schnittman. Radiation Transport Around Kerr Black Holes. *ArXiv Astrophysics e-prints*, astro-ph/0601406, January 2006.

[171] J. D. Schnittman and E. Bertschinger. The Harmonic Structure of High-Frequency Quasi-periodic Oscillations in Accreting Black Holes. ApJ, 606:1098–1111, May 2004.

[172] J. D. Schnittman and J. H. Krolik. X-ray Polarization from Accreting Black Holes: The Thermal State. ApJ, 701:1175–1187, August 2009.

[173] J. D. Schnittman, J. H. Krolik, and J. F. Hawley. Light Curves from an MHD Simulation of a Black Hole Accretion Disk. ApJ, 651:1031–1048, November 2006.

[174] R. Shafee, J. E. McClintock, R. Narayan, S. W. Davis, L.-X. Li, and R. A. Remillard. Estimating the Spin of Stellar-Mass Black Holes by Spectral Fitting of the X-Ray Continuum. ApJ, 636:L113–L116, January 2006.

[175] R. Shafee, J. C. McKinney, R. Narayan, A. Tchekhovskoy, C. F. Gammie, and J. E. McClintock. Three-Dimensional Simulations of Magnetized Thin Accretion Disks around Black Holes: Stress in the Plunging Region. ApJ, 687:L25–L28, November 2008.

[176] N. I. Shakura and R. A. Sunyaev. Black holes in binary systems. Observational appearance. A&A, 24:337–355, 1973.

[177] N. I. Shakura and R. A. Sunyaev. A theory of the instability of disk accretion on to black holes and the variability of binary X-ray sources, galactic nuclei and quasars. MNRAS, 175:613–632, June 1976.

[178] S. L. Shapiro. Accretion onto Black Holes: the Emergent Radiation Spectrum. ApJ, 180:531–546, March 1973.

[179] S. L. Shapiro. Accretion onto Black Holes: the Emergent Radiation Spectrum. II. Magnetic Effects. ApJ, 185:69–82, October 1973.

[180] S. L. Shapiro. Spin, Accretion, and the Cosmological Growth of Supermassive Black Holes. ApJ, 620:59–68, February 2005.

[181] S. L. Shapiro and S. A. Teukolsky. *Black holes, white dwarfs, and neutron stars: The physics of compact objects*. New York, Wiley-Interscience, 663 p., 1983.

[182] P. Sharma, E. Quataert, G. W. Hammett, and J. M. Stone. Electron Heating in Hot Accretion Flows. ApJ, 667:714–723, October 2007.

[183] P. Sharma, E. Quataert, and J. M. Stone. Spherical accretion with anisotropic thermal conduction. MNRAS, 389:1815–1827, October 2008.

[184] R. V. Shcherbakov and F. K. Baganoff. Inflow-Outflow Model with Conduction and Self-consistent Feeding for Sgr A*. ApJ, 716:504–509, June 2010.

[185] R. V. Shcherbakov and L. Huang. General relativistic polarized radiative transfer: building a dynamics-observations interface. MNRAS, 410:1052–1063, January 2011.

[186] R. V. Shcherbakov, R. F. Penna, and J. C. McKinney. Constraining the Accretion Flow in Sgr A* by General Relativistic Dynamical and Polarized Radiative Modeling. *ArXiv e-prints*, July 2010.

[187] Z.-Q. Shen, K. Y. Lo, M.-C. Liang, P. T. P. Ho, and J.-H. Zhao. A size of ˜1AU for the radio source Sgr A* at the centre of the Milky Way. Nature, 438:62–64, November 2005.

[188] W. B. Sparks, J. A. Biretta, and F. Macchetto. The Jet of M87 at Tenth-Arcsecond Resolution: Optical, Ultraviolet, and Radio Observations. ApJ, 473:254–+, December 1996.

[189] H. Steppe, C. J. Salter, R. Chini, E. Kreysa, W. Brunswig, and J. Lobato Perez. Millimeter continuum measurements of extragalactic radio sources. A&AS, 75:317–351, October 1988.

[190] J. C. Tan, H. Beuther, F. Walter, and E. G. Blackman. A Search for Molecular Gas in the Nucleus of M87 and Implications for the Fueling of Supermassive Black Holes. ApJ, 689:775–781, December 2008.

[191] A. Tchekhovskoy, J. C. McKinney, and R. Narayan. Simulations of ultrarelativistic magnetodynamic jets from gamma-ray burst engines. MNRAS, 388:551–572, August 2008.

[192] K. S. Thorne. Disk-Accretion onto a Black Hole. II. Evolution of the Hole. ApJ, 191:507–520, July 1974.

[193] N. J. Turner. On the Vertical Structure of Radiation-dominated Accretion Disks. ApJ, 605:L45–L48, April 2004.

[194] E.P. Velikhov. Stability of an ideally conducting liquid flowing between cylinders rotating in a magnetic field. *Sov. Phys. JETP*, 36:995–998, 1959.

[195] S. U. Viergutz. Image generation in Kerr geometry. I. Analytical investigations on the stationary emitter-observer problem. A&A, 272:355–+, May 1993.

[196] M. Volonteri and M. J. Rees. Rapid Growth of High-Redshift Black Holes. ApJ, 633:624–629, November 2005.

[197] R. C. Walker, C. Ly, W. Junor, and P. J. Hardee. A VLBA movie of the jet launch region in M87. *Journal of Physics Conference Series*, 131(1):012053–+, October 2008.

[198] B. L. Webster and P. Murdin. Cygnus X-1-a Spectroscopic Binary with a Heavy Companion ? Nature, 235:37–38, January 1972.

[199] K. C. Westfold. The Polarization of Synchrotron Radiation. ApJ, 130:241–+, July 1959.

[200] J. Wilms, C. S. Reynolds, M. C. Begelman, J. Reeves, S. Molendi, R. Staubert, and E. Kendziorra. XMM-EPIC observation of MCG-6-30-15: direct evidence for the extraction of energy from a spinning black hole? MNRAS, 328:L27–L31, December 2001.

[201] F. Yuan. Possible evidence for the disc origin for the powering of jets in Sgr A* and nearby elliptical galaxies. MNRAS, 319:1178–1184, December 2000.

[202] F. Yuan, E. Quataert, and R. Narayan. Nonthermal Electrons in Radiatively Inefficient Accretion Flow Models of Sagittarius A*. ApJ, 598:301–312, November 2003.

[203] Y.-F. Yuan, X. Cao, L. Huang, and Z.-Q. Shen. Images of the Radiatively Inefficient Accretion Flow Surrounding a Kerr Black Hole: Application in Sgr A*. ApJ, 699:722–731, July 2009.

[204] F. Yusef-Zadeh, H. Bushouse, M. Wardle, C. Heinke, D. A. Roberts, C. D. Dowell, A. Brunthaler, M. J. Reid, C. L. Martin, D. P. Marrone, D. Porquet, N. Grosso, K. Dodds-Eden, G. C. Bower, H. Wiesemeyer, A. Miyazaki, S. Pal, S. Gillessen, A. Goldwurm, G. Trap, and H. Maness. Simultaneous Multi-Wavelength Observations of Sgr A* During 2007 April 1-11. ApJ, 706:348–375, November 2009.

[205] M. Zamaninasab, A. Eckart, G. Witzel, M. Dovciak, V. Karas, R. Schödel, R. Gießübel, M. Bremer, M. García-Marín, D. Kunneriath, K. Mužić, S. Nishiyama, N. Sabha, C. Straubmeier, and A. Zensus. Near infrared flares of Sagittarius A*. Importance of near infrared polarimetry. A&A, 510(26):A260000+, January 2010.

[206] Y. B. Zeldovich and I. D. Novikov. *Relativistic astrophysics. Vol.1: Stars and relativity.* Chicago: University of Chicago Press, 1971.

[207] J.-H. Zhao, K. H. Young, R. M. Herrnstein, P. T. P. Ho, T. Tsutsumi, K. Y. Lo, W. M. Goss, and G. C. Bower. Variability of Sagittarius A*: Flares at 1 Millimeter. ApJ, 586:L29–L32, March 2003.

Appendix A

`GEOKERR`: FAST AND ACCURATE PHOTON ORBITS IN KERR SPACETIME

A.1 Geodesic Equations of Motion

In Boyer-Lindquist coordinates (t,r,θ,ϕ), the Kerr line element can be written,

$$\begin{aligned} ds^2 &= -\rho^2\frac{\Delta}{\Sigma^2}dt^2 + \frac{\Sigma^2}{\rho^2}\left(d\phi - \frac{2ar}{\Sigma^2}dt\right)^2 \sin^2\theta + \\ &\quad \frac{\rho^2}{\Delta}dr^2 + \rho^2 d\theta^2, \end{aligned} \tag{A.1}$$

with the definitions,

$$\Delta = r^2 - 2r + a^2, \quad \rho^2 = r^2 + a^2\cos^2\theta, \tag{A.2}$$

$$\Sigma^2 = (r^2 + a^2)^2 - a^2\Delta\sin^2\theta, \tag{A.3}$$

where a is the angular momentum of the black hole and in this Appendix we use units with $G = c = M = 1$.

Carter (1968) [42] demonstrated the separability of the Hamilton-Jacobi equation for geodesics,

$$-2\,\frac{\partial S}{\partial\lambda} = g^{\mu\nu}\frac{\partial S}{\partial x^\mu}\frac{\partial S}{\partial x^\nu}, \tag{A.4}$$

where S is Hamilton's principal function (the classical action) and λ is an affine parameter. The separation reduces the equations of motion to quadratures [45] relating the coordinates r and θ:

$$\int^r \frac{dr}{\sqrt{R}} = \int^\theta \frac{d\theta}{\sqrt{\Theta}}, \tag{A.5}$$

where

$$\begin{aligned} R = [(r^2 \quad &+ \quad a^2)E - aL_z]^2 - \\ &\Delta \quad [\mathcal{Q} + (L_z - aE)^2 + \delta_1 r^2] \end{aligned} \tag{A.6}$$

$$\Theta = \mathcal{Q} - \quad [\quad a^2(\delta_1 - E^2) + L_z^2 \csc^2\theta] \cos^2\theta; \tag{A.7}$$

and the constants of the motion are the angular momentum about the black hole spin axis, L_z, the energy, E, and Carter's constant $\mathcal{Q}$. $\delta_1 = 0\,(1)$ for null (timelike) geodesics.

The equations of motion for the cyclic coordinates are

$$t \quad = \quad \lambda E + 2 \int^r r[r^2 E - a(L_z - aE)] \frac{dr}{\Delta\sqrt{R}} \tag{A.8}$$

$$\begin{aligned} \phi \quad = \quad & a \int^r [(r^2 + a^2)E - aL_z] \frac{dr}{\Delta\sqrt{R}} \; + \\ & \int^\theta (L_z \csc^2\theta - aE) \frac{d\theta}{\sqrt{\Theta}}, \end{aligned} \tag{A.9}$$

with

$$\lambda = \int^r \frac{r^2}{\sqrt{R}}\, dr + a^2 \int^\theta \frac{\cos^2\theta}{\sqrt{\Theta}}\, d\theta. \tag{A.10}$$

The signs of the integrals in r and θ are independent and arbitrary, but are fixed for a given geodesic. It may seem odd that these equations lend themselves to the choice of r or θ as independent variable to determine the cyclic coordinates t and ϕ. However, this is the natural outcome of the separation of the Hamilton-Jacobi equation.

A.2 Reduction to Carlson Integrals

In reducing the equations of motion from the previous section, we closely follow the treatment given in Appendix A of Rauch & Blandford (1994) [160]. First change variables to (t, u, μ, ϕ) with $\mu = \cos\theta$, $u = 1/r$. This set is more useful computationally, since the location of an observer at infinity is mapped to $u = 0$. The domain of u is then $0 \le u \le u_+ \le 1$, where u_+ is the location of the event horizon. Similarly, $-1 \le \mu \le 1$. Then the definitions $q^2 \equiv Q/E^2$, $l \equiv L_z/E$, and $\gamma \equiv E/m$ put the equations of motion in dimensionless form. The integral equation relating u and μ is

$$s_\mu \int \frac{d\mu}{\sqrt{M(\mu)}} = s_u \int \frac{du}{\sqrt{U(u)}}; \tag{A.11}$$

where

$$\begin{aligned} M &= q^2 + (\tilde{a}^2 - q^2 - l^2)\mu^2 - \tilde{a}^2\mu^4 & \text{(A.12)} \\ U &= (1 - \gamma^{-2}) + 2\gamma^{-2}u + (\tilde{a}^2 - q^2 - l^2)u^2 + \\ &\qquad 2[(a-l)^2 + q^2]u^3 - a^2q^2u^4, & \text{(A.13)} \end{aligned}$$

and $\tilde{a}^2 = (1 - \gamma^{-2})a^2$. This Appendix only considers null geodesics, so that $\gamma^{-2} = 0$ throughout. The arbitrary signs have been written explicitly, and are chosen to be $s_x = \text{sign}(\dot{x})$, where a dot refers to a derivative with respect to affine parameter. This is done so that both sides of (A.11) are always positive. The equations for the other coordinates become

$$\begin{aligned} t - t_0 &= s_\mu \int a^2\mu^2 \frac{d\mu}{\sqrt{M}} + \\ &\quad s_u \int \frac{2a(a-l)u^3 + a^2u^2 + 1}{u^2(u/u_+ - 1)(u/u_- - 1)} \frac{du}{\sqrt{U}} & \text{(A.14)} \\ \phi - \phi_0 &= s_\mu \int \frac{l\mu^2}{1 - \mu^2} \frac{d\mu}{\sqrt{M}} + \\ &\quad s_u \int \frac{2(a-l)u + l}{(u/u_+ - 1)(u/u_- - 1)} \frac{du}{\sqrt{U}}, & \text{(A.15)} \end{aligned}$$

where $u_\pm = [1 \pm \sqrt{1 - a^2}]^{-1}$. The limits of integration have been omitted due to complications in accounting for turning points. This is discussed in more detail below.

Given initial and final values of u and μ, we can compute t and ϕ. Since the μ integral is easier to invert and this method is of more general utility, u is taken as the independent variable and the goal is to solve for μ_f given μ_0, u_0 and u_f. In certain applications it is more convenient to choose μ as the independent variable. For example, in the case of thin disk accretion we know the inclination angle as well as the value of μ where the geodesic intersects the disk. Section A.3 gives solutions for u_f given μ_0, μ_f and u_0 to handle these cases.

Table A.1. Reduction of I_u

	Case	Parameter Range	Arguments (a_i, b_i);(f_j, g_j, h_j)	$u \, \epsilon \, [,]$	RB94
1	Cubic (3 real)	$a = 0, q^2 + l^2 \geq 27$ or $u \leq u_2$ $a \neq 0, q^2 = 0, \lvert l \rvert \neq \lvert a,$	$(-u_1, 1)$, $(u_2, -1)$, $(u_3, -1)$	$[0, u_2]$[b]	1,3,8,10
2	Cubic (3 real)	$a = 0, q^2 + l^2 \geq 27$ or $u \geq u_3$ $a \neq 0, q^2 = 0, \lvert l \rvert \neq \lvert a,$	$(-u_1, 1)$, $(-u_2, 1)$, $(-u_3, 1)$	$[u_3, u_+)$[c]	2,4,9,11
3	Cubic (1 real)	$a = 0, q^2 + l^2 < 27$ or $a \neq 0, q^2 = 0, l \neq a$	$(-u_1, 1)$;$(2u_1[(a-l)^2 + q^2]^{-1}, f/u_1, 1)$	$[0, u_+)$	5,7,12
4	No roots	$q^2 = 0, l = a$	...	$[0, u_+)$	6
5	Quartic (2 real)	$a \neq 0$, $q^2 > 0$	$(-u_1, 1)$,$q_s(u_4, -1)$;[d]$([-a^2 q^2 u_1 u_4]^{-1}, [u_1^{-1} + u_4^{-1}]f, 1)$	$[0, u_+)$	13,19
6	Quartic (0 real)	$a \neq 0$, $q^2 < 0$	$\left(e^{-1/2}, \frac{d}{e(h_2 - h_1)}, h_1\right.$[a]$\left.\right)$, $(e^{-1/2}, -g_1, h_1^{-1})$	$[0, u_+)$	14
7	Quartic (4 real)	$a \neq 0$, $q^2 \neq 0$, $u \leq u_2$	$(-u_1, 1)$, $(u_2, -1)$, $(u_3, -1)$,$(u_4, -1)$	$[0, u_2]$[b]	15,17
8	Quartic (4 real)	$a \neq 0$, $q^2 \neq 0$, $u \geq u_3$	$(-u_1, 1)$, $(-u_2, 1)$, $(-u_3, 1)$,$(u_4, -1)$	$[u_3, u_+)$[c]	16,18

[a] h_1 is found from solving Eq. (A.21) and selecting one of the two real roots. d, e are defined in Eq. (A.22).

[b] When $u_2 = u_3$, the domain of u is $[0, u_2)$.

[c] When $u_2 = u_3$, the domain of u is (u_3, u_+).

[d] $q_s = sign(q^2)$.

A.2.1 Reduction of I_u

Call the left-hand side (LHS) and right-hand side (RHS) of (A.11) I_μ and I_u respectively, and start with the reduction of I_u:

$$I_u = s_u \int \frac{du}{\sqrt{U(u)}}. \tag{A.16}$$

Except in the special case with $a = l, q^2 = 0$, $U(u)$ is either a quartic or cubic and its roots are denoted u_i with $i = 1 - 3, 4$, and ordered increasingly. If real, $u_1 < 0$ and in the quartic case, $u_4 > 1$ or $u_4 < 0$. They are of no physical significance. When all roots are real, the allowed regions for the integrand are $u > u_3$ and $u < u_2$ so that U is positive. Thus the roots are the turning points for null geodesics starting outside u_2 and inside u_3 respectively in both the cubic and quartic cases. There can be no more than one turning point, since the allowed region is bounded on one side either by infinity or the event horizon. When one or both pairs of roots are complex, there is no turning point in u.

Upon encountering a turning point, the sign of u is reversed, so that the total integral is the sum of the integral from u_0 to the turning point and that from u_f to the turning point. The idea is to ensure that the integrals in u and μ monotonically increase along a geodesic. In a sense this allows the independent variable to take the place of the affine parameter, which cannot be used since it is a function of u and μ.

Carlson (1988, 1989) [37, 38] contain formulas for evaluation of integrals of the form,

$$[p] = \int_y^x \prod_{i=1}^{5} (a_i + b_i t)^{p_i/2} dt; \tag{A.17}$$

with all quantities real, $x > y$, and $a_i + b_i t > 0$ for $y < t < x$. The form of a given integral is described by the vector $[p]$, which contains the powers, p_i, of the factored roots. Cases with one or two pairs of complex roots are handled in Carlson (1991, 1992) [39, 40], where they are written in terms of real quantities as

$$[p] = \int_y^x (f + gt + ht^2)^{p_2/2} \prod_{i=1,4,5} (a_i + b_i t)^{p_i/2} dt \tag{A.18}$$

for one pair of complex roots or

$$[p] = \int_y^x \prod_{i=1}^{2} (f_i + g_i t + h_i t^2)^{p_i/2} (a_5 + b_5 t)^{p_5/2} dt \tag{A.19}$$

for two. In using this form, it is assumed that each power p_i of an irreducible quadratic is written twice in the vector $[p]$. In other words, when one pair of roots is complex, $p_2 = p_3$. When all roots are complex, $p_2 = p_3$ and $p_1 = p_4$.

To ensure that $x > y$ in cases where a turning point may be present, integrals are written in pieces involving the relevant turning point, u_*, and the number of turning points along the portion of the geodesic being followed, N_u (either 0 or 1):

$$I_u = s_u \left(\int_{u_0}^{u_*} \frac{du}{\sqrt{U}} - (-1)^{N_u} \int_{u_f}^{u_*} \frac{du}{\sqrt{U}} \right). \tag{A.20}$$

The Carlson papers reduce all elliptic forms to a set of four fundamental integrals, known as the R-functions [157], which replace Legendre's integrals of the first, second and third kind. They are all integrals from 0 to ∞ and hence don't require a limit of integration to be a turning point, greatly simplifying complex root cases where no physical turning point is present. This is one of many advantages of Carlson's approach. As is the case for Legendre's formulation, any elliptic integral can be reduced to a sum of Carlson's R-functions. Where Legendre integrals are used in this Appendix, they are calculated in terms of the R-functions using the formulas in Press et al. (1992) [157]. The integrals encountered here are always of the form $p = [-1, -1, -1, -1, p_5]$ for quartic cases and $p = [-1, -1, -1, p_5]$ for cubic cases. Thus the form of coordinate integrals in the following will be specified by p_5 alone.

To maintain as much generality as possible, all integrals are written as above in terms of their roots. In cubic cases the roots are found from solving the cubic equation, while for quartic cases they are found numerically using the routine `zroots.f` from Press et al. (1992). Finally, instead of writing out the explicit formulas from Carlson's papers and going through the algebra separately in each case, we have written routines for each case. This is much simpler and of more general utility, since numerous integrals must be done to calculate the coordinates of a point along a geodesic.

The integral I_u has $p_5 = 0$ and is given by Carlson (1989) [38] Eq. (2.12) for real roots for cubic cases. Quartic cases are found in Carlson (1988) [37] Eq. (2.13) for real roots and Carlson (1992) [40] Eq. (2.36) for all complex roots. The quartic and cubic cases with a single pair of complex roots are given by Carlson (1989) [38] Eq. (3.8). The necessary arguments to the Carlson routines are listed by case in Table A.1, along with case definitions, appropriate domains of u, and the corresponding cases in Appendix A of Rauch & Blandford (1994) [160].

As can be seen from Table A.1, writing formulas in terms of the roots of U has the advantage of unifying many disparate cases from previous work. Equal roots cases, which describe orbits approaching the unstable circular photon orbits, cannot strictly speaking be treated identically to other real roots cases as shown in the table. Here, integration to the turning point diverges. The code flags for these cases and integrates them directly from u_0 to u_f, and the arguments listed in the table are still valid. In practice, however, except for the well known Schwarzschild unstable circular orbits with $q^2 + l^2 = 27$, equal roots cases are almost impossible to trigger. This is because the Carlson routines as written maintain accuracy until $|u_2 - u_3| \lesssim 10^{-12}$, which is usually more precise than the determination of the imaginary parts of the roots.

For one pair of complex roots, the arguments f, g and h are found by setting $U(u) = q_s(u_4 - u)(u - u_1)(f + gu + hu^2)$, where $q_s = \mathrm{sign}(q^2)$, and matching powers of u. When all roots are complex, setting $U(u) = (f_1 + g_1 u + h_1 u^2)(f_2 + g_2 u + h_2 u^2)$ yields five non-linear equations for our six unknown coefficients. The degree of freedom is used to simplify the equations, and a sixth degree polynomial is solved numerically for h_1:

$$h_1^6 - \frac{c}{\sqrt{e}} h_1^5 - h_1^4 + \sqrt{e}\left[2\frac{c}{e} - \left(\frac{d}{e}\right)^2\right] h_1^3 - h_1^2 - \frac{c}{\sqrt{e}} h_1 + 1 = 0, \tag{A.21}$$

where

$$c = a^2 - l^2 - q^2, \;\; d = 2[(a - l)^2 + q^2], \;\; e = -a^2 q^2. \tag{A.22}$$

The only pair of real solutions to this equation correspond to the values of h_1, h_2.

As a full example of one of these reductions, consider case 5 from Table A.1 with $u_0 < u_f$ ($s_u = 1$). This is the Kerr case with no physical turning points. From A.18, we see that $b_1 = 1$, $b_4 = -q_s$, $a_1 = -u_1$, $a_4 = q_s u_4$, $x = u_f$, $y = u_0$. The sign q_s is used to keep each factor positive. Matching the powers of $U(u)$ as described above gives $f = -q_s/(u_1 u_4 e)$, $g = (u_4 + u_1)/(u_1 u_4) f$, $h = 1$. Following Carlson (1991) [39], we define

$$\begin{aligned}
X_i &= \sqrt{a_i + b_i x}, \;\; Y_i = \sqrt{a_i + b_i y}, && \text{(A.23)}\\
\xi &= \sqrt{f + gx + hx^2}, \;\; \eta = \sqrt{f + gy + hy^2}, && \text{(A.24)}\\
c_{ij} &= \sqrt{2 f b_i b_j - g(a_i b_j + a_j b_i) + 2 h a_i a_j}, && \text{(A.25)}\\
M &= \frac{(X_1 Y_4 + Y_1 X_4)}{x - y}\sqrt{(\xi + \eta)^2 - h(x-y)^2}, && \text{(A.26)}\\
L_{\pm}^2 &= M^2 + c_{14}^2 \pm c_{11} c_{44}. && \text{(A.27)}
\end{aligned}$$

Then,

$$I_u = \frac{4}{\sqrt{|e|}} R_F(M^2, L_-^2, L_+^2). \tag{A.28}$$

R_F is computed using the routine from Press et al. (1992). Equations for Carlson elliptic integrals with $p_5 \neq 0$ can similarly be found in the Carlson papers listed above.

A.2.2 Inversion of I_μ

Next, the I_μ integral needs to be inverted to solve for μ_f. As with $U(u)$, the roots of the biquadratic $M(\mu)$, $M_\pm$, determine the physical turning points in μ. When $M_- > 0$, there are four real roots and the orbit cannot cross the equatorial plane. The physical turning points correspond to the two roots with the same sign as μ_0 and are denoted $\mu_\pm = \mathrm{sign}(\mu_0)\sqrt{M_\pm}$. When $M_- < 0$, the physical turning points are $\mu_\pm = \pm\sqrt{M_+}$ and are symmetric about the equatorial plane. We can calculate the number of times the geodesic has crossed a μ turning point from the magnitude of the I_u integral. This is done by noting that the maximum value of $\int_{\mu_f}^{\mu_+}$ is $\int_{\mu_-}^{\mu_+}$ and its minimum value is zero. In this derivation the integrand $d\mu/\sqrt{M}$, common to all integrals, is omitted. Then, for $s_\mu = 1$,

$$\int_{\mu_0}^{\mu_+} + (N-1)\int_{\mu_-}^{\mu_+} \leq I_u \leq \int_{\mu_0}^{\mu_+} + N\int_{\mu_-}^{\mu_+}, \tag{A.29}$$

where N is the number of turning points reached in μ, and $\mu_\pm$ are the upper and lower turning points in μ. The integrals are written in these pieces so that they are always positive, as required for use with Carlson's integrals. This condition can be written more concisely as

$$N = \left\lceil \frac{I_u - \int_{\mu_0}^{\mu_+}}{\int_{\mu_-}^{\mu_+}} \right\rceil, \tag{A.30}$$

where $\lceil\ \rceil$ is the ceiling function. If $s_\mu = -1$, then the first turning point reached is μ_-. The condition can then be written

$$-\left[\int_{\mu_0}^{\mu_-} + (N-1)\int_{\mu_+}^{\mu_-}\right] \le I_u \le -\left[\int_{\mu_0}^{\mu_-} + N\int_{\mu_+}^{\mu_-}\right]. \tag{A.31}$$

Using $\int_{\mu_0}^{\mu_-} = \int_{\mu_0}^{\mu_+} - \int_{\mu_-}^{\mu_+}$, we can rewrite this in terms of the same integrals used above:

$$-\int_{\mu_0}^{\mu_+} + N\int_{\mu_-}^{\mu_+} \le I_u \le -\int_{\mu_0}^{\mu_+} + (N+1)\int_{\mu_+}^{\mu_-}. \tag{A.32}$$

Finally,

$$N = \left\lfloor \frac{I_u + \int_{\mu_0}^{\mu_+}}{\int_{\mu_-}^{\mu_+}} \right\rfloor, \tag{A.33}$$

and $\lfloor\ \rfloor$ is the floor function. To write out the general solution for $I_u = I_\mu$ for arbitrary number of turning points and s_μ, we include coefficients for the various pieces of the I_μ integral:

$$I_u = \alpha_1 \int_{\mu_0}^{\mu_+} + \alpha_2 \int_{\mu_-}^{\mu_f} + \alpha_3 \int_{\mu_-}^{\mu_+}. \tag{A.34}$$

The coefficients are functions of s_μ and N determined by writing down specific cases. For example, α_1 reflects whether the integration is positive or negative from μ_0 to μ_f and is easily seen to be $\alpha_1 = s_\mu$. Similarly, α_2 reflects whether the last turning point reached is μ_- or μ_+. Thus the coefficient is $\alpha_2 = s_\mu(-1)^N$. The third coefficient is slightly more complicated and turns out to be

$$\alpha_3 = 2\left\lfloor \frac{2N + 3 - s_\mu}{4} \right\rfloor - 1. \tag{A.35}$$

Armed with the number of turning points and the coefficients, we solve for μ_f by inverting the second integral on the RHS of (A.34):

$$\int_{\mu_-}^{\mu_f} \frac{d\mu}{\sqrt{M}} = \frac{1}{\alpha_2}\left(I_u - \alpha_1 \int_{\mu_0}^{\mu_+} - \alpha_3 \int_{\mu_-}^{\mu_+}\right). \tag{A.36}$$

Calling the RHS I and writing out the square root on the LHS for the general case ($a \neq 0$, $q^2 \neq 0$) gives

$$I = \frac{1}{|a|}\int_{\mu_-}^{\mu_f} \frac{d\mu}{\sqrt{(M_+ - \mu^2)(\mu^2 - M_-)}}. \tag{A.37}$$

Carlson (2005) [41] contains a table for inverting integrals of the form

$$I = \int_y^x \frac{dt}{\sqrt{(a_1 + b_1 t^2)(a_2 + b_2 t^2)}}, \tag{A.38}$$

where all quantities are real, $x > y$, $0 \leq y < x$ and either $y = 0$, $x = \infty$ or one limit is a root of the integrand. The latter case applies here.

$M_- > 0$

When $M_- > 0$, all requirements are met as written, and

$$\mu_f = \mu_- nd\,(J, k), \quad J = \mu_+ |a| I, \quad k^2 = 1 - \frac{\mu_-^2}{\mu_+^2}, \tag{A.39}$$

where $nd\,(J,k) = 1/dn(J,k)$ and dn is a Jacobi-Elliptic function. The μ integral terms in I are calculated as

$$\int_{\mu_0}^{\mu_f} \frac{d\mu}{\sqrt{M(\mu)}} = \frac{1}{A}F(x,k) \tag{A.40}$$

where $F(x,k)$ is Legendre's integral of the first kind [1], $x = \sqrt{\frac{M_+ - \mu_0^2}{M_+ - M_-}}$, $A = |a|\mu_+$ and k is the same as above. The integral between turning points is the complete elliptic integral $K(k)$.

$M_- < 0$

When $M_- < 0$, $y < 0$ in (A.38) so that (A.39) is no longer valid. Since the integrand is an even function of μ, we can write

$$I = \frac{1}{|a|}\int_{-\mu_f}^{\mu_+}\frac{d\mu}{\sqrt{(\mu_+^2-\mu^2)(\mu^2-M_-)}}, \tag{A.41}$$

which is in the correct form, except that $-\mu_f$ can be negative. This causes no problems. In this case,

$$\mu_f = \mu_- cn(J,k), \quad J = \sqrt{\mu_+^2 - M_-}|a|I, \quad k^2 = \frac{\mu_+^2}{\mu_+^2 - M_-}, \tag{A.42}$$

and we've used $\mu_- = -\mu_+$ for $M_- < 0$. The μ terms in I are computed the same as in (A.40), with k defined in (A.39), $x = \sqrt{1-\frac{\mu_0^2}{\mu_+^2}}$ and $A = |a|\sqrt{M_+ - M_-}$. The integral between the turning points here is twice the complete elliptic integral $K(k)$.

$q^2 = 0$

A special case is encountered when $q^2 = 0$. $M(\mu)$ has a double root at $\mu = 0$, causing I_μ to diverge there, and preventing these orbits from reaching the equatorial plane. Hence, they have at most one physical turning point. In this case I_μ is elementary, and the solution for μ_f is

$$\mu_f = \mu_+ \operatorname{sech}\left[|a\mu_+|I_u - s_\mu s_1 \operatorname{sech}^{-1}(\mu_0/\mu_+)\right], \tag{A.43}$$

where $s_1 = \operatorname{sign}(\mu_0)$.

a = 0

Finally, when $a = 0$ (the Schwarzschild case) the μ_f integral is again elementary. The solution for μ_f is then,

$$\mu_f = \mu_- \cos\left[\frac{1}{\alpha_2}\left(\sqrt{\frac{d}{2}}I_u - \alpha_1\cos^{-1}\left(\frac{\mu_0}{\mu_+}\right) - \alpha_3\,\pi\right)\right]. \tag{A.44}$$

A.2.3 t and ϕ coordinate integrals

Given the solution for μ_f, equations for the coordinates t and ϕ can be reduced to elliptic integrals as well. Each coordinate is expressed as a sum of integrals over u and μ. As is done above, the u terms are reduced to Carlson's formulation, and the μ terms to Legendre's.

The μ integral term in (A.14), which we'll denote T_μ, can be written as a single Legendre integral of the 2nd kind. For example, the μ_0 term in the $M_- < 0$ case is reduced as follows:

$$\begin{aligned} T_\mu &= |a| \int_{\mu_0}^{\mu_+} \frac{\mu^2 d\mu}{\sqrt{(\mu_+^2 - \mu^2)(\mu^2 - M_-)}} \\ &= |a|\mu_+ \int_0^x dt \frac{1 - t^2}{\sqrt{(1 - t^2)(1 - t^2 - \frac{M_-}{\mu_+^2})}} \\ &= A \int_0^x dt \frac{1 - t^2 - \frac{M_-}{\mu_+^2}}{\sqrt{(1 - t^2)(1 - t^2 - \frac{M_-}{\mu_+^2})}} + a^2 M_- I_u \\ &= AE(x,k) + a^2 M_- I_u, \end{aligned} \tag{A.45}$$

where $E(x,k)$ is the Legendre integral of the second kind with arguments x and k defined in the previous section. The substitution $t = \sqrt{1 - \mu_0/\mu_+}$ is made between lines one and two, and M_-/μ_+^2 is added and subtracted from the numerator between lines two and three. In the $M_- > 0$ case, T_μ is given by the first term of the above formula, with the arguments A, k, x for that case given with the solution for μ_f in Subsection A.2.2.

The μ term in the ϕ component formula (A.15) can be reduced to a Legendre integral of the 3rd kind in analogous fashion. For the $M_- < 0$ case we proceed as follows:

$$\begin{aligned} \Phi_\mu &= -lI_u + \frac{l}{|a|} \int_{\mu_0}^{\mu_+} \frac{1}{1 - \mu^2} \frac{d\mu}{\sqrt{({\mu_+}^2 - \mu^2)(\mu^2 - M_-)}} \\ &= -lI_u + \\ & \quad \frac{l}{|a|\mu_+} \int_0^x \frac{1}{1 - \mu_+^2 + {\mu_+}^2 t^2} \frac{dt}{\sqrt{(1 - t^2)((1 - \frac{M_-}{\mu_+^2}) - t^2)}} \\ &= -lI_u + \frac{l}{A(1 - M_+)} \Pi(n; x, k) \end{aligned} \tag{A.46}$$

where $\Pi(n;x,k)$ is the Legendre integral of the 3rd kind and $n = \frac{\mu_+^2}{1-\mu_+^2}$. The formula for the $M_- > 0$ case is the same, with $n = \frac{M_+ - M_-}{1 - M_+}$ and the other arguments defined in Subsection A.2.2 above. Note that we are using the sign convention for n from [157], which is opposite that in Abramowitz & Stegen [1].

T_u, the u integral term in (A.14), is expanded with partial fractions, and after a little algebra is written

$$\begin{aligned} T_u \quad = \quad & s_u u_r \Bigg[\left(2a(a-l) + \frac{a^2}{u_+} + \frac{1}{u_+^3} \right) \int \frac{1}{(u/u_+ - 1)} \frac{du}{\sqrt{U}} \\ & - \left(2a(a-l) + \frac{a^2}{u_-} + \frac{1}{u_-^3} \right) \int \frac{1}{(u/u_- - 1)} \frac{du}{\sqrt{U}} \\ & + \left(\frac{1}{u_-^2} - \frac{1}{u_+^2} \right) \int \frac{du}{u\sqrt{U}} + \frac{1}{u_r} \int \frac{du}{u^2\sqrt{U}} \Bigg], \end{aligned} \tag{A.47}$$

where $u_r \equiv \frac{u_+ u_-}{u_+ - u_-} = -(2\sqrt{1-a^2})^{-1}$ is negative. Three of the terms have $p_5 = -2$ and one has $p_5 = -4$. When a limit of integration is at infinity ($u = 0$), this integral blows up, as it should. In practice, the code picks a non-infinite starting radius large enough that the geodesic trajectories from infinity to the starting radius differ negligibly from their flat space counterparts.

Then,

$$\begin{aligned} \Phi_u \quad = \quad & s_u u_r \Bigg[\left(\frac{l}{u_+} + 2(a-l) \right) \int \frac{1}{(u/u_+ - 1)} \frac{du}{\sqrt{U}} - \\ & \left(\frac{l}{u_-} + 2(a-l) \right) \int \frac{1}{(u/u_- - 1)} \frac{du}{\sqrt{U}} \Bigg], \end{aligned} \tag{A.48}$$

where both integrals are already calculated as part of T_u.

Finally, the dimensionless affine parameter can also be calculated along the path from (A.10) without any additional integrals:

$$\lambda' = s_u \int \frac{du}{u^2\sqrt{U}} + a^2 s_\mu \int \frac{\mu^2 d\mu}{\sqrt{M}}. \tag{A.49}$$

The first term is from T_u and the second term is T_μ.

Component integrals are calculated the same way as I_u or I_μ respectively. That is, μ component integrals are calculated in pieces using the appropriate coefficients as described above while u component integrals are calculated with reference to the physical turning point, if one exists. These are all the integrals required to compute null geodesics in Kerr

Table A.2. Solution for u_f

	u_f[a]	J[c]	m_1	c_1	c_2	c_3
1	$u_1 + u_{21} cd^2 J$	$c_1[I_\mu - I_u(u_0, u_2)]$	$\frac{u_{32}}{u_{31}}$	$\frac{\sqrt{u_{31} d}}{2}$	...	...
2	$u_1 + u_{31} dc^2 J$	$c_1[I_\mu + I_u(u_3, u_0)]$	$\frac{u_{32}}{u_{31}}$	$\frac{\sqrt{u_{31} d}}{2}$	...	...
3	$\frac{c_2 + u_1 - (c_2 - u_1) cnJ}{1 + cnJ}$	$c_1[I_\mu + I_u(u_1, u_0)]$	$\frac{1}{2} + \frac{6u_1 + c_3}{8c_2}$	$\sqrt{2dc_2}$	$\sqrt{u_1(3u_1 + c_3)}$	$\frac{a+l}{a-l}$
4	...	...	...	...	...	...
5	$\frac{u_4 c_5 + q_s u_1 c_4 - (q_s u_4 c_5 - u_1 c_4) cnJ}{(c_4 - q_s c_5) cnJ + q_s c_4 + c_5}$[b]	$c_1[I_\mu + I_u(u_b, u_0)]$	$q_s \frac{(c_4 + q_s c_5)^2 - (u_4 - u_1)^2}{4 c_4 c_5}$	$\sqrt{e c_4 c_5}$	...	...
6	$c_3 + \frac{n(1 + c_2^2) scJ}{1 - c_2 scJ}$	$s_u c_1[I_\mu + I_u(c_3, u_0)]$	$\left(\frac{c_4 - c_5}{c_4 + c_5}\right)^2$	$\frac{\sqrt{e}}{2}(c_4 + c_5)$	$\sqrt{\frac{4n^2 - (c_4 - c_5)^2}{(c_4 + c5)^2 - 4n^2}}$	$m + c_2 n$[d]
7	$\frac{u_2 - c_2 u_3 sn^2 J}{1 - c_2 sn^2 J}$	$c_1[I_\mu - I_u(u_0, u_2)]$	$\frac{u_{41} u_{32}}{u_{42} u_{31}}$	$\frac{\sqrt{e c_3}}{2}$	$\frac{u_{21}}{u_{31}}$	$u_{42} u_{31}$
8	$\frac{u_3 - c_2 u_2 sn^2 J}{1 - c_2 sn^2 J}$	$c_1[I_\mu + I_u(u_3, u_0)]$	$\frac{u_{41} u_{32}}{u_{42} u_{31}}$	$\frac{\sqrt{e c_3}}{2}$	$\frac{u_{43}}{u_{42}}$	$u_{42} u_{31}$

[a] $snJ = sn(J, m_1)$, $cnJ = cn(J, m_1)$, $scJ = sn(J, m_1)/cn(J, m_1)$ and $m_1 = 1 - k^2$ is used instead of k. $u_{xy} \equiv u_x - u_y$.

[b] $q_s = \mathrm{sign}(q^2)$. If $q_s = 1$ then $u_a = u_4$, $u_b = u_1$. Otherwise, $u_a = u_1, u_b = u_4$.

[c] $I_u(y, x) = s_u \int_y^x \frac{du}{\sqrt{U(u)}}$.

[d] Complex roots are written as $m \pm in$, $p \pm ir$ and are ordered so that $m > p$ and $n > 0$.

spacetime. These equations for the ϕ, t coordinates are written in Boyer-Lindquist coordinates. For certain applications, Kerr-Schild coordinates are used instead. We note here for completeness the analytic transformations between our Boyer-Lindquist coordinates and these Kerr-Schild coordinates ($\tilde{t}$,$\tilde{u}$,$\tilde{\mu}$,$\tilde{\phi}$) [76],

$$\tilde{t} = t + \log\Delta - u_r \log\left(\frac{1 - u[1 + \sqrt{1 - a^2}]}{1 - u[1 - \sqrt{1 - a^2}]}\right), \tag{A.50}$$

$$\tilde{\phi} = \phi - a\, u_r \log\left(\frac{1 - u[1 + \sqrt{1 - a^2}]}{1 - u[1 - \sqrt{1 - a^2}]}\right), \tag{A.51}$$

$$\tilde{u} = u, \tag{A.52}$$

$$\tilde{\mu} = \mu. \tag{A.53}$$

The transformations are valid outside the event horizon, where Δ and the numerators of the log terms are positive.

Table A.3 Auxillary Constants used in table A.2

	c_4	c_5
5	$\sqrt{(m-u_4)^2+n^2}$	$\sqrt{(m-u_1)^2+n^2}$
6	$\sqrt{(m-p)^2+(n+r)^2}$	$\sqrt{(m-p)^2+(n-r)^2}$

A.3 Solution for u_f

For some applications, it is preferable to use μ as the independent variable and solve for u_f given u_0. In particular, consider geodesics connecting an observer at infinity with a thin, equatorial accretion disk. The initial polar angle is the inclination of the observer. The final polar angle is $\pi/2$ ($\mu_f = 0$), and we solve for the radial coordinate where the ray intersects the disk. This method, however, is of less general utility than that described above. Even in simple geometries, the number of turning points in μ along a geodesic is not known in advance as it must be to use μ as the independent variable. One way around this is to calculate all geodesics connecting the observer with the disk for a fixed number of μ turning points [48, 195].

The approach in solving for u_f is the same as in solving for μ_f. The integral I_μ is computed as a Legendre integral of the first kind. Given the number of turning points, I_μ is computed in pieces as shown above using the coefficients $\alpha_{1,2,3}$.

After finding I_μ, we invert I_u. This inversion ranges from relatively straightforward to algebraically formidable. As examples, we discuss cubic and quartic real roots cases in detail. Table A.2 gives the solution for u_f in all cases. This problem was first addressed by Agol (1997) [2] and the solutions here are from its Table 5.2 with some modification.

For our first example, consider the first two cases of Table A.1 where there are three real roots. The integral to invert is

$$I_\mu = s_u\left(\int_{u_0}^{u_+}\frac{du}{\sqrt{U(u)}} \pm \int_{u_f}^{u_+}\frac{du}{\sqrt{U(u)}}\right), \tag{A.54}$$

where u_+ is the relevant turning point: u_2 or u_3. Denote the first term I_{u_+}, and write the second term in terms of the roots of the integrand:

$$I_\mu - I_{u_+} = \pm\frac{s_u}{\sqrt{d}}\int_{u_f}^{u_+}\frac{du}{\sqrt{(u-u_1)(u-u_2)(u-u_3)}}, \tag{A.55}$$

where $d = 2[(a-l)^2 + q^2]$. This can be put in the form (A.38) with the substitution $z = \sqrt{u-u_1}$:

$$\pm I = \int_{\sqrt{u_f-u_1}}^{\sqrt{u_+-u_1}}\frac{dz}{\sqrt{[z^2+(u_1-u_2)][z^2+(u_1-u_3)]}}, \tag{A.56}$$

where

$$I \equiv \frac{\sqrt{d}}{2}\left(I_\mu - I_{u_+}\right), \tag{A.57}$$

and I_{u_+} is determined from the same Carlson formulas as for I_u above.

Comparing (A.56) with (A.38), we see that $a_1 = u_1 - u_2$, $a_2 = u_1 - u_3$ and $b_1 = b_2 = 1$. If $u_+ = u_3$, then the limits of integration must be switched, since by definition $x > y$. These integrals correspond to the third row, third and fourth columns of Table 1 from Carlson (2005) [41], and the solutions for u_f are

$$\begin{aligned} u_f &= u_1 + (u_2-u_1)\, cd^2(J,k), \quad u_0 \le u_2 && \text{(A.58)}\\ &= u_1 + (u_3-u_1)\, dc^2(J,k), \quad u_0 \ge u_3, && \text{(A.59)}\end{aligned}$$

with

$$\begin{aligned} J &\equiv \sqrt{u_3-u_1}\, I, \qquad k^2 = \frac{u_2-u_1}{u_3-u_1}, && \text{(A.60)}\\ dc(J,k) &\equiv \frac{dn(J,k)}{cn(J,k)}, \qquad cd(J,k) \equiv \frac{cn(J,k)}{dn(J,k)}, \end{aligned}$$

where cn, dn are Jacobi-Elliptic functions. Note that the result does not depend on whether or not a turning point has been reached, since both cn and dn are even in J.

When $U(u)$ has four real roots and $u \le u_2$,

$$I_\mu - I_{u_+} = \pm\frac{s_u}{\sqrt{e}}\int_{u_f}^{u_2}\frac{du}{\sqrt{(u-u_1)(u-u_2)(u-u_3)(u_4-u)}}, \tag{A.61}$$

where $e = |aq|$. With the substitution $z = \sqrt{\frac{u_2-u}{u_3-u}}$, this becomes

$$\pm I = \int_0^{\sqrt{\frac{u_2-u_f}{u_3-u_f}}} \frac{dz}{\sqrt{[z^2+(u_1-u_2)][z^2+(u_1-u_3)]}}, \tag{A.62}$$

where

$$I \equiv \frac{\sqrt{e}}{2}\left(I_\mu - I_{u_+}\right). \tag{A.63}$$

Again comparing with (A.38) and using Carlson (2005) [41], we find

$$u_f = \frac{u_3(u_2-u_1)sn^2 - u_2(u_3-u_1)}{(u_2-u_1)sn^2-(u_3-u_1)}, \tag{A.64}$$

where

$$\begin{aligned} sn &= sn(J,k), \qquad J = \sqrt{(u_4-u_2)(u_3-u_1)}I & \text{(A.65)}\\ k^2 &= \frac{(u_4-u_3)(u_2-u_1)}{(u_4-u_2)(u_3-u_1)}. & \text{(A.66)} \end{aligned}$$

Again the result is independent of whether or not a turning point is present. In (A.54) above, the sign of the second term on the RHS depends on whether a turning point is present. This allows us to determine the number of turning points in u.

When complex roots are present, the reduction to standard form (A.38) is much more difficult. It is discussed in Erdèlyi et al. (1981) [64], and relevant formulas for the inversion can be found there and in Byrd & Friedman (1971) [36]. In particular, our cases 3,5 are from Byrd & Friedman equations 239.00 (p86) and 259.00, 260.00 (p133,135). Our formula for case 6 is based on Erdèlyi et al. Table 2, p310-311. The intricacy of these reductions demonstrates the advantage of Carlson's method. The computation of integrals is equally efficient with complex or real roots. Unfortunately, when inversion is required, Carlson (2005) is only a somewhat more compact version of Legendre's original notation and offers no real advantage over previous work.

A.4 Code checks and speed tests

Using the solution for μ_f, the equality of I_μ and I_u has been checked to machine accuracy (at least 14 significant digits in all cases). Once found, μ_f can be used as an input to recover u_f. In this way, the two routines have been shown to agree in all cases. Precision in the calculation is limited by error in the determination of the roots of $U(u)$. An advantage of using Carlson's formulation is that all component integrals are computed without reference to the complex roots, which often have less numerical precision than real ones. Formulas for u_f, discussed in Section A.3, are also written in terms of real quantities leading to higher accuracy.

Certain special cases can be integrated analytically for all components, providing independent checks on component integral formulas. These include μ cases with $q^2 = 0$, u cases with $q^2 = 0$, $l = a$ and u cases with equal physical real roots, corresponding to unstable circular photon orbits. In all of these cases, the component integral formulas above agree with the analytic results to machine accuracy. The component integral formulas above also reduce to those derived separately for the Schwarzschild case, $a = 0$. All of the formulas given here for μ_f agree with those in tables 1-2 of Rauch & Blandford [160]. The Schwarzschild formulas were also tested against the approximate formulas given by Beloborodov (2002) [20].

Further, the implementations of Carlson's integral tables have been checked extensively using the Mathematica `NIntegrate` function. The same is true of the t and ϕ formulas, as well as the individual integral components I_u, T_u, and I_μ, T_μ, Φ_μ.

The R-function routines maintain accuracy until $a \lesssim 10^{-5}$ or $q^2 \lesssim 10^{-10}$. If such parameters are encountered, the code will give a warning and set the offending value to zero.

The geodesic computations have been checked against calculations done by the code used in Falcke et al. (2000) [70] and are found to be in excellent agreement. The FORTRAN implementation of our code is found to be faster than that one by a factor of about 5, due to the fact that our code computes the minimum number of R-functions possible, and shares them between routines when necessary. The code from Agol (1997) [2] was found to be

~ 100 times faster than numerical integration in the case of tracing geodesics from infinity to a thin disk. This is an optimal problem for an analytic code, since we can solve for the point where $\mu = 0$, whereas a numerical code must integrate the geodesic from infinity until it reaches that point, and then zoom in on the intersection to find an approximate solution to the desired accuracy. In addition, this example didn't include the t and ϕ coordinates, which are sped up by a much smaller factor than u and μ.

As a lower bound for the speed improvement of our code over numerical integration, a routine was written to integrate the photon four momentum for all coordinates with respect to affine parameter using the implementation of the Bulirsch-Stoer method from Press et al. (1992) [157]. We then compared the integration of many points along a single geodesic starting from infinity with this numerical code and our analytic one. This is the ideal case for numerical integration, since the intermediate points calculated along the ray are no longer wasted as in the first example. For the case considered with no turning points in u or μ, the analytic code was found to be faster by a factor of ~ 3.

However, our numerical code for integrating geodesics is much simpler than a complete code would have to be. It cannot handle turning points, and requires knowledge of the affine parameter on the ray in order to know where the region of interest in the integration is. In practice, turning points would have to be detected and a scheme for determining the region of interest in affine parameter implemented. Alternatively, a somewhat more complicated scheme such as the Hamiltonian method described in Schnittman & Bertschinger (2004) [171] could be adopted. In any case, these additions would slow down geodesic computation. We conservatively estimate, then, that the lower bound for the speed advantage of our analytic code over numerical integration is a factor of ~ 5. A similar test for the case of integrating down to the thin disk yielded a speed difference of a factor of ~ 300, leading to an upper bound on the speed advantage of ~ 500, which is in good agreement with the naive estimate of multiplying the speedup found by Agol [2] by the speedup factor between our code and the one presented there. Then the range of speedup that can be expected by using the analytic code described here is a factor between $5 - 500$ depending mostly on the application, but also on the specific implementation of the numerical integration code. These estimates apply only to comparisons at equivalent accuracy – in particular,

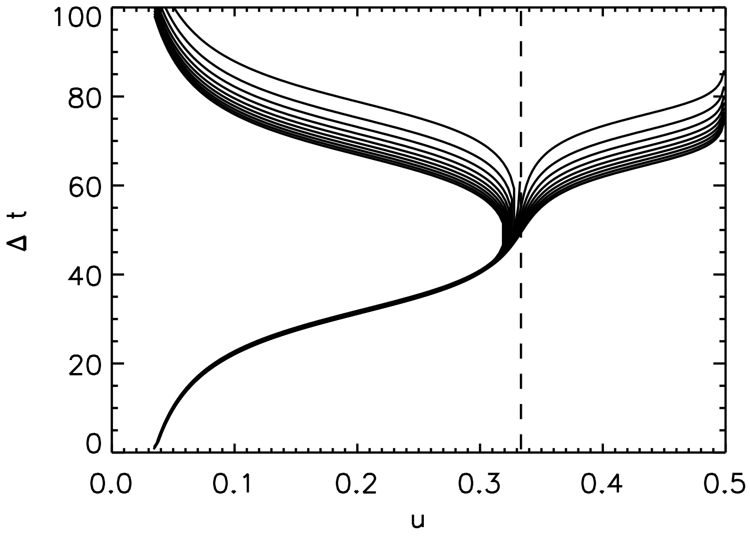

Figure A.1 Change in time vs. radial coordinate in the Schwarzschild metric for geodesics near the circular photon orbit (dashed line), as described in Section A.5.

different numerical algorithms with lower accuracy thresholds may be significantly faster than `geokerr` [62].

The analytic formulation is also much more flexible. It can calculate an arbitrary number of points beginning and ending anywhere on any geodesic, provided that the constants of the motion can be calculated. This is exploited in the thin disk toy models below, where we solve for the point $\mu_f = 0$. It could also allow, for example, a calculation of Compton scattering by tracing rays out from every point on a geodesic, and computing the scattered intensity into that point as a separate ray tracing computation. In any event, the flexibility inherent to an analytic method could allow for more sophisticated calculations in the future, which wouldn't be possible with a numerical code. The main disadvantage of using an analytic code is that the affine parameter cannot be used as an independent variable, which may be desirable for adaptive integration techniques in radiative transfer applications, for example.

A.5 Implementation

This section provides an overview of the various routines used by the code described above, and examples of their use. The README file online covers everything in this section in greater detail. The FORTRAN 77 source file `geokerr.f` contains the main program as well as the key routines, `geokerr`, `geomu`, `geor` and `geophitime`, and supporting functions. Inputs are given through command line prompt or a text file. Inputs from previous command line runs may be saved for future use. These inputs include constants of motion for the desired geodesics, initial and final u and initial μ, the number of turning points in u (ignored if the constants do not admit physical turning points), and the sign of $\dot{u}$ and $\dot{\mu}$. Constants of the motion are required and may be specified either as the impact parameters at infinity (α, β), as is most convenient in ray tracing applications, or as the dimensionless angular momentum, l, and Carter's constant, q^2. When any other information is not provided, the program assumes geodesics which trace out the entire domain of u, from the starting point and back or until the event horizon is reached.

The program calls the main subroutine, `geokerr`, which calls `geomu` to fill in missing inputs and calculate μ_f. Alternatively, `geokerr` can solve for u_f using `geor`. Subsequently, `geophitime` calculates the ϕ and t integrals using the Carlson routines. The program loops over constants of the motion for a chosen initial polar angle and black hole spin. Results are written to standard output by default, and should be redirected from the terminal to a text file in most cases. It is also possible to input the name of the desired output file. The subroutine `geokerr` encapsulates most of the code functionality, and can fairly easily be adapted to another front end other than the program used here. See the README file accompanying the code or online for more detail.

As an example use of the code, consider tracing rays over a rectangular grid in $-4 \leq \alpha \leq 8$, $-6 \leq \beta \leq 6$ for a near extreme black hole, $a = .998$. The observer is at infinity in the equatorial plane ($\mu_0 = 0$), and 20 rays will be traced over each dimension. The input file for this situation can be found online.[1]

Output is arranged as follows. The constants of the motion are listed for each geodesic

---

[1] http://www.astro.washington.edu/agol/geokerr/exfiles/abgrid.in

in the top line, followed by columns giving u_f, μ_f, Δt, $\Delta\phi$, λ. The format used for output can be changed with a tiny modification to the source code. See the README file for more details. Plotting the affine parameter evaluated at either the event horizon, or once the geodesic returns to its initial radius, as a function of impact parameters for this data with $160,000$ geodesics produces Figure 2.1 as explained below.

For less standard batch runs, it may be necessary to generate the input file from a simple program. Consider a set of geodesics in the Schwarzschild metric ($a = 0$) to study the unstable circular photon orbits. The given parameters are chosen to be $u_0 = 1/30$, $u_f = u_+ = .5$, $\mu_0 = .9$, $\beta = 0$ and an array of values for α near $\sqrt{27}$.

The piece of code to write an appropriate input file is available online.[2] Plotting the change in time as a function of final radial coordinate produces Figure A.1.

---

[2] http://www.astro.washington.edu/agol/geokerr/exfiles/inputex.f

Appendix B

GENERAL RELATIVISTIC POLARIZED RADIATIVE TRANSFER

The polarized radiative transfer equation can be written in the form,

$$\frac{d}{ds}\begin{pmatrix} I \\ Q \\ U \\ V \end{pmatrix} = \begin{pmatrix} j_I \\ j_Q \\ j_U \\ j_V \end{pmatrix} - \begin{pmatrix} \alpha_I & \alpha_Q & \alpha_U & \alpha_V \\ \alpha_Q & \alpha_I & \rho_V & \rho_U \\ \alpha_U & -\rho_V & \alpha_I & \rho_Q \\ \alpha_V & -\rho_U & -\rho_Q & \alpha_I \end{pmatrix}\begin{pmatrix} I \\ Q \\ U \\ V \end{pmatrix} \tag{B.1}$$

which is the same form as the unpolarized case (Eq. (2.3)), except that I_ν and j_ν are now vectors with components corresponding to the Stokes parameters (I, Q, U, V) and the 4x4 transfer matrix, K, takes the place of the scalar absorption coefficient α_ν.

In the context of synchrotron radiation, the transfer equation can be simplified by aligning the magnetic field with Stokes U, so that $j_U = \alpha_U = \rho_U = 0$. Then j_Q, α_Q (j_V, α_V) correspond to the emission and absorption coefficients for linear (circular) polarization and j_I, α_I correspond to j_ν, α_ν from the unpolarized case. The transfer coefficients $\rho_{Q,V}$ describe the effects of Faraday conversion and rotation respectively.

The radiative transfer coefficients are computed in the fluid rest frame, where ν is the emitted frequency, related to the observed frequency at infinity through the redshift, $g = \nu_0/\nu$. Then the transfer equation is recast into general relativistic form by using the invariant forms for the intensity, emissivity and transfer matrix. The required invariants are the photon occupation numbers, $\mathcal{I} = \mathbf{I}/\nu^3$ the invariant emissivity, $\mathcal{J} = \mathbf{j}/\nu^2$ and the invariant transfer matrix $\mathcal{K} = \nu\mathbf{K}$, where $\mathbf{I}$, $\mathbf{j}$ and $\mathbf{K}$ are the intensity and emissivity vectors and the transfer matrix from Eq. B.1.

The polarization at infinity is measured with respect to the local horizontal and vertical axes defining the camera (Chapter 2). After transforming this basis to the fluid frame, the transfer equation can be rotated from the basis aligned with the magnetic field to that as observed at infinity. There are then two steps: to relate the Stokes basis at infinity with that at points in the accretion flow, and to find the angle between the transported basis and the projected magnetic field.

B.1 Parallel Transport of the Polarization Basis

The basis vectors relating the local polarization to that at infinity are everywhere perpendicular to the wave four-vector, and can be related between different points on a geodesic via parallel transport. The time components of these basis vectors can be assumed to vanish without any loss of generality [47, 45]. In the case of the Kerr metric, this procedure is simplified by the existence of a complex constant called the Walker-Penrose constant, which can be calculated from k^μ and a vector perpendicular to it, a^μ, in Boyer-Lindquist coordinates as [46, 47, 45]:

$$\begin{aligned} K_1 - iK_2 = (r - ia\cos\theta)((k^t a^r - k^r a^t) + a\sin^2\theta(k^r a^\phi - k^\phi a^r) \\ -i[(r^2+a^2)(k^\phi a^\theta - a^\phi k^\theta) - a(k^t a^\theta - k^\theta a^t)]\sin\theta) \end{aligned} \tag{B.2}$$

where a is the dimensionless black hole spin (not to be confused with the basis four-vector a^μ). The real and imaginary parts of the constant, K_1 and K_2, provide two constraints on the transported basis vectors, while the orthogonality condition $k^\mu a_\mu = 0$ provides a third. Since the basis vectors are already only defined up to a multiple of the wave vector, these constraints suffice to calculate their coordinates anywhere along the ray. The orthonormality condition $a^\mu a_\mu = 1$ can be used to check the result. Taking $a^t = 0$ leaves three linear equations for the three remaining components of a^μ:

$$K_1 = \delta_1 a^r + \delta_2 a^\theta + \delta_3 a^\phi \tag{B.3}$$

$$K_2 = \gamma_1 a^r + \gamma_2 a^\theta + \gamma_3 a^\phi \tag{B.4}$$

$$k^\mu a_\mu = 0 \tag{B.5}$$

with

$$\begin{aligned}
\delta_1 &= rk^t - ra\sin^2\theta k^\phi && \text{(B.6)}\\
\delta_2 &= a^2\sin\theta\cos\theta k^t - a\cos\theta\sin\theta(r^2+a^2)k^\phi && \text{(B.7)}\\
\delta_3 &= ra\sin^2\theta k^r + a\cos\theta\sin\theta(r^2+a^2)k^\theta && \text{(B.8)}\\
\gamma_1 &= a\cos\theta k^t - a^2\cos\theta\sin^2\theta k^\phi && \text{(B.9)}\\
\gamma_2 &= r(r^2+a^2)\sin\theta k^\phi - ar\sin\theta k^t && \text{(B.10)}\\
\gamma_3 &= a^2\cos\theta\sin^2\theta k^r - r(r^2+a^2)\sin\theta k^\theta. && \text{(B.11)}
\end{aligned}$$

The components of a^μ can then be calculated as:

$$a^r = \frac{K_1 + \tilde{\delta}_2/\tilde{\gamma}_2 K_2}{\tilde{\delta}_1 + \tilde{\gamma}_1/\tilde{\gamma}_2\tilde{\delta}_2} \tag{B.12}$$

$$a^\theta = \frac{1}{\tilde{\gamma}_2}(K_2 - \tilde{\gamma}_1 a^r) \tag{B.13}$$

$$a^\phi = -\frac{g_{11}a^r k^r + g_{22}f^\theta k^\theta}{g_{33}k^\phi + g_{03}k^t}. \tag{B.14}$$

where

$$\tilde{\gamma}_i, \tilde{\delta}_i = \gamma_i, \delta_i - \gamma_3, \delta_3 \frac{g_{ii}k^i}{g_{33}k^\phi + g_{03}k^t} \tag{B.15}$$

$g_{\mu\nu}$ are the covariant metric components and $i = 1, 2$.

Transforming the polarization basis vectors at infinity then requires knowledge of K_1 and K_2. These can be found from the asymptotic form of B.2. In the case of transporting the unit vectors $\hat{\theta}$, $\hat{\phi}$ at infinity, they are given by $K_1 = \beta$, $K_2 = \gamma$ and $K_1 = \gamma$, $K_2 = -\beta$ respectively, where $\gamma = -\alpha - a\sin\theta$.

B.2 Transformation to the Orthonormal Fluid Frame

The final step is to relate the emission coefficients and the transfer matrix computed in the fluid frame aligned with the magnetic field to the transported polarization basis. This requires finding the angle between the transported polarization basis vectors and the magnetic field vector projected into the polarization plane. A straightforward method for this is to use the fluid four-velocity to transform into the orthonormal frame comoving with the fluid where the four-velocity is $\hat{u^{\mu}} = (1, 0, 0, 0)$. The basis four-vectors of the transformation are [18, 185, 109]:

$$\begin{aligned} e^{\mu}_{(t)} &= u^{\mu}, && \text{(B.16)} \\ e^{\mu}_{(r)} &= (u_r u^t, -(u_t u^t + u_{\phi} u^{\phi}), 0, u_r u^{\phi})/N_r, && \text{(B.17)} \\ e^{\mu}_{(\theta)} &= (u_{\theta} u^t, u_{\theta} u^r, 1 + u_{\theta} u^{\theta}, u_{\theta} u^{\phi})/N_{\theta}, && \text{(B.18)} \\ e^{\mu}_{(\phi)} &= (u_{\phi}, 0, 0, -u_t)/N_{\phi}, && \text{(B.19)} \end{aligned}$$

where the upper (lower) indices are lowered (raised) with the Kerr (Minkowski) metric and,

$$\begin{aligned} N_r^2 &= -g_{rr}(u_t u^t + u_{\phi} u^{\phi})(1 + u_{\theta} u^{\theta}), && \text{(B.20)} \\ N_{\theta}^2 &= g_{\theta\theta}(1 + u_{\theta} u^{\theta}), && \text{(B.21)} \\ N_{\phi}^2 &= -(u_t u^t + u_{\phi} u^{\phi})\Delta \sin^2\theta, && \text{(B.22)} \\ \Delta &= r^2 - 2r + a^2. && \text{(B.23)} \end{aligned}$$

Four-vectors in the coordinate frame are transformed as,

$$A_{(\alpha)} = e^{\mu}_{(\alpha)} A_{\mu}. \tag{B.24}$$

The projected magnetic field is then found in the orthonormal, comoving basis as

$$\hat{\mathbf{B}}_{\perp} = \hat{\mathbf{B}} - \hat{\mathbf{k}}(\hat{\mathbf{B}} \cdot \hat{\mathbf{k}})/k^2, \tag{B.25}$$

where bolded quantities are three-vectors and hats denote quantities in the comoving, orthonormal frame. The angle χ between the projected magnetic field and the polarization basis is,

$$\begin{aligned} \sin\chi &= (\hat{\mathbf{a}} \cdot \hat{\mathbf{B}}_{\perp})/|\hat{\mathbf{B}}_{\perp}|, && \text{(B.26)} \\ \cos\chi &= -(\hat{\mathbf{b}} \cdot \hat{\mathbf{B}}_{\perp})/|\hat{\mathbf{B}}_{\perp}|. && \text{(B.27)} \end{aligned}$$

This procedure can be used to check the methods used previously to compute the redshift and the angle between the magnetic field and wave four-vectors, since $\hat{k}^t = 1/g$ and $\theta_B = \arccos\left(\frac{\hat{\mathbf{k}}\cdot\hat{\mathbf{B}}}{|\hat{\mathbf{k}}||\hat{\mathbf{B}}|}\right)$.

B.3 Transfer Equation

With χ in hand, the polarized radiative transfer equation can be written as,

$$\frac{d\mathcal{I}}{d\lambda} = \mathcal{J} - \hat{\mathcal{K}}\mathcal{I} \tag{B.28}$$

where λ is an affine parameter, $\hat{\mathcal{K}} = g^{-1}R(\chi)KR(-\chi)$ and,

$$R(\chi) = \begin{pmatrix} 1 & 0 & 0 & 0 \\ 0 & \cos 2\chi & -\sin 2\chi & 0 \\ 0 & \sin 2\chi & \cos 2\chi & 0 \\ 0 & 0 & 0 & 1 \end{pmatrix}, \tag{B.29}$$

is a rotation matrix mixing the Q and U Stokes parameters due to the transformation from the magnetic to the polarization basis and to the parallel transport of the polarization four-vector along the ray.

Equation B.28 includes all relativistic effects. The bending of light is accounted for by the calculation of null geodesics (Appendix A), the gravitational redshifts and Doppler shifts due to fluid motions are included in g, computed either via the locally non-rotating or the comoving (fluid) orthonormal frame. The parallel transport of the polarization basis provides a straightforward means to include the parallel transport of the polarization four-vector along the ray.

Appendix C

POLARIZED SYNCHROTRON EMISSION AND ABSORPTION COEFFICIENTS FOR THERMAL AND POWER LAW PARTICLE DISTRIBUTIONS

The subject of radiation from gyrating electrons in a magnetic field has been extensively studied, especially in the relativistic "synchrotron" limit where the electron energy $\gamma \gtrsim 1$ [199, 88, 89, 112, 169, 23, 131, 104, 168]. However, a consistent treatment of the derivation of the polarized emission and absorption coefficients for the two most commonly used particle distributions (thermal and power law) is still lacking. This appendix gives examples of deriving the various coefficients from integrating the single particle polarized synchrotron emissivity over distributions of particles and provides approximate formulae for their evaluation. The results are compared to emissivities found in the literature and in some cases to numerical integration.

The Stokes basis in the emitting frame has $B = (0, 0, 1)$, $\mathbf{e^1} = (-\cos\theta, 0, \sin\theta)$ and $\mathbf{e^2} = (0, 1, 0)$ where θ is the angle between B and the wave-vector k and $\mathbf{e^1}$, $\mathbf{e^2}$ are aligned with Stokes Q and U and the projection of B onto the Stokes basis is entirely along $\mathbf{e^2}$. Then the vacuum emissivity can be written as a rank-2 tensor [e.g. 132]:

$$\eta^{\alpha\beta} = \frac{\sqrt{3}e^2}{8\pi c}\nu_b \sin\theta H^{\alpha\beta}(\nu,\theta), \tag{C.1}$$

where e is the electron charge, c is the speed of light, $\nu_b = \frac{eB}{2\pi mc}$, and

$$H^{11} = F\left(\frac{\nu}{\gamma^2\nu_c}\right) - G\left(\frac{\nu}{\gamma^2\nu_c}\right), \tag{C.2}$$

$$H^{22} = F\left(\frac{\nu}{\gamma^2\nu_c}\right) + G\left(\frac{\nu}{\gamma^2\nu_c}\right), \tag{C.3}$$

$$H^{12} = -H^{21} = \frac{4i\cot\theta}{3\gamma}H\left(\frac{\nu}{\gamma^2\nu_c}\right), \tag{C.4}$$

where ν is the emitted frequency, γ is the electron Lorentz factor, $\nu_c = 3/2\nu_b\sin\theta$ and

$$
\begin{aligned}
F(x) &= x\int_x^\infty dy K_{5/3}(y), && \text{(C.5)}\\
G(x) &= xK_{2/3}(x), && \text{(C.6)}\\
H(x) &= \int_x^\infty dy K_{1/3}(y) + xK_{1/3}(x), && \text{(C.7)}
\end{aligned}
$$

are the synchrotron functions for total, linearly and circularly polarized emission respectively and $K_\alpha(z)$ is the modified Bessel function.

To compute the emissivity from a distribution of electrons, these formulae are integrated over the particle distribution:

$$
j^{\alpha\beta} = \int_0^\infty d\gamma N(\gamma)\eta^{\alpha\beta}. \tag{C.8}
$$

The Stokes emissivities are then given as $j_I = j^{22} + j^{11}$, $j_Q = j^{22} - j^{11}$, $j_U = j_{12} + j_{12}$, and $j_V = i(j_{12} - j_{21})$. For this Stokes basis, j_U vanishes.

The two most commonly used particle distributions for astrophysical sources are the relativistic thermal (Maxwell) distribution,

$$
N(\gamma) = \frac{n\gamma^2\beta\exp\left(-\gamma/\theta_e\right)}{\theta_e K_2(1/\theta_e)} \tag{C.9}
$$

where n is the electron number density and $\theta_e = kT/mc^2$ is the dimensionless electron temperature; and the power law distribution,

$$
N(\gamma) = \begin{cases} n(p-1)(\gamma_1^{1-p} - \gamma_2^{1-p})^{-1}\gamma^{-p} & \gamma_1 < \gamma < \gamma_2 \\ 0 & \text{otherwise} \end{cases}
$$

where $\gamma_{1,2}$ are the low- and high-energy cutoffs of the distribution.

We consider these two cases in turn and derive approximate formulae for their evaluation.

C.1 Ultrarelativistic Thermal Distribution

For the thermal distribution, substituting Eq. C.9 into Eq. C.8 with $\beta \simeq 1$ and $\theta_e \gg 1$ gives,

$$j^{\alpha\beta} = \frac{\sqrt{3}ne^2\nu_b \sin\theta}{8\pi\theta_e(2\theta_e^2)} \int_0^\infty d\gamma\gamma^2 \exp(-\gamma/\theta_e) H^{\alpha\beta}(\nu,\theta), \tag{C.10}$$

where the approximate form of the modified bessel function for small argument $K_2(z) \to 2z^2$ was used. First substitute $z \equiv \gamma/\theta_e$ so that,

$$j^{\alpha\beta} = \frac{\sqrt{3}ne^2\nu_b \sin\theta\theta_e^2}{8\pi c(2\theta_e^2)} \int_0^\infty dz z^2 \exp(-z) H^{\alpha\beta}(\nu,\theta). \tag{C.11}$$

Finally, we substitute γ for z in the synchrotron functions and use the relations between $j^{\alpha\beta}$ and $j_{I,Q,V}$ to find:

$$j_I(\nu,\theta) = \frac{ne^2\nu}{2\sqrt{3}c\theta_e^2} I_I(x), \tag{C.12}$$

$$j_Q(\nu,\theta) = \frac{ne^2\nu}{2\sqrt{3}c\theta_e^2} I_Q(x), \tag{C.13}$$

$$j_V(\nu,\theta) = \frac{2ne^2\nu\cot\theta}{3\sqrt{3}c\theta_e^3} I_V(x), \tag{C.14}$$

where $x \equiv \nu/(\theta_e^2\nu_c)$, and the thermal synchrotron integrals are,

$$I_I(x) = \frac{1}{x}\int_0^\infty dz z^2 \exp(-z) F\left(\frac{x}{z^2}\right), \tag{C.15}$$

$$I_Q(x) = \frac{1}{x}\int_0^\infty dz z^2 \exp(-z) G\left(\frac{x}{z^2}\right), \tag{C.16}$$

$$I_V(x) = \frac{1}{x}\int_0^\infty dz z \exp(-z) H\left(\frac{x}{z^2}\right). \tag{C.17}$$

This result agrees with the formulae from previous work [169, 122, 99]. The integrals can be approximated analytically with high accuracy by matching the asymptotic behavior for small and large arguments and fitting polynomials in the transition region [122]. We find the following approximate forms,

$$I_I(x) = 2.5651(1 + 1.92x^{-1/3} + 0.9977x^{-2/3}) \exp(-1.8899x^{1/3}), \tag{C.18}$$

$$I_Q(x) = 2.5651(1 + 0.932x^{-1/3} + 0.4998x^{-2/3}) \exp(-1.8899x^{1/3}), \tag{C.19}$$

$$I_V(x) = (1.8138x^{-1} + 3.423x^{-2/3} + 0.02955x^{-1/2} + 2.0377x^{-1/3}) \exp(-1.8899x^{1/3}), \tag{C.20}$$

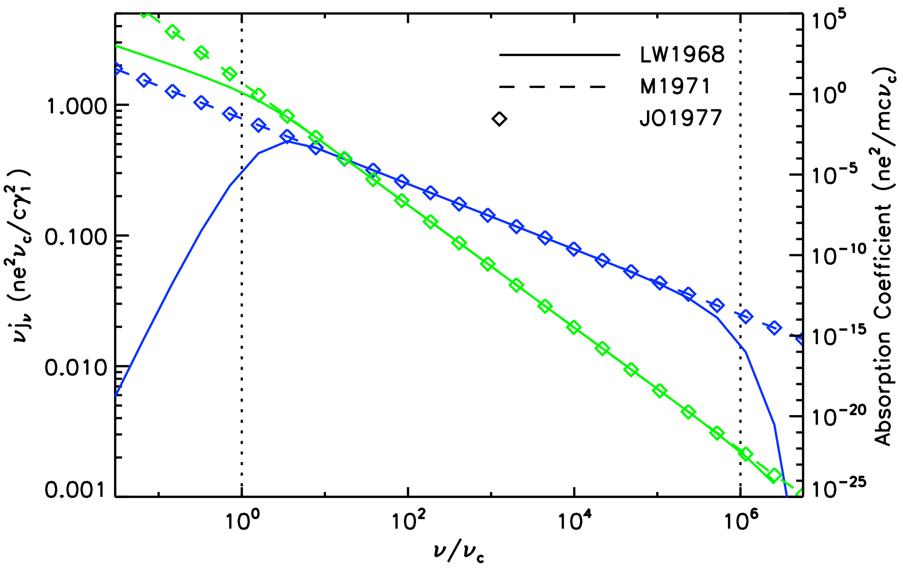

Figure C.1 Total emission (blue) and absorption (green) coefficients from this work and Legg & Westfold (solid), Melrose (dashed) and Jones & Odell (diamonds).

all agree with numerical integration to within $\lesssim$ 1% for all x. The function $I_I(x)$ here corresponds to $I(x_M)$ from Mahadevan et al.

The absorption coefficients can be computed from the emission coefficients assuming local thermodynamic equilibrium so that Kirchoff's Law, $j_\nu = \alpha_\nu B_\nu$, holds with B_ν the blackbody function [e.g. 168].

C.2 Power Law Distribution

In this case, $x \equiv \nu/(\gamma^2\nu_c)$ is used to change the variable of integration to x after plugging in the distribution (Eq. C):

$$j^{\alpha\beta} = \frac{(p-1)ne^2\nu_c}{4\sqrt{3}c(\gamma_1^{1-p} - \gamma_2^{1-p})} \left(\frac{\nu}{\nu_c}\right)^{-\frac{p-1}{2}} \int_{x_1}^{x_2} dx x^{\frac{p-3}{2}} H^{\alpha\beta}(\nu, \theta). \tag{C.21}$$

Then the three emissivities can be written:

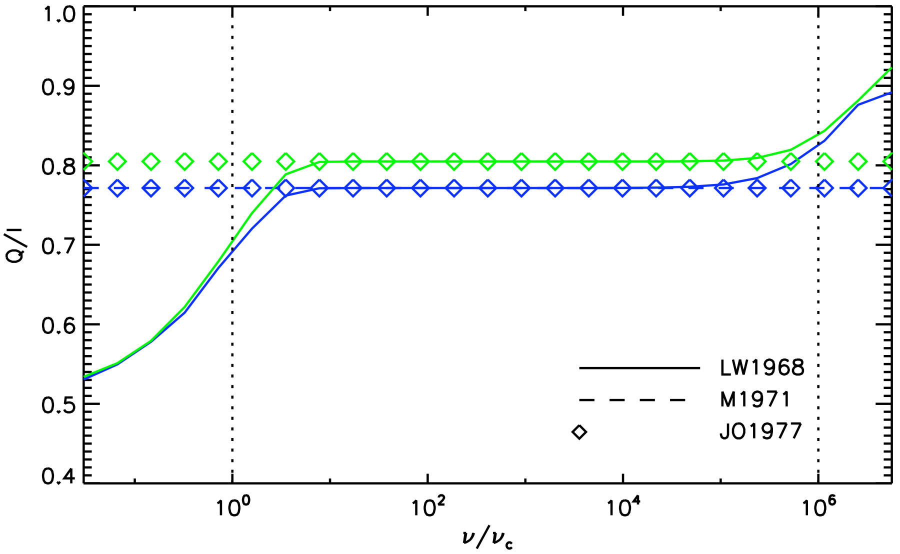

Figure C.2 Linear polarization fraction in emission (blue) and absorption (green) coefficients from this work and Legg & Westfold (solid), Melrose (dashed) and Jones & Odell (diamonds).

$$
\begin{aligned}
j_I &= \frac{ne^2(p-1)\nu_c}{2\sqrt{3}c(\gamma_1^{1-p}-\gamma_2^{1-p})}\left(\frac{\nu}{\nu_c}\right)^{-\frac{p-1}{2}}[G_I(x_1)-G_I(x_2)], && \text{(C.22)}\\
j_Q &= \frac{ne^2(p-1)\nu_c}{2\sqrt{3}c(\gamma_1^{1-p}-\gamma_2^{1-p})}\left(\frac{\nu}{\nu_c}\right)^{-\frac{p-1}{2}}[G_Q(x_1)-G_Q(x_2)], && \text{(C.23)}\\
j_V &= \frac{2ne^2(p-1)\nu_c\cot\theta}{3\sqrt{3}c(\gamma_1^{1-p}-\gamma_2^{1-p})}\left(\frac{\nu}{\nu_c}\right)^{-\frac{p}{2}}[G_V(x_1)-G_V(x_2)], && \text{(C.24)}\\
& && \text{(C.25)}
\end{aligned}
$$

where the power law synchrotron integrals are,

$$
\begin{aligned}
G_I(x) &= \int_x^\infty dz z^{\frac{p-3}{2}}F(z), && \text{(C.26)}\\
G_Q(x) &= \int_x^\infty dz z^{\frac{p-3}{2}}G(z), && \text{(C.27)}\\
G_V(x) &= \int_x^\infty dz z^{\frac{p}{2}-1}H(z). && \text{(C.28)}
\end{aligned}
$$

In many prior studies [112, 23, 131, 104] the integrals are performed analytically for the frequency range $\nu_{c,min} \ll \nu \ll \nu_{c,max}$ where the limits of integration, $x_{1,2} = \nu/(\gamma_{1,2}^2 \nu_c)$ can be extended to 0 and ∞.

For the primary non-thermal source considered in this thesis, M87,

$$\nu_{c,min} \sim 2 \times 10^{11} \left(\frac{B}{10G}\right)\left(\frac{\gamma_1}{100}\right)^2 \mathrm{Hz}, \tag{C.29}$$

uncomfortably close to frequencies of interest for mm-VLBI for $\gamma_1 \gtrsim 30$. We then keep the finite limits of integration and numerically tabulate the integrals G_I, G_Q and G_V as functions of x for desired values of p. This procedure can be sped up significantly using the relation [199],

$$\begin{aligned} L(x; s, \alpha) &\equiv \int_x^\infty d\xi \xi^{s-1} \int_\xi^\infty dy K_\alpha(y) \\ &= \frac{\alpha+s}{s} \int_x^\infty d\xi \xi^{s-1} K_\alpha(\xi) - \frac{x^s}{s}\left[\int_x^\infty dy K_{\alpha+1}(y) - K_\alpha(x)\right] \end{aligned} \tag{C.30}$$

to reduce the double integrals to single integrals. The results agree with those in Legg & Westfold Eq. (33) after using a recurrence relation,

$$2K'_\alpha(x) = -(K_{\alpha+1} + K_{\alpha-1}), \tag{C.31}$$

and noting that $K_{-\alpha}(x) = K_\alpha(x)$ to transform the Bessel functions in $H(x)$.

To check against approximate formulae elsewhere, we extend the limits of integration to 0 and ∞ and use,

$$I(s,\alpha) \equiv \int_0^\infty dx x^s K_\alpha(x) = 2^{s-1}\Gamma\left(\frac{s+\alpha+1}{2}\right)\Gamma\left(\frac{s-\alpha+1}{2}\right) \tag{C.32}$$

$$\begin{aligned} J(s,\alpha) &\equiv L(0; s+1, \alpha-1) = \frac{\alpha+s}{s+1} I(s, \alpha-1) \\ &= \frac{\alpha+s}{s+1} 2^{s-1}\Gamma\left(\frac{s+\alpha}{2}\right)\Gamma\left(\frac{s-\alpha}{2}+1\right) \end{aligned} \tag{C.33}$$

to find the approximate forms $G_{I,Q,V}(0) - G_{I,Q,V}(\infty)$:

$$\begin{aligned}
G_I(0) &= J\left(\frac{p-1}{2}, \frac{5}{3}\right) = \frac{2^{\frac{p-3}{2}}(p+7/3)}{p+1}\Gamma\left(\frac{p}{4}+\frac{7}{12}\right)\Gamma\left(\frac{p}{4}-\frac{1}{12}\right), && \text{(C.34)}\\
G_Q(0) &= I\left(\frac{p-1}{2}, \frac{2}{3}\right) = \frac{p+1}{p+7/3}G_I(0), && \text{(C.35)}\\
G_V(0) &= J\left(\frac{p}{2}-1, \frac{1}{3}\right) + I\left(\frac{p}{2}, \frac{1}{3}\right)\\
&= \frac{2^{\frac{p}{2}-1}(p+2)}{p}\Gamma\left(\frac{p}{4}+\frac{1}{3}\right)\Gamma\left(\frac{p}{4}+\frac{2}{3}\right), && \text{(C.36)}\\
G_{I,Q,V}(\infty) &= 0 && \text{(C.37)}
\end{aligned}$$

leading to the approximate emissivities:

$$\begin{aligned}
j_I^0 &= \frac{ne^2(p-1)\nu_c}{2\sqrt{3}c(\gamma_1^{1-p}-\gamma_2^{1-p})}\left(\frac{\nu}{\nu_c}\right)^{-\frac{p-1}{2}} 2^{\frac{p-3}{2}}\frac{p+7/3}{p+1}\Gamma\left(\frac{p}{4}+\frac{7}{12}\right)\Gamma\left(\frac{p}{4}-\frac{1}{12}\right), && \text{(C.38)}\\
j_Q^0 &= \frac{p+1}{p+7/3}j_I^0, && \text{(C.39)}\\
j_V^0 &= \frac{2ne^2(p-1)\nu_c\cot\theta}{3\sqrt{3}c(\gamma_1^{1-p}-\gamma_2^{1-p})}\left(\frac{\nu}{\nu_c}\right)^{-\frac{p}{2}} 2^{\frac{p}{2}-1}\frac{p+2}{p}\Gamma\left(\frac{p}{4}+\frac{1}{3}\right)\Gamma\left(\frac{p}{4}+\frac{2}{3}\right). && \text{(C.40)}
\end{aligned}$$

These results agree with those of several authors.

In the case of non-thermal emission, the absorption coefficient cannot be simply related to the emissivity using Kirchoff's Law, and instead we use [132]:

$$\alpha^{\alpha\beta} = -\frac{c}{m\nu^2}\int_0^\infty d\gamma\gamma^2\frac{d}{d\gamma}\left[\frac{N(\gamma)}{\gamma^2}\right]\eta^{\alpha\beta}(\gamma,\nu,\theta). \qquad \text{(C.41)}$$

The derivation is analogous to that for the emissivity, and the results are:

$$\alpha_I = \frac{ne^2(p-1)(p+2)}{4\sqrt{3}mc\nu_c(\gamma_1^{1-p}-\gamma_2^{1-p})}\left(\frac{\nu}{\nu_c}\right)^{-\frac{p}{2}-2}\left[Ga_I(x_1)-Ga_I(x_2)\right], \qquad \text{(C.42)}$$

$$\alpha_Q = \frac{ne^2(p-1)(p+2)}{4\sqrt{3}mc\nu_c(\gamma_1^{1-p}-\gamma_2^{1-p})}\left(\frac{\nu}{\nu_c}\right)^{-\frac{p}{2}-2}\left[Ga_Q(x_1)-Ga_Q(x_2)\right], \qquad \text{(C.43)}$$

$$\alpha_V = \frac{ne^2(p-1)(p+2)\cot\theta}{3\sqrt{3}mc\nu_c(\gamma_1^{1-p}-\gamma_2^{1-p})}\left(\frac{\nu}{\nu_c}\right)^{-\frac{p+5}{2}}\left[Ga_V(x_1)-Ga_V(x_2)\right] \qquad \text{(C.44)}$$

where the power law absorption integrals are,

$$Ga_I(x) = \int_x^\infty dz z^{\frac{p}{2}-1} F(z), \tag{C.45}$$

$$Ga_Q(x) = \int_x^\infty dz z^{\frac{p}{2}-1} G(z), \tag{C.46}$$

$$Ga_V(x) = \int_x^\infty dz z^{\frac{p-1}{2}} H(z). \tag{C.47}$$

Again extending the limits of integration, we find agreement with approximate formulae in the literature:

$$Ga_I(0) = \frac{p+10/3}{p+1} 2^{\frac{p}{2}-1} \Gamma\left(\frac{p}{4}+\frac{5}{6}\right) \Gamma\left(\frac{p}{4}+\frac{1}{6}\right), \tag{C.48}$$

$$Ga_Q(0) = \frac{p+2}{p+10/3} Ga_I(0) \tag{C.49}$$

$$Ga_V(0) = \frac{p+3}{p+1} 2^{\frac{p-1}{2}} \Gamma\left(\frac{p}{4}+\frac{7}{12}\right) \Gamma\left(\frac{p}{4}+\frac{11}{12}\right), \tag{C.50}$$

$$Ga_{I,Q,V}(\infty) = 0. \tag{C.51}$$

Figure C.1 compares numerical integration of the exact formulae in Equations (C.22) and (C.42) with the forms from the literature. Figure C.2 compares the linear polarization fraction from the exact and approximate forms.